Fluid Characterization by Resonant Nanomechanical Sensing

Inauguraldissertation
zur
Erlangung der Würde eines Doktors der Philosophie
vorgelegt der
Philosophisch-Naturwissenschaftlichen Fakultät
der Universität Basel
von

Benjamin A. Bircher

aus Küttigen, Aargau, Schweiz

Basel, Schweiz, 2014

Genehmigt von der Philosophisch-Naturwissenschaftlichen Fakultät
auf Antrag von

Prof. Dr. Henning Stahlberg & Prof. Dr. Ernst Meyer

Basel, den 11. November 2014

Prof. Dr. Jörg Schibler

Namensnennung-Keine kommerzielle Nutzung-Keine Bearbeitung 3.0 Schweiz
(CC BY-NC-ND 3.0 CH)

Sie dürfen: **Teilen** — den Inhalt kopieren, verbreiten und zugänglich machen

Unter den folgenden Bedingungen:

Namensnennung — Sie müssen den Namen des Autors/Rechteinhabers in der von ihm festgelegten Weise nennen.

Keine kommerzielle Nutzung — Sie dürfen diesen Inhalt nicht für kommerzielle Zwecke nutzen.

Keine Bearbeitung erlaubt — Sie dürfen diesen Inhalt nicht bearbeiten, abwandeln oder in anderer Weise verändern.

Wobei gilt:

- **Verzichtserklärung —** Jede der vorgenannten Bedingungen kann **aufgehoben** werden, sofern Sie die ausdrückliche Einwilligung des Rechteinhabers dazu erhalten.
- **Public Domain (gemeinfreie oder nicht-schützbare Inhalte) —** Soweit das Werk, der Inhalt oder irgendein Teil davon zur Public Domain der jeweiligen Rechtsordnung gehört, wird dieser Status von der Lizenz in keiner Weise berührt.
- **Sonstige Rechte —** Die Lizenz hat keinerlei Einfluss auf die folgenden Rechte:
    - Die Rechte, die jedermann wegen der Schranken des Urheberrechts oder aufgrund gesetzlicher Erlaubnisse zustehen (in einigen Ländern als grundsätzliche Doktrin des **fair use** bekannt);
    - Die **Persönlichkeitsrechte** des Urhebers;
    - Rechte anderer Personen, entweder am Lizenzgegenstand selber oder bezüglich seiner Verwendung, zum Beispiel für **Werbung** oder Privatsphärenschutz.
- **Hinweis —** Bei jeder Nutzung oder Verbreitung müssen Sie anderen alle Lizenzbedingungen mitteilen, die für diesen Inhalt gelten. Am einfachsten ist es, an entsprechender Stelle einen Link auf diese Seite einzubinden.

Quelle: http://creativecommons.org/licenses/by-nc-nd/3.0/ch/ Datum: 12.11.2013

Summary

Microfluidic technologies allow handling and characterizing liquid samples on the micro- to picoliter scale. Thereby, the viscosity and mass density are key properties of such samples, because they characterize their flow behavior. The viscosity of a liquid indicates its resistance to flow, whereas the density quantifies the mass per volume. Molecular transformations, such as chemical polymerization, protein folding and aggregation, or nucleic acid hybridization, influence both properties. Therefore, measuring them is fundamental for basic research, quality control, and process monitoring. Since many, especially biological, samples are only available in small quantities and/or expensive, reducing sample consumption is essential. Furthermore, the acquisition time of viscosity measurements nowadays is on the order of minutes, limiting the characterization of large numbers of samples. Hence, increasing the time resolution and the throughput is another significant requirement.

It was early noticed that the dynamics of nanomechanical resonators are strongly influenced by the surrounding fluid. This effect can be utilized to measure the fluid properties, specifically the viscosity and mass density. In this thesis, resonant nanomechanical cantilevers were, therefore, employed with focus on the application of higher modes of vibration.

First, a suitable method to excite and detect the strongly damped cantilever resonances encountered in liquid was realized: Photothermal excitation uses an intensity-modulated laser to induce cantilever vibration. Its direct and local energy transfer avoids distortions arising in prevalent excitation methods, such as piezo-acoustic excitation, and results in spurious-free resonance spectra. To detect the nanometer vibrations of the cantilevers, a second laser was used in an optical beam deflection configuration. Such optical excitation/detection method is accurate and robust, however, it is only suitable for transparent liquids. Technical details about the developed setup are provided in the appendix of this thesis. Due to the small dimensions of the microfluidic channel containing the cantilever sensors, the influence of proximate surfaces was investigated. Placing a vibrating cantilever below a critical distance to a surface induces squeeze-film damping. The magnitude and range of this undesirable effect on higher mode vibrations was characterized and incorporated in the fluid channel design. The above findings are generally applicable to atomic force microscopy and nanomechanical sensing in liquid.

Next, the ability of the sensor to measure viscosity and mass density of liquids was assessed. Dynamic properties of the cantilever resonator were derived from resonance spectra and converted into the surrounding liquid properties, using adapted hydrodynamic models. Multiple modes of vibration covered a broad frequency range in the order of kHz to MHz. A stringent temperature control was implemented, due to the high temperature dependency of the measured parameters. To investigate time-resolved processes, free-radical polymerization reactions were tracked and characterized. The shear-thinning behavior of the polymer solutions, i.e., the non-Newtonian effect of decreasing viscosity with increasing frequency, was resolved by the instrument. The time to characterize a 5 μL sample was on the order of 1 min.

Finally, the setup was optimized for automated high-throughput screening of microliter sample droplets. The droplets were generated by an automated sampler and separated by fluorinated oil. To achieve the required time resolution, a higher vibrational mode was tracked using two phase-locked loop demodulators. This allowed to derive the viscosity and mass density of the liquid surrounding the resonator with a temporal resolution of about 1 ms. The instrument was able to detect $\sim$1 μL droplets at a rate on the order of 1 s per droplet.

The developed viscosity and mass density sensor opens several possibilities. We recently initiated the study of stimulus-responsive polymers for glucose sensing and the unfolding behavior of proteins. This, by solely measuring changes in viscosity after introducing the analyte or inducing denaturation. Future work could involve monitoring of RNA hybridization and protein aggregation into fibrils.

Acknowledgements

First and foremost, I would like to sincerely thank Luc Duempelmann and Roger Krenger. They both performed projects under my supervision as part of their master studies. This thesis would not be in the present state without their excellent contributions. Luc worked in particular on photothermal excitation and the real-time viscosity sensor. Roger conducted squeeze-film damping measurements, worked on glucose-sensing polymers and evaluated the high-throughput viscometer in the initial phase. Both developed a great share of the instrument control software in LabVIEW.

To no lesser extend I am grateful to my advisers Thomas Braun and Henning Stahlberg for their enthusiasm about my work, freedom to pursuit my own ideas, help and reference points when required. Furthermore, I would like to especially thank them for giving me the opportunity to visit conferences in Paris, Stanford, Madrid and across Switzerland and to attend the PhD summer school at the Technical University of Denmark.

I wish to acknowledge Ernst Meyer and Thomas Pfohl, members of my PhD advisory committee, for their interest, inputs and support. Special thanks goes to Ernst for co-refereeing my thesis.

Thank goes to Shirley A. Müller. Without her contributions on correcting, editing and constructively criticizing my work and manuscripts, I am convinced they would not have been published. I greatly acknowledge Paul Baumgartner, Bill Anderson, Ken Goldie, and Karen Bergmann the good souls running the C-CINA and Raymond Strittmatter (mechanical workshop Biozentrum), Andreas Tonin (electronics workshop, Physics), Sascha Martin (mechanical workshop, Physics) and their co-workers for their help and excellent work.

I would like to express great appreciation to my collaborators: François Huber, Natalija Backmann, Hans Peter Lang, and Christoph Gerber at the Institute of Physics for their support on cantilever sensors in general and straightforward help on sensor preparation; Jonas Pollard, Kasper Renggli and Nico Bruns at the Adolphe Merkle Institute in Fribourg (former University of Basel) for always finding a way to meet my stringent specifications to perform polymerization reactions and their expertise in polymer synthesis; Joachim Köser, Olfa Glaied, and David Waldmeier at the Fachhochschule Nordwestschweiz for their contributions on stimulus-responsive polymers; and Mike Touzin, Christof Huber and Martin Anklin from Endress+Hauser Flowtec AG for their interest in the project.

Furthermore, I would like to thank Tim Sharpe at the Biozentrum Biophysics Facility for his open-mindedness and for providing the instruments required for reference measurements; Thilo Glatzel for helping me without hesitation; and Christian Schönenberger and Audrey Fischer at the Swiss Nanoscience Institute for supporting the ARGOVIA project NoViDeMo. I would like to acknowledge my (former) colleagues Andrej Bieri, Christoph von Arx, Christopher Bleck, Dominic Giss, Gabriel Schweighauser, Jan Burri, Jörg Ziegler, Michael Gerspach, Nora Sauter, Sebastian Scherrer, Simon Kemmerling, and Stefan Arnold for helpful suggestions, support, coffee and lunch breaks and the good atmosphere.
I am grateful to André Graf for his expertise on software and different point of view on my work, Tobias Bühlmann for exchange about PhD related issues, Michael Walther for discussions on nanomechanical sensing, Nina Meier for her valuable input on layout and typography and Luc Duempelmann, Andrej Bieri and Andreas Bircher for proof-reading this thesis.
Last but definitely not least, I am grateful to my parents, my two sisters, my close friends and my partner Anja for accompanying and supporting me during my PhD studies.

Contents

Chapter 1

Introduction

1.1 Nanomechanical sensing

Sensors that transduce and amplify signals into an observable quantity are of fundamental importance. The technological revolution triggered by the first optical microscopes eventually led to the invention of atomic force microscopy (AFM) [1], where a sharp tip attached to a microcantilever beam is used to scan over a sample surface. The topography of the surface is reflected in the deflection of the microcantilever that can be measured. Common microcantilevers are $\sim$ 100 μm long, $\sim$ 10 μm wide and $\sim$ 1 μm thick — a comparison to the size of a human hair is shown in Figure 1.1. The potential of such microcantilever sensors for label-free physical, chemical and biological sensing was early recognized [2].
A general sensor principle is depicted in Figure 1.2a. It contains an input signal (e.g., an analyte to be detected), a selectivity filter, one or multiple transduction mechanisms and an output signal. Selectivity is the property of a sensor to exclusively respond to a specific input, e.g., an analyte or physical quantity. It can be achieved by functionalizing the sensor surface with a molecule that specifically binds the targeted analyte [3] or by suppressing spurious effects below the limit of detection, e.g., by preconditioning the sample [4]. The transduction involves the translation of the measurand, e.g., analyte binding, temperature variation or fluid property change, into measurable signal that can be subsequently detected and converted into an electrical output signal. Two methods are commonly employed to operate nanomechanical cantilever sensors: static mode and dynamic mode (Figure 1.2b and c). In static mode, the deflection of a microcantilever, which depends on surface and bulk stresses, is monitored. Surface-stress is caused by steric effects and electrostatic interactions of adsorbate layers, mostly nucleic acids, proteins or self-assembled monolayers [5]. In contrast, changes in bulk stress can originate from temperature gradients or arise in bi-material configurations that can be employed as highly-sensitive calorimeters [6]. In this thesis, I will focus on the dynamic mode operation where the microcantilever is vibrating at resonance.

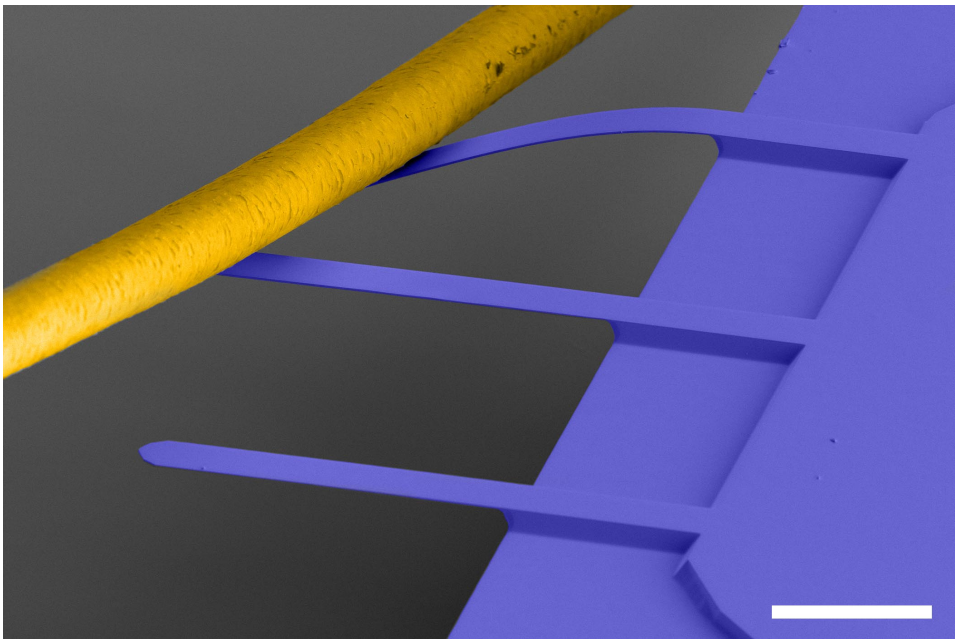

Figure 1.1: False-colored scanning electron microscope image of a hair of mine and three microcantilevers (scale bar: 100 μm, image courtesy Ken Goldie).

The frequency of such resonator is determined by its effective stiffness k_{eff} and effective mass m_{eff} [3]:

$$f = \frac{1}{2\pi}\sqrt{\frac{k_{\text{eff}}}{m_{\text{eff}}}}, \quad k_{\text{eff}} = k_{\text{c,eff}} + \Delta k, \quad m_{\text{eff}} = m_{\text{c,eff}} + \Delta m. \tag{1.1}$$

With $k_{\text{c,eff}}$ and $m_{\text{c,eff}}$ being the effective stiffness and mass of the cantilever and Δk and Δm changes in these properties. Besides the fundamental mode of vibration, there is an infinite number of higher vibrational modes, also referred to as higher harmonics. Figures 1.3a and b, respectively, show the first three flexural mode of vibration for a microcantilever (clamped at one end) and a bridge resonator (clamped at both ends). Both are commonly employed geometries for beam-based sensors [7]. Another important figure of merit, besides the frequency f, is the damping acting on nanomechanical resonators. The sum of all dissipative effects is quantified by the damping coefficient c [7]. It is convenient to utilize the quality factor Q, a measure for the number of oscillation cycles during the ring-down of the resonator (Figure 1.3c) [4]:

$$Q = \frac{\sqrt{k_{\text{eff}} m_{\text{eff}}}}{c}. \tag{1.2}$$

By employing the principle, that changes in mass will shift the frequency, weighing biological and chemical molecules, bacteria, yeast cells and viruses at femtogram (air) and nanogram (liquid) resolution was achieved [5, 8, 9]. Higher modes of vibration thereby provided a

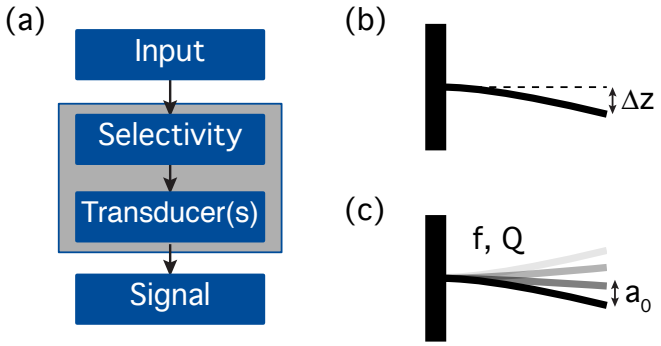

Figure 1.2: (a) Schematic diagram of a sensor (adapted from Reference [3]). Modes of operation: (b) Static mode (deflection Δz) and (c) dynamic mode (amplitude a_0, frequency f, quality factor Q).

higher sensitivity [10]. It is evident from Equation 1.1, that the elastic properties (stiffness) of adsorbates also influence the frequency. Therefore, adsorption to the resonator surface will not only increase the mass, but also the stiffness of the resonator, leading to opposing effects [11]. Measuring not only the frequency but also the quality factor, allows to disentangle the effects of adsorbate mass and stiffness [12]. Furthermore, measuring multiple modes of vibration allows to determine viscoelastic properties of the adsorbate layer [13]. So far, homogeneous adsorbate layers were considered. This assumption, however, does not hold for the adsorption of single particles and layers with partial surface coverage. Because of their mode shape (see Figure 1.3a), higher modes exhibit a different mass sensitivity along the cantilever. Therefore, they can be used to account for the position of adsorbent particles and derive the correct adsorbate mass [14–17]. This principle was for example used to measure the mass and position of single 500 kDa proteins (attogram) adsorbed to bridge resonators in vacuum [18]. Another emerging type of nanomechanical sensors is the suspended channel resonator (SCR). It resembles a hollow cantilever containing a built in microchannel resulting in picoliter liquid volumes. Its major advantage is the operation in vacuum, were much higher sensitivities are achieved [19]. SCRs were employed to measure the buoyant mass of single cells and biomolecules [19], nanoparticles [20] and amyloid fibril formation [21] at attogram resolution in liquid. Furthermore, the thermo-mechanical bending of bi-material microchannel cantilevers was used for infrared spectroscopy [22].
Fluid surrounding the resonator also alters the effective mass m_{eff} and damping c and, therefore, changes its dynamic properties. Such fluid loading depends on the viscosity and mass density and is usually considered an undesired effect because it decreases the mass sensitivity [23]. However, employing this effect for fluid characterization has recently drawn increasing interest [24] and is discussed in Section 1.3.

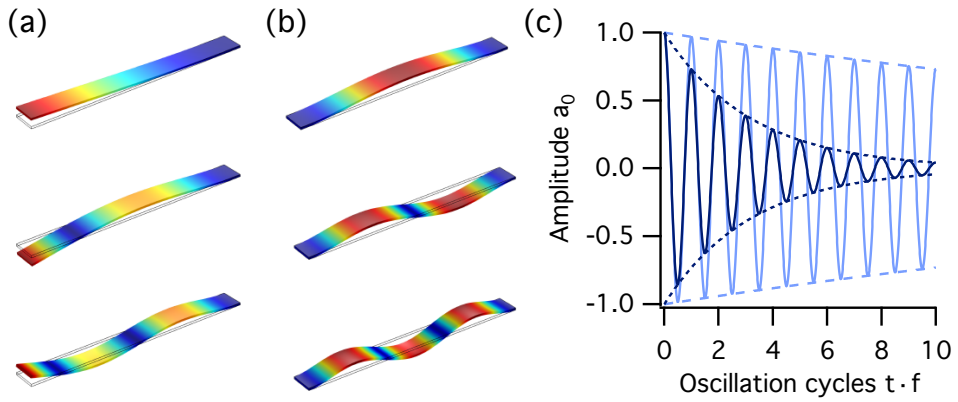

Figure 1.3: First three flexural resonant mode shapes of common nanomechanical sensor geometries: (a) Singly clamped cantilever, fixed on the right-hand side, and (b) doubly clamped bridge resonator, fixed on both ends. (c) Ring-down curve of a resonator with a quality factor of 10 (fast decay) and 100 (slow decay).

The challenge to actuate and detect nanomechanical cantilever vibrations on the order of 1 Å to few 100 nm, led to the development of various techniques. The most straightforward way is to use thermal fluctuations (k_BT), which drive the resonator to a certain amplitude depending on its stiffness k_{eff} and the ambient temperature T. According to the equipartition theorem, $\langle a_0 \rangle \sim \sqrt{k_BT/k_{\text{eff}}}$ [4], root-mean-square amplitudes $\langle a_0 \rangle$ on the order of nanometers ($k_{\text{eff}} = 10^{-3}$ N/m) to picometers ($k_{\text{eff}} = 10^{2}$ N/m) are expected. Because the signal-to-noise ratio can be improved by increasing the amplitude, different techniques to drive resonators are used. The most common method is piezo-acoustic excitation, where a vibrating piezo placed close to the resonator transfers mechanical energy. However, it was realized that the indirect energy transfer also excites resonances of the surroundings, leading to so called spurious resonance peaks that can mask the response of the cantilever [25]. Therefore, direct cantilever excitation methods were investigated: Thermal methods, where vibration is induced by thermo-mechanical means, employ resistor (Joule) or laser (photothermal) heating to drive the resonator [7]. Figure 1.4 compares a resonance peak recorded in water driven by photothermal excitation and piezo-acoustic excitation. Event though the piezo-acoustic spectrum is of high quality, spurious distortions are still visible. In contrast, the photothermal excitation matches the model with high accuracy. Other direct excitation methods include electrostatic, magnetomotive (Lorentz force) and magnetic excitation [7]. The detection methods can be divided into optical and electrical techniques [4, 7]. Optical detection is very robust and accurate, however, the surroundings need to be transparent at the employed laser wavelengths. The most widely used technique is the optical lever (optical beam deflection), where the reflected laser beam is used to measure the angular displacement of the resonator. Interferometric detection (e.g., Fabry-Perot interferometers [26] and

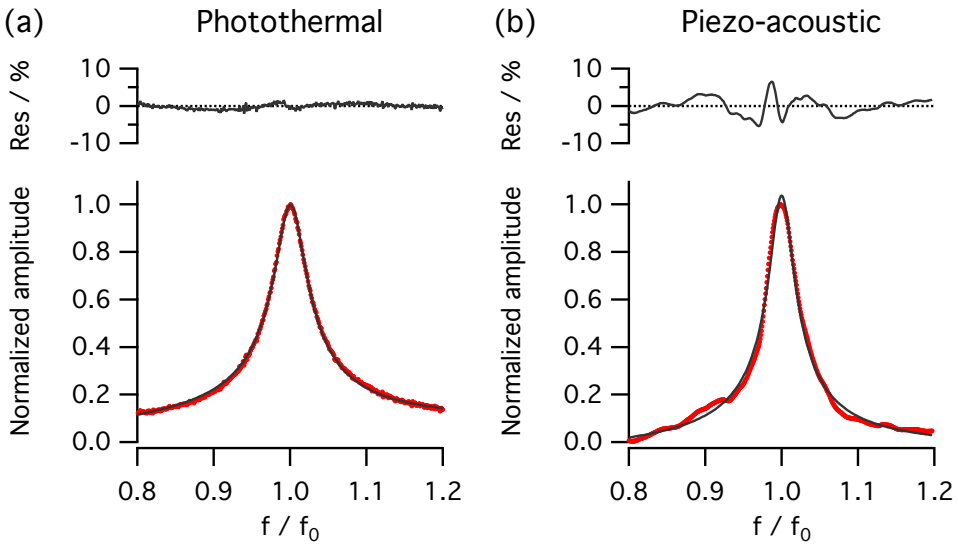

Figure 1.4: Resonance peak recorded using (a) photothermal and (b) piezo-acoustic excitation. The thin black line represents a harmonic oscillator model. The residuals between the data and the model are shown in the top panel.

laser Doppler vibrometers [27]) using a coherent light source has a higher resolution but also increased complexity [4]. Furthermore, integrated waveguides were employed, where the light coupling efficiency was correlated to the deflection of the cantilever [7]. Electrical detection methods are based on capacity, piezoelectricity, piezoresistivity and conductivity [7]. The challenge entailed by these methods is their implementation in liquid, where electrical insulation is crucial [28].

1.2 Fluid properties

1.2.1 Definition

A variety of properties are required to entirely characterize a fluid. Transport properties as the viscosity and thermal conductivity quantify transport of momentum and energy. Thermodynamic properties include the mass density, temperature, etc. and account for properties such as the mass per volume and mean molecular velocity [29]. Here, I will focus on the viscosity and mass density of fluids, because of their major impact on the dynamics of nanomechanical resonators. The definition of the mass density is [29]

$$\rho \equiv \lim_{\Delta V \to V_\epsilon} \frac{\Delta m}{\Delta V}, \tag{1.3}$$

Table 1.1: Viscosity and mass density of some liquids at $T = 293$ K [32].

Liquid	Viscosity η / mPa s	Density ρ / g/cm^3
Water	1.002	0.998
Methanol	0.792	0.586
Ethanol	1.203	0.789
Glycerol	1460	1.261

where V and m are volume and mass of the fluid and V_ϵ the continuum limit, i.e., the smallest volume where a fluid element still has a sufficient number of molecules, that its properties can be considered unaffected by molecular fluctuations. The unit of the mass density is kg/m^3. The dynamic viscosity η (simply referred to as viscosity in this thesis) of an incompressible, Newtonian fluid is constant and relates an applied shear stress σ to the resulting rate of shear strain $\dot{\gamma}$, i.e., the rate of deformation [30]:

$$\eta \equiv \frac{\sigma}{\dot{\gamma}}. \tag{1.4}$$

Because the units of strain rate and shear stress, respectively, are $[\dot{\gamma}] = \text{s}^{-1}$ and $[\sigma] = \text{N/m}^2$ the unit of viscosity is N·s/m^2 or Pa·s. It is important to consider that the viscosity of fluids is highly temperature dependent. It decreases for liquids, whereas it increases for gases with increasing temperature [31]. Therefore, the subsequent discussion assumes the temperature to be constant. Viscosities and mass densities of some common liquids at 293 K are tabulated in Table 1.1.

For a more descriptive definition of viscosity, a fluid is placed between two surfaces of area A, separated by a distance d, and a shear force F_x is applied to the upper surface (Figure 1.5a). For small separation distances d, this will result in a linear velocity gradient $du_x(z)/dz$ that is equal to the strain rate $\dot{\gamma}$. Furthermore, the shear stress equals the force per area, thus, $\sigma = F_x/A$. Due to the no-slip boundary condition, the fluid in vicinity to the surface has the same velocity, i.e., $u_x(0) = 0$ [31]. Rewriting Equation 1.4 leads to

$$\sigma = \frac{F_x}{A} = \eta \frac{du_x(z)}{dz}. \tag{1.5}$$

It can be seen from this relation that flow only occurs ($u_x > 0$) as long as a finite force is applied ($F_x > 0$). Furthermore, the higher the viscosity the more force is required to reach a certain flow velocity, therefore, the viscosity is a measure for the resistance of the fluid to flow. A similar situation is shown in Figure 1.5b, where the bottom surface is conducting an in-plane oscillatory motion at frequency f. Due to the no-slip boundary condition, the fluid is coupled to the surface. The decay length of the velocity is called viscous boundary layer δ

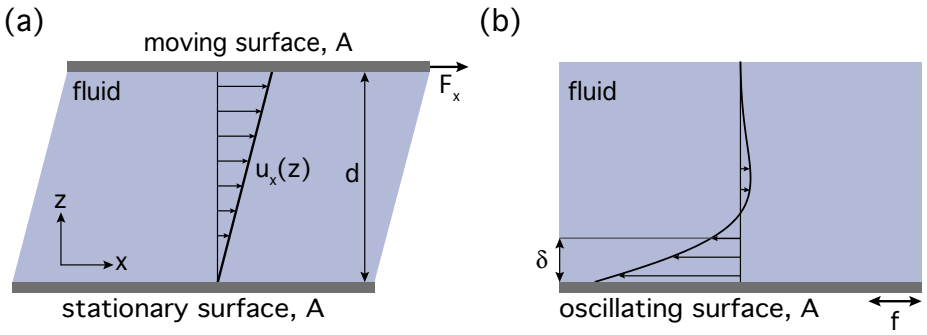

Figure 1.5: (a) Flow velocity of a fluid sheared between two surfaces, the z-origin is at the stationary surface; adapted from [30] (b) Flow velocity above a surface oscillating at frequency f at maximum deflection; δ is the viscous boundary layer [31].

and indicates the distance from an oscillating surface, where the flow velocity dropped by $1/e$ [33]. The viscous boundary layer is a function of the fluid viscosity η and density ρ and the frequency f [31]:

$$\delta = \sqrt{\frac{\eta}{\pi \rho f}}. \tag{1.6}$$

For frequencies encountered with nanomechanical resonators the boundary layers are ranging from 18 μm (1 kHz) to 0.6 μm (1 MHz), and, thus, are comparable to commonly employed cantilever dimensions.

1.2.2 Viscosity of solutions

A solution is defined as a liquid (solvent) containing dissolved particles (solutes). The viscosity of such a solution depends on the concentration, size and shape of the dissolved components as well as on interactions between them. The ratio between solution η and solvent viscosity η_0 is termed relative viscosity η_r:

$$\eta_r \equiv \frac{\eta}{\eta_0}. \tag{1.7}$$

For non-interacting suspensions of hard spheres, the relative viscosity was derived by Einstein [34]. It only depends on the volume fraction φ occupied by the particles,

$$\eta_r = (1 + [\eta]\varphi), \tag{1.8}$$

where $[\eta]$ is called intrinsic viscosity and equals 2.5 for spherical particles. Due to the assumption of non-interacting particles, this relation is only valid for very small volume frac-

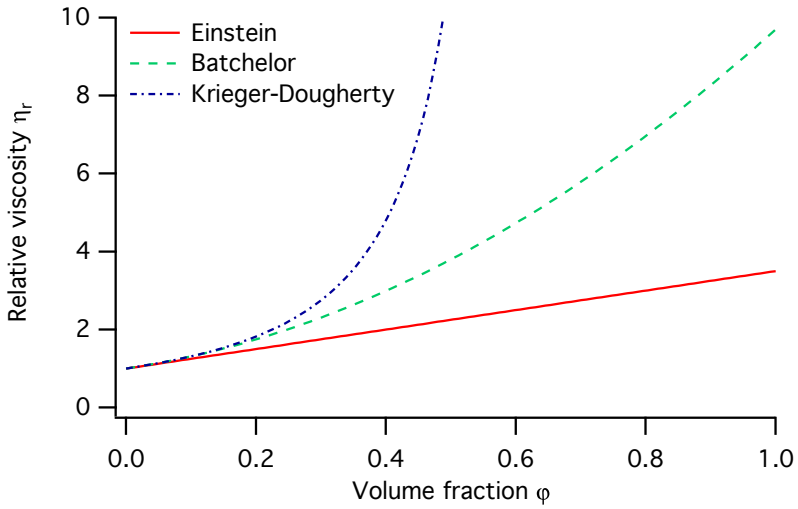

Figure 1.6: Models to describe the relative viscosity of suspensions by Einstein (Equation 1.8), Batchelor (Equation 1.9), and Krieger-Dougherty (Equation 1.10).

tions $\varphi < 0.03$. Batchelor derived the higher order term, validating the equation for volume fractions $\varphi < 0.10$ [34]:

$$\eta_r = (1 + [\eta]\varphi + 6.2\varphi^2). \tag{1.9}$$

An empirical expression valid for arbitrary particle shapes and concentrations was presented by Krieger-Dougherty [34]:

$$\eta_r = \left(1 - \frac{\varphi}{\varphi_m}\right)^{-[\eta]\varphi_m}, \tag{1.10}$$

where φ_m corresponds to the maximum-packing volume fraction, ~ 0.64 for spheres. Figure 1.6 shows a comparison of the above equations. In the low-concentration regime ($\varphi \ll 0.1$) they coincide well. However, at higher concentrations, deviations become substantial. Even though, these models were derived assuming a suspension of solid particles, they are routinely applied to polymer and protein solutions. Modified Krieger-Dougherty models were, e.g., applied to describe the concentration-viscosity behavior of globular proteins [35]. Furthermore, the intrinsic viscosity $[\eta]$ of dilute polymer solutions can be empirically related to the polymer molecular weight MW by the Mark-Houwink equation [34]: $[\eta] = C_0 MW^{C_1}$, where C_0 and C_1 are parameters depending on the polymer-solvent system. To estimate the molecular weight MW, a dilution series of the polymer is usually measured and fitted with one of the above models to determine $[\eta]$.

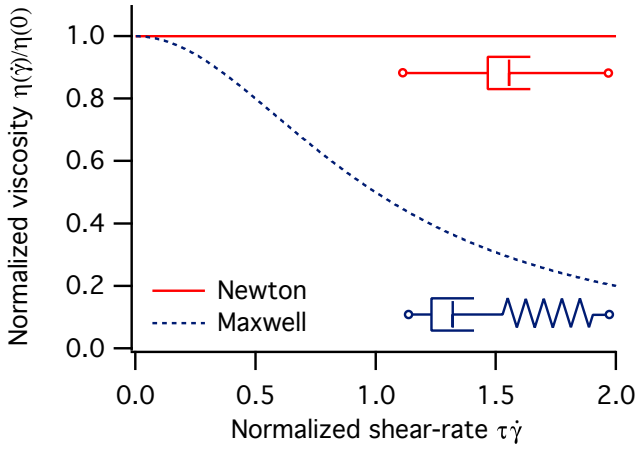

Figure 1.7: Normalized viscosity of a Newtonian (red curve) and a non-Newtonian Maxwell (dashed blue curve) fluid plotted against the shear-rate.

1.2.3 Non-Newtonian fluids

So far the viscosity η of a given liquid at a certain temperature was assumed to be a constant. However, experiments have shown that the viscosity of many solutions varies with the applied shear rate $\dot{\gamma}$. To account for this, the viscosity is redefined as a function of the shear-rate:

$$\eta(\dot{\gamma}) \equiv \frac{\sigma}{\dot{\gamma}}. \tag{1.11}$$

Fluids showing such complex behavior are termed non-Newtonian and the corresponding field of research is called rheology [30, 34]. The behavior originates from the fact, that such fluids have a certain elastic component, in addition to their viscosity. Thus, they exhibit a hybrid behavior between an elastic solid (Hookean) and viscous fluid (Newtonian). The shear-rate–viscosity behavior can become arbitrarily complex and depends on many parameters. Comprehensive literature is available for the interested reader [30, 34]. A commonly observed behavior of many dilute polymer [30, 34] and protein [35] solutions is shear-thinning, where the viscosity decreases with increasing shear-rate. Figure 1.7 compares a Newtonian to a shear-thinning (non-Newtonian) fluid, described by the Maxwell model. A Newtonian fluid can be modeled by a dashpot that dissipates energy independent of shear-rate (constant viscosity). The mechanical equivalent of a shear-thinning fluid, is a dashpot coupled to a linear elastic spring (Maxwell model), possessing a relaxation time τ, which characterizes the frequency-onset of shear thinning. At low frequencies ($\dot{\gamma}\tau < 1$), the energy is dissipated by the dashpot leading to a high viscosity. In contrast, at high frequencies ($\dot{\gamma}\tau > 1$), the spring is deformed and the dashpot is bypassed leading to less dissipation, i.e., lower viscosity. As a rule of thumb, the higher the molecular weight and the aspect ratio of a solute, the higher its

concentration and the higher the applied shear-rate, the more likely it is to encounter non-Newtonian effects. Pure solvents and small dissolved molecules usually display Newtonian behavior over large frequency ranges. For example solutions of glycerol are widely accepted to be Newtonian and therefore used as viscosity standards [36]. However, at very high frequencies obtained with vibrating nanoparticles (20 GHz), there are recent indications for the onset of the non-Newtonian regime of glycerol [37].
To relate steady-shear viscosity data to dynamic oscillatory viscosity data (compare Figure 1.5a to b), the empirical Cox-Merz rule can be employed. It states that the steady-shear viscosity $\eta(\dot{\gamma})$ is equal to the dynamic oscillatory viscosity $\eta^*(2\pi f)$ [34, 38]:

$$\eta(\dot{\gamma}) = \eta^*(2\pi f). \tag{1.12}$$

It was observed that Equation 1.12 only holds for dilute polymer solutions [39] and moderate molecular weights [40]. Large deviations were also observed at high protein concentration [35]. Nevertheless, it remains an important relation to compare data from steady-shear and oscillatory shear measurements and is, e.g., applied to compare cantilever-rheometer to steady-shear rheometer data [41].

1.3 Fluid property sensors

Microfluidic implementations of viscosity and density sensors become increasingly important [42]. First and foremost, they reduce the sample volume required for a single measurement, making them suitable for rare and/or expensive samples, as encountered in many biological applications. Besides the reduced sample consumption, microfluidic viscometers have the advantage of a small thermal inertia [43], facilitating a fast temperature equilibration. Furthermore, shear forces acting on the fluid are small due to the small amplitude of vibration and, thus, shear heating of the sample, encountered in macroscopic viscometers [36], is negligible. Interfacing with other microfluidic sensors can be facilitated and the rate of exchange of liquid samples, i.e., homogeneous sample distribution in the measurement fluid channel, scales inversely with the dimensions. Finally, using micrometer sized resonators allows to access the high-frequency regime, which allows to extend the range of rheological measurements or to increase the measurement speed.
The viscosity and mass density of the fluid surrounding a microcantilever has a large impact on its dynamic properties. The putative drawback of such fluid damping, however, attracts increasing interest for fluid characterization [24]. Early literature reported characterization of the frequency and quality factor of cantilevers immersed in fluids of known properties [44–46]. Even the hydrolysis of DNA was monitored, though without deducing quantitative viscosity values [47]. The emergence of comprehensive fluid dynamic models, introduced and discussed in Chapter 2, entailed many experimental studies. For a given cantilever, the

Table 1.2: Liquids and solutions† characterized using cantilever based Newtonian viscosity and density sensors. The measured viscosity η and density ρ ranges are indicated.

Reference	Year	Characterized liquids	η / mPa s	ρ / g/mL
Cakmak *et al.* [48]	2014	blood plasma	—	—
Heinisch *et al.* [49]	2014	glycerol†, acetone-isoprop.	0.93–216	1.00–1.24
Bircher *et al.* [50]	2013	glycerol†, polyacrylamide†	1.0–20	1.00–1.18
Cakmak *et al.* [51]	2013	glycerol†, plasma, serum	0.95–3.02	1.0–1.1
Hur *et al.* [52]	2013	glycerol†	1.0–600	1.0–1.26
Rust *et al.* [53]	2013	glycerol†, DNA†	1.0–1.7	1.00–1.03
Xu *et al.* [54]	2013	toluene	0.40–0.56	—
Paxman *et al.* [55]	2012	glycerol†, ethanol†	1–45	0.7–1.2
Youssry *et al.* [56]	2011	dodecane, silicone oils	1.67–553	0.75–1.00
Hennemeyer *et al.* [57]	2008	glucose†, fructose†, sucrose†	0.9–20	—
Schilowitz *et al.* [58]	2008	hexadecane, dodecane	28.7–55.6	0.86
McLoughlin *et al.* [59]	2007	poly(ethylene glycol)†	0.93–2.25	1.00–1.03
Wilson *et al.* [60]	2007	glycerol†	1.0–2.4	1.00-1.04
McLoughlin *et al.* [61]	2006	ethanol†	0.8–2.6	0.8–1
Papi *et al.* [62]	2006	glycerol†	—	—
Boskovic *et al.* [63]	2002	acetone, CCl_4, butanol	0.31–2.5	0.79–1.60
Bergaud *et al.* [64]	2000	ethanol	1.35	0.79

models basically relate the dynamic properties of the cantilever (frequency f and quality factor Q) to the surrounding fluid properties (density ρ and viscosity η):

$$(f, Q) \xrightarrow{\text{Hydrodynamic model}} (\eta, \rho). \tag{1.13}$$

Table 1.2 gives a literature overview on viscosity and density sensors using flexural vibrations of microcantilevers. Only papers that derived viscosity and density values from the resonator characteristics, and not *vice versa*, were considered. Furthermore, it is emphasized that also partially immersed cantilevers [65], doubly clamped beams [66–69], lateral (in-plane) [70] and torsional modes [71] and suspended channel resonators (SCRs) [72] were used for the same purpose. Table 1.2 confirms the general acceptance of glycerol solutions for viscosity sensor calibration and a trend towards complex samples, such as polymers, DNA and blood. The instrumentation details for the cantilever viscosity and density meters, including employed excitation and detection methods and required sample volume, are provided in Table 1.3. Recording thermal noise or piezo-acoustic spectra directly from an atomic force microscopy setup, was the most popular method in the early literature reports. Yet, because this was not suitable for higher viscous samples or macroscopic cantilevers and introduced spurious resonances, respectively, magnetomotive (Lorentz force) and magnetic excitation

Table 1.3: Excitation and detection methods and sample volume V for cantilever based viscosity and density sensors (OBD: optical beam deflection).

Reference	Year	Excitation	Detection	V/μL
Cakmak *et al.* [48]	2014	magnetic	vibrometer	10
Heinisch *et al.* [49]	2014	magnetomotive	magnetomotive	—
Bircher *et al.* [50]	2013	photothermal	OBD	5
Cakmak *et al.* [51]	2013	magnetic	diffractive	150
Hur *et al.* [52]	2013	piezoelectric	piezoelectric	—
Rust *et al.* [53]	2013	magnetomotive	magnetomotive	10
Xu *et al.* [54]	2013	magnetomotive	Wheatstone bridge	—
Paxman *et al.* [55]	2012	thermal noise	OBD	100
Youssry *et al.* [56]	2011	magnetomotive	vibrometer	—
Hennemeyer *et al.* [57]	2008	thermal noise	OBD	—
Schilowitz *et al.* [58]	2008	piezo-acoustic	OBD	4000
McLoughlin *et al.* [59]	2007	thermal noise	OBD	—
Wilson *et al.* [60]	2007	piezoelectric	piezoelectric	—
McLoughlin *et al.* [61]	2006	magnetic	OBD	—
Papi *et al.* [62]	2006	—	OBD	100
Boskovic *et al.* [63]	2002	thermal noise	OBD	—
Bergaud *et al.* [64]	2000	piezo-acoustic	OBD	50

is quite common nowadays. For precise determination of the frequency and quality factor, it is essential that the excitation method does not introduce spurious resonances. Optical detection methods, such as optical beam deflection, vibrometers or diffractive techniques, still dominate. But electrical and magnetomotive read-out techniques are on the rise to overcome the restriction to transparent samples entailed by optical detection. Furthermore, reports on rheological measurements of non-Newtonian liquids using cantilevers, recently became available in literature [73–77]. Besides the challenge of formulating fluid dynamic models accounting for non-Newtonian behavior, rheological samples mostly are highly viscous and non-transparent. This entails a complete redesign of the experimental setup and makes microscopic cantilevers, which have a smaller dynamic range, less suitable.

Besides microcantilevers there is a variety of other methods to determine the viscosity and partially the mass density of fluids in microliter volumes. Among others, they comprise MEMS plate [78, 79], membrane [80], tuning fork [81], shear-mode [82], and opto-mechanical [83] resonators; beads trapped by magnetic [84] and optical [85, 86] fields and attached to cantilevers [87]; pressure gradients across micro-channels [88–90] or between parallel flows [91–93]; fluorescent probes [94] and image-analysis based approaches [90, 95].

Last but not least, it is important to consider commercially available instruments. During the past years, viscometers have shown a sharp decrease in sample volume required

for a measurement, indicating an increasing demand for such techniques. They comprise the following principles (the minimal sample consumption of the considered instruments is < 1 mL and is indicated): Rolling-ball viscometers, MINIVIS II (400 μL, Grabner Instruments) and Lovis 2000 M/ME (100 μL, Anton Paar), capillary viscometer, Viscosizer 200 (50 μL, Malvern), rectangular-slit viscometers, m-VROC (>20 μL, RheoSense) and m-VROCi (100 μL, Malvern), vibrating piston viscometer, VISCOlab 5000 (75 μL, Cambridge Viscosity), and dynamic light scattering, DWS RheoLab II rheometer ($\sim 400\mu$L, LS Instruments).

1.4 Thesis overview

The goal of this thesis was to evaluate resonant nanomechanical cantilevers for fluid characterization applications. Therefore, the following aspects were investigated:

- **Chapter 2** reviews the theoretical background on cantilever dynamics in vacuum and under fluid loading. Furthermore, the harmonic oscillator theory, which describes resonant behavior, is summarized.
- **Chapter 3** reports the implementation of photothermal excitation in the developed setup. It is able to excite higher-mode vibrations of microcantilevers in liquid, without introducing spurious resonance peaks. Heating effects are assessed by solving the heat equation using finite element analysis and are compared to measured values. The efficiency of the excitation is analytically calculated and compared to the measured resonant behavior of the cantilever.
  Published in Micro Nano Lett. **8**, 770 (2013) [96]
- **Chapter 4** evaluates the behavior of the microcantilever resonators in microfluidic containers. Placing the resonator close to a solid surface introduces squeeze-film damping, caused by the fluid confined in between. The magnitude of the effect on higher-mode vibrations is measured and discussed.
  Published in EPJ Tech. Instrum. **1**, 10 (2014) [97]
- **Chapter 5** shows the application of the microcantilever sensor for fluid viscosity and mass density measurements with microliter sample consumption. Furthermore, free-radical polymerization reactions were monitored in a time-resolved manner. The shear-thinning properties of the polymer solutions were resolved by the sensor.
  Published in Anal. Chem. **85**, 8676 (2013) [50]
- **Chapter 6** presents a method to characterize the viscosity and mass density with high temporal resolution. To screen 1 μL sample droplets at a high rate on the order of 1 Hz, a two-phase flow configuration was employed.
- **Chapter 7** concludes the thesis and gives an outlook and perspective on applications of the instrument.
- **Appendix A** provides technical details on the developed setup to excite and detect resonant microcantilever vibrations using photothermal excitation and optical lever detection. Furthermore, protocols for sensor preparation and fluid cell fabrication as well as a brief overview on the developed software are given.

Chapter 2

Theoretical Background

Abstract

This chapter provides an overview on the underlying theories employed in this thesis. First, the harmonic oscillator theory is introduced, which describes resonator data. Next, the Euler-Bernoulli beam theory is derived and reviewed. Finally, theories describing hydrodynamic forces acting on cantilevers under various conditions are summarized. It is emphasized that in the theoretical models the angular or radial frequency ω (unit: rad/s) is used, whereas the temporal frequency f (unit: Hz) is usually measured. They are related by $\omega = 2\pi f$.

2.1 Harmonic oscillations

Countless experiments and theoretical studies have shown that the dynamic response of nanomechanical resonators can be described by a harmonic oscillator model with good accuracy [98]. Therefore, this section gives an overview on the theoretical background of the harmonic oscillator, which was used to describe the measured data.

2.1.1 Simple harmonic oscillator

The potential energy E_{pot} of a one degree of freedom (1 DOF) harmonic oscillator described by an effective or equivalent mass m_{eff} connected to a linear elastic spring k_{eff} is given by [99]

$$E_{\text{pot}}(z) = \frac{1}{2} k_{\text{eff}} z^2, \tag{2.1}$$

where z is the displacement from the equilibrium position ($z = 0$). A schematic of such simple harmonic oscillator (SHO) is shown in Figure 2.1a. By calculating the gradient of the

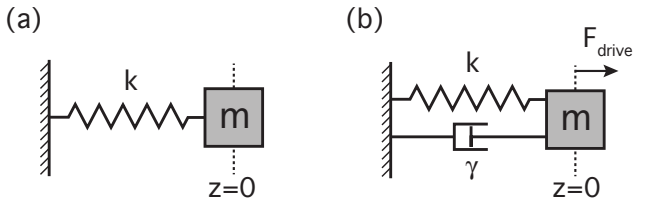

Figure 2.1: Schematic of a (a) simple harmonic (SHO) and (b) driven damped harmonic (DDHO) oscillator. A point mass m is attached to a linear elastic spring k. Damping is modeled by dashpot γ and the equilibrium position ($z = 0$) is indicated by the dotted line.

potential energy $F = -\frac{dE_{\text{pot}}(z)}{dz}$ and comparing to Newton's second law $F = m_{\text{eff}}\frac{d^2z(t)}{dt^2}$, the equation of motion in absence of damping and any external forces can be formulated:

$$m_{\text{eff}}\frac{d^2z(t)}{dt^2} + k_{\text{eff}}z(t) = 0. \tag{2.2}$$

Inserting the following ansatz $z(t) = a_0e^{i(\omega t+\phi)}$, with a_0 being the amplitude of vibration, leads to the well known solution for the eigenfrequency or natural frequency of the harmonic oscillator:

$$\omega_0 = \sqrt{\frac{k_{\text{eff}}}{m_{\text{eff}}}}. \tag{2.3}$$

2.1.2 Driven damped harmonic oscillator

Introducing a damping force, quantified by coefficient $\gamma = \frac{\omega_0}{Q}$ for $Q \gg 1$, which depends on the eigenfrequency ω_0 and the quality factor Q; and a periodical driving force F_{drive} extends Equation 2.2 to

$$m_{\text{eff}}\left(\frac{d^2z(t)}{dt^2} + \gamma\frac{dz(t)}{dt} + \omega_0^2z(t)\right) = F_{\text{drive}}(t) = F_0e^{i\omega t}. \tag{2.4}$$

By inserting the same ansatz as above $z(t) = a_0e^{i(\omega t+\phi)}$ into Equation 2.4 and separating the real and imaginary part, the following relations are found:

$$\left(\omega_0^2 - \omega^2\right)\sin\phi + \gamma\omega\cos\phi = 0, \tag{2.5}$$

$$\left(\omega_0^2 - \omega^2\right)\cos\phi - \gamma\omega\sin\phi = \frac{F_0}{a_0m_{\text{eff}}}. \tag{2.6}$$

To obtain the steady-state amplitude a_0, Equations 2.5 and 2.6 are squared, added and solved by inserting the trigonometric identity $\sin^2(x) + \cos^2(x) = 1$ [99]:

$$a_0(\omega) = \frac{F_0/m_{\text{eff}}}{\sqrt{\left(\omega_0^2 - \omega^2\right)^2 + (\gamma\omega)^2}} = \frac{F_0/m_{\text{eff}}}{\sqrt{\left(\omega_0^2 - \omega^2\right)^2 + \left(\frac{\omega_0\omega}{Q}\right)^2}}. \tag{2.7}$$

The amplitude response at different quality factors Q is shown in Figure 2.2a. At lower quality factors the peak amplitude decreases and its position shifts towards lower values. The point of maximal amplitude is called resonance frequency ω_R and can be found by solving $\frac{da_0}{d\omega} = 0$:

$$\omega_R = \sqrt{\omega_0^2 - \frac{\gamma^2}{2}} = \omega_0\sqrt{1 - \frac{1}{2Q^2}}. \tag{2.8}$$

Note that for weak damping ($\gamma \ll \omega_0$ or $Q \gg 1$) the eigenfrequency and resonance frequency coincide $\omega_R \approx \omega_0$.
By rearranging Equation 2.5 and using the relation $\frac{\cos x}{\sin x} = \cot x$ we obtain

$$\cot(\phi) = -\frac{\omega_0^2 - \omega^2}{\gamma\omega}. \tag{2.9}$$

Using $\cot(x) = \tan\left(\pi\left(n + \frac{1}{2}\right) - x\right)$ and identifying $n = -1$ by applying the boundary condition $\phi(\omega = 0) = 0$, leads to the solution for the steady-state phase-lag:

$$\phi(\omega) = \arctan\left(\frac{\omega_0^2 - \omega^2}{\gamma\omega}\right) - \frac{\pi}{2} = \arctan\left(Q\frac{\omega_0^2 - \omega^2}{\omega_0\omega}\right) - \frac{\pi}{2}. \tag{2.10}$$

The phase response at different quality factors Q is plotted in Figure 2.2b. The phase-lag between the drive and the oscillator at the phase-turning point $\omega = \omega_0$ is $-\frac{\pi}{2}$, i.e., at resonance the oscillator lags behind the excitation by 90°.
In summary, harmonic oscillations are entirely characterized by their radial eigenfrequency ω_0 and quality factor Q. Thereby $\omega_0 = 2\pi f_0$ and $Q = \frac{\omega_0}{\gamma}$ for $Q \gg 1$. f_0 is the eigenfrequency and γ is the half-power bandwidth of the resonance peak, both having the unit Hz. At the eigenfrequency ω_0 most energy is absorbed by the resonator. Q is a measure for the energy dissipated per oscillation cycle [98]:

$$Q = 2\pi\frac{E_{\text{resonator}}}{\Delta E_{\text{cycle}}}, \tag{2.11}$$

where $E_{\text{resonator}}$ and ΔE_{cycle}, respectively, are the average energy stored in the resonator and lost per oscillation cycle.

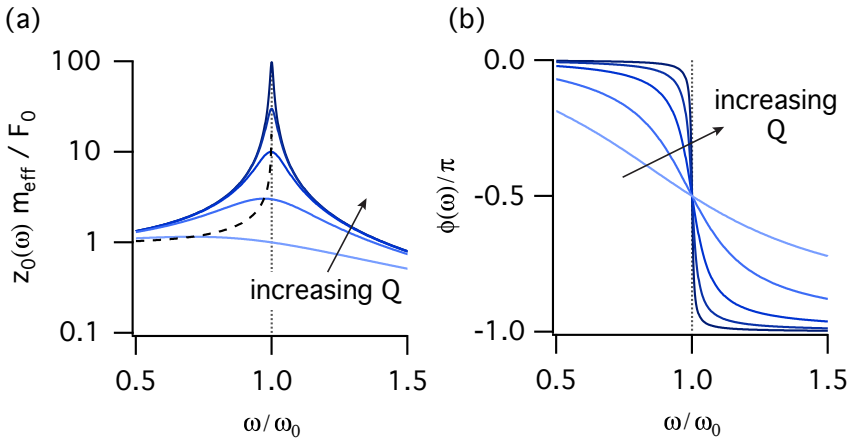

Figure 2.2: Steady-state amplitude (a) and phase (b) response of a driven damped harmonic oscillator for quality factors Q of 1, 3, 10, 30 and 100. The dotted vertical line represents the eigenfrequency ω_0 and the dashed line in (a) the resonance frequency ω_R, describing the peak maximum.

2.2 Undamped microcantilever dynamics

2.2.1 Euler-Bernoulli beam theory

The next section gives a detailed description of the Euler-Bernoulli equation governing dynamic cantilever behavior. A schematic representation of such beam is given in Figure 2.3a. Countless experiments and theoretical studies confirmed that cantilever beams with micrometer and even nanometer dimensions can be described by classical continuum mechanics [98]. The most extensive analytical approach to describe dynamics of vibrating beams is the Timoshenko model, however, if assumptions (a) – (c) below are met, the Euler-Bernoulli beam theory is recovered [100]. It is subsequently derived under the following assumptions:

(a) The cantilever aspect ratios L/b and L/h are large ($L \gg b, h$),

(b) The deflection W is far smaller than any cantilever dimension ($W \ll h, b, L$),

(c) The cantilever material is linear elastic,

(d) Intrinsic dissipative effects c_0 are negligible,

(e) The cross section is uniform along the beam,

(f) The cantilever material is homogeneous.

Figure 2.3b shows a schematic of a cantilever beam of thickness h, width b and length L. An external force per unit length F causes a shear force V and bending moment M to act on

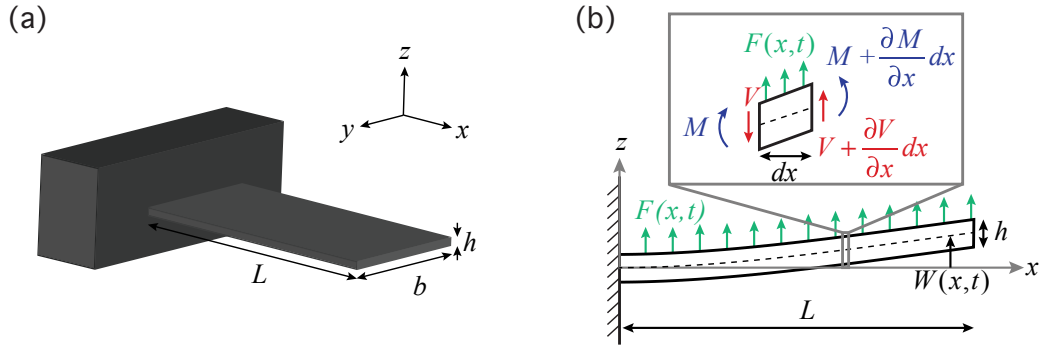

Figure 2.3: (a) Schematic of a cantilever beam of length L, width b and thickness h. (b) Longitudinal cross section of the same cantilever, indicating an infinitesimal element dx of the beam where shear force V and bending moment M are acting. The deflection function $W(x,t)$ of the cantilever is indicated (panel (b) adapted from Reference [101]).

each element of length dx. Balancing the forces ($\sum F = 0$) and moments ($\sum M = 0$) and neglecting higher order terms leads to [101]:

$$-\frac{\partial V}{\partial x} + F = \mu_c \frac{\partial^2 W(x,t)}{\partial t^2}, \tag{2.12}$$

$$V = \frac{\partial M}{\partial x}, \tag{2.13}$$

where $\mu_c = \rho_c bh$ is the linear mass density, with ρ_c being the mass density of the cantilever material and $W(x,t)$ the deflection function of the cantilever beam. The basic form of the Euler-Bernoulli beam theory relates the bending moment M to the curvature of the beam under the assumption of small deflections [101]:

$$M = E(x) I_z(x) \frac{\partial^2 W(x,t)}{\partial x^2}, \tag{2.14}$$

where E is the Young's modulus, a material constant, and I_z the area moment of inertia. The area moment of inertia of a beam of rectangular cross section in z-direction is given by [98]

$$I_z = \int_A z^2 dA = \int_{-h/2}^{h/2} \int_{-b/2}^{b/2} z^2 dy dz = \frac{z^3 b}{3}\Big|_{-h/2}^{h/2} = \frac{bh^3}{12}. \tag{2.15}$$

Combining Equations 2.12, 2.13 and 2.14 leads to the equation of motion:

$$\frac{\partial^2}{\partial x^2}\left(E(x) I_z(x) \frac{\partial^2 W(x,t)}{\partial x^2}\right) + \mu_c(x) \frac{\partial^2 W(x,t)}{\partial t^2} = F, \tag{2.16}$$

$$\text{with} \quad F = \underbrace{-c_0 \frac{\partial W(x,t)}{\partial t}}_{F_\text{c}} + F_\text{ext}. \tag{2.17}$$

F_c represents intrinsic dissipation by damping coefficient c_0, which correlates with the beam velocity, and F_ext is an arbitrary external force. Because of approximation (d) (see beginning of this section) and absence of external forces, the total force equals zero, $F = 0$. Furthermore, due to assumptions (e) and (f), the Young's modulus, the area moment of inertia and the linear mass density become independent of x, i.e. $E(x) = E$, $I_z(x) = I_z$ and $\mu_c(x) = \mu_c$. Consequently, Equation 2.16 can be simplified to

$$EI_z \frac{\partial^4 W(x,t)}{\partial x^4} + \mu_c \frac{\partial^2 W(x,t)}{\partial t^2} = 0. \tag{2.18}$$

Equation 2.18 can be solved by separation of the variables into a temporal $\Psi(t)$ and spatial $\Phi(x)$ term [101]. The ansatz for the temporal function $\Psi(t)$ is a harmonic oscillation with angular frequency $\omega_{0,n}$.

$$W(x,t) = \underbrace{e^{i\omega_{0,n}t}}_{\Psi(t)} \Phi(x). \tag{2.19}$$

Inserting Equation 2.19 into 2.18 and defining $\beta_n^4 \equiv \frac{\mu_c \omega_{0,n}^2}{EI_z}$ leads to

$$\frac{d^4\Phi(x)}{dx^4} = \frac{\mu_c \omega_{0,n}^2}{EI_z} \Phi(x) = \beta_n^4 \Phi(x). \tag{2.20}$$

The boundary conditions for a clamped-free cantilever beam are [101]:

$$\Phi(0) = \frac{d\Phi(0)}{dx} = 0, \tag{2.21}$$

at the clamped end ($x = 0$) because translation and bending is constrained.

$$M = EI_z \frac{d^2\Phi(L)}{dx^2} = 0, \quad V = EI_z \frac{d^3\Phi(L)}{dx^3} = 0, \tag{2.22}$$

at the free end ($x = L$) because it is free to move and, thus, the bending moment M (Equation 2.14) and shear force V (Equation 2.13) must be zero. The resulting boundary-value problem can be solved analytically using the following ansatz [101]:

$$\Phi(x) = a_1 \cos(\beta_n x) + a_2 \sin(\beta_n x) + a_3 \cosh(\beta_n x) + a_4 \sinh(\beta_n x). \tag{2.23}$$

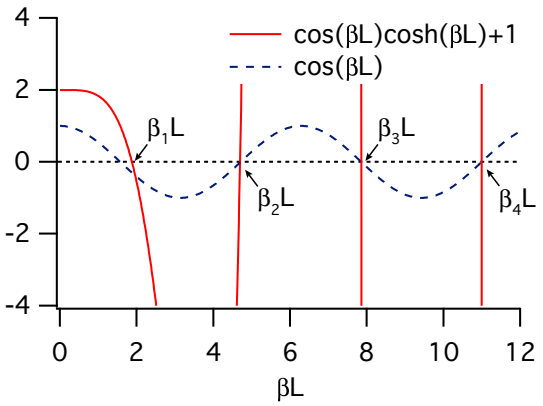

Figure 2.4: The eigenvalues $\beta_n L$ for a clamped-free cantilever beam found by solving for the positive roots of $\cos(\beta L)\cosh(\beta L) + 1$ (solid line). The dashed line represents the asymptotic solution $\cos(\beta L)$ for large βL. The first four eigenvalues are indicated.

The first three derivatives of $\Phi(x)$ are:

$$\frac{d\Phi(x)}{dx} = -a_1 \sin(\beta_n x) + a_2 \cos(\beta_n x) + a_3 \sinh(\beta_n x) + a_4 \cosh(\beta_n x), \tag{2.24}$$

$$\frac{d^2\Phi(x)}{dx^2} = -a_1 \cos(\beta_n x) - a_2 \sin(\beta_n x) + a_3 \cosh(\beta_n x) + a_4 \sinh(\beta_n x), \tag{2.25}$$

$$\frac{d^3\Phi(x)}{dx^3} = a_1 \sin(\beta_n x) - a_2 \cos(\beta_n x) + a_3 \sinh(\beta_n x) + a_4 \cosh(\beta_n x). \tag{2.26}$$

Applying boundary conditions 2.21 and 2.22 leads to $a_1 = -a_3$, $a_2 = -a_4$ and

$$\frac{a_2}{a_1} = \frac{\sin(\beta_n L) - \sinh(\beta_n L)}{\cos(\beta_n L) + \cosh(\beta_n L)} = -\frac{\cos(\beta_n L) + \cosh(\beta_n L)}{\sin(\beta_n L) + \sinh(\beta_n L)}. \tag{2.27}$$

By rearranging and reducing the fractions to a common denominator, the following solution is found:

$$\underbrace{\sin^2(\beta_n L) + \cos^2(\beta_n L)}_{1} + \underbrace{\cosh^2(\beta_n L) - \sinh^2(\beta_n L)}_{1} + 2\cos(\beta_n L)\cosh(\beta_n L) = 0, \tag{2.28}$$

which simplifies to

$$\cos(\beta_n L)\cosh(\beta_n L) + 1 = 0. \tag{2.29}$$

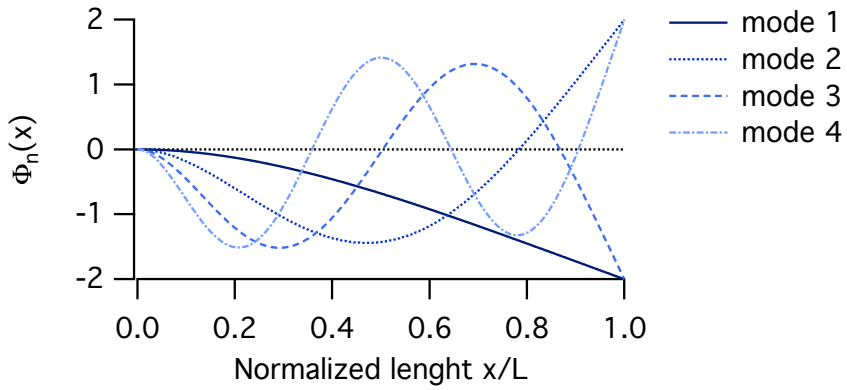

Figure 2.5: Eigenfunctions or mode shapes Φ_n of a cantilever undergoing flexural vibrations. Shown are the first four modes n = 1–4.

Equation 2.29 can be numerically solved resulting in $(\beta_1 L) = 1.875$, $(\beta_2 L) = 4.694$, $(\beta_3 L) = 7.855$, $(\beta_4 L) = 10.996, \ldots$ (see Figure 2.4 and Table 2.1). Rewriting the equation allows to find the asymptotic form for $(\beta_n L) \gg 1$

$$\cos(\beta_n L) + \frac{1}{\cosh(\beta_n L)} \approx \cos(\beta_n L) = 0, \tag{2.30}$$

with the analytical solutions

$$(\beta_n L) = \pi \left(n - \frac{1}{2} \right) \quad \text{with} \quad n = 1, 2, 3, \ldots . \tag{2.31}$$

A comparison between the numerically and asymptotically calculated eigenvalues is given in Table 2.1. Knowing the eigenvalues allows to solve Equation 2.27: $a_2/a_1 = -0.7341$, -1.0185, -0.9992, $-1.0000, \ldots$. The asymptotic solution of a_2/a_1 for $n \gg 1$ is -1. The final solution of the eigenfunctions, also referred to as flexural mode shapes is

$$\Phi_n(x) = a_1 \left(\cos(\beta_n x) - \cosh(\beta_n x) + \frac{a_2}{a_1} \left(\sin(\beta_n x) - \sinh(\beta_n x) \right) \right), \tag{2.32}$$

where a_1 remains undefined as long as no external force is applied. Figure 2.5 shows the first four solutions using $a_1 = 1$. Each mode has n stagnant nodes where $\Phi_n = 0$, one at the clamped end ($x = 0$) and the remaining ones distributed along the cantilever. The normalized gradient $d\Phi_n/dx$ and curvature $d^2\Phi_n/dx^2$ of the cantilever is shown in Figure 2.6. These results give important insights to optimize the laser position on the cantilever used for detection and excitation. The employed optical beam deflection system utilizes a laser beam to measure the angular displacement of the cantilever. Consequently, it is sensitive to the gradient, which is highest at the cantilever tip ($x = L$, see Figure 2.6a) for all modes [102].

Table 2.1: Numeric and asymptotic solutions of the eigenvalues $\beta_n L$ of mode n, calculated using Equation 2.29 and 2.31, respectively. The two functions converge quickly with an error of $\Delta < 1‰$ for $n \geq 3$. The ratio of the modal eigenfrequency $\omega_{0,n}$ to the fundamental eigenfrequency $\omega_{0,1}$ as well as the ratio of effective resonator mass m_{eff} to cantilever mass m_c are shown.

Mode n	Numeric $\beta_n L$	Asymptotic $\beta_n L$	Δ / ‰	$\omega_{0,n}/\omega_{0,1} = \beta_n^2/\beta_1^2$	$m_{\text{eff},n}/m_c = 3/(\beta_n L)^4$
1	1.8751	1.5708	-162.3	1.00	$2.43{\cdot}10^{-1}$
2	4.6941	4.7124	3.9	6.27	$6.18{\cdot}10^{-3}$
3	7.8548	7.8540	-0.1	17.55	$7.88{\cdot}10^{-4}$
4	10.9955	10.9956	0.0	34.39	$2.05{\cdot}10^{-4}$
5	14.1372	14.1372	0.0	56.84	$7.51{\cdot}10^{-5}$
6	17.2788	17.2788	0.0	84.91	$3.37{\cdot}10^{-5}$
7	20.4204	20.4204	0.0	118.60	$1.73{\cdot}10^{-5}$
8	23.5619	23.5619	0.0	157.90	$9.73{\cdot}10^{-6}$
9	26.7035	26.7035	0.0	202.81	$5.90{\cdot}10^{-6}$
10	29.8451	29.8451	0.0	253.34	$3.78{\cdot}10^{-6}$

Strictly speaking, this only applies for infinitely small laser spots, but is considered a good approximation for spot sizes $w_{\text{laser}} \ll L$ [103]. In contrast, the beam curvature is highest at the clamped end ($x = 0$, see Figure 2.6b). The efficiency of photothermal excitation, where a laser periodically heats the cantilever to induce vibration, is proportional to the beam curvature [104]. Thus, it is most efficient to excite multiple modes simultaneously, by positioning the excitation laser close to the clamped end of the cantilever.
Next, the undamped eigenfrequencies, also referred to a vacuum frequencies, for each mode can then be calculated using Equations 2.15 and 2.20:

$$\omega_{0,n} = \frac{(\beta_n L)^2}{L^2}\sqrt{\frac{EI_z}{\mu_c}} = \frac{(\beta_n L)^2 h}{L^2}\sqrt{\frac{E}{12\rho_c}}. \tag{2.33}$$

This important relation only requires the material properties and the dimensions of the cantilever beam. For a given material the vacuum frequency scales linearly with the thickness h and with the inverse square of the length L of the cantilever. For higher modes, the vacuum frequency correlates quadratically with the eigenvalue (see Table 2.1). Employing the definition for the spring constant of a cantilever [105],

$$k_{\text{eff}} = \frac{3EI_z}{L^3} = \frac{Ebh^3}{4L^3}, \tag{2.34}$$

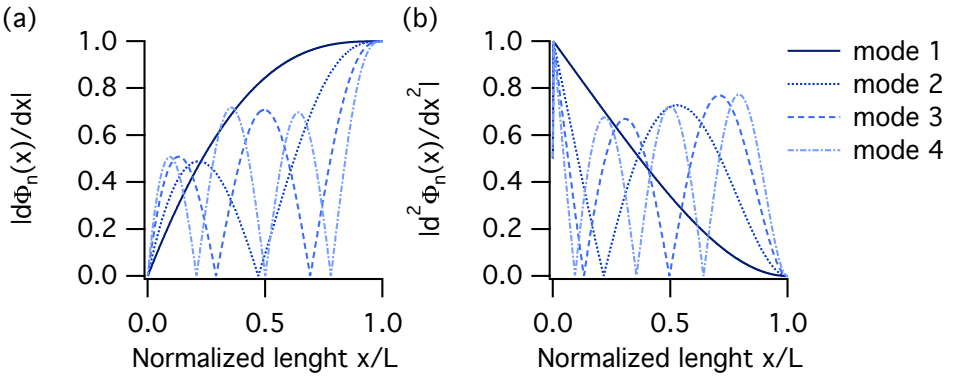

Figure 2.6: (a) Gradient $d\Phi_n/dx$ and (b) curvature $d^2\Phi_n/dx^2$ of mode 1–4 of the cantilever. Shown are the absolute values normalized to 1.

allows to identify the effective mass of the cantilever by comparing $\omega_0 = \sqrt{k_{\text{eff}}/m_{\text{eff},n}}$ (Equation 2.3) to Equation 2.33:

$$m_{\text{eff},n} = \frac{3\rho_c hbL}{(\beta_n L)^4} = \frac{3m_c}{(\beta_n L)^4}. \tag{2.35}$$

The effective mass decreases with the fourth power along higher modes, which is the reason for the quadratic increase of the vacuum frequencies (see Table 2.1). It is emphasized that some authors included the eigenvalue $\beta_n L$ in the effective spring constant [106], resulting in a constant effective mass.
In summary, the full spatial and temporal behavior of a cantilever undergoing undamped flexural vibrations can be described by combining Equations 2.19, 2.27 and 2.32:

$$\begin{aligned} W_n(x,t) = a_1 e^{i\omega_{0,n}t}\Bigg(&\cos(\beta_n x) - \cosh(\beta_n x) \\ &+ \frac{\sin(\beta_n L) - \sinh(\beta_n L)}{\cos(\beta_n L) + \cosh(\beta_n L)} \left(\sin(\beta_n x) - \sinh(\beta_n x)\right) \Bigg). \end{aligned} \tag{2.36}$$

The eigenvalue $\beta_n L$ is calculated by solving Equation 2.29 and the vacuum frequency $\omega_{0,n}$ using Equation 2.33.

2.2.2 Finite element analysis

Finite element analysis (FEA) was used to numerically calculate the undamped eigenfrequencies of the employed cantilevers. The cantilevers were modeled as isotropic, linear elastic material using the *Solid Mechanics Interface* in COMSOL Multiphysics 4.3a. The three-dimensional models were meshed with 25'000–30'000 elements. The boundary condition at the clamped end of the beam was set as a fixed constraint. The initial value was a small dis-

Table 2.2: Vacuum frequencies $f_{0,n} = \omega_{0,n}/2\pi$ in kHz calculated analytically (Euler-Bernoulli, Equation 2.33) and numerically (finite element analysis, FEA). The Young's modulus and mass density of silicon are $E = 169$ GPa and $\rho_c = 2330$ kg/m^3, respectively.

	300 μm × 35 μm × 2 μm			500 μm × 100 μm × 4 μm		
Mode n	FEA	Analytical	Δ / %	FEA	Analytical	Δ / %
1	29.4	30.6	3.98	22.2	22.0	-0.89
2	183.9	191.6	4.17	139.1	137.9	-0.85
3	514.6	536.5	4.25	389.6	386.3	-0.87
4	1008.3	1051.3	4.27	764.0	756.9	-0.93
5	1666.7	1737.8	4.27	1264.0	1251.2	-1.01
6	2489.4	2596.0	4.28	1889.7	1869.1	-1.09

turbance in the displacement field of 10^{-10} m in z-direction. Subsequently, the *Eigenvalue* and *Eigenfrequency* solver nodes were used to calculate the eigenfrequencies and eigenmodes of the cantilever. The first fifteen eigenmodes are shown in Figure 2.7. Besides the flexural (out-of-plane) modes considered here, lateral (in-plane) and torsional (twisting) modes were also identified. A comparison between analytically and numerically (FEA) calculated flexural mode frequencies is given in Table 2.2. The 300 μm × 35 μm × 2 μm cantilevers have a tapered end with a length of about 15 μm. This additional mass is not considered in the analytical model, thus it slightly overestimates the frequencies. Regardless, the deviations are below 5%. For the rectangular 500 μm × 100 μm × 4 μm cantilevers, the deviations are in the order of 1%.

2.3 Microcantilever dynamics in liquid

2.3.1 Hydrodynamic forces

It was early noted that the medium a vibrating beam is immersed in, has an impact on its dynamic behavior [107]. To theoretically describe this behavior, Equation 2.16 from the previous section is employed with an additional hydrodynamic force term F_{hydro}:

$$EI\frac{\partial^4 W(x,t)}{\partial x^4} + \mu_c\frac{\partial^2 W(x,t)}{\partial t^2} + c_0\frac{\partial W(x,t)}{\partial t} = F_{\text{drive}}(x,t) + F_{\text{hydro}}(x,t). \tag{2.37}$$

The hydrodynamic forces can be decomposed into an inertial and dissipative term [108]:

$$F_{\text{hydro}}(x,t) = -\mu_f\frac{\partial^2 W(x,t)}{\partial t^2} - c_v\frac{\partial W(x,t)}{\partial t}, \tag{2.38}$$

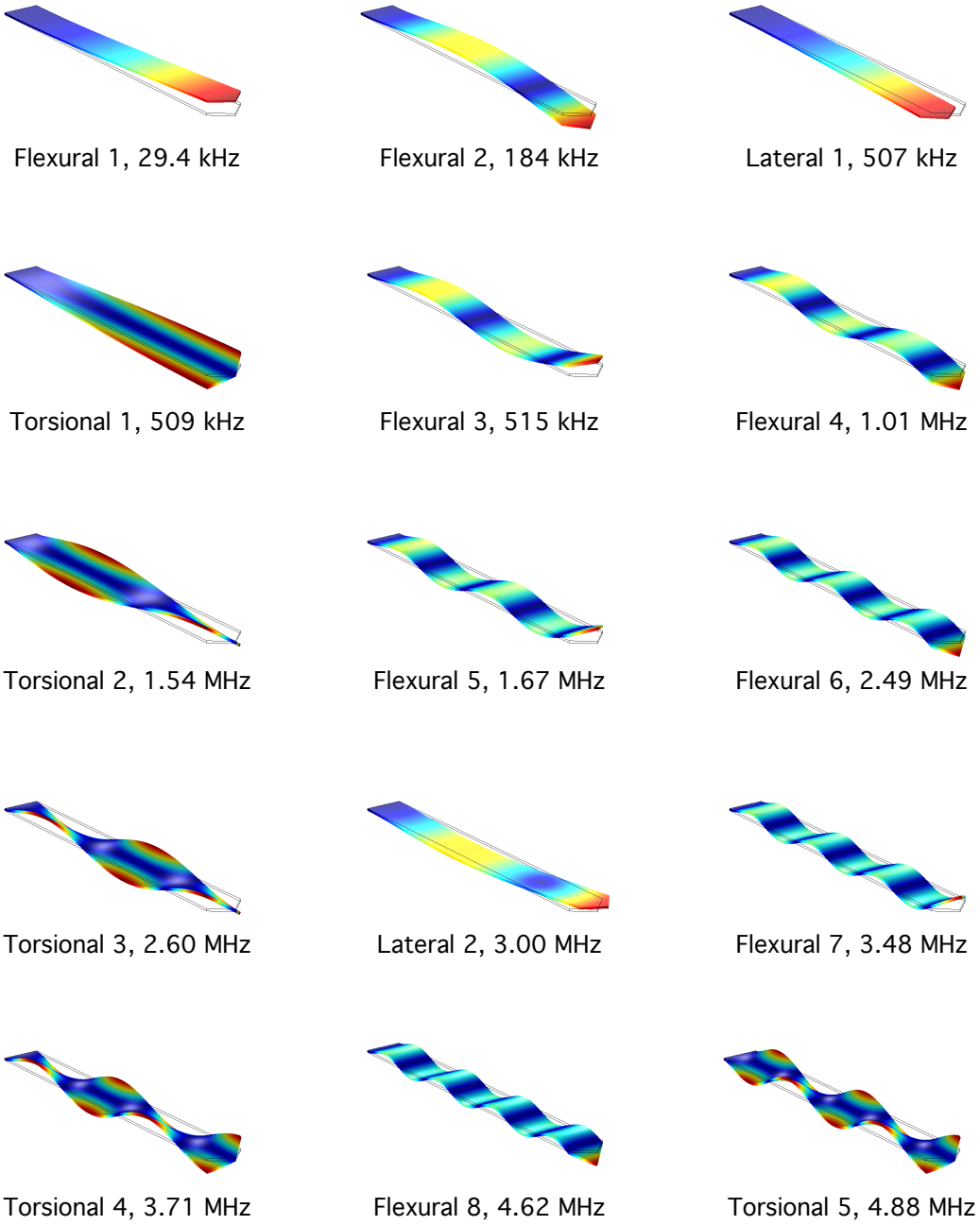

Figure 2.7: The first fifteen eigenmodes of a microcantilever (300 μm $\times$ 35 μm $\times$ 2 μm) calculated by finite element analysis. Flexural (out-of-plane), lateral (in-plane) and torsional (twisting) modes and their corresponding eigenfrequencies are shown, the color coding indicates the RMS amplitude.

where μ_f is the co-moving or added fluid mass per length and c_v the viscous damping coefficient per length. μ_f is related to the cantilever mass per length μ_c by the added mass coefficient $a_m = \mu_f/\mu_c$. Inserting Equation 2.38 into 2.37 leads to:

$$EI\frac{\partial^4 W(x,t)}{\partial x^4} + \mu_c(1+a_m)\frac{\partial^2 W(x,t)}{\partial t^2} + (c_0+c_v)\frac{\partial W(x,t)}{\partial t} = F_{\text{drive}}(x,t). \quad (2.39)$$

Because the intrinsic dissipation is much smaller than the fluid damping ($c_0 \ll c_v$) for high aspect-ratio cantilevers, it is neglected [109]. Usually a complex, dimensionless hydrodynamic function Γ is introduced to describe the inertial (real part, added mass) and dissipative (imaginary part, viscous damping) hydrodynamic forces [33, 110, 111]. The added mass μ_f and viscous damping c_v per unit length are related to Γ by

$$\mu_f = \frac{\pi}{4}\rho_f b^2 \Re(\Gamma), \quad (2.40)$$

$$c_v = \frac{\pi}{4}\rho_f b^2 \omega \Im(\Gamma). \quad (2.41)$$

For small dissipative effects ($Q_n \gg 1$) the coupling between the modes is weak and each mode can be described by a harmonic oscillator (see Reference [111] and Section 2.1). Thus, the eigenfrequency ω_n and quality factor Q_n can be generally described by

$$\frac{\omega_n}{\omega_{0,n}} = \left(1+\frac{\pi\rho_f b}{4\rho_c h}\Re(\Gamma)\right)^{-\frac{1}{2}} = \left(1+\frac{\mu_f}{\mu_c}\right)^{-\frac{1}{2}} \quad \text{for} \quad Q_n \gg 1, \quad (2.42)$$

$$Q_n = \frac{\frac{4\rho_c h}{\pi\rho_f b}+\Re(\Gamma)}{\Im(\Gamma)} = \frac{(\mu_c+\mu_f)\omega_n}{c_v} \quad \text{for} \quad Q_n \gg 1. \quad (2.43)$$

Because Γ, as we will see, depends on the frequency ω_n, Equation 2.42 is solved by an iterative process until the results are consistent to a certain precision [112]. To find a solution for Γ the Navier-Stokes equations, characterizing the flow field around the cantilever, need to be solved. For small vibrational amplitudes in liquid, the linearized incompressible Navier-Stokes equation and incompressible continuity equation are applicable [113]:

$$\rho_f\frac{\partial \mathbf{u}}{\partial t} = -\nabla p + \eta_f\nabla^2\mathbf{u}, \quad \nabla\cdot\mathbf{u} = 0, \quad (2.44)$$

where $\mathbf{u}$ is the flow velocity field and p the pressure [114]. Analytical, semi-analytical and numerical approaches were employed to solve Equation 2.44. An overview on theoretical models describing the hydrodynamic forces acting on vibrating cantilevers immersed in fluid is given in Table 2.3. All models adopt the no-slip boundary condition that is assumed to be valid because slip lengths are in the range of nanometers [115], whereas the dominant length scale of the flow is in the micrometer range. An indication for the validity of these assumptions are multiple experimental verifications [46, 64, 112, 116–118].

Table 2.3: Overview on theoretical models describing hydrodynamic forces acting on a cantilever immersed in a Newtonian fluid. Provided are mode number and type (flexural: F, torsional: T, in-plane: IP); geometrical assumptions (if not otherwise mentioned, $a_0/h, h/b, b/L \ll 1$); fluid properties and boundaries (bounded: presence of a nearby solid surface); and special remarks. The models employed in this thesis are highlighted.

Reference		Vibrational modes		Geometry	Fluid			Remarks
		Number	Type		Viscous	Bounded	Compressible	
Elmer 1997	[119]	arbitrary	F					
Hirai 1998	[120]	$n = 1$	F		√			String of beads
Kirstein 1998	[121]	$n = 1$	F		√			
Sader 1998	[111]	$n = 1$	F		√			
Açıkalın 2003	[122]	$n = 1$	F		√			
Maali 2005	[33]	$n = 1$	F		√			
Green 2005	[123]	$n = 1$	F, T		√	√		
Van Eysden 2006	[124]	arbitrary	F, T					
Van Eysden 2007	[125]	arbitrary	F, T		√			
Dareing 2007	[126]	$n = 1$	F		√	√		$\rho_f = 0$
Tung 2008	[127]	$n = 1$	F		√	√		
Van Eysden 2009	[128]	arbitrary	F, T		√		√	
Brumley 2010	[129]	$n = 1$	F, IP	$0 \leq h/b \leq \infty$	√			
Clark 2010	[130]	$n \leq 3$	F		√			
Aureli 2012	[131]	$n = 1$	T	$a_0/b \sim 1$	√			
Aureli 2012	[132]	$n = 1$	F	$a_0/b \sim 1$	√			
Grimaldi 2012	[133]	$n = 1$	F	$a_0/b \sim 0.1$	√	√		
Facci 2013	[134]	$n = 1$	F	$a_0/b \sim 0.1, b/L \sim 1$	√			
Phan 2013	[135]	$n = 1$	F, IP	$a_0/b \sim 0.1, h/b \sim 1$	√			

In the following, the dimensionless numbers governing the fluid flow and the hydrodynamic functions from the employed models by Sader [111], Van Eysden and Sader [125] and Tung *et al.* [127] are introduced. The dimensionless number most significant for cantilever vibration in fluid is the Reynolds number [121, 125, 128],

$$Re \equiv \frac{\omega \rho_f b^2}{\eta_f}, \tag{2.45}$$

which quantifies the ratio between inertial and viscous forces. The width of the cantilever b represents the dominant length scale of the flow, ω is the angular frequency, and ρ_f and η_f are the fluid density and viscosity, respectively. It is emphasized that this definition of the Reynolds number deviates from the common definition $Re^* = \rho_f u b/\eta_f$, with u being the flow velocity [114], and is also referred to as "frequency parameter" or "dimensionless frequency" [129]. Various definitions of *Re* differ by a factor of 4 [33, 111, 123, 127, 130, 132, 135] or 2π [131, 133, 134]. The Reynolds numbers of microcantilevers in liquid are $Re \sim 10$ [111]. However, employing higher modes of vibration $f \sim 10^6$ Hz and cantilever widths $b \sim 100$ μm leads to $Re \sim 10^5$. In the case of macroscopic cantilevers or very high frequencies, $Re \to \infty$ and viscous effects become negligible. By comparing the definition of *Re* to the viscous boundary layer δ (see Equation 1.6) we find that $Re = 2(b/\delta)^2$. Thus, it is also a measure of the ratio squared between the cantilever dimensions and the boundary layer thickness.

A readily applicable formulation of the hydrodynamic function for fundamental mode vibrations of a cantilever was introduced by Sader [111]. It was derived under the same assumptions introduced in Section 2.2.1 and by solving the 2D flow field around the cantilever:

$$\Gamma_{\mathrm{f}}(Re/4) = \Omega(Re/4)\Gamma_{\mathrm{circ}}(Re/4). \tag{2.46}$$

Thereby, $\Omega(Re/4)$ is a polynomial correction function provided in Reference [111] and $\Gamma_{\mathrm{circ}}(Re/4)$ is the hydrodynamic function for a beam of circular cross section:

$$\Gamma_{\mathrm{circ}}(Re/4) = 1 + \frac{4iK_1\left(-i\sqrt{iRe/4}\right)}{\sqrt{iRe/4}K_0\left(-i\sqrt{iRe/4}\right)}, \tag{2.47}$$

where K_0 and K_1 are zeroth and first order modified Bessel functions of the second kind and i is the imaginary unit satisfying $i = \sqrt{-1}$. As shown in Figure 2.8 the hydrodynamic function for a cylindrical (Equation 2.47) and rectangular (Equation 2.46) beam vibrating in the fundamental mode are very similar. Deviations in the range $10^0 \leq Re \leq 10^3$ are below 11% for the real and 5% for the imaginary part. Both, inertial (real part) and dissipative (imaginary part) forces decrease with increasing *Re*. Even though, the theory assumes an

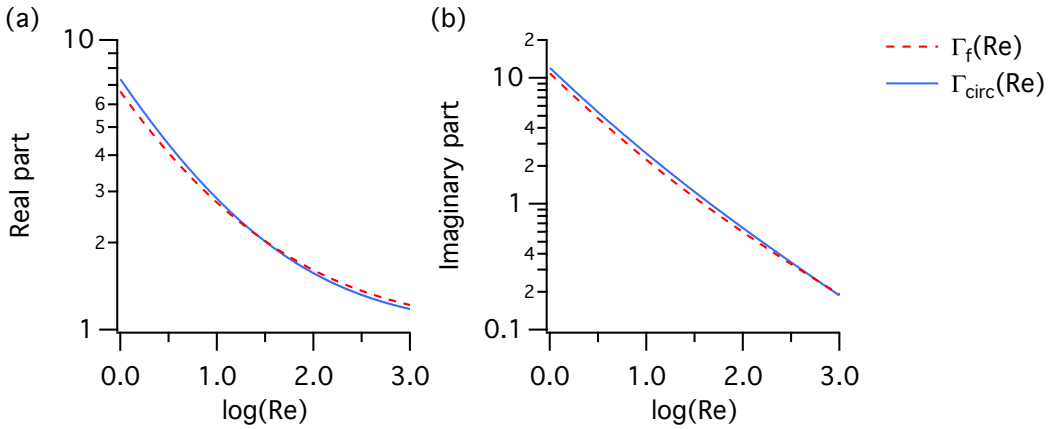

Figure 2.8: (a) Real and (b) imaginary part of the hydrodynamic function for a beam of circular $\Gamma_{\text{circ}}(Re/4)$ and rectangular $\Gamma_{\text{f}}(Re/4)$ cross-section, vibrating in the fundamental mode immersed in an unbounded fluid [111]. The Reynolds number is defined as $Re = \omega\rho_f b^2/\eta_f$.

infinitely long beam, good agreement between theory and experiments was found for aspect ratios $L/b > 4$ [116].

Usually, calculating the flow field around the cantilever in 2D (yz-planes, see Figure 2.3a) is sufficient. However, in case of higher modes ($n > 1$) [125] or aspect ratios $b/L \sim 1$ [134], flow along the longitudinal axis of the cantilever must not be neglected. The deviations become significant for mode numbers $n > 2$ in liquid [33], thus, the 3D flow field needs to be solved. To account for these effects a normalized mode number,

$$\kappa_n \equiv (\beta_n L)\frac{b}{L}, \tag{2.48}$$

is required in addition to the Reynolds number *Re*. It is a measure for the relative aspect ratio for a given higher flexural mode of vibration and depends on the eigenvalue $(\beta_n L)$ and the geometrical aspect ratio b/L (width/length). For moderate mode numbers and common microcantilever aspect ratios ($b/L \sim 10^{-1}$), normalized mode numbers are on the order of $\kappa_n \sim 1$. The hydrodynamic function for different normalized mode numbers is shown in Figure 2.9. Inertial forces (real part) generally decrease with increasing mode number, i.e., larger κ_n, whereas dissipative forces (imaginary part) show a more complex behavior. For $\kappa_n \to 0$ the hydrodynamic function for the fundamental mode $\Gamma_f(Re/4)$ is recovered. Because the calculation of $\Gamma_\kappa(Re, \kappa_n)$ is computationally expensive, values were calculated for a range of $10^0 \leq Re \leq 10^4$ and $0.1 \leq \kappa_n \leq 20$ and stored in a lookup table [136].

So far, cantilever vibrations in an unbounded, i.e., infinitely extended, fluid were considered. This, however, is not a valid assumption in many scanning force and sensing applications

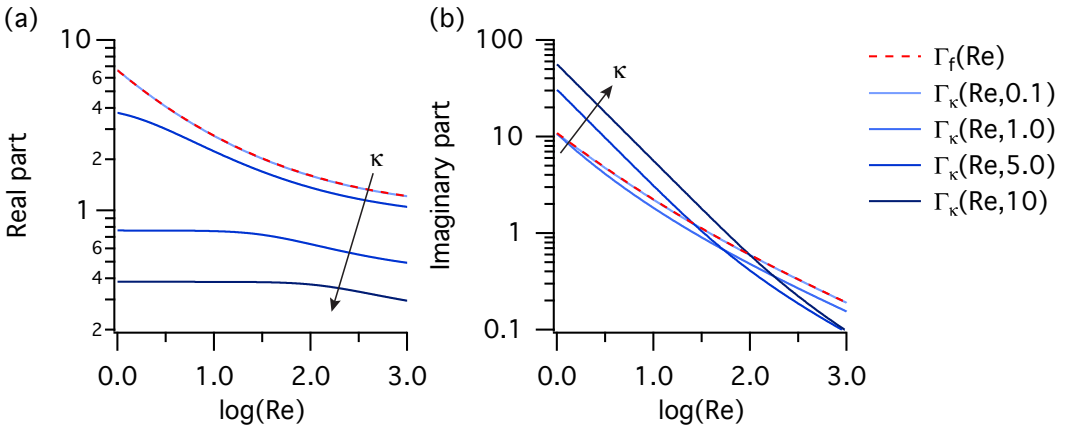

Figure 2.9: (a) Real and (b) imaginary part of the hydrodynamic function $\Gamma_\kappa(Re, \kappa_n)$ for higher flexural mode vibrations of a cantilever immersed in fluid for normalized mode numbers $\kappa_n = (\beta_n L)b/L$ of 0.1, 1.0, 5.0, and 10.0 [125]. For comparison the hydrodynamic function $\Gamma_f(Re)$ for fundamental mode vibrations is shown. The Reynolds number is defined as $Re = \omega\rho_f b^2/\eta_f$.

where a microcantilever is placed close to a solid surface. To account for the influence of a proximate surface the normalized gap [123],

$$H \equiv \frac{g}{b}, \tag{2.49}$$

is introduced. It quantifies the ratio between the cantilever-surface spacing g and cantilever width b, i.e., dominant length scale of the flow. Because higher modes were not considered in the analysis, the hydrodynamic function Γ_H only depends on Re and H. A semi-analytical formulation based on the extended results by Green and Sader [123] was derived by Tung *et al.* [127]. It is emphasized that the definition of H in the hydrodynamic function by Tung deviates by a factor of 2 from Equation 2.49. Figure 2.10 shows the hydrodynamic function $\Gamma_H(Re/4, 2H)$ for different normalized gaps H. For gaps $H \gg 1$ the effect of the surface diminishes and the hydrodynamic load converges with the unbounded case Γ_f. For $H < 1$ a strong increase in dissipation (imaginary part) is predicted. This is due to the fact that fluid in the cavity between the cantilever and the surface is displaced during each oscillation cycle, increasing viscous dissipation.

In the following paragraph, the validity of the assumptions of a continuous, incompressible fluid and non-turbulent flow are verified. To assess if the continuum hypothesis is valid the Knudsen number is employed [137]:

$$Kn \equiv \max\left\{\frac{\lambda^*}{g}, \frac{\lambda^*}{b}\right\}, \tag{2.50}$$

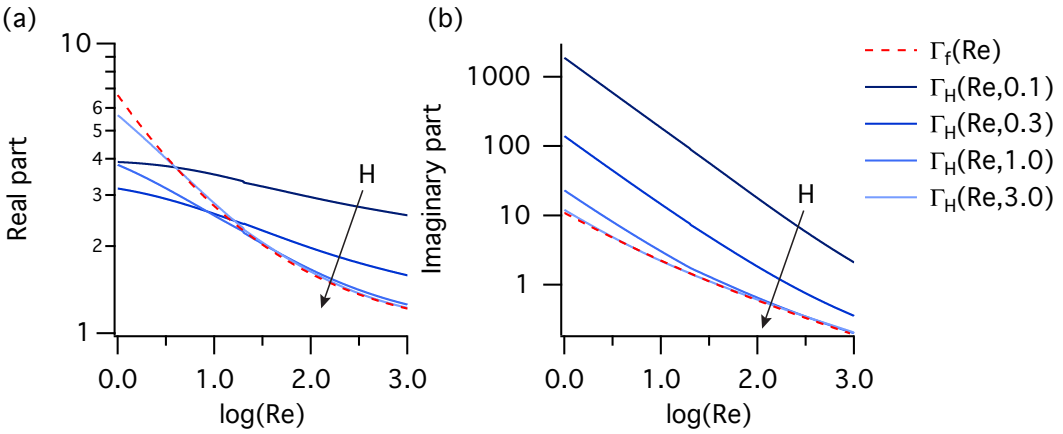

Figure 2.10: (a) Real and (b) imaginary part of the hydrodynamic function $\Gamma_H(Re/4, 2H)$ for a cantilever vibrating close to a surface for normalized gaps $H = g/b$ of 0.1, 0.3, 1.0, and 3 [127]. For comparison the hydrodynamic function $\Gamma_f(Re/4)$ in an unbounded fluid is shown. The Reynolds number is defined as $Re = \omega\rho_f b^2/\eta_f$.

where λ^* is the mean free path of the molecules in the fluid and either g or b the dominant length scale of the flow. For $Kn \sim 1$ the mean free path of the molecules is in the order of the cantilever dimensions, thus, statistical mechanics need to be employed. However, in liquid $\lambda^* \sim 0.1$ nm [114] and minimal employed gap sizes $g \sim 1$ μm and cantilever widths $b \sim 10$ μm result in $Kn \sim 10^{-4}$. Thus, the fluid can be treated as a continuum and the Navier-Stokes equation is applicable (see Equation 2.44). Furthermore, the Navier-Stokes equation is usually linearized, i.e., the non-linear convective term considering turbulent flow is neglected [114]. The scaled Navier-Stokes equations from Reference [138] indicates that the convective term is negligible for

$$\frac{KC}{2\pi}\sqrt{\frac{Re}{2}} \ll 1, \tag{2.51}$$

where the Keulegan-Carpenter number is defined as [132]

$$KC \equiv 2\pi\frac{a_0}{b}, \tag{2.52}$$

with a_0 being the amplitude of vibration of the cantilever. Since amplitudes of vibration in liquid are on the order of $a_0 \sim 1$ nm (see Appendix A and Reference [33]), the obtained Keulegan-Carpenter numbers are very small, $KC \sim 10^{-4}$. For accessible Reynolds numbers $Re \sim 10^5$, the product $KC\sqrt{Re} \sim 0.01$ and, thus, the condition in Equation 2.51 is fulfilled (flow regime A^* in Reference [139]). In conclusion, the flow can be assumed non-turbulent even at high Reynolds numbers, as long as the vibrational amplitudes are very small. Fi-

nally, the importance of fluid compressibility is assessed. Usually the spacial wavelength of the beam is much smaller than the wavelength of sound in the fluid. However, at high frequencies the sound wavelength decreases and becomes equal to the spacial wavelength of the beam. In this case energy is dissipated as sound waves resulting in lower quality factors. To quantify this effect the normalized wave number [128],

$$\varsigma \equiv \frac{\omega b}{c_{\text{sound}}}, \tag{2.53}$$

is introduced, where c_{sound} is the speed of sound of the medium the cantilever is immersed in. As long as $\varsigma \ll \kappa_n$ compressibility can be neglected. Thus, a critical mode number, above which compressibility becomes significant, can be formulated [128]:

$$n_{\text{crit}} \sim \frac{0.596\kappa_n}{\varsigma} = \frac{0.178 c_{\text{sound}}}{f_{0,1} L}. \tag{2.54}$$

In water $c_{\text{sound}} = 1482$ m/s (at $T = 298$ K [140]), thus critical mode numbers n_{crit} ranging from 23 (500 μm $\times$ 100 μm $\times$ 4 μm) to 33 (350 μm $\times$ 35 μm $\times$ 2 μm) were found. Such high modes cannot be measured in the frequency bandwidth of a common optical beam deflection system which is usually in the order of 1 MHz. In contrast, for cantilevers immersed in gas, where c_{sound} is about five times lower than in liquid, compressibility becomes significant at accessible mode numbers [118] and, thus, should be considered.

2.3.2 Response of higher flexural modes of vibration

Next, the sensitivity of higher flexural modes of vibration to changes liquid properties is discussed. Therefore, the theory by Van Eysden and Sader [125], introduced in the previous section, is used to describe the hydrodynamic load and Equation 2.42 to calculate eigenfrequencies:

$$f_n = f_{0,n} \left(1 + \frac{\pi}{4} \frac{\rho b}{\rho_c h} \Re \left(\Gamma_\kappa(Re, \kappa_n) \right) \right)^{-\frac{1}{2}}. \tag{2.55}$$

The quality factor was calculated according to Equation 2.43:

$$Q_n = \frac{\frac{4}{\pi} \frac{\rho_c h}{\rho_f b} + \Re(\Gamma_\kappa(Re, \kappa_n))}{\Im(\Gamma_\kappa(Re, \kappa_n))}. \tag{2.56}$$

Table 2.4 shows the calculated eigenfrequencies and quality factors in water for the first five modes. The fluid loading has a drastic impact and reduces the frequencies by up to 70% compared to the vacuum frequency. The higher the mode number, the smaller the relative frequency shift due to the fluid and the higher the quality factor. To visualize the sensitivity

Table 2.4: Calculated eigenfrequencies f_n and quality factors Q_n of a microcantilever ($300 \times 35 \times 2$ μm^3) vibrating at the n-th flexural mode in water ($\eta = 1.005$ mPa·s, $\rho = 998.25$ kg/m^3). For comparison the corresponding vacuum frequencies $f_{0,n}$ and their ratios to the eigenfrequencies are provided.

n	f_n / kHz	Q_n	$f_{0,n}$ / kHz	$f_n/f_{0,n}$
1	9.3	2.65	30.6	0.30
2	67.1	5.81	191.6	0.35
3	201.1	9.35	536.5	0.37
4	414.4	13.01	1051.3	0.39
5	715.2	16.83	1737.8	0.41

of each mode to changes in viscosity and mass density, the gradient of f_n and Q_n normalized to their values in water (see Table 2.4) was calculated:

$$\nabla \tilde{f}_n = \frac{\partial \tilde{f}_n}{\partial \eta}\Delta\eta + \frac{\partial \tilde{f}_n}{\partial \rho}\Delta\rho, \tag{2.57}$$

$$\nabla \tilde{Q}_n = \frac{\partial \tilde{Q}_n}{\partial \eta}\Delta\eta + \frac{\partial \tilde{Q}_n}{\partial \rho}\Delta\rho, \tag{2.58}$$

where $\Delta\eta = \log(10^{-2}$ Pa·s) and $\Delta\rho = 1800$ kg/m^3 are the plotted viscosity and density range, respectively. Furthermore, the sensitivities S of f_n and Q_n are reflected in the partial derivatives with respect to viscosity and density:

$$S_{\eta,f} = \frac{\partial f_n}{\partial \eta}, \quad S_{\rho,f} = \frac{\partial f_n}{\partial \rho}, \quad S_{\eta,Q} = \frac{\partial Q_n}{\partial \eta}, \quad S_{\rho,Q} = \frac{\partial Q_n}{\partial \rho}, \tag{2.59}$$

with the following units $[S_{\eta,f}]$ = Hz/(Pa·s), $[S_{\rho,f}]$ = Hz/(kg/m^3), $[S_{\eta,Q}]$ = 1/(Pa·s) and $[S_{\rho,Q}]$ = 1/(kg/m^3). Figures 2.11 and 2.12 show calculated [125] eigenfrequencies f_n and quality factors Q_n of the first five flexural modes of vibration of a cantilever immersed in a fluid with viscosity η and mass density ρ. The sensitivities to viscosity ($S_{\eta,f}$, $S_{\eta,Q}$) and density ($S_{\rho,f}$, $S_{\rho,Q}$) changes as well as the direction of the gradient $\nabla \tilde{f}_n$ are plotted, indicating whether f_n and Q_n rather respond to variations in viscosity or density. For reference the sensitivities in water are provided in Table 2.5.

Overall, the sensitivity increases for fluids with low viscosity and mass density, e.g. gases, and with higher mode numbers n. The eigenfrequency f_n (Figure 2.11) decreases with increasing viscosity and density, but is mainly governed by the density ($S_{\rho,f} > S_{\eta,f}$ in most conditions). At lower frequencies, i.e., Reynolds numbers *Re*, the viscous effects become dominant and start influencing the frequency (upper right-hand quadrant and at lower modes). In contrast, higher mode eigenfrequencies, i.e., high Reynolds numbers *Re*, are weakly influenced by the

Table 2.5: Calculated sensitivities S of a microcantilever ($300 \times 35 \times 2$ μm^3) vibrating at the n-th flexural mode in water ($\log(\eta) = -3$, $\rho = 998.25$ kg/m^3). Sensitivities of the eigenfrequency and quality factor to viscosity ($S_{\eta,f}$, $S_{\eta,Q}$) and density ($S_{\rho,f}$, $S_{\rho,Q}$) changes are shown, respectively.

Mode n	$S_{\eta,f}$ kHz/(mPa·s)	$S_{\rho,f}$ Hz/(kg/m^3)	$S_{\eta,Q}$ 1/(mPa·s)	$S_{\rho,Q}$ 10^{-3}/(kg/m^3)
1	-0.85	-3.74	-1.06	0.34
2	-2.99	-27.73	-2.39	0.63
3	-5.68	-83.16	-3.92	0.92
4	-8.35	-170.13	-5.56	1.18
5	-10.80	-290.64	-7.32	1.43

viscosity. The quality factor Q_n (Figure 2.12) is, in first approximation, independent of the density ($S_{\rho,Q} \ll S_{\eta,Q}$). Q_n and the sensitivity $S_{\eta,Q}$ decrease with increasing viscosity. The slight increase in Q_n with increasing density is due to the fact, that the resonator (cantilever and co-moving fluid) has a higher effective mass.

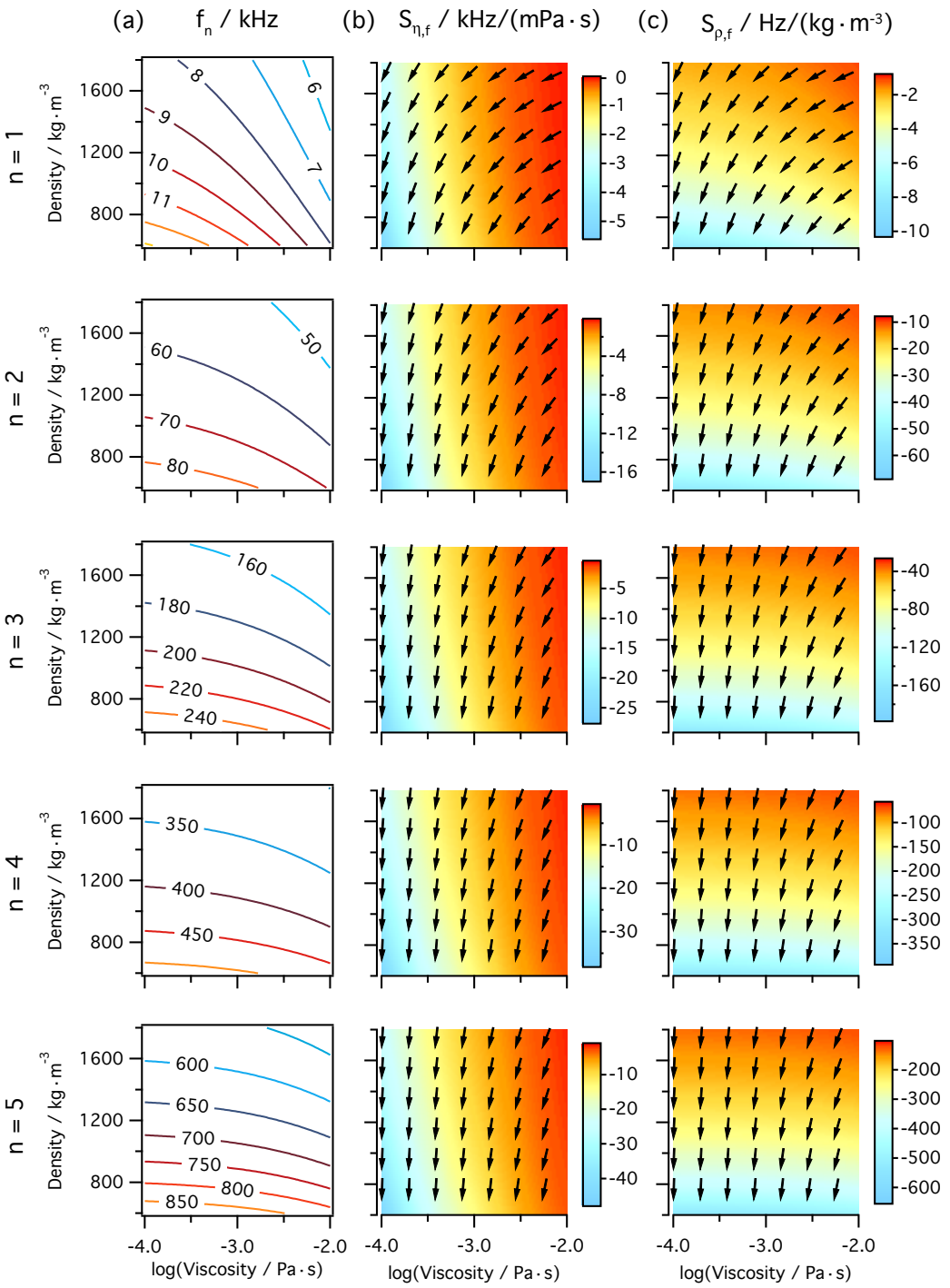

Figure 2.11: Sensitivities of the eigenfrequencies: (a) Calculated eigenfrequencies f_n of flexural mode n of a microcantilever ($300 \times 35 \times 2\ \mu\text{m}^3$), immersed in a fluid of certain viscosity and mass density. Directions of the gradient fields $\nabla \tilde{f}_n$ (black arrows in b and c) and sensitivities (color coded) to (b) viscosity ($S_{\eta,f}$) and (c) density ($S_{\rho,f}$) changes are shown.

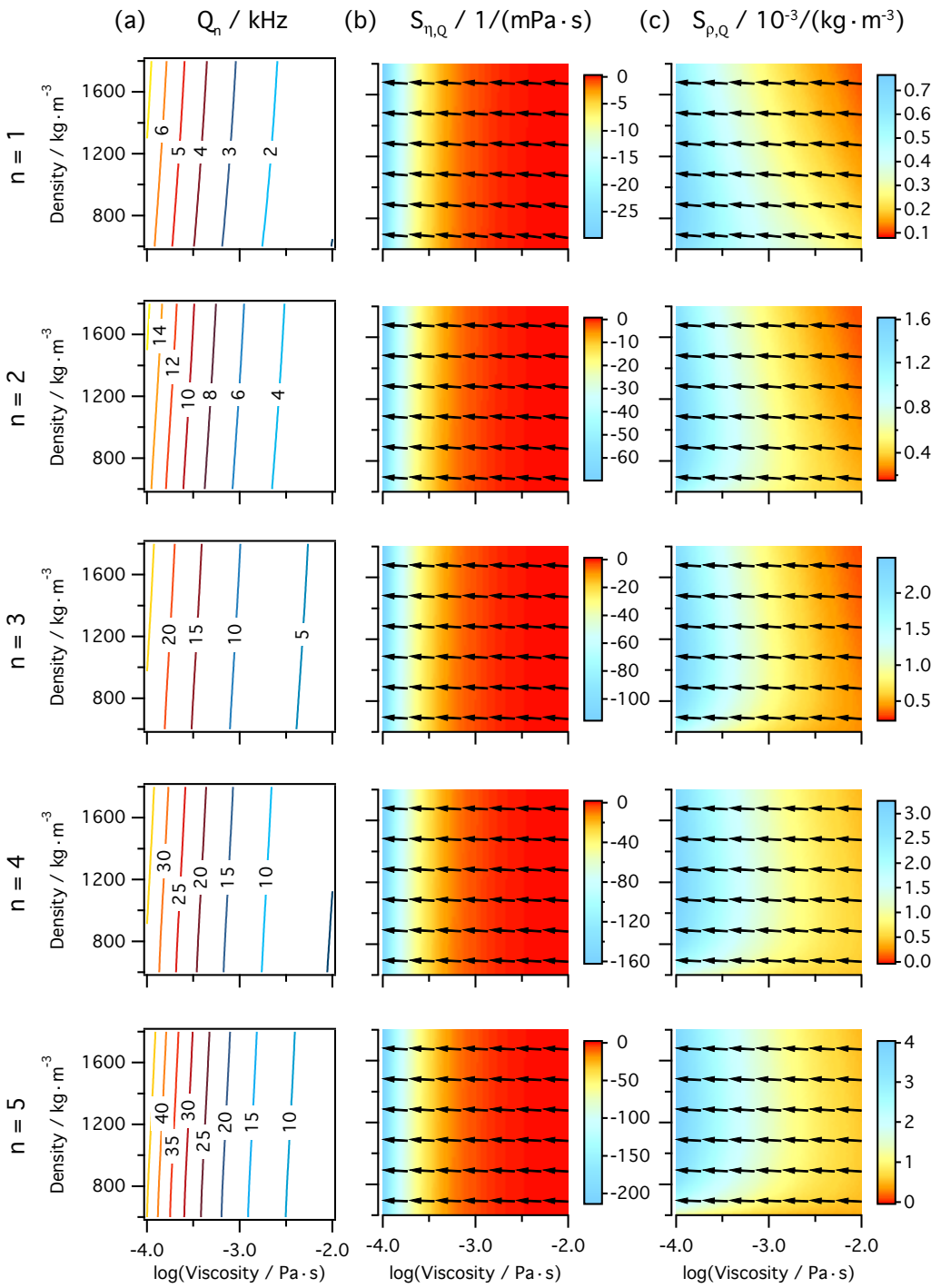

Figure 2.12: Sensitivities of the quality factors: (a) Calculated quality factors Q_n of flexural mode n of a microcantilever ($300 \times 35 \times 2\ \mu\text{m}^3$), immersed in a fluid of certain viscosity and mass density. Directions of the gradient fields $\nabla\tilde{Q}_n$ (black arrows in b and c) and sensitivities (color coded) to (b) viscosity ($S_{\eta,Q}$) and (c) density ($S_{\rho,Q}$) changes are shown.

Chapter 3

Photothermal excitation of microcantilevers in liquid: Effect of the excitation laser position on temperature and vibrational amplitude

Benjamin A. Bircher[1], Luc Duempelmann[1], Hans Peter Lang[2], Christoph Gerber[2], and Thomas Braun[*,1]

[1] Center for Cellular Imaging and NanoAnalytics, Biozentrum, University of Basel, Mattenstrasse 26, CH-4058 Basel, Switzerland

[2] Swiss Nanoscience Institute, University of Basel, Klingelbergstrasse 82, CH-4056 Basel, Switzerland

[*] E-mail: thomas.braun@unibas.ch

Published in Micro & Nano Letters, **8**(11), 770–774 (2013), **DOI:** 10.1049/mnl.2013.0352

Abstract

Demands to improve the sensitivity and measurement speed of dynamic scanning force microscopy and cantilever sensing applications necessitate the development of smaller cantilever sensors. As a result, methods to directly drive cantilevers, such as photothermal or magnetic excitation, are gaining in importance. Here, we report the effect of photothermal excitation of microcantilevers on the increase in steady-state temperature and the dynamics of higher mode vibrations. First, the local temperature increase upon continuous irradiation with laser light at different positions along the cantilever was measured and compared to finite element analysis data. The temperature increase was highest when the heating laser was positioned at the free end of the cantilever. Next, the laser intensity was modulated to drive higher flexural modes to resonance. The dependence of cantilever dynamics on the excitation laser position was assessed and was in good agreement with analytical expressions. An optimal position to simultaneously excite all flexural modes of vibration with negligible

heating was found at the clamped end of the cantilever. Our findings are essential for optimization of the excitation efficiency to minimize the rise in temperature and avoid damaging delicate samples or functionalization layers.

3.1 Introduction

Driving a microcantilever in air or liquid is a prerequisite for dynamic mode scanning force microscopy [141] and mechanical sensing applications [142]. Available techniques include acoustic, magnetic and photothermal excitation. Due to its simplicity and robustness, acoustic excitation, which employs a vibrating piezoelectric crystal, is by far the most often applied. Its major drawbacks are spurious resonances, which result in the well known "forest of peaks" [143]. Particularly in liquid, the indirect energy transfer excites resonances originating from the chip body and fluid cell surfaces, impeding detection of the cantilever response. Although technical improvements have reduced some of these problems [144, 145], approaches in which the cantilever is directly excited are still preferred [25], particularly when the latter is immersed in viscous fluids. Magnetic excitation, where a magnetic field exerts a periodic force on the cantilever, has been successfully applied to drive cantilevers in liquid (for details see Han et al. [146]). When photothermal excitation is employed, an intensity-modulated laser periodically heats the cantilever and thus induces bending. This type of excitation was first applied to bridge resonators [147] and subsequently to cantilevers in air and liquids [44, 148]. The direct energy transfer avoids spurious resonances, and thus renders photothermal excitation suitable for atomic force microscopy [149, 150], force spectroscopy [151] and sensing applications [152]. Driving frequencies up to several megahertz have been accessed [153]. Further, theoretical frameworks have identified the underlying mechanisms, allowing the experimental parameters to be optimized [104, 154, 155]. Highly efficient excitation can be achieved by using an asymmetric cantilever cross section [156] and optimizing the cantilever absorption properties to match the wavelength of the excitation laser [153]. Understanding laser-induced heating of the cantilever and its surroundings is of major importance because it could, e.g., alter the surrounding fluid properties [157] or damage delicate samples.

Here we report the influence of the excitation laser position on the local steady-state temperature distribution and the amplitude of higher flexural modes of vibration in liquid. Steady-state heating by an incident laser with constant intensity is modeled using finite element analysis and compared to the temperature indirectly measured via bi-material bending of the gold-coated cantilever [158]. While focusing the intensity-modulated excitation laser at different positions along the cantilever, the amplitudes of higher flexural modes of vibration are measured and compared to analytical expressions [104, 159].

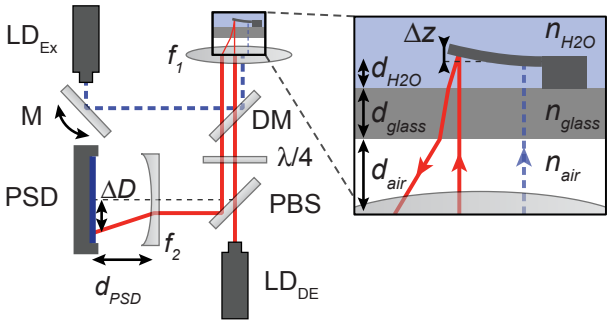

Figure 3.1: Setup employed to heat the cantilever and detect its deflection. The detection beam (red line) originating from a 780 nm laser diode ($\mathrm{LD_{DE}}$) is focused onto the cantilever using a $4\times$ objective (f_1). The reflected beam is directed onto a position sensitive detector (PSD) using a polarizing beam splitter (PBS). A concave lens (f_2) that is separated from the PSD by d_{PSD} is inserted to enhance the deflection signal. Δz and ΔD are the deflection of the cantilever and the induced laser spot displacement on the PSD, respectively. The heating / driving laser ($\mathrm{LD_{EX}}$, 406 nm; blue dashed line) is coupled in using a dichroic mirror (DM). A mirror (M) allows its position on the cantilever to be controlled. Distances are the cantilever-glass slide spacing $d_{\mathrm{H_2O}}$, the thickness of the glass slide d_{glass} and the glass slide-objective (f_1) distance d_{air}. The parameters $n_{\mathrm{H_2O}}$, n_{glass} and n_{air} are the refractive indices of the corresponding media.

3.2 Materials and methods

3.2.1 Experimental setup

Figure 3.1 shows the experimental setup consisting of two laser diodes to respectively heat ($\mathrm{LD_{EX}}$, 406 nm) and detect the deflection ($\mathrm{LD_{DE}}$, 780 nm) of the cantilever. The wavelengths are chosen so that $\approx 67\%$ of the heating and $< 3\%$ of the detection laser intensity is absorbed by the cantilever gold coating. The detection laser spot is positioned at the tip of the cantilever during all experiments, resulting in the highest response for all flexural modes of vibration. The Gaussian spot size on the cantilever, determined using the knife-edge method [160], was 12 μm for $\mathrm{LD_{DE}}$ and 29 μm for $\mathrm{LD_{EX}}$. The deflection of the cantilever Δz is geometrically related to the displacement ΔD of the laser spot on the position sensitive detector (PSD) [161]. Considering the different refractive indices of the media the laser beam passes through,

$$\Delta z = \frac{L}{4} \frac{|f_2|}{n_{\mathrm{H_2O}} \left(\frac{d_{\mathrm{H_2O}}}{n_{\mathrm{H_2O}}} + \frac{d_{\mathrm{glass}}}{n_{\mathrm{glass}}} + \frac{d_{\mathrm{air}}}{n_{\mathrm{air}}} \right) (|f_2| + d_{\mathrm{PSD}})} \Delta D. \tag{3.1}$$

The parameters are: Focal length of the concave lens, $f_2 = -50$ mm; length of the cantilever, $L = 500$ μm; refractive indices, $n_{\mathrm{H_2O}} = 1.33$, $n_{\mathrm{glass}} = 1.50$, $n_{\mathrm{air}} = 1.00$; distances,

$d_{H_2O} = 0.5$ mm, $d_{glass} = 1.0$ mm, $d_{air} = 43.5$ mm and $d_{PSD} = 95$ mm as indicated in Figure 3.1. The static displacement on the PSD is $10\times$ amplified (AM502, Tektronix; bandwidth: 100 Hz) and recorded using a custom LabVIEW (National Instruments) software. For dynamic measurements, an AC signal is modulated on the DC component of the excitation laser. The cantilever response is $10\times$ amplified (SIM911, Stanford Research Systems; bandwidth: 1 MHz) and recorded using a vector network analyzer (MS4630B, Anritsu). Silicon cantilevers with nominal dimensions of $500 \times 100 \times 4$ μm^3 (IBM Zurich Research Laboratory, Rüschlikon, Switzerland) where used for the experiments. Their bottom surface is coated with a 20 nm-thick gold layer. More details of the setup and the cantilever preparation are provided in reference [50]. The cantilevers were immersed and kept in nanopure water for all experiments. The temperature of the fluid cell was stabilized at 293.15 K to an accuracy of 0.3 K.

3.2.2 Steady-state temperature increase by continuous laser irradiation

Temperature measured by bi-material cantilever deflection

The difference in the linear thermal expansion coefficients of the two materials causes a bi-material cantilever beam, subjected to a temperature change of ΔT, to deflect by Δz. Thus, deflection can be used as a measure of the average cantilever temperature, assuming a homogeneous temperature distribution along the beam. Even though the response is complex and non-linear over a wide temperature range [162], it can be linearized for small temperature changes [158, 163],

$$\Delta T = \frac{t_{Si}^2 K(t_{Au}, t_{Si}, E_{Si}, E_{Au})}{3L^3 (\gamma_{Au} - \gamma_{Si}) (t_{Au} + t_{Si})} \Delta z. \tag{3.2}$$

The thickness of the cantilever t_{Si} was determined in a calibration step (see Results and discussion) and the thickness of the deposited gold layer t_{Au} was 20 nm. K is a function depending on the thicknesses and Young's moduli of the two layers and is provided in reference [158]. The linear thermal expansion coefficients and Youngś moduli were $\gamma_{Si} = 2.59 \cdot 10^{-6}$ K^{-1}, $\gamma_{Au} = 14.2 \cdot 10^{-6}$ K^{-1}, $E_{Si} = 169$ GPa and $E_{Au} = 79$ GPa [162]. The deflection Δz was measured while positioning the laser at different places on the cantilever and switching on the laser until a steady-state deflection was reached. To account for small variations in the baseline (< 5 nm), the deflection before laser switch-on was subtracted from the steady-state deflection after laser switch-on. Two different incident laser powers where employed for these measurements: 2.4 mW and 4.9 mW with corresponding power densities of 2.3 MW/m^2 and 4.6 MW/m^2 on the cantilever.

Temperature simulated by finite element analysis

Finite element (FE) simulations reported in the literature were performed to study the effect of laser irradiation on microstructures [155, 164–166]. In the present work, the increase

in temperature of the cantilever immersed in water, due to the heat deposited by the incident excitation laser, was simulated via a 3-dimensional FE analysis using the Heat Transfer module in COMSOL Multiphysics [167]. Due to the small scale and localization of the heat sources, conductive heat transfer was assumed to be the major dissipative mechanism, and convective heat transfer and radiation were assumed to be negligible. The heat equation [167] then reduces to,

$$\rho C_p \frac{\partial T}{\partial t} - \nabla \cdot (k \nabla T) = Q, \tag{3.3}$$

where ρ, C_p, k, Q and T are the mass density, the heat capacity at constant pressure, the thermal conductivity, an inward heat flux and the temperature. All material properties were taken from the COMSOL Multiphysics material library. A total of $\sim 300\,000$ elements were meshed; thereby, the region around the cantilever was meshed with higher resolution. More than 97% of the detection laser power was reflected. Therefore, it does not cause significant heating, and was not considered in the simulations. The excitation laser was modelled as a boundary heat source on the surface of the cantilever, thus neglecting light absorption by the surrounding fluid. Because the penetration depth of the optical field is very small compared to the thickness of the cantilever, the absorbed power density was estimated to be $Q_{\mathrm{EX}} = P_{\mathrm{in}}(1 - R)/(\pi r^2)$, where P_{in} is the incident laser power, $R = 0.33$ the reflectance at wavelength $\lambda = 406$ nm and $r = 15$ μm the radius of the heat source. The boundary conditions were defined as follows: The silicone cell enclosing the fluid was assumed to be thermally insulating; the bottom face of the fluid and the cantilever chip (see Figure 3.1) were taken to be in ideal thermal contact with the glass slide. The vertical faces of the glass slide were set as open boundaries, thus extending it infinitely in the horizontal direction and allowing heat to flow outwards; being temperature controlled, the bottom of the glass slide was modelled as a heat sink at a constant temperature of 293.15 K. Numerical results were processed by taking cross-sectional temperature profiles and calculating the average temperature of the cantilever.

3.2.3 Photothermal excitation of higher flexural modes

Photothermal excitation is achieved by an intensity-modulated laser, which periodically heats the microcantilever and, thus, induces vibration. The force per length exerted on the cantilever through the differential longitudinal stress produced by the heat from the laser, is a convolution between the temperature distribution ΔT and the second derivative of the spatial mode profile Φ_n of the vibrating cantilever [104, 159]. Under the assumption of harmonic vibration, the normalized amplitude of vibration at the tip of the cantilever scales linearly with the applied force per unit length, leading to the following expression:

$$A(x_0) = A_0 \int_0^L \Delta T(x; x_0) \frac{d^2 \Phi_n(x)}{dx^2} dx, \tag{3.4}$$

where x is the coordinate along the cantilever axis and x_0 the position of the excitation laser; A_0 is a normalization factor determined for each mode individually; $\Phi_n(x)$ is the spatial distribution of the n-th eigenmode of the cantilever [168]; $\Delta T(x; x_0)$ is the temperature distribution along the beam. For dynamic cantilever excitation, only the alternating component of $\Delta T(x; x_0)$ is of importance. Therefore, ΔT was described by a Gaussian function resembling the intensity distribution of the laser spot. To obtain the amplitude, resonance spectra were recorded while moving the excitation laser along the cantilever. Fitting a simple harmonic oscillator model allowed the angular deflection amplitude to be determined for each mode individually. To precisely determine the relative excitation spot position and normalize the data, Equation 3.4 was fitted to the profiles of modes 2 to 6 simultaneously using a global fit algorithm. For all dynamic experiments a peak-to-peak amplitude of 7 mW was modulated onto a constant laser power of 4.9 mW.

3.3 Results and discussion

3.3.1 Steady-state temperature upon continuous laser irradiation in liquid

The steady-state temperature increase in liquid, induced by continuous laser irradiation at different positions along the cantilever, was evaluated by two independent approaches: (i) Indirect measurement by the bi-material bending of the cantilever and (ii) finite element (FE) simulations.

First, the thickness of the bi-material cantilever was calibrated. The ambient temperature was changed stepwise from 293.15 to 297.15 K, resulting in upward cantilever deflections ranging from 0 to 36 nm. As reported previously [163] and discussed above (see Materials and methods), the temperature-deflection dependence was linear (correlation coefficient $R = 0.998$). By fitting Equation 3.2 to the data, the thickness of the cantilever was determined to be $t_{\mathrm{Si}} = 3.0$ μm. The calibrated thickness deviates from the nominal value (4 μm) due to variations in the fabrication process and systematic deviations in the geometrically determined deflection (Equation 3.1). After calibration, the deflection upon continuous laser irradiation at different positions along the beam (illustrated in Figure 3.2a) was recorded and converted into an average increase in temperature using Equation 3.2 (Figure 3.2b). Close to the chip a thicker support region defines the clamped end of the cantilever (position (1), Figure 3.2a). Positioning the laser further towards the tip of the cantilever (positions (2) and (3), Figure 3.2a), resulted in higher deflections and, thus, higher temperatures as shown in Figure 3.2b. Turning on the laser was followed by heating-related deflection resulting in a steady-state value within a few seconds; turning the laser off again reversed the process. The maximum deflection was 56 nm indicating an increase in the average cantilever temperature of about 6 K. The observed reversibility and repeatability of this process indicates that

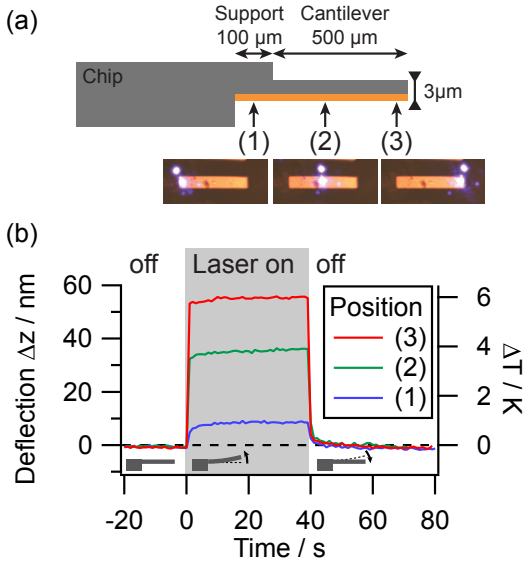

Figure 3.2: Static deflection induced by laser heating: (a) Schematic of the sensor indicating the 20 nm gold layer (yellow) and the thicker support region (length 100 μm), which connects the cantilever (500 μm) to the chip (drawing not in scale). The laser spot was positioned on the support (1), towards the middle of the cantilever (2) and at its tip (3) as shown by the micrographs; the second spot (beside the cantilever) is a reflection from the glass slide. (b) Cantilever deflection Δz and increase in average cantilever temperature ΔT upon 4.9 mW laser irradiation at different positions on the cantilever.

ablation of the cantilever coating, previously observed at higher power densities in air [165], did not occur.

The results of the finite element (FE) simulations employed to determine the temperature profiles of the cantilever and its surroundings are shown in Figure 3.3a. A confined hot spot forms around the position of the heating laser. The maximal local temperature change found by FE analysis was 11 K for 4.9 mW laser irradiation at the tip of the cantilever. The average increase in the temperature of the cantilever material was calculated from the simulated data (solid lines in Figure 3.3b), for comparison with values derived from the measured deflection of the cantilever using Equation 3.2 (markers in Figure 3.3b). As indicated by the simulations, the assumed homogeneous temperature distribution is a poor description of the temperature profile along the beam (Figure 3.3a). This accompanying uncertainty in the experimentally derived temperature data, may be the main reason why the simulation apparently overestimates the average temperature increase in the first half of the cantilever and underestimates it towards the tip. Importantly, even though the two independent data sets differ slightly, both reveal the same temperature behavior along the cantilever beam (Figure 3.3b). The shape of the profiles identifies thermal conduction through the cantilever

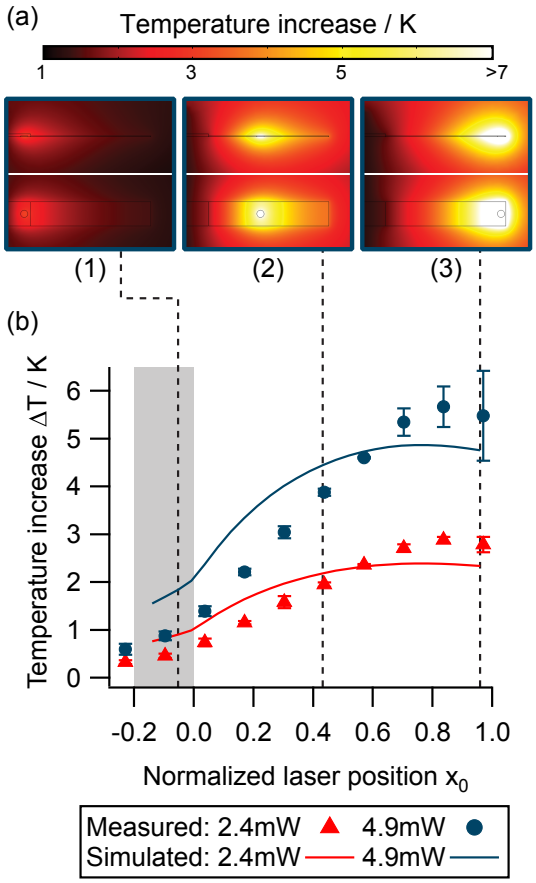

Figure 3.3: Steady-state temperatures for different laser positions x_0: (a) Side and top views of simulated profiles along the central cross section of the cantilever for the laser positions (power 4.9 mW) indicated by the numbers in Figure 3.2a. (b) Simulated and measured average temperatures of the cantilever upon laser irradiation with powers of 2.4 mW and 4.9 mW. The temperature was determined from the deflection of the bi-material cantilever (shown are the mean and standard deviation of three consecutive measurements). The shaded area indicates the thicker cantilever support region (Figure 3.2a).

material as the major mechanism for heat dissipation. Moving the heating laser closer to the clamped end (support) improves the thermal conductance [169], dissipating a larger fraction of the incident power through the cantilever chip. Due to its lower thermal conductivity, the surrounding liquid provides insufficient heat drain when the laser is positioned towards the tip of the cantilever, resulting in a larger temperature increase.

3.3.2 Dependence of laser spot position on higher mode excitation

The dynamic response of higher flexural modes of vibration excited by an intensity-modulated laser at different positions along a cantilever immersed in liquid was investigated. A photothermally driven amplitude spectrum is shown in Figure 3.4a. The cantilever resonance peaks are well resolved because the spectrum is free of spurious resonances. The fundamental mode is not recorded, because its resonance frequency is below the high-pass filter frequency of the excitation electronics. Figure 3.4b shows the normalized amplitude for flexural modes of vibration 2 to 6 for different excitation laser positions. Except for the region towards the clamped end of the cantilever ($x_0 = 0$), the amplitude profiles are in good agreement with theoretical values (Equation 3.4). An optimal excitation position within the support region ($x_0 = -0.06$) was identified for mode 3 and higher (Figure 3.4, black arrow). It resulted in amplitudes up to 2.5 times higher than those obtained by positioning the laser on the cantilever itself and the difference was more pronounced for higher modes. This feature is most likely due to the specific geometry of the cantilevers employed: The thicker support region (position (1) in Figure 3.2a) is an efficient heat sink. Therefore, the temperature decreases more rapidly after a laser pulse, allowing higher local peak-to-peak temperature variations at high frequencies. These are in turn transduced into larger vibrational amplitudes and, thus, a more efficient excitation of higher modes, or higher frequencies in general.

3.4 Conclusions

Understanding the interaction of laser radiation with microstructures is of major importance for the optical excitation of microcantilevers in fluid, picowatt calorimetry [169], thermodynamic measurements of thin films [165] and the dynamics of micro actuators [164]. Finite element simulations and deflection-derived measurements of the laser-induced temperature increase at different positions on a microcantilever were in good agreement. Conductive heat transfer through the cantilever material was identified as the dominant heat dissipation mechanism of a cantilever in liquid irradiated by a laser. Furthermore, the dynamic response of the cantilever, driven photothermally by an intensity-modulated laser at different positions, was studied. These findings allowed the optimal position of the excitation laser spot on the cantilever to be determined for different flexural modes of vibration. Placing the spot in the support region of the cantilever used, resulted in the most efficient

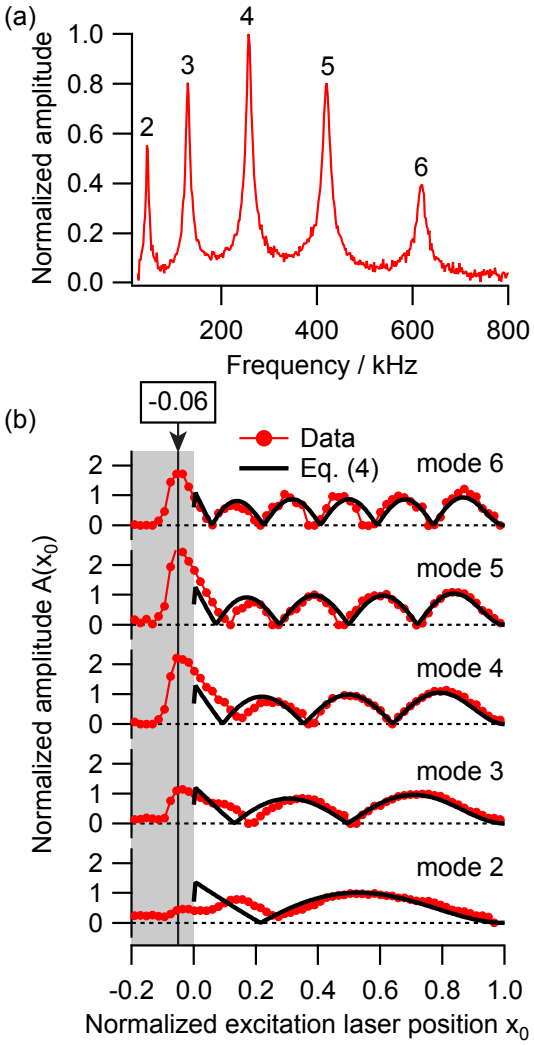

Figure 3.4: (a) Normalized amplitude spectrum recorded with the excitation laser at the optimal position (position -0.06; black arrow in panel b). Flexural mode numbers are indicated and the amplitude is normalized to the highest peak. (b) Amplitudes of flexural modes 2 to 6 as a function of the excitation laser position x_0 on the cantilever. Red markers indicate measured values and solid black lines denote theoretical values. The shaded area indicates the support region (Figure 3.2a). The profiles were normalized to the theoretical values of each mode separately.

excitation along all flexural modes greater than two, while the temperature increase was minimal (< 2 K). We hypothesize that the efficient heat sink properties of the support promote local high-frequency temperature variations, which would explain why the effect was more pronounced at higher frequencies. These findings are of particular interest because high resonance frequencies, achieved by using higher modes or smaller cantilever dimensions, increase the sensitivity [142]. Improving the excitation efficiency and thus reducing the temperature increase, allows optical excitation to be employed without damaging functionalization layers in sensing applications or sample surfaces in dynamic mode scanning force microscopy by thermal denaturation. Major parameters to be considered are: (i) The cantilever geometry and material, (ii) the excitation laser spot size determining the power density and (iii) the position of the excitation laser on the cantilever.

Acknowledgements

The authors gratefully acknowledge Henning Stahlberg (C-CINA, University of Basel, Switzerland) for providing infrastructure and facilities; Shirley A. Müller (C-CINA) for critically reading the manuscript; Michel Despont and Ute Drechsler (IBM Research GmbH, Rueschlikon, Switzerland) for providing cantilever arrays; Kenneth N. Goldie (C-CINA) for determining the cantilever dimensions by scanning electron microscopy. This work was supported by SNF grant 200021/130594, NCCR Nano and ARGOVIA project NoViDeMo.

Chapter 4

Influence of squeeze-film damping on higher-mode microcantilever vibrations in liquid

Benjamin A. Bircher*,[1], Roger Krenger[1], and Thomas Braun*,[1]

[1]Center for Cellular Imaging and NanoAnalytics, Biozentrum, University of Basel, Mattenstrasse 26, CH-4058 Basel, Switzerland

* E-mail: benjamin.bircher@unibas.ch, thomas.braun@unibas.ch

Published in EPJ Instrumentation and Techniques, **1**, 10 (2014), **DOI:** 10.1140/epjti/s40485-014-0010-6

Abstract

The functionality of atomic force microscopy (AFM) and nanomechanical sensing can be enhanced using higher-mode microcantilever vibrations. Both methods require a resonating microcantilever to be placed close to a surface, either a sample or the boundary of a microfluidic channel. Below a certain cantilever-surface separation, the confined fluid induces squeeze-film damping. Since damping changes the dynamic properties of the cantilever and decreases its sensitivity, it should be considered and minimized. Although squeeze-film damping in gases is comprehensively described, little experimental data is available in liquids, especially for higher-mode vibrations. We have measured the flexural higher-mode response of photothermally driven microcantilevers vibrating in water, close to a parallel surface with gaps ranging from $\sim$ 200 μm to $\sim$ 1 μm. A modified model based on harmonic oscillator theory was used to determine the modal eigenfrequencies and quality factors, which can be converted into co-moving fluid mass and dissipation coefficients. The range of squeeze-film damping between the cantilever and surface decreased for eigenfrequencies (inertial forces) and increased for quality factors (dissipative forces) with higher

mode number. The data can be employed to improve the quantitative analysis of AFM measurements, design miniaturized sensor fluid cells, or benchmark theoretical models.

4.1 Background

Damping is an important design criterion for micro- and nanometer sized resonators, because surface forces dominate body forces at small dimensions [170]. Immersing a resonator, e.g., a microcantilever, in fluid drastically changes its dynamic properties. The eigenfrequencies and quality factors decrease due to hydrodynamic forces, which can be decomposed into an inertial (added mass) and dissipative (viscous damping) term [171]. Additionally, placing the resonator close to a solid surface leads to squeeze-film damping, where displacement of the fluid between the resonator and the surface during each vibration period introduces additional added mass and viscous damping [172]. The damping occurring by both mechanisms has direct impact on atomic force microscopy (AFM) and dynamically operated nanomechanical sensors. With progressing miniaturization, squeeze-film damping starts to dominate other dissipative effects and, thus, needs to be considered and characterized [173].
Furthermore, higher modes of vibration are increasingly used. In multifrequency AFM imaging, higher modes allow the material characteristics, e.g., mechanical, magnetic or electrical properties, of the substrate to be measured [174]. To reduce squeeze-film damping, AFM samples have been placed on pillars [175], or cantilever geometries have been optimized by focused-ion beam milling [176]. In cantilever-based sensor applications, the use of higher vibrational modes provides increased mass sensitivity [10] and allows the elastic properties [13] and the position of adsorbates [14] to be disentangled. Squeeze-film damping needs to be considered below a certain critical dimension of the AFM cantilever tip or container in which the cantilever sensor is mounted.
To our knowledge, squeeze-film damping of micrometer-sized cantilevers vibrating in higher modes in liquid has not been measured to date. In contrast, it has been thoroughly investigated for resonators immersed in gases, because of its importance for micro-electromechanical systems (MEMS), e.g., torsional mirrors [177] or cantilevers [126]. Even though, less attention has been paid to the problem in liquids, both analytical and numerical methods have been employed to model the behavior of cantilevers immersed in liquid and vibrating in close proximity to a surface. Analytical approaches [123] account for dissipative and inertial effects in the liquid, but due to the assumption of a two-dimensional flow field higher modes of vibration were not considered. Numerical approaches can effectively describe different cantilever-surface inclination angles, vibrational modes, and varying external driving forces [127, 171, 173]. However, semi-analytical equations describing the hydrodynamic load acting on cantilevers under squeeze-film damping only consider the fundamental mode

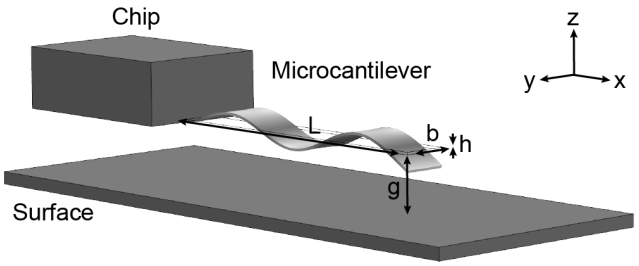

Figure 4.1: Diagram of a microcantilever vibrating close to a surface. A cantilever of length L, width b and thickness h, is vibrating at flexural mode $n = 4$. The cantilever-surface gap g was varied from $\sim$ 200 μm to $\sim$ 1 μm. Liquid confined in the gap causes additional hydrodynamic forces due to squeeze-film damping. The amplitude of vibration is drawn not to scale.

of vibration [123, 127]. Squeeze-film damping in liquid is governed by two dimensionless quantities, the Reynolds number, *Re*, and the normalized gap, H [123]:

$$Re = \frac{\pi \rho_f f_n b^2}{2\eta_f},\ H = \frac{g}{b}, \tag{4.1}$$

where b is the width of the cantilever, ρ_f the fluid density, η_f the fluid viscosity, f_n the cantilever eigenfrequency in liquid, and g the gap between the cantilever and the surface (see Figure 4.1). The cantilever width, b, is the dominant length scale of the flow [123]. If the vibration amplitudes are orders of magnitude smaller than b, i.e., Keulegan-Carpenter numbers $\ll 1$ [133], the effect becomes independent of the amplitude [108]. Furthermore, the continuum hypothesis is valid because the mean-free-path of the molecules in liquid is very small compared to the dominant length b and the gap size g, i.e., Knudsen numbers $\ll 1$ [133].

Experimental investigations of cantilevers with dimensions ranging from centimeters to micrometers, immersed in water, buffer, organic solvents and oils are reported in the literature [108, 133, 172, 178–180]. However, all experimental studies on microcantilevers in liquid and close to a surface, were limited to the fundamental mode ($n = 1$) [178–180]. Here we present the full spectral response of microcantilevers vibrating in water at different distances from a polydimethylsiloxane (PDMS) surface. PDMS was selected because of its abundant use for the fabrication of microfluidic devices. Spurious-free resonance spectra were obtained by driving the microcantilevers photothermally [96], and several higher flexural modes of vibration were characterized.

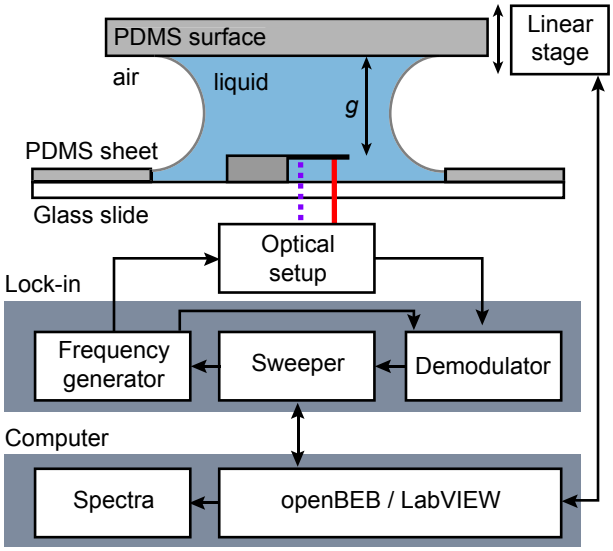

Figure 4.2: Experimental setup. Diagram of the experimental setup used to measure the dynamic response of a microcantilever vibrating in close proximity to a PDMS surface. The cantilever vibration was driven (purple dashed line) and detected (red solid line) optically using two laser beams. Cantilever chips were fixed on the bottom of a cavity used to confine the liquid. A PDMS surface attached to a motorized linear stage was moved down towards the cantilever, while continuously acquiring resonance spectra using a lock-in amplifier. The setup was controlled by software written in openBEB and LabVIEW.

4.2 Methods

4.2.1 Experimental setup

Measurements were made as the upper surface of a small cavity containing water was moved closer to the immersed microcantilever. A diagram of the experimental setup is shown in Figure 4.2. Cantilever vibration was driven by photothermal excitation induced by an intensity-modulated laser beam (405 nm), and detected by monitoring the deflection of a second laser beam (780 nm) using the optical setup described previously [50, 96]. A mirror galvanometer (GSV011, Thorlabs) was added to the setup to automatically control the low-pass filtered position ($f_{\mathrm{lp}} = 1$ kHz) of the laser spot on the position-sensitive detector (PSD) used to monitor cantilever vibration (measurement bandwidth ~ 850 kHz). A Zurich Instruments HF2 lock-in amplifier was employed to record cantilever resonance spectra by sweeping a given range of excitation frequencies and demodulating the corresponding phase and amplitude (lock-in bandwidth = 4.38 Hz, filter order = 24 dB/octave, 1000 data points). The setup was controlled using LabVIEW (National Instruments) and measurements were automated using the openBEB macro language [181]. The automation involved acquisition

of spectra, adjusting the cantilever-surface gap, and adjusting the laser power and position of the laser spot on the position-sensitive detector using a proportional-integral-derivative (PID) controller. The whole setup was temperature controlled to 293 K within ± 0.2 K.
Tipless silicon microcantilevers (NSC12/tipless/noAl, MikroMasch) with nominal dimensions of 250 μm x 35 μm x 2 μm and calculated spring constants of 0.76 N/m were employed. The data reported in the Supporting Information was obtained using longer microcantilevers (300 μm x 35 μm x 2 μm and 350 μm x 35 μm x 2 μm) following the same protocol. A comparison of the different cantilevers is provided in the Supporting Information (Table C.1). To improve reflectivity and avoid unspecific adsorption, 20 nm gold was coated at the bottom side of the cantilevers and they were passivated with short polyethylene glycol chains, as described previously [50].
The cavity containing the water was formed using PDMS (SYLGARD 184, Dow Corning) and a glass microscope slide (AA00000112E, Menzel-Gläser), exploiting surface tension forces (see Figure 4.2). The base was fabricated by reversibly bonding a 150 μm-thick PDMS sheet with a 10 mm wide circular hole at its center to the glass slide. The 300 μm-thick cantilever chip was attached to the glass slide at the center of the hole using UV curable glue (F-UVE-61, Newport). The thickness of the chip was sufficient ($H = 8.6$) to exclude any influence of the glass surface on cantilever dynamics. Furthermore, as the thickness of the PDMS sheet (150 μm) was less than the thickness of the chip, access from above was retained. A flat upper cavity surface was fabricated by pouring degassed PDMS onto a silicon wafer to a thickness of about 5 mm and baking for 4 hours at 60°C. The PDMS was subsequently removed from the wafer and cut to give a circular disk with a diameter of 15 mm. The diameter exceeded all dimensions of the microcantilevers by at least an order of magnitude to avoid edge effects. The rougher surface of the disc was fixed to a kinematic mirror mount (KM05/M, Thorlabs), which was in turn mounted on an encoded piezo motor linear stage (CONEX-AG-LS25-27P, Newport) with a nominal precision of 0.2 μm. The cavity allowed the cantilever to be immersed in ~ 200 μL of water.
The flat upper PDMS surface was manually aligned parallel to the cantilever. To do this, a piece of silicon wafer was attached to the surface by adhesion forces to render it reflective. The read-out laser was then focused on the silicon surface and detected by the PSD otherwise used to measure the cantilever deflection. The residual angular misalignment was estimated to be less than 1 mrad (0.06°). The same procedure was repeated after rotating the PSD by 90° to align the angle perpendicular to the longitudinal axis of the cantilever.
To determine the coarse contact point, the surface was approached to the cantilever until a large deviation in the deflection signal was observed. Next, the surface was withdrawn to a distance where it had no influence on the cantilever vibration ($g \approx 200$ μm, $H \approx 6$). To adjust the gap, the motorized linear stage was operated in a closed-loop configuration. After recording a spectrum the position was stored and the surface was moved closer to the cantilever. The step size was reduced as the gap decreased, to account for the non-linearity

of squeeze-film damping. Next, for a more precise gap determination, the model of Tung et al. [127] was fitted to the frequency data of the fundamental mode (see Figure 4.5a) with parameters $f_{1,\text{vac}}$ and a gap offset:

$$\frac{f_1}{f_{1,\text{vac}}} = \left(1 + \frac{\pi\rho_f b}{4\rho_c h}\Re\left(\Gamma_{\text{Tung}}(Re, 2H)\right)\right)^{-\frac{1}{2}}. \tag{4.2}$$

The offset was then subtracted from the z-position of the measurement to align the data. We emphasize that the definition of H by Tung et al. [14] differs by a factor of two from Equation 4.1.

4.2.2 Data analysis

All data analysis was performed using custom scripts in IGOR Pro (Wavemetrics, see Supporting Information). Both amplitude and phase spectra contain the eigenfrequencies and quality factors of the vibrational modes. However, at small cantilever-surface gaps the resonance peaks in the amplitude spectrum become indistinguishable due to the strong peak broadening, i.e., low quality factors (see Figure 4.3). Furthermore, large differences in peak amplitude among higher modes of vibration complicate fitting and introduce dependencies on the initial parameters. In contrast, the phase shifts of each mode remain well resolved even at low quality factors. Thus, phase spectra were used to extract the modal eigenfrequencies and quality factors (see Figure 4.4). To weight each mode by the same amount on least squares fitting, the frequency spacing was transformed from linear ($p = 1$), i.e., equally spaced, to a power law according to

$$f^*(m) = \left(\frac{m}{M-1}\left(f_{m=M}^p - f_{m=0}^p\right) + f_{m=0}^p\right)^{\frac{1}{p}}, \tag{4.3}$$

where m is a data point in the spectrum ranging from 0 to $M-1$, M the total number of points, $f_m = 0$ the lowest and $f_m = M$ the highest frequency in the measured data and p the power of the transformation required for each mode of vibration to be assigned an equal number of data points. The value of p was estimated to be 0.514 from the calculated widths of the resonance peaks of all employed cantilevers in an unbounded fluid [125]. The phase values corresponding to the transformed frequencies f^* were linearly interpolated from the measured data.

The following expression was used to extract the mode-dependent eigenfrequencies, f_n, and quality factors, Q_n, from the phase spectrum using a Levenberg-Marquardt algorithm (see Figure 4.4):

$$\phi(f) = \phi_{\text{c}}(f, f_1, Q_1, \ldots, f_N, Q_N) + \phi_{\text{th}}(f, \tau_{\text{th}}) + \phi_{\text{el}}(f, f_{\text{el}}, c_{\text{off}}) \tag{4.4}$$

$$= \sum_{n=1}^{N} \arctan\left(Q_n \frac{f_n^2 - f^2}{f_n f}\right) - 2\pi f \tau_{\text{th}} + \arctan\left(\frac{f_{\text{el}}}{f}\right) + c_{\text{off}}, \tag{4.5}$$

where the cantilever response ϕ_{c} is the sum of damped harmonic oscillators with f_n and Q_n over all recorded modes N, ϕ_{th} is the linear thermal lag due to photothermal excitation with time constant τ_{th} [182] and ϕ_{el} (center frequency f_{el} and offset c_{off}) is an empirical first-order filter that considers the phase responses of the measurement electronics. The filter center frequency f_{el} and the time constant τ_{th} were determined on the first spectrum recorded far from the surface ($H \gg 1$) and then held constant.
The linearized equation of motion for a cantilever of length L, width b, thickness h and mass density ρ_c is [108]:

$$EI \frac{\partial^4 Z(x,t)}{\partial x^4} + \mu_c \left(1 + a_m\right) \frac{\partial^2 Z(x,t)}{\partial t^2} + c \frac{\partial Z(x,t)}{\partial t} = F_{\text{drive}}(x,t), \tag{4.6}$$

where $Z(x,t)$ is the z-direction flexural displacement at position x along the cantilever beam at time point t, E and $I = bh^3/12$ the Young's modulus and area moment of inertia of the cantilever, $\mu_c = \rho_c bh$ the mass per unit length of the cantilever, a_m the added mass coefficient quantifying the co-moving fluid mass relative to the cantilever mass, c the sum of structural and viscous damping per unit length, F_{drive} an external driving force per unit length. The parameters used for the following calculations are provided in Table 4.1. The added mass coefficients a_m were calculated from the measured eigenfrequencies f_n [171]:

$$a_m = \left(\frac{f_{n,\text{vac}}}{f_n}\right)^2 - 1. \tag{4.7}$$

The vacuum frequencies $f_{\text{vac},n}$ for each mode n were determined far from the surface ($H \gg 1$), where the added mass coefficient can be calculated for higher modes, with normalized mode number κ, according to the theory by Van Eysden and Sader [125]:

$$a_m = \frac{\pi \rho_f b}{4 \rho_c h} \Re\big(\Gamma_{\text{VanEysden}}(Re, \kappa)\big) \text{ for } H \gg 1. \tag{4.8}$$

The damping coefficients per unit length were calculated as [108, 176]

$$c = \mu_c (1 + a_m) \frac{2\pi f_n}{Q_n}. \tag{4.9}$$

Table 4.1: Parameters for the employed silicon cantilevers immersed in water.

Cantilever properties		
L	Length	250 μm
b	Width	35 μm
h	Thickness	2 μm
ρ_c	Mass density	2330 kg·m^{-3}
μ_c	Mass per unit length	0.163 mg·m^{-1}
E	Young's modulus	169 GPa
I	Area moment of inertia	23.3 μm^4
Q_n	Quality factor of mode n	
f_n	Eigenfrequency of mode n	Hz
$f_{n,vac}$	Vacuum frequency of mode n	Hz
a_m	Added mass coefficient	
c	Damping per unit length	Pa·s
Fluid properties		
ρ_f	Mass density	998.25 kg·m^{-3}
η_f	Viscosity	1.005 mPa·s
Gap properties		
g	Gap	m
H	Normalized gap	

4.3 Results and discussion

To measure the effects of squeeze-film damping, a tipless microcantilever (250 μm x 35 μm x 2 μm) was placed close to a surface and the gap, g, was varied from ~ 200 μm to ~ 1 μm using a motorized stage (Figure 4.1). Experiments using longer cantilevers are reported in the Supporting Information. Photothermal excitation was employed to drive the microcantilever to resonance. Amplitude and phase spectra were acquired by sweeping an excitation frequency range from 0.5 kHz to 800 kHz and recording the corresponding cantilever response. As shown in Figure 4.3 for different cantilever-PDMS surface gaps, the spectra span four flexural modes of vibration. The influence of the cantilever-surface gap became substantial for $H = g/b < 1$, causing the resonance peaks to shift towards lower frequencies and broaden significantly (decreasing quality factors). A model, consisting of a sum of damped harmonic oscillators and terms considering the measurement setup (see Methods, Equation 4.4), described the experimental phase data with good accuracy (Figure 4.4). Applying this model to the data, allowed the eigenfrequency, f_n, and quality factor, Q_n, of each mode n, to be extracted at different cantilever-surface gaps, g (Figure 4.5).

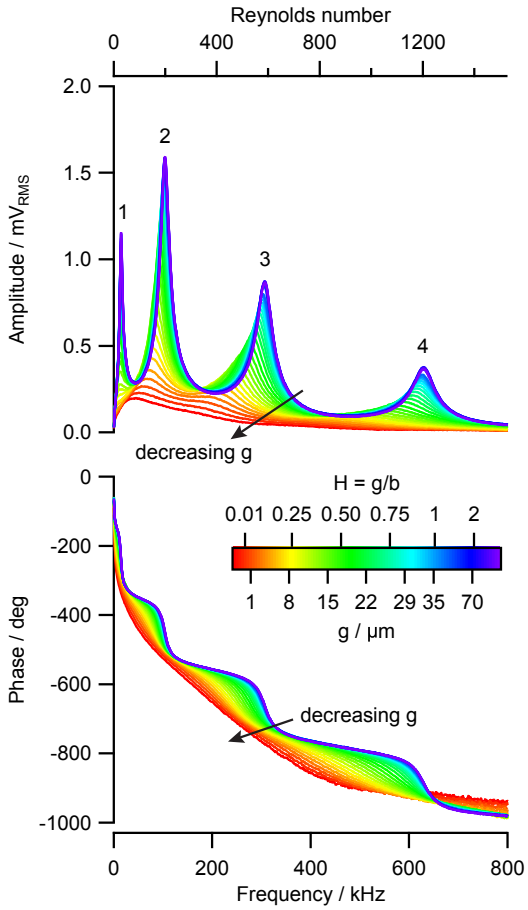

Figure 4.3: Amplitude and phase spectra of a microcantilever vibrating at different gaps g to a surface. The amplitude (upper plot) and phase (lower plot) response of a microcantilever (250 μm x 35 μm x 2 μm) vibrating in water at different distances from a surface are shown as a function of frequency and the corresponding Reynolds number (Re). The flexural mode numbers are written above the resonance peaks. Absolute (g) and normalized (H) cantilever-surface separations are indicated. The color scale is not linear; far from the surface the increment in g was set larger because the effect diminishes (superimposed purple curves). The spectra are overlayed; the red curves (small g) are at the back.

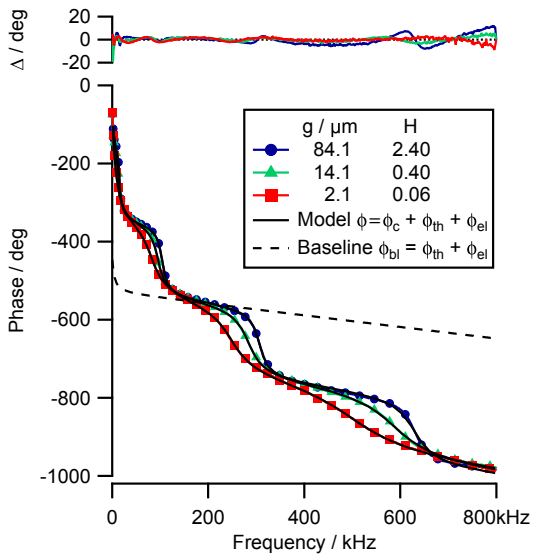

Figure 4.4: Phase model and data. Lower plot: Phase data recorded at three different cantilever-surface gap heights (only every twentieth marker is shown), the model ϕ (solid black line) and the baseline ϕ_{bl} (dashed black line) included in the model to account for the phase response of the photothermal excitation ϕ_{th} and the measurement electronics ϕ_{el}. Upper plot: The difference between the model and the experimental data, Δ; to extract the eigenfrequencies and quality factors from the data, Δ was minimized using a Levenberg-Marquardt algorithm.

To compare cantilevers from different chips, f_n and Q_n were normalized to the values indicated by experimental data recorded far from the surface, where its presence had no influence (see Methods). As shown in Figure 4.6a, due to squeeze-film damping the eigenfrequencies of all modes decrease as the cantilever-surface gaps become smaller. Further, even though some of the differences are slight, it is clear that higher-mode eigenfrequencies are less influenced by the proximity of the surface. In contrast, the higher-mode quality factors are affected when the cantilever-surface gap is still comparatively large (Figure 4.6b) and the fundamental mode is influenced least. To quantitatively compare the effects, a characteristic cantilever-surface gap g_n^* was defined for the fundamental mode as $g_1^* = b/2 = 17.5\ \mu$m ($H_1^* = 0.5$). At g_1^* the frequencies (mean $\pm$ SD) of the fundamental vibration dropped to (93.4 ± 0.7)% and the quality factors to (77.8 ± 7.5)% of the initial value. Corresponding characteristic gaps (g_n^*), where the frequencies and quality factors dropped by the amounts measured for g_1^*, were then determined for the higher modes of vibration. As shown in Figure 4.7, the characteristic gap decreases for the eigenfrequencies and increases for the quality factors with increasing mode number. Similar behavior was observed for longer cantilevers (see Supporting Information), however, the effect seems to diminish with increasing can-

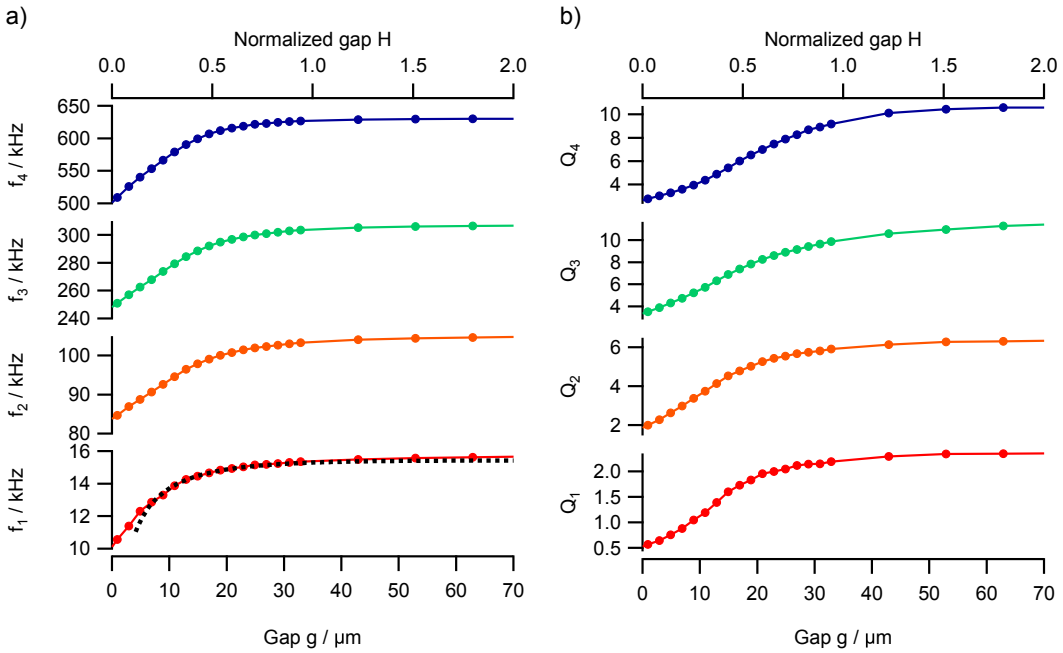

Figure 4.5: Absolute eigenfrequencies and quality factors. Representative measurement of the absolute (a) eigenfrequencies f_n and (b) quality factors Q_n of modes 1 to 4. The dashed line in (a) was calculated according to the theory describing the fundamental mode of vibration [127].

tilever length. To estimate the range of squeeze-film damping, i.e., the gap where the onset of the effect occurs, the characteristic gap was multiplied by a factor of two. Because of the definition, the range of squeeze-film damping for the fundamental mode is $H = 1$. The ranges for modes 2 to 4 (mean $\pm$ SD) were 0.93 ± 0.18, 0.84 ± 0.21, and 0.74 ± 0.21 for the eigenfrequencies and 1.22 ± 0.35, 1.55 ± 0.37, and 1.67 ± 0.20 for the quality factors. The critical gap for the frequencies, i.e., where the surface has no influence on the dynamics of the microcantilever, can be estimated from the fundamental mode, which is affected first. In contrast, the critical gap for the quality factors depends on the highest mode measured. To obtain a more general description of the results, the added mass coefficient, a_m, and the damping coefficient, c, were calculated for each mode. While the added mass coefficient a_m quantifies the co-moving fluid mass relative to the cantilever mass and is a measure of the inertial loading, the damping coefficient c equals the energy dissipation per unit length acting on the cantilever. The required vacuum frequencies were calculated using Equations 4.7 and 4.8 (see Methods) and the eigenfrequencies recorded in the unbounded fluid, i.e., far from the surface (Table 4.2). The observed vacuum frequency variations mainly originate from manufacturing-related uncertainties in the dimensions of the microcantilevers. Subsequently, the added mass coefficients could be determined (see Methods, Equation 4.7). The

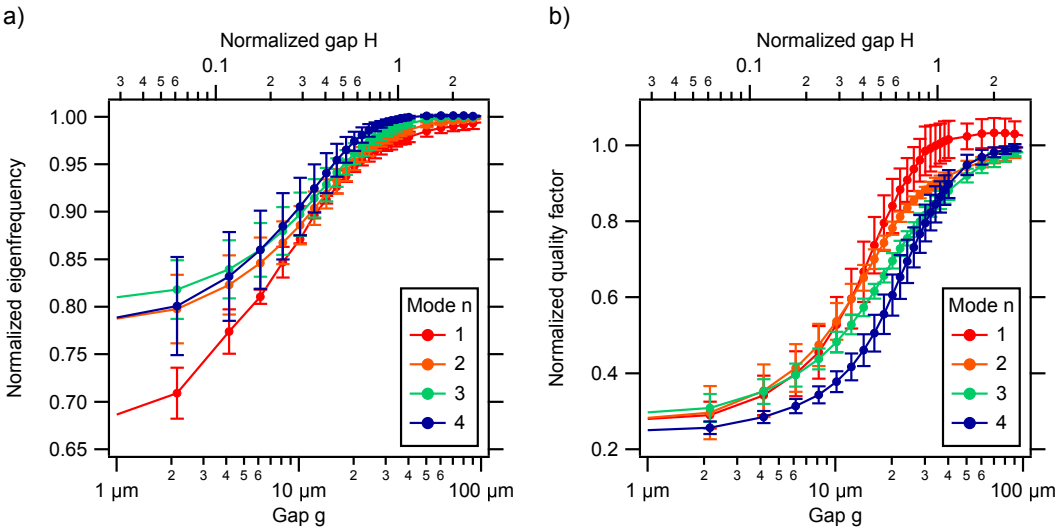

Figure 4.6: Normalized eigenfrequencies and quality factors. (a) Eigenfrequencies and (b) quality factors of a microcantilever, vibrating at different gaps g to a surface. All values were normalized to the values measured far from the surface. The means ± SD are shown (N = 3).

values without the influence of squeeze-film damping ($H \gg 1$) are provided in Table 4.2. Note that some authors defined the added mass coefficient as the co-moving mass relative to the fluid mass displaced by the static cantilever [108, 172]. For direct comparison with their values, a_m has to be multiplied by ρ_c/ρ_f , i.e., ~ 2.3 in the present case. The damping coefficients c are the sum of structural, c_s, and viscous, c_v, damping. For microcantilevers immersed in liquid, structural damping is orders of magnitude smaller than viscous damping ($c_s \ll c_v$), and can thus be neglected [172]. The damping coefficients were calculated using the measured quality factors and eigenfrequencies (Equation 4.9, see Methods). Table 4.2 shows the damping coefficients without the influence of squeeze-film damping ($H \gg 1$). Even though higher-modes dissipate less energy per oscillation cycle (higher quality factors),

Table 4.2: Vacuum frequencies, added mass coefficients and damping coefficients measured far from the surface (mean ± SD).

Mode n	$f_{n,vac}$ / kHz	$a_{m,H\gg1}$	$c_{H\gg1}$ / mPa·s
1	44.8 ± 5.4	9.17 ± 0.20	67.8 ± 1.6
2	277 ± 15	6.78 ± 0.03	116.2 ± 11.1
3	768 ± 34	5.75 ± 0.01	186.7 ± 4.43
4	1512 ± 52	5.05 ± 0.01	372.0 ± 26.9

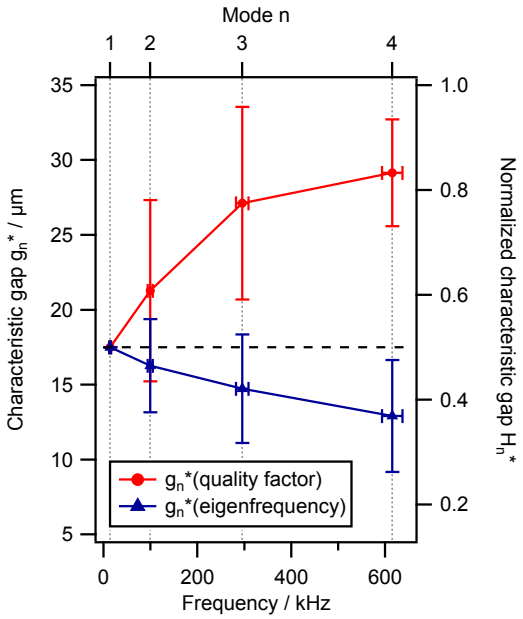

Figure 4.7: Characteristic gap to estimate the range of squeeze-film damping. The characteristic gap g_n^* is normalized to the fundamental mode of vibration ($n = 1$) at $H_1^* = 0.5$ (dashed line). It is the cantilever-surface gap, where the frequencies (blue triangles) and quality factors (red circles) dropped to, respectively, 93.4% and 77.8% of their initial values. The range of the squeeze-film damping can be estimated by calculating $2H_n^*$, i.e., $H = 1$ for the fundamental mode. The means $\pm$ SD (N = 3) are shown, mode numbers n are indicated on the top axis.

they have larger damping coefficients due to their higher eigenfrequencies (cycles/second). Figure 4.8 shows how the added mass and damping coefficients increase due to squeeze-film damping. The magnitude of the observed shift in added mass coefficients decreased with mode number, whereas the shift in damping coefficients increased.

4.4 Conclusion

We have measured the squeeze-film damping on higher flexural mode vibrations of micro-cantilevers placed in proximity to a parallel surface in liquid. Due to the strong damping only a direct excitation method, such as the employed photothermal excitation [96], obtains spurious-free resonance spectra. A model consisting of a sum of harmonic oscillators was employed to extract the modal eigenfrequencies and quality factors from the phase spectra, and described the measured data well. Correct alignment of the data, i.e., calibration of the gap g, was crucial and limited the precision of the measurements. As predicted [123, 127], strong squeeze-film damping of the fundamental mode was observed for normalized gaps

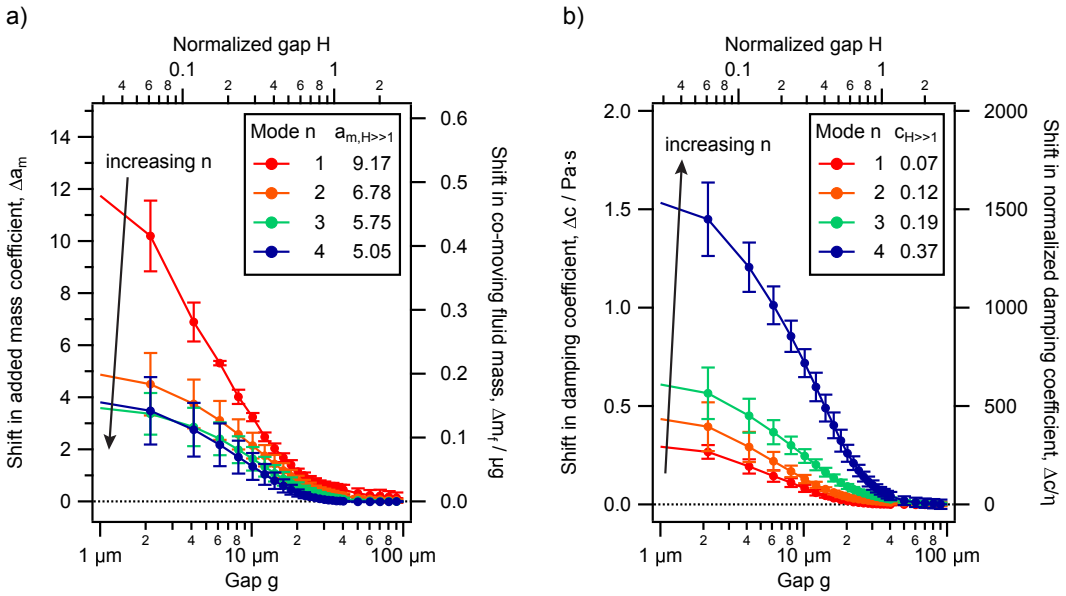

Figure 4.8: Shift in added mass and damping coefficients due to squeeze-film damping. (a) The shift in the added mass coefficient Δa_m quantifies the co-moving fluid mass relative to the cantilever mass and is a measure for the inertial loading; the shift in the absolute fluid mass Δm_f is provided on the right axis. (b) The shift in damping coefficient Δc equals the dissipation per unit length acting on the cantilever; the shift in dissipation normalized to the fluid viscosity η is provided on the right axis. The shifts Δa_m and Δc caused exclusively by squeeze-film damping were calculated by subtracting the values recorded in the unbound fluid, $a_{m,H\gg1}$ and $c_{H\gg1}$, provided in the figure legend. The means $\pm$ SD (N = 3) are shown.

$H < 1$. With increasing mode number the range of squeeze-film damping decreased for the eigenfrequencies (inertial forces) and increased for the quality factors (dissipative forces). Furthermore, the effect seems to depend on the length of the cantilever that determines the spatial wavelength of each mode. This important finding should be considered for the design of sensor containers and cantilever tip geometries, because the quality factor is directly related to the sensitivity of the sensor [174]. The observed behavior is likely due to the three-dimensional nature of the flow field generated by higher modes, where gradients along the length of the cantilever must not be neglected [127]. For theoretical models, this entails the introduction of another parameter, besides the normalized gap H and the Reynolds number *Re*, related to the spatial wavelength of the cantilever, i.e., depending on the mode number as well as the cantilever length (similar to the normalized mode number in [125]). Finally, added mass and damping coefficients were calculated to support the comparability of the data. The shift in added mass decreased with mode number as predicted by numerical models [171]. The opposite was observed for the damping coefficients, which increased. More

work is required to identify the underlying mechanisms governing squeeze-film damping acting on higher modes. Nevertheless, our data from microcantilevers with common dimensions, allows the magnitude of the squeeze-film damping effect to be assessed.

Acknowledgements

The authors gratefully acknowledge Henning Stahlberg (C-CINA, Biozentrum, University of Basel) for financial support and providing facilities, Shirley Müller (C-CINA, Biozentrum, University of Basel) for critically reading and discussing the manuscript, Francois Huber and Hans Peter Lang (SNI, Institute of Physics, University of Basel) for their support on cantilever preparation, Stefan Arnold and Andrej Bieri (C-CINA, Biozentrum, University of Basel) for fruitful discussions. This work was supported by ARGOVIA grant NoViDeMo and Swiss National Science Foundation grant SNF 200020_146619.

Chapter 5

Real-time viscosity and mass density sensors requiring microliter sample volume based on nanomechanical resonators

Benjamin A. Bircher[1], Luc Duempelmann[1], Kasper Renggli[2], Hans Peter Lang[3], Christoph Gerber[3], Nico Bruns[2], and Thomas Braun[*,1]

[1]Center for Cellular Imaging and NanoAnalytics, Biozentrum, University of Basel, Mattenstrasse 26, CH-4058 Basel, Switzerland
[2]Department of Chemistry, University of Basel, Klingelbergstrasse 80, CH-4056 Basel, Switzerland
[3]Swiss Nanoscience Institute, University of Basel, Klingelbergstrasse 82, CH-4056 Basel, Switzerland
[*] E-mail: thomas.braun@unibas.ch

Reproduced with permission from Analytical Chemistry **85**(18), 8676–8683 (2013), DOI: 10.1021/ac4014918.

Abstract

A microcantilever based method for fluid viscosity and mass density measurements with high temporal resolution and microliter sample consumption is presented. Nanomechanical cantilever vibration is driven by photothermal excitation and detected by an optical beam deflection system using two laser beams of different wavelengths. The theoretical framework relating cantilever response to the viscosity and mass density of the surrounding fluid was extended to consider higher flexural modes vibrating at high Reynolds numbers. The performance of the developed sensor and extended theory was validated over a viscosity range of 1 to 20 mPa·s and a corresponding mass density range of 998 to 1176 kg/m^3 using reference fluids. Separating sample plugs from the carrier fluid by a two-phase configuration in combination with a microfluidic flow cell, allowed samples of 5 μL to be sequentially measured under continuous flow, opening the method to fast and reliable screening applica-

tions. To demonstrate the study of dynamic processes, the viscosity and mass density changes occurring during the free radical polymerization of acrylamide were monitored and compared to published data. Shear-thinning was observed in the viscosity data at higher flexural modes, which vibrate at elevated frequencies. Rheokinetic models allowed the monomer-to-polymer conversion to be tracked in spite of the shear-thinning behavior, and could be applied to study the kinetics of unknown processes.

5.1 Introduction

Viscosity and mass density are key characteristics of fluids. They depend on the solvent, as well as on the physicochemical properties of the dissolved components. Viscosity measurements are used to characterize solutions of polymers and biopolymers [91]. Whereas the density is mainly related to concentration and hydrodynamic volume, the viscosity depends on concentration, molecular weight, shape and interactions of the solute molecules. Classical viscosity or mass density measurements require milliliter samples with a time resolution on the order of minutes. Recently, new sensing methods that allow either microfluidic viscosity [90] or mass density [183, 184] measurements were presented. Notably, most of these new viscosity measurement techniques rely on fluorescent labels or optical readout and subsequent image processing. In contrast, combined viscosity and mass density sensing methods are mostly based on mechanical resonators. They employ resonating microtubes [185], micro-electromechanical systems [79], surface acoustic wave devices [186], tuning forks [187], quartz crystal microbalances [188], and microcantilevers [63]. Due to the wide application range of microcantilevers in scanning probe microscopy, comprehensive theoretical frameworks considering arbitrary modes of vibration have been developed [111, 125] and experimentally tested [63, 64, 116, 117]. Reported applications include characterization of polymer solutions [59], concentration determination of sugar solutions [57] and viscosity measurements of hydrocarbons and silicone oils [56] and ethanol solutions [55, 61]. A comprehensive review on fluidic applications using microcantilevers is given by Kim, Kihm, and Thundat [24] Only few papers report time-resolved changes in cantilever resonance parameters in fluids while viscosity and mass density are changed [46, 47]. Furthermore, reviewing viscosity and mass density data measured using microcantilevers led us to the conclusion that careful calibration and a vibrational spectrum without spurious resonance peaks are essential to achieve good accuracy.

In this paper we use resonating nanomechanical cantilevers embedded in a microliter fluid cell, as transducers for real-time viscosity and mass density measurements. Photothermal excitation of the cantilever was implemented, and the use of higher flexural modes of vibration was studied. The performance of the instrument was evaluated using glycerol solutions. A segmented two-phase flow allowed sequential measurements to be performed using sam-

ple volumes as low as 5 μL. Subsequently, the use of the method to monitor polymerization reaction kinetics with microliter sample consumption was investigated.

5.2 Materials and methods

Unless otherwise indicated, nanopure water was used and chemicals were purchased from Sigma-Aldrich (Buchs, Switzerland) and used without further purification.

5.2.1 Experimental setup

The experimental setup employed to excite and detect higher flexural mode cantilever vibrations in liquid is shown in Figures 5.1a and b. By sweeping given ranges of frequencies (sweep time 1.0 to 1.67 s), amplitude and phase spectra of arbitrary flexural modes are recorded on a vector network analyzer (MS4630B, Anritsu, Kanagawa, Japan). The reference signal is applied to the excitation laser driving the cantilever (LD_{EX}; 406 nm, 4.4 mW_{DC}, peak-to-peak modulation amplitude 7.0 mW_{pp} at the output aperture of the objective; LP406-SF20, Thorlabs, Newton, New Jersey, USA). The dynamic response is monitored using the detection laser (LD_{DE}; 780 nm, 0.8 mW_{DC}; 51nanoFCM-H06, Schäfter + Kirchhoff GmbH, Hamburg, Germany), which is reflected off the free end of the cantilever. The optical deflection signal is directed onto a position-sensitive detector (PSD; 2L10_SU7, SiTek Electro Optics, Partille, Sweden); a motorized translational stage keeps the laser spot centered on the PSD. Photocurrents from two opposing electrodes on the PSD are converted by home-built transimpedance amplifiers (bandwidth: 850 kHz) and fed into a differential amplifier (gain: $10\times$; SIM910/SIM911, Stanford Research Systems, Sunnyvale, CA, USA; or DA1822, Teledyne LeCroy, Chestnut Ridge, NY, USA). The differential signal is fed back into the network analyzer (lock-in bandwidth: 300/500 Hz) and divided by the signal originating from a reference photodiode (PD; PDA36A, Thorlabs, Newton, New Jersey, USA). Specifically developed, object-oriented LabVIEW software (National Instruments, Austin, Texas, USA) is used to control and record data from the network analyzer. Amplitude and phase spectra are recorded and saved consecutively. A Lorentzian curve fitting routine allows resonance frequencies and quality factors to be tracked in real-time. Furthermore, the software monitors the deflection and intensity of the signal on the position-sensitive detector, stabilizes the temperature of the fluid cell to $20 \pm 0.01^{\circ}$C, and controls the valve and syringe pump used for sample injection.

5.2.2 Fluid cell and sample injection

A syringe pump (KDS900, KD Scientific, Holliston, MA, USA) and a ten port valve (VV-C2H-1340EH, VICI, Schenkon, Switzerland) equipped with two sample loops (10 and 50 μL) allow sequential injection of samples into the fluid cell using a carrier fluid, either water or

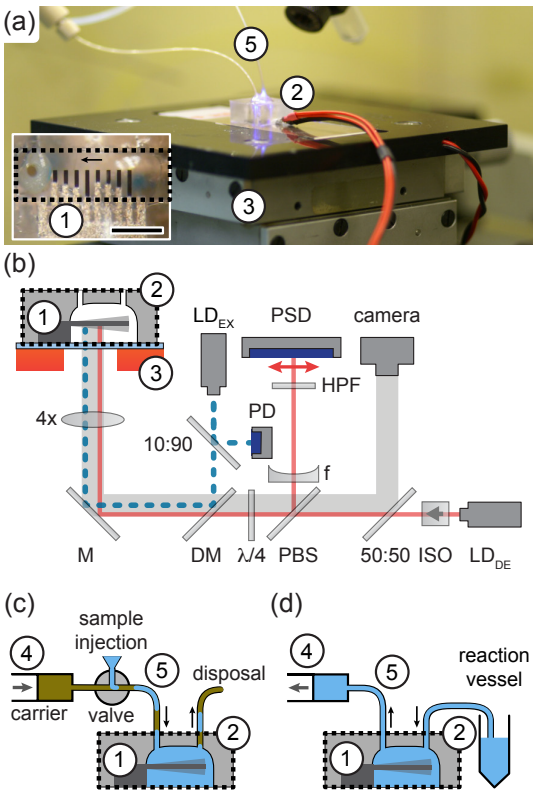

Figure 5.1: (a) Photograph and (b) schematic diagram of the experimental setup. Inset: Micrograph of the fluid cell; the dotted black line indicates the fluid channel and the arrow the flow direction (scale bar: 1 mm). Configurations of the fluidic setup: (c) Sequential sample injection and (d) sample aspiration from an external vessel. The cantilever chip (1) is integrated in a PDMS fluid cell (2) mounted on a temperature-controlled stage (3). A syringe pump (4) allows injection or aspiration of sample into the fluid cell through PEEK tubes (5). The beam (dashed blue line, b) from an intensity-modulated excitation laser (LD_{EX}) is split 10:90 between a reference photodiode (PD) and a dichroic mirror (DM), respectively. It is directed upwards by a broadband mirror (M) and focused onto the cantilever by an objective lens ($4\times$). To detect the vibration, the reflected beam of the detection laser (LD_{DE}; solid red line, b) originating from the cantilever, is directed through a concave lens (f = -50 mm) onto a position-sensitive detector (PSD), by combining a polarizing beam splitter (PBS) and a lambda-quarter plate ($\lambda/4$). An optical high-pass filter (HPF) is inserted to avoid disturbances on the PSD. An optical isolator (ISO) is used to avoid back reflection into the laser diode. Optical access for a camera is provided by a 50:50 beam splitter.

hydrocarbon oil, at flow rates between 0.1 and 50 μL/min (Figure 5.1c). To monitor a polymerization process in an external vessel, sample is aspirated into the fluid cell as illustrated by Figure 5.1d. All measurements are performed under continuous flow. The parts are connected with polyether ether ketone (PEEK) tubes (inner diameter 250 μm). The fluid cell (volume < 2 μL) is molded in polydimethylsiloxane (PDMS) [189]. The required master template was produced from a cantilever chip body and a glass rod (diameter 1 mm) glued to a microscopy glass slide. Replica are fabricated by pouring degassed PDMS (SYLGARD® 184, Dow Corning, Midland, MI, USA) onto the master template and baking at 60°C for at least 4 h. After activation in a 30 W oxygen plasma for 30 s (PDC-002, Harrick Plasma, Ithaca, NY, USA), a cantilever chip is inserted and the fluid cell is bonded to a microscopy glass slide. The dimensions of the fluid cell where chosen to ensure that boundary effects, such as squeeze film damping, are negligible [123].

5.2.3 Cantilever preparation

Arrays comprised of cantilevers with different lengths (IBM Zurich Research Laboratory, Rueschlikon, Switzerland; nominal dimensions $500/300/250/200 \times 100 \times 4$ μm^3), were cleaned in piranha solution (30% hydrogen peroxide and 96% sulfuric acid, 1:1) for 30 min, washed four times in water, once in isopropanol and dried in air. To passivate the silicon, cantilevers were incubated in 10 mM 2-(methoxy(polyethyleneoxy)propyl)trimethoxysilane (90%, ABCR, Karlsruhe, Germany) in ethanol for 30 min at room temperature. Subsequently, a 2 nm titanium layer (Johnson Matthey, Zurich, Switzerland) followed by a 20 nm gold layer (Goodfellow, Huntingdon, England) were deposited using an electron-beam evaporator (EVA 300, Alliance Concept, Cran Gevrier, France). The gold layer was then passivated in 1 mM (1-Mercapto-11-undecyl)tetra(ethylene glycol) (95%, ASEMBLON Inc., Redmond, WA, USA) in ethanol for 30 min at room temperature, washed in water and rinsed with isopropanol. Cantilevers were stored under argon atmosphere until use. For all experiments, only the cantilevers with the highest aspect ratio were used ($500 \times 100 \times 4$ μm^3).

5.2.4 Glycerol reference solutions and free radical polymerization reaction

Viscosity and mass density standards were prepared from weighed amounts of water and glycerol. The glycerol concentrations ranged from 30.5% to 73.0% (w/w) and corresponding viscosity and mass density values were calculated according to theory [190, 191]. The reference solutions were mixed and filtered through a sterile 0.20 μm filter. Water was used as carrier fluid for the reference measurements. A total of 45 μL of each glycerol reference solution was injected into the fluid cell at 5 μL/min (first 15 μL) and measured at 2 μL/min (following 30 μL). Subsequently, the fluid cell was purged with water at 2 μL/min. For segmented two-phase flow experiments a hydrocarbon oil (Viscosity and Density Standard N1.0, 19044;

1.03 mPa·s, 779 kg/m^3) was used as carrier fluid and 5 μL samples were sequentially injected at a constant flow rate of 5 μL/min (see Figure 5.1c).
To study the free radical polymerization of acrylamide at room temperature in a time-resolved manner, the monomer acrylamide (3.4%, 478 mM, 109 equivalents) and the catalyst tetramethylethylenediamine (TEMED; 6.6 mM, 1.5 equiv.) were dissolved in water and placed in an Eppendorf tube (total sample volume: 1.5 mL). The solution was fed into the fluid cell by aspirating it at a rate of 1 μL/min (see Figure 5.1d). The polymerization reaction was initiated by adding ammonium persulfate (APS; 4.4 mM, 1 equiv.) and the flow rate was increased to 10 μL/min for 1 min to overcome the dead volume of the connecting tube ($\approx$ 5 μL). Subsequently, the flow rate was decreased to 1 μL/min and kept at this value during the entire reaction (65 min). The total sample consumption during the reaction was 75 μL. As the reaction was carried out in air and the water was not deoxygenated, atmospheric oxygen was present in the reaction mixture and quenched the reaction in the initial phase. The final degree of conversion of the reaction was determined by ^{1}H-NMR spectroscopy using a Bruker DPX-NMR (400 MHz) instrument (Bruker, Billerica, MA, USA). 0.4 mL of sample was added to 0.4 mL of D_2O (Cambridge Isotope Laboratory Tewksbury, MA, USA) and analyzed by ^{1}H-NMR at room temperature. The degree of conversion was calculated from the baseline corrected spectra using the integrals of the vinyl protons of the monomer and the protons of the polymer backbone.

5.2.5 Data analysis and hydrodynamic forces

The following procedure was followed to measure the viscosity and mass density using a vibrating cantilever immersed in the fluid under test: (i) The eigenfrequency and quality factor of the cantilever were experimentally determined; (ii) the hydrodynamic function, relating these parameters to the viscosity and mass density of the fluid, was solved; (iii) after a calibration step, the fluid properties were determined. To determine the eigenfrequency and quality factor of the cantilever, a damped harmonic oscillator model was fitted to the amplitude and phase spectra individually [23] (see Supporting Information D). The hydrodynamic function Γ (see below for details) introduced by Sader and Van Eysden [111, 125], relates the eigenfrequency f_n and quality factor Q_n of a vibrating cantilever to the viscosity and mass density of the surrounding fluid,

$$f_n = f_{n,\text{vac}} \left(1 + \frac{\pi w \rho}{4 t \rho_c} \Re\left(\Gamma(Re, \kappa_n)\right)\right)^{-\frac{1}{2}}, \tag{5.1}$$

$$Q_n = C_{n,\text{cal}} \frac{\frac{4t\rho_c}{\pi w \rho} + \Re\left(\Gamma(Re, \kappa_n)\right)}{\Im\left(\Gamma(Re, \kappa_n)\right)}. \tag{5.2}$$

The Reynolds number [125] $Re = 2\pi f_n \rho w^2/\eta$, quantifies inertial against viscous forces and the normalized mode number $\kappa_n = w\alpha_n/L$, is related to the spatial wavelength of the

beam. The parameters t, w, L, ρ_c, f_n and Q_n are the thickness, width, length, average mass density (2330 kg/m^3), eigenfrequency and quality factor of mode n, with eigenvalue α_n (see Supporting Information D), of the cantilever immersed in a fluid of mass density ρ and viscosity η. The real part $\Re(\Gamma)$ of the hydrodynamic function describes inertial forces, whereas the imaginary part $\Im(\Gamma)$ represents dissipative forces exerted by the fluid. Compressibility of the fluid should be considered when the spatial wavelength of a flexural mode exceeds the acoustic wavelength in the fluid at the corresponding frequency. In aqueous solutions this condition is met for flexural mode numbers above 24 for the cantilevers employed [128]. Because the highest detectable mode is far below this value, compressibility was neglected in the analysis. The employed model furthermore assumes the no-slip boundary condition [113]. Equation 5.1 is solved by an iterative process [112], because the hydrodynamic function depends on the eigenfrequency. A calibration step is required to account for uncertainties in the dimensions of the cantilever as well as to compensate for non-ideal effects. It is performed in a single reference fluid, water in the present case, at the start of every series of experiments. The calibration factors, the vacuum frequency [63] $f_{n,\text{vac}}$ and the quality factor calibration constant $C_{n,\text{cal}}$, are determined for each flexural mode n by a root-finding algorithm in IGOR Pro (WaveMetrics, Lake Oswego, OR, USA), using Equation 5.1 and 5.2. Once determined, the calibration factors $f_{n,\text{vac}}$ and $C_{n,\text{cal}}$ are used to calculate the viscosity and mass density of the fluid under test.

The approach used to describe the hydrodynamic function Γ is discussed in the following. Higher modes of vibration entail high Reynolds numbers Re due to their elevated eigenfrequencies f_n. The numerical calculation of Γ for such high Re requires a large number of terms to reach convergence [113], which would demand both very high numerical precision and computing time. Therefore, empirical implementations of Γ have been developed and successfully applied [33, 132]. We introduce an approximation, which is valid for $Re \geq 10^3$ and therefore complements previously reported descriptions of the hydrodynamic load:

$$\Gamma = \left(a + b \cdot \Re\left[\Gamma_{\kappa_n \to \infty}(Re, \kappa_n)\right]\right) + i\left(Re^{-c} + d \cdot \Im\left[\Gamma_{\kappa_n \to \infty}(Re, \kappa_n)\right]\right) \quad \text{for} \quad Re \geq 10^3, \quad (5.3)$$

$$\Gamma_{\kappa_n \to \infty} = \frac{8}{\pi \kappa_n} \frac{\sqrt{\kappa_n^2 - iRe}}{\sqrt{\kappa_n^2 - iRe} - \kappa_n} \quad \text{as} \quad \kappa_n \to \infty. \quad (5.4)$$

The approximation is based on the corrected asymptotic solution $\Gamma_{\kappa_n \to \infty}$ from Van Eysden and Sader [125], valid for higher normalized mode numbers κ_n. The parameters a, b and c, d are correction terms for the real and imaginary components, respectively. The following requirements are fulfilled by the approximation: In the asymptotic limit $Re \to \infty$, the real part of the hydrodynamic function approaches the values of the inviscid theory [124] with good accuracy, whereas the imaginary part reaches zero. Furthermore, the correction

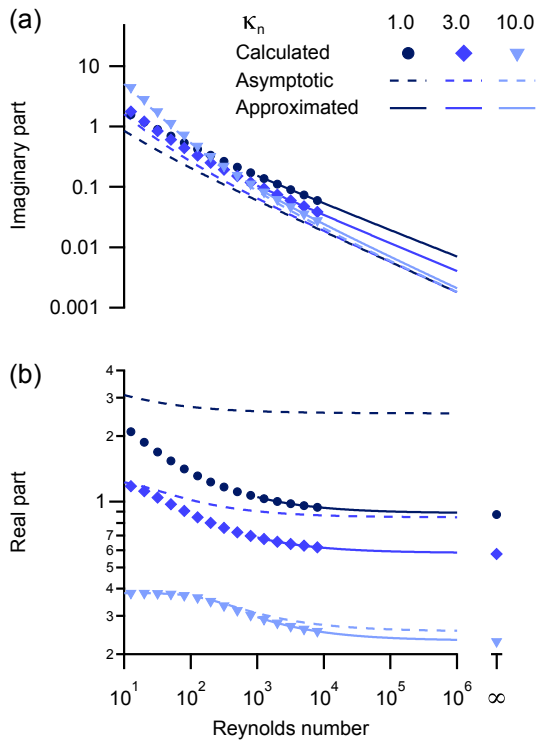

Figure 5.2: Log-log plot of the imaginary (a) and real (b) part of the hydrodynamic function Γ for various values of the normalized mode number κ_n. Calculated [125] (markers), asymptotic [125] (dashed lines; Equation 5.4) and approximated (solid lines; Equation 5.3) values are shown. For better visibility every other calculated value has been omitted. The results of the inviscid theory [124] are indicated in the real part (∞).

terms $a, Re^{-c} \to 0$ and $b, d \to 1$ for $\kappa_n \gg 1$ to recover the asymptotic solution (Equation 5.4). The correction parameters were determined by fitting the real and imaginary part of the approximation to the numerically calculated values in the range $Re = \{10^3, \ldots, 10^4\}$ and $\kappa_n = \{0.1, \ldots, 20\}$ and are provided in the Supporting Information D. Discrete values of Γ were numerically calculated according to literature [125] for $Re = \{10^0, \ldots, 10^4\}$ and $\kappa_n = \{0.1, \ldots, 20\}$. Figure 5.2 shows numerically calculated, asymptotic and approximated values of the hydrodynamic function for various κ_n. Because the Reynolds numbers obtained in the experiments are in the order of 10^2 to 10^5, a combination of the numerically calculated and approximated values of the hydrodynamic function was used. The transition region ($Re = \{10^3, \ldots, 10^4\}$) was described by a linearly weighted average of both functions.

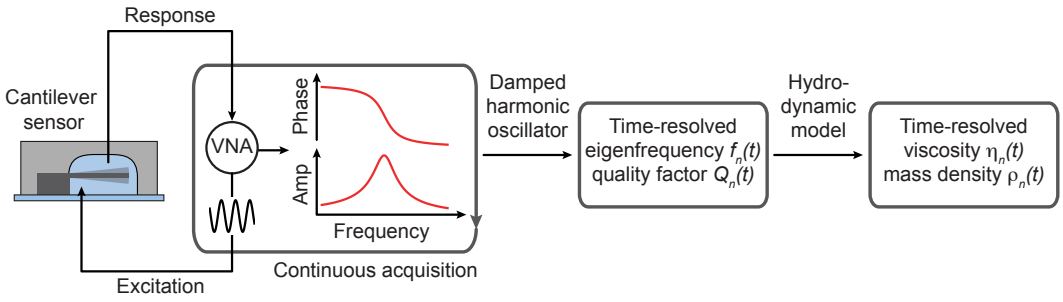

Figure 5.3: Measuring principle: A vector network analyzer (VNA) applies a frequency swept excitation signal to the immersed cantilever sensor and detects its response. Resulting phase and amplitude spectra are acquired continuously. Time-resolved values of the eigenfrequency f_n and quality factor Q_n are determined by fitting a damped harmonic oscillator model to the spectra. The values are converted into viscosity and mass density data by using a hydrodynamic model, which quantifies the cantilever-fluid interactions (see Materials and Methods).

5.3 Results and discussion

A microcantilever based method for fluid viscosity and mass density measurements with high temporal resolution and microliter sample consumption is presented (Figure 5.1). The measurements are achieved by monitoring higher flexural mode vibrations of a cantilever immersed in the liquid under test. The measuring principle is depicted in Figure 5.3. In the following, we present (i) the dynamics of vibrating microcantilevers driven by optical excitation in liquid, (ii) the validation of the instrument performance with liquids of known viscosity and mass density, (iii) an optimized sample delivery procedure involving a two-phase flow and (iv) the application of the sensor to characterize chemical polymerization reactions.

5.3.1 Photothermal excitation of resonating cantilevers in liquid

The phase and amplitude response of a resonating cantilever immersed in liquids of different viscosity and mass density, namely water and glycerol solutions, are shown in Figure 5.4. The cantilever was embedded in a molded fluid cell with a volume below 2 μL. Vibration was induced photothermally and detected using an optical beam deflection setup (Figure 5.1). The high spring constants of the cantilevers [106] and the viscous surroundings require efficient excitation to drive higher flexural modes at a detectable amplitude. Photothermal excitation allows cantilever vibration to be induced without mechanical contact [104, 192]. Thus, the excitation system is completely separated from the fluid cell. To ensure efficient photothermal excitation of higher flexural modes, the excitation laser was positioned close to the

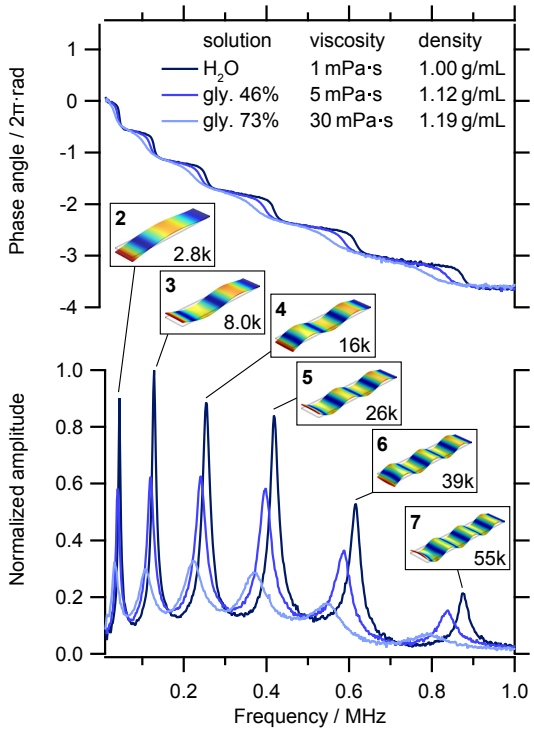

Figure 5.4: Phase and amplitude response of a photothermally driven cantilever ($500 \times 100 \times 4\ \mu m^3$) immersed in liquids of different viscosity and mass density, namely water (H_2O) and glycerol solutions (gly. w%). The flexural mode number (bold), the corresponding Reynolds number in water and the mode shape are indicated above the resonance peaks. Note the absence of spurious resonances. The first flexural mode is not visible due to high-pass filtering. The angular deflection amplitude is normalized to the highest peak.

clamped end of the cantilever beam, where the curvature is highest. In contrast, the detection laser was focused at the free end of the cantilever, where maximal angular deflection occurs. Furthermore, the efficiency was improved by matching the excitation and detection laser wavelengths to the absorption properties of the cantilever coating [153], in this case gold. At the excitation wavelength of 406 nm, the absorption of gold is about 67% [193], allowing efficient heating that is in turn transduced into a bending moment. In contrast, the absorption of gold is < 3% (reflectivity > 97%) [193] at 780 nm rendering this wavelength suitable for the detection laser. Advantages of photothermal excitation are (i) undisturbed resonance spectra, (ii) suitable integration into microfluidics, (iii) scalability, e.g., scanning over arrays of cantilevers, and (iv) separation of the excitation and detection system from microfluidics, allowing flexible fluid cell designs. Potential drawbacks of photothermal excitation and optical detection include: (i) Only applicable to optically transparent sample

fluids, (ii) requires a two-step alignment, and (iii) local fluid heating (see Supporting Information D).
The resonance spectra shown in Figure 5.4 are free of any spurious resonances. The phase and amplitude response of a cantilever is an entanglement of various effects depending on: (i) The properties of the fluid, i.e., increasing viscosity and mass density decrease the quality factor, shift the eigenfrequencies towards lower values and reduce the amplitude of vibration; the shifts are more pronounced for higher modes, (ii) the mechanical properties and dimensions of the cantilever, (iii) the position, thermal lag and the spot size of the photothermal excitation, (iv) the phase-lag and bandwidth (850 kHz) of the electronics and (v) the degree of angular bending, i.e., the stronger angular bending of higher flexural modes increases the response detected in the optical beam deflection system.

5.3.2 Viscosity and mass density measurements of reference fluids

After calibration in water (1.01 mPa·s, 998 kg/m^3; average of 10 spectra) at the start of a flow-through measurement, viscosities and mass densities of the sample fluids were calculated from the measured eigenfrequencies and quality factors. Mass density mainly affects the co-moving mass and thus the eigenfrequency of the resonator. In contrast, viscous forces alter the dissipation and thus govern the quality factor. The influence of the viscosity on the eigenfrequency is due to the boundary-layer thickness [31] which extends further for lower modes, and thus increases the co-moving mass.
A calibration step is essential to avoid systematic errors. Deviations of the vacuum frequency from the calculated values are mainly caused by the uncertainty in the average thickness of the cantilevers, and become more pronounced at higher modes [10]. The quality factor is affected by various dissipative mechanisms. For the cantilevers employed, viscous dissipation dominates by orders of magnitude [109]. Because only fluid in closest vicinity to the cantilever is probed, i.e., within the viscous boundary-layer [31], local heating effects originating from the incident lasers must be considered. Finite element analysis suggests that the average heating inside the probed fluid volume (< 1 nL) is below 2.3 K (see Supporting Information D). Because the viscosity has a stronger temperature dependence than the mass density [157], an increase in temperature mainly alters the quality factor. To account for these interfering effects, the vacuum frequency and a quality factor calibration constant were determined using water as a calibration fluid.
Figure 5.5 shows measured viscosity and mass density values of reference fluids (glycerol solutions) derived from the different flexural modes. The analysis was performed for the phase as well as for the amplitude spectra. The accuracy is mainly governed by the peak amplitude, which defines the signal-to-noise ratio. In general, higher modes show less variance because of the larger absolute shifts in eigenfrequency and quality factor. At high viscosities, values derived from higher modes deviate from the reference values. Due to the larger absolute

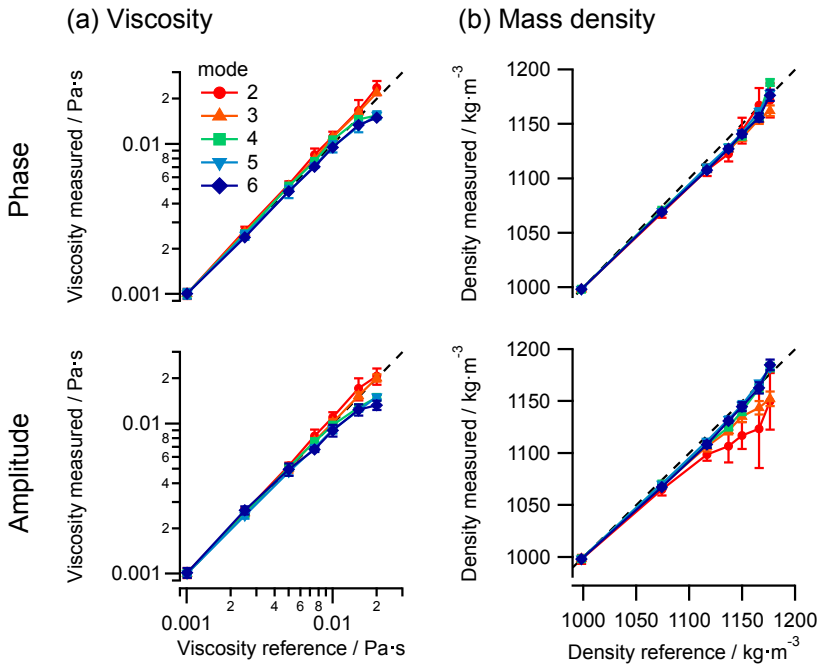

Figure 5.5: (a) Viscosity and (b) mass density values of glycerol solutions, derived from the amplitude (bottom) and phase (top) response of flexural modes 2 to 6, after calibration in water. Reference values are indicated by the dashed lines [190, 191]. The data points show the mean and standard deviation derived from 10 spectra.

shifts observed at higher modes, the response saturates more rapidly impairing accurate determination of the viscosity values. The deviations in mass density derived from amplitude spectra of lower modes are due to the decreasing peak amplitudes, which hinders the precise determination of the eigenfrequency. After a single reference calibration in water, quantitative viscosity measurements performed on the reference fluids were accurate to within 25% (phase) and 34% (amplitude) in a range from 1 to 20 mPa·s (12% (phase) and 10% (amplitude) for 1 to 10 mPa·s). Mass density values were determined within 1% (phase) and 4% (amplitude) from 998 to 1176 kg/m^3. These values are comparable [56] or better [60] than the ones reported for similar viscosity ranges using cantilevers. The more the sample characteristics deviated from those of the calibration fluid and the higher the viscosity, the more the measured values differed from literature values and the larger the standard deviations. Better accuracy can be obtained using a multi-reference calibration [57] or cantilevers with a higher aspect ratio [55]. Furthermore, the precision can be adjusted by adapting the cantilever dimensions to a certain measurement range.

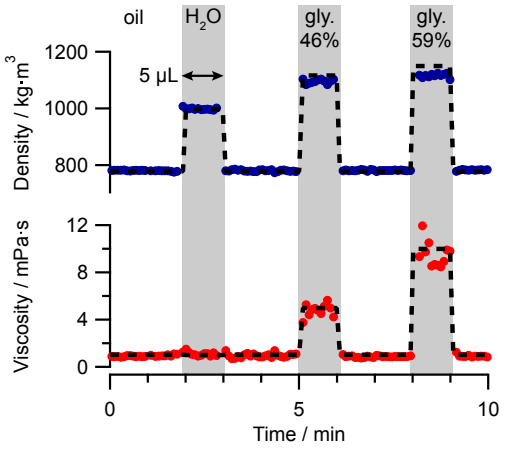

Figure 5.6: Viscosity and mass density values derived from the 4th flexural mode upon sequential injection of 5 μL samples using a hydrocarbon oil as carrier fluid. The use of a hydrophobic carrier phase prevents dispersion and thus delivers the sample to the cantilever transducer at its initial concentration. After calibration in the carrier fluid (oil), water (H_2O) and different glycerol solutions (gly. w%) were injected. Reference values are indicated by the dashed lines [190, 191].

5.3.3 Segmented two-phase flow to avoid sample dispersion

Dilution of the sample by dispersion into an aqueous carrier fluid leads to deviations in viscosity and mass density. Such Taylor dispersion [194] increases with the initial solute concentration and the flow rate. Therefore, efficient delivery of the sample liquid to the sensor is crucial for accurate measurements in flow-through instruments. The use of an oil phase as carrier fluid [195], which effectively prevents sample dilution, allows smaller sample volumes to be measured. As illustrated in Figure 5.6, the use of a hydrocarbon oil resulted in a segmented two-phase flow, allowing fast and reliable screening of samples as small as 5 μL. Measured viscosity and mass density values are in good agreement with literature values (dashed lines [190, 191]) for both the carrier and the samples [194]. Furthermore, the measured values returned to the baseline immediately after each sample plug, clearly indicating that there was no unspecific adsorption to the cantilever. During sample injection and purging the laser beams are scattered due to (i) the different refractive indices of the fluids and (ii) interfacial forces deflecting the cantilever, leading to a temporary decrease in laser intensity. To account for this, data points recorded below a certain laser intensity threshold were excluded from the analysis (see Supporting Information D). In summary, miniaturization and optimized liquid handling significantly improved the sensor characteristics. These findings might also be applicable to other transducer technologies.

5.3.4 Real-time monitoring of free radical polymerization reactions

The polymerization of acrylamide was selected as a model system to demonstrate the study of dynamic processes and to validate the results delivered by the sensor by comparing them to published rheokinetic data [196]. The specific viscosity of a polyacrylamide (PAa) solution η_{sp} is proportional to the polymer concentration c and the viscosity average molar mass $\overline{M}_v$ according to $\eta_{sp} \propto c^6 \overline{M}_v^{3.4}$ [196]. This equation can be expanded into a rheokinetic model that links the measured viscosity at any given reaction time to the monomer-to-polymer conversion of the reaction (see Supporting Information D and reference [196]).
Figure 5.7a shows time-resolved viscosity and mass density data derived from flexural modes 2 to 6. After recording a stable baseline in acrylamide monomer solution, the reaction was initiated by adding ammonium persulfate (+APS). As atmospheric oxygen was present, the reaction started after a lag-phase (t_0). Viscosity hardly increased in the initial polymerization phase due to the weak viscosity-concentration dependence at low polymer concentrations. A strong increase in viscosity was observed in the next stage, i.e., at higher polymer concentrations, until saturation, which was reached when most monomer had been converted into polyacrylamide. The difference in the absolute cantilever response in the polyacrylamide solution (PAa, Figure 5.7a) is explained by the occurrence of shear-thinning at higher frequencies. The measured mass density deviated towards lower values, even though an increase was expected (see Supporting Information D). The employed hydrodynamic model does not account for the non-Newtonian behavior of the solution [125], therefore misinterpreting shear-thinning as a decrease in mass density. The deviation becomes more pronounced at lower modes, where the eigenfrequency strongly depends on an entanglement of viscosity and mass density. In contrast, the eigenfrequencies of higher modes are almost independent of the viscosity and, thus, reproduce the mass density with higher accuracy.
To validate the use of the sensor for kinetic measurements, a rheokinetic model [196] was fitted to the viscosity data (Figure 5.7a, solid black lines; see Supporting Information D for details). The rheokinetic model describes the measured data well and was used to calculate the degree of conversion β of the reaction over time as shown in Figure 5.7b. In the initial stage ($\beta < 25\%$) of the polymerization, it cannot be accurately determined due to the weak viscosity-concentration dependence. Even though shear-thinning occurred, the determined degrees of conversion are consistent along all modes. As expected for a free radical polymerization [196], the degree of conversion is well described by a first order kinetic with a second order initiation reaction (solid black lines in Figure 5.7b). The degree of conversion at the end of the reaction additionally determined by ^{1}H-NMR was $(96 \pm 2)\%$. In good agreement, the rheokinetic model extrapolated to 95% (Figure 5.7b). These results approve the use of nanomechanical cantilevers to monitor the kinetics of polymerization reactions solely by measuring changes in viscosity.

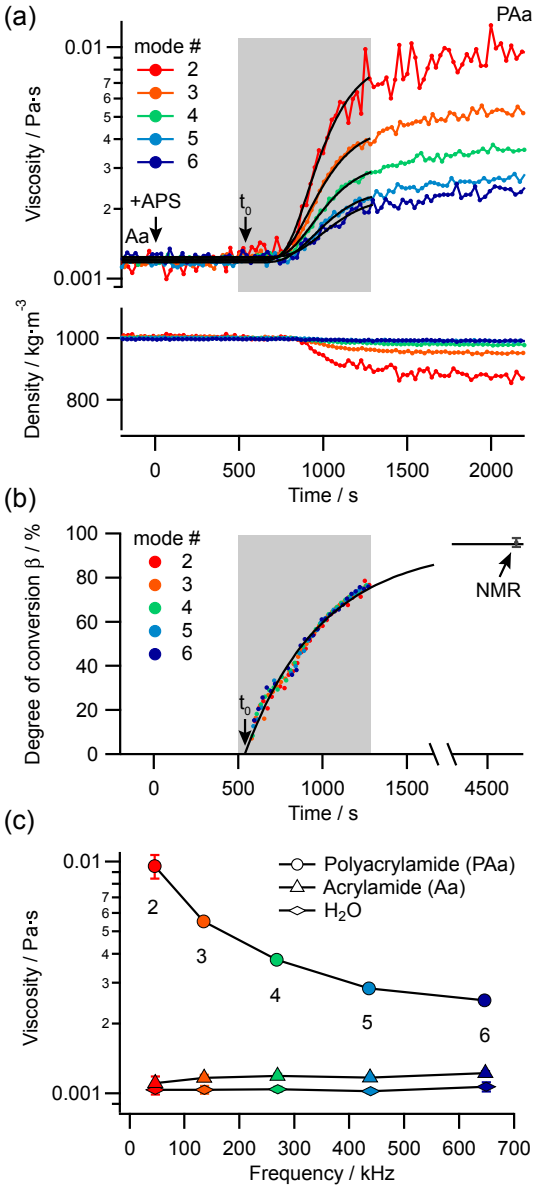

Figure 5.7: Free radical polymerization of acrylamide. (a) Viscosity and mass density data derived from phase spectra. The acrylamide solution (Aa) was initiated with ammonium persulfate (+APS). After a lag-phase (t_0) due to the presence of oxygen, the reaction started and the viscosity increased until the monomer became depleted (PAa). (b) The degree of conversion during the reaction (grey area) was determined by fitting rheokinetic models [196] to the viscosity data (solid black lines in a). It is well described by a first order kinetic with a second order initiation reaction (solid black line in b). The degree of conversion at the end of the reaction was furthermore determined by ^{1}H-NMR. (c) Frequency dependent viscosity of the polymer solution (polyacrylamide), the monomer solution (acrylamide) and water (H_2O; mode numbers are indicated).

Figure 5.7c shows the shear-thinning behavior of the polymer solution (PAa) [40] determined at the end of the reaction. In contrast, the monomer solution (Aa) and the solvent (H_2O) displayed Newtonian (frequency independent) behavior. Recently introduced theoretical models for the characterization of viscoelastic fluids using microcantilevers account for such non-Newtonian behavior. However, they only consider the fundamental flexural mode and require prior knowledge of the mass density [197]. Extending such models to higher modes would enable viscoelastic behavior to be characterized over a wide range of frequencies.

5.4 Conclusions

The method presented uses nanomechanically resonating cantilevers to achieve quantitative, time-resolved fluid viscosity and mass density measurements. The implemented photothermal excitation method avoided spurious resonances and allowed integration of the sensor into PDMS microfluidics, where piezoelectric excitation is unsuitable [198]. Embedding the cantilever transducer in a microfluidic PDMS cell and implementing a two-phase fluidic system avoided sample dispersion, allowing measurements to be reproducibly made with 5 μL sample volumes. The hydrodynamic model of Van Eysden and Sader [125] was adapted to allow higher flexural modes, i.e., vibration at high Reynolds numbers, to be considered. The extended model was validated using Newtonian reference solutions prepared from glycerol.
Using the microcantilever based instrument it was possible to follow the free radical polymerization of acrylamide in a time-resolved manner with a total sample consumption of just 75 μL during 65 min. Non-Newtonian shear-thinning behavior observed in the viscosity data revealed limitations of the theoretical framework employed, impairing accurate determination of the mass density, especially at lower modes of vibration. Despite the observed shear-thinning, the degree of monomer-to-polymer conversion was determined using rheokinetic models [196], and was consistent for all modes of vibration. In future, the instrument could be used to determine the kinetic constants of unknown reactions. Further, the very small sample volumes required make it ideally suited to monitor polymerization kinetics in microreactors [199] or in reactions that have to be conducted on a very small scale, e.g., to explore the parameters for expensive (bio)catalysts [200]. In addition to its use to characterize chemical polymerization reactions, the presented sensor should allow biological aggregation processes to be investigated.

Acknowledgement

The authors gratefully acknowledge Henning Stahlberg (C-CINA, University of Basel) for providing infrastructure and facilities; Shirley A. Müller (C-CINA, Univ. Basel) for criti-

cally reading the manuscript; Bernd Rinn (CISD, D-BSSE, ETHZ) and Patrick Vogt (URZ, Univ. Basel) for support with numerical calculations; François Huber and Natalija Backmann (SNI, Univ. Basel) for help with the sensor passivation; Andreas Hierlemann and Alexander Stettler (BEL, D-BSSE, ETHZ) for assistance on PDMS fabrication; Andreas Tonin (Electronics Workshop, Dept. Physics, Univ. Basel) and Raymond Strittmatter (Mechanical Workshop, Biozentrum, Univ. Basel) for their electronic and mechanical design and manufacture; Michel Despont and Ute Drechsler (IBM Research GmbH, Rüschlikon, Switzerland) for providing cantilever arrays; as well as Thomas Pfohl (Department of Chemistry, Univ. Basel) and Ernst Meyer (Dept. Physics, Univ. Basel) for fruitful discussions. This work was supported by SNF grant 200021/130594, NCCR Nano and ARGOVIA project NoViDeMo.

Chapter 6

Automated high-throughput viscometer using resonant nanomechanical sensors

Benjamin A. Bircher[1], Roger Krenger[1], and Thomas Braun[1]

[1]Center for Cellular Imaging and NanoAnalytics, Biozentrum, University of Basel, Mattenstrasse 26, CH-4058 Basel, Switzerland

Abstract

Most established methods to determine the viscosity and mass density of liquids have two major drawbacks: Sample consumption (milliliters) and measurement time (minutes). Resonant nanomechanical cantilevers promise to overcome these limitations. Although sample consumption has already been significantly reduced, the time resolution was rarely addressed to date. We present a method to reduce the time and user interaction required for such measurements. It features (i) a droplet-generating automatic sampler using fluorinated oil to separate microliter sample droplets, (ii) a PDMS-based microfluidic measurement cell containing the resonant microcantilevers, (iii) dual phase-locked loop frequency tracking of a higher-mode resonance to achieve millisecond time resolution, and (iv) data analysis to extract the resonance parameters and calculate the viscosity and mass density of the surrounding liquid. Series of 2 μL droplets of glycerol, glucose and urea solutions separated by fluorinated oil could be screened at a rate of $\sim$ 5 s per sample droplet, validating the principle. After a single-point calibration in water the accuracy of the viscosity and mass density values were within 24% and 15%, respectively, for a range of 1–11 mPa·s and 998–1175 kg/m^3.

6.1 Introduction

The flow behavior of a fluid is governed by its viscosity and mass density, making these properties of fundamental importance for many industrial processes [42]. Furthermore, the fluid properties of a solution can be related to its condition, including the coagulation properties of blood [201] and the folding state of proteins [92]. Since many biological samples are only available in small quantities, reducing the amount of sample consumed by a viscosity and mass density measurement is an essential requirement. Furthermore, as it is often necessary to characterize large numbers of samples, high-throughput methods are becoming increasingly important.

Resonant structures as cantilevers, suspended-channels [72], quartz crystals, doubly clamped beams, and membranes [42] have all been employed to probe viscosity in small volumes. The use of resonant microcantilevers has the advantage that their interaction with a fluid is comprehensively described due to their abundant use in atomic force microscopy [111, 125]. Furthermore, they can be employed to simultaneously measure the viscosity and mass density of a fluid in sub-microliter volumes [63]. Proof-of-concept viscosity measurements using microcantilevers were made in solvents [63] and hydrocarbons [58]; solutions of sugars [57], ethanol [55], polymers [50] and DNA [53]; and in coagulating blood plasma [201]. Models assuming Newtonian flow behavior were assumed in each case [111, 125]. In resonant microcantilever systems, usually the eigenfrequency and quality factor are extracted from a resonance spectrum and related to the viscosity and mass density of the surrounding fluid [63, 111]. The time resolution of this method is limited by the time to acquire a resonance spectrum; usually a few seconds.

Here, the method of Goodbread et al. [202] was further developed to continuously monitor the eigenfrequencies and quality factors of microcantilevers in liquid with a time resolution of about 1 ms. Microcantilevers were driven by photothermal excitation that allowed phase-locked loop frequency tracking over a wide range of ~ 60 kHz. The improved method was applied to screen microliter sample droplets for their viscosity and mass density in a two-phase, i.e., oil/sample, flow configuration.

6.2 Materials and methods

6.2.1 Reference solutions

Reference solutions were prepared by weighing and dissolving glycerol (A1123, AppliChem), glucose (G7021, Sigma-Aldrich) and urea (U5128, Sigma-Aldrich), respectively, in nanopure water. The glucose solutions and the glycerol solutions were characterized with an AMVn viscometer and DMA 4500 M density meter (Anton Paar). Reference viscosity and mass density values for the urea solutions were taken from the literature [32].

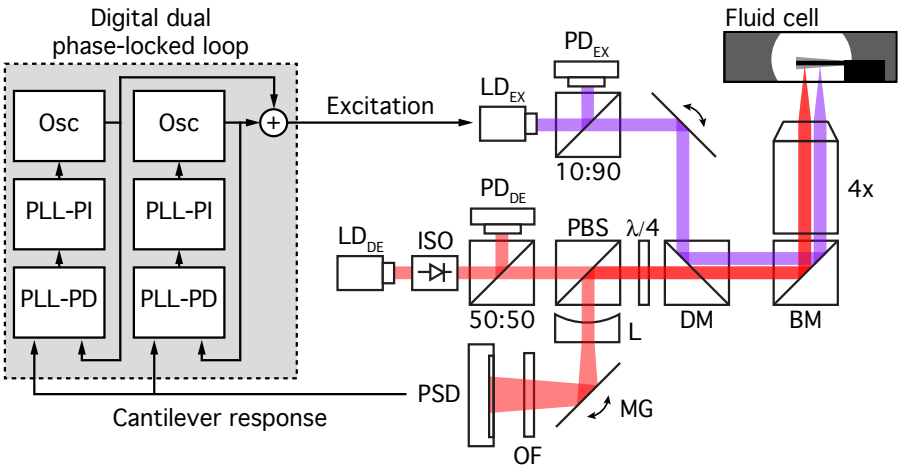

Figure 6.1: Schematic of the electronic and optical setup. Optical beam deflection system used to detect microcantilever vibration: The beam of a 780 nm diode laser (LD_{DE}; red) sequentially passes an optical isolator (ISO), a beam-splitter (50:50) to monitor the intensity on a photodiode (PD_{DE}), a polarizing beam-splitter (PBS), a lambda-quarter plate ($\lambda/4$) and a dichroic mirror (DM), and is reflected off a broadband mirror (BM). After focusing by passage through a microscope objective ($4\times$), it is reflected from the microcantilever and coupled onto the position-sensitive detector (PSD) using the polarizing beam-splitter (PBS). A concave lens (L) increases the displacement of the laser on the PSD. A mirror galvanometer (MG) automatically aligns the laser spot on a position-sensitive detector (PSD) and an optical filter (OF) blocks interfering light. Photothermal excitation used to drive the microcantilevers: An intensity modulated 405 nm diode laser (LD_{EX}; violet) is coupled in using the dichroic mirror (DM). A digital dual phase-locked loop (PLL) is used to detect the cantilever frequencies. The signal from the PSD is fed into the dual PLL consisting of two parallel phase-detectors (PLL-PD), PI controllers (PLL-PI), and oscillators (Osc). The output of the oscillators is mixed and applied to LD_{EX}, thus, modulating its intensity.

6.2.2 Electronic and optical setup

The optical and electronic setup employed is described in Ref. [50]. However, certain modifications were necessary to perform the measurements described below (see Fig. 6.1). A Zurich Instruments HF2-PLL was employed to record open-loop spectra using the lock-in amplifiers; to track frequencies using the dual phase-locked loop (PLL); and to control the laser intensity and position on the position sensitive detector (PSD) using the proportional-integral (PI) controllers. Open loop spectra were acquired at a lock-in bandwidth between 10–100 Hz. The PLL target bandwidth was set between 100 and 500 Hz, which resulted in the following parameters: 4^{th} order input filter with a time constant $\sim 10\ \mu$s (PLL-PD) and PLL PI-feedback gains of $P \sim 10$ and $I \sim 1$ ms (PLL-PI). Furthermore, the detection laser

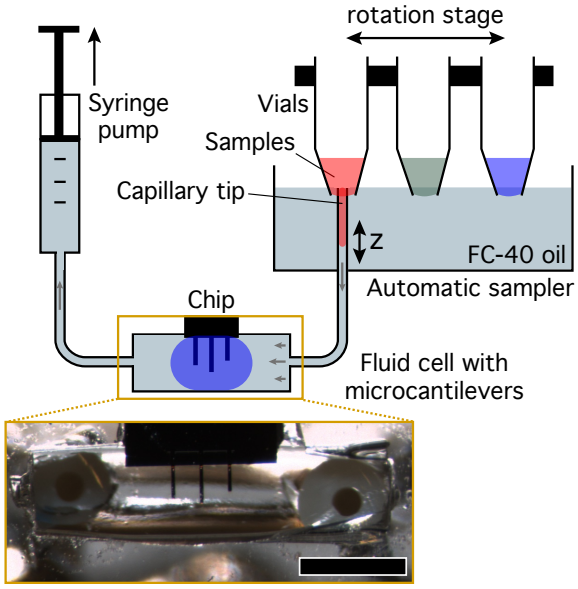

Figure 6.2: Schematic of the fluidic setup. The whole fluidic system is filled with fluorinated oil (FC-40). Samples float on the FC-40 oil and are confined by vials with an open end. 12 vials are mounted in a rotatable stage. Sample droplets are aspirated using a capillary that is controlled by a z-motor, and are separated by oil aspirated when the capillary is withdrawn. Each vial is addressed by rotating the stage. The droplets are pumped into the fluid cell containing the resonant microcantilevers. A syringe pump ensures a constant flow rate. Inset: Micrograph of the fluid cell (scale bar: 1 mm).

position was continuously aligned on the position sensitive detector (PSD) using a mirror galvanometer (MG in Fig. 6.1; GSV011, Thorlabs). This is of special importance to correct for refractive index changes between the fluorinated oil and the aqueous samples. To this end, the deflection signal was amplified (10×, SIM911, SRS), low-pass filtered ($f_{\mathrm{LP}} = 1$ kHz, SIM965, SRS) and fed into the PI loop ($P = 0.01$, $I = 10\ \mathrm{s}^{-1}$) that controls the mirror galvanometer. The incident intensity on the PSD was controlled by a second PI loop ($P = 10$, $I = 1000\ \mathrm{s}^{-1}$) to a setpoint between 330 μW and 450 μW by adjusting the detection laser current. The fluid cell was temperature stabilized to 20°C with a precision of ± 0.05°C.

6.2.3 Fluidic setup

A schematic of the fluidic setup is shown in Fig. 6.2. The main components are the droplet generating automatic sampler, the fluid cell containing the microcantilever sensors, and a syringe pump to obtain a constant flow rate. The 1 μL fluid cell was fabricated according to the protocol in Ref. [50]. However, due to the smaller microcantilever dimensions a channel radius of 400 μm was employed, housing three silicon microcantilevers (350/300/250 μm long,

35 μm wide, 2 μm thick; MikroMasch, NSC12/tipless/noAl, see inset in Fig. 6.2). The microcantilevers were prepared according to Ref. [50] and the 300 μm long microcantilever was used for all measurements. A PDMS-based solution (*Regenabweiser*, Stolz GmbH) was used to render the fluid cell more hydrophobic (see Supplementary Information E). It was previously shown that this is crucial to obtain homogeneous droplets and reproducible droplet handling [203]. Hence, the fluidic system was incubated with the PDMS-based solution prior to a measurement session for >10 min and purged with water afterwards.
The droplet-generating automatic sampler is based on the compartment-on-demand platform described in Ref. [204]. As depicted in Fig. 6.2, the aqueous samples are confined in open-ended 200 μL vials (AB-1182, ThermoScientific) that are slightly immersed in fluorinated oil, which has a higher mass density (FC-40, Sigma-Aldrich; mass density: 1855 kg/m^3, viscosity: 4.1 mPa·s at 25°C). The head of liquid sample above the oil surface determines the position of the oil-sample interface within the vials. A fused silica capillary with a polyimide coating (TSP-250350, BGB-Analytik) gives access to the sample from below through the FC-40 oil. The z-displacement of the capillary was controlled by a linear stepper motor (UBL23N08B1MZ55, Saia-Burgess) with a nominal step size of 0.041 mm. To address each vial, the disk holding 12 vials was rotated with a rotational stepper motor (UBB23N08RAZ320, Saia-Burgess) connected to a step-down gear with a reduction ratio of $16\frac{2}{3}$ (UGM16ANN, Saia-Burgess), resulting in 400 steps per revolution. Both stepper motors were driven by SE2 control electronics boards (463666080, Saia-Burgess) controlled by a LabVIEW DAQ card (NI USB-6009, National Instruments). Custom written LabVIEW software and the openBEB [181] framework were used to synchronize the stepper motors and automatize the measurements (see Supplementary Information E). A KDS900 syringe pump (KD Scientific) equipped with a 2.5 mL glass syringe (1002C, #81460, Hamilton) was employed to maintain a constant flow rate of 60 μL/min. The immersion time of the capillary tip in oil, pure water or aqueous sample was used to control the aspirated volumes. The reservoir of the automatic sampler was filled with $\sim$ 15 mL of fluorinated oil (FC-40). Between 10 μL and 40 μL of sample or pure water was placed in the vials. 2 μL droplets of each sample were sequentially aspirated. In between the samples, 2 μL droplets of water were aspirated to rinse the fluid cell and check for unspecific adsorption to the microcantilever, cross-contamination between the droplets, and baseline drift. All droplets were separated by 4 μL of FC-40 oil. The dead volume between the sample vials and the fluid cell was $\sim$ 20 μL, thus, the time delay after aspirating the first droplet and its arrival in the fluid cell was 20 s.

6.2.4 Dual phase-locked loop data analysis

A dual phase-locked loop (PLL) was used to measure the eigenfrequency and quality factor of a cantilever resonance with a high time resolution. The applied measurement principle is a further development of the gated PLL described by Goodbread et al. [202]. The gated PLL

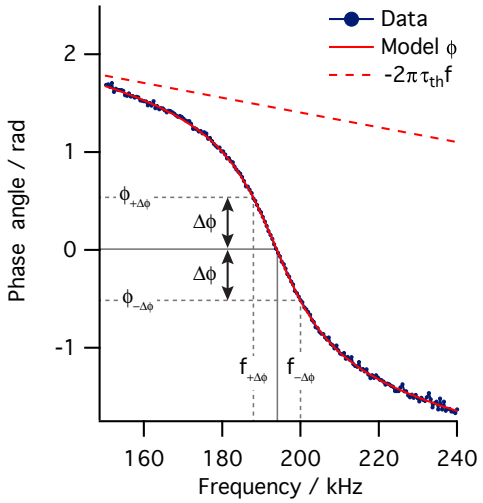

Figure 6.3: Representative phase spectrum of the third mode of vibration with eigenfrequency $f_3 = 194$ kHz, quality factor $Q_3 = 8.4$ and thermal time constant $\tau_{\text{th}} = 1.2$ μs. The measured data (blue markers), model (solid red curve, Eq. 6.1), and linear thermal lag included in the model (dashed red curve) are shown. The eigenfrequency and sideband frequencies and their corresponding phases are indicated by the solid and dashed grey lines, respectively.

switches between excitation and readout to eliminate crosstalk [53]. Furthermore, the phase setpoint is alternately set to different values allowing the quality factor to be determined. The setup presented here, simultaneously tracks two sideband frequencies, $f_{+\Delta\phi}$ and $f_{-\Delta\phi}$, at certain phase setpoints, $\phi_{+\Delta\phi}$ and $\phi_{-\Delta\phi}$, using a dual PLL (see Fig. 6.1). This is possible because crosstalk between the employed photothermal excitation (405 nm) and optical detection (780 nm) lasers can be avoided using optical filters. Continuous sideband frequency tracking allowed changes in eigenfrequency and quality factor to be measured with a time resolution only limited by the bandwidth of the PLL [205], i.e., in the order of a few milliseconds (PLL bandwidth ~ 500 Hz).

Photothermal excitation introduces a non-linear phase shift, depending on the position of the excitation laser [206]. However, in a small frequency interval, i.e., a single vibrational mode, the phase shift can be approximated by a linear phase delay, characterized by time constant τ_{th} [182]. τ_{th} has to be considered in the analysis and can be extracted from measured phase spectra by fitting the phase response of a damped harmonic oscillator combined with a phase delay (see Fig. 6.3 and Ref. [97]):

$$\phi = \arctan\left(Q_n \frac{f_n^2 - f^2}{f_n f}\right) - 2\pi\tau_{\text{th}} f + \phi_{\text{offset}}, \tag{6.1}$$

with frequency f, eigenfrequency f_n and quality factor Q_n of mode n, and arbitrary phase offset ϕ_{offset}. As a first approximation the thermal time constant τ_{th} can be neglected, reducing the complexity and allowing f_n and Q_n to be readily extracted from Eq. 6.1 by inserting the sideband frequencies $f_{+\Delta\phi}$ and $f_{-\Delta\phi}$. Due to symmetry,

$$f_n \approx \frac{f_{+\Delta\phi} + f_{-\Delta\phi}}{2} \quad \text{for} \quad \tau_{\text{th}} f_n \ll 1, \tag{6.2a}$$

$$Q_n \approx \frac{f_n f_{+\Delta\phi}}{f_n^2 - f_{+\Delta\phi}^2} \tan\left(\phi_{+\Delta\phi}\right) \quad \text{for} \quad \tau_{\text{th}} f_n \ll 1. \tag{6.2b}$$

According to Eq. 6.1, the setpoints of the two PLL loops, $\phi_{+\Delta\phi}$ and $\phi_{-\Delta\phi}$, with a finite thermal time constant τ_{th}, are:

$$\phi_{+\Delta\phi} = \arctan\left(Q_n \frac{f_n^2 - f_{+\Delta\phi}^2}{f_n f_{+\Delta\phi}}\right) - 2\pi\tau_{\text{th}} f_{+\Delta\phi}, \tag{6.3a}$$

$$\phi_{-\Delta\phi} = \arctan\left(Q_n \frac{f_n^2 - f_{-\Delta\phi}^2}{f_n f_{-\Delta\phi}}\right) - 2\pi\tau_{\text{th}} f_{-\Delta\phi}. \tag{6.3b}$$

where $f_{+\Delta\phi}$ and $f_{-\Delta\phi}$ are the corresponding measured sideband frequencies; note that the offset ϕ_{offset} is included in the setpoints. Once τ_{th} had been determined from a phase spectrum using Eq. 6.1 (see Fig. 6.3), a find roots algorithm in Igor Pro (WaveMetrics) was employed to numerically solve this system of equations for f_n and Q_n using the approximate results from Eqs. 6.2a and 6.2b as initial parameters.

6.3 Results and discussion

6.3.1 Dual phase-locked loop tracking

To measure the eigenfrequency f_n and quality factor Q_n of a vibrational mode n with a high time resolution, i.e., high bandwidth, a dual phase-locked loop (PLL) was employed. Two sideband frequencies, adjacent to the eigenfrequency, were measured and converted into the corresponding values of f_n and Q_n. To measure the required photothermal time constant τ_{th}, a calibration spectrum was recorded in water, by sweeping a range of frequencies around the eigenfrequency, prior to each measurement. A representative phase spectrum with the sideband frequencies indicated is shown in Fig. 6.3. The measured time constants of ~ 1 μs, are within the range of values reported in literature [182]. Next, the behavior of the sideband frequencies, when the eigenfrequencies and quality factors changed, was calculated (Fig. 6.4). In first approximation, changes in f_n shift both sidebands by the same amount. In contrast, changes in Q_n shift the sidebands relative to each other. Thermal time constants with the magnitude of those measured, only influence the response significantly for quality factors below 10. The optimal sideband phase setpoint, with an offset $\Delta\phi$ relative to the phase at

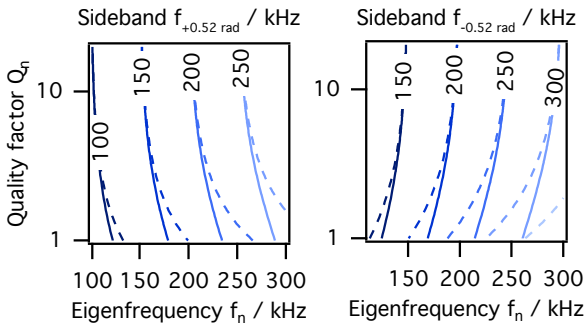

Figure 6.4: Contour plots of the calculated sideband frequencies (Eqs. 6.3a and 6.3b), depending on the eigenfrequency f_n and quality factor Q_n with $\tau_{\mathrm{th}} = 0$ (solid lines) and $\tau_{\mathrm{th}} = 1\ \mu$s (dashed lines). The phase setpoint of the sideband is $\Delta\phi = 0.52$ rad $= 30$ deg relative to the phase at the eigenfrequency. The quality factor axis has a logarithmic scaling.

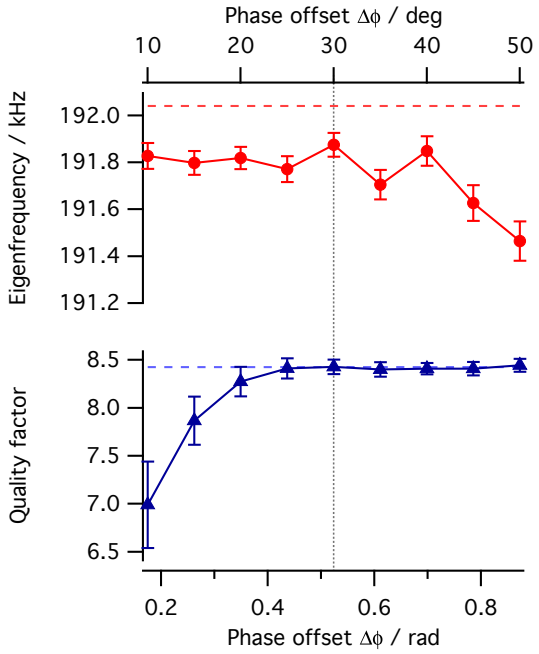

Figure 6.5: Mean and standard deviation (over a period of 10 s) of the eigenfrequency f_n and quality factor Q_n for sidebands positioned at different phase offsets $\Delta\phi$. The dashed horizontal lines represent reference values extracted from a phase spectrum using Eq. 6.1. The dotted vertical line indicates the optimal phase offset ($\Delta\phi = 0.52$ rad $= 30$ deg) used for the measurements.

the eigenfrequency, is not immediately apparent. Considering that the signal-to-noise ratio and the slope of the phase are both highest at the eigenfrequency (for $Q \gg 1$; see Fig. 6.3), the selected phase offset should be as small as possible, i.e., both sidebands should be placed in close vicinity around the eigenfrequency. However, the shift in sideband frequency due to a quality factor change is highest for a large phase offset (see Eq. 6.2b). Furthermore, setting the sidebands too close together, results in overlap of the input demodulator filters and can disturb the PLL tracking. This also occurs at high quality factors, e.g. in air, due to the narrow width of the resonance peak. Therefore, an optimal position is expected at intermediate phase offsets and was evaluated by measuring f_n and Q_n in water and altering the phase setpoints. As shown in Fig. 6.5, f_n has a small systematic offset and deviates from the reference value at higher $\Delta\phi$. In contrast, Q_n is determined most accurately using high $\Delta\phi$. At $\Delta\phi = 0.52$ rad (30 deg), both f_n and Q_n can be determined with good accuracy, thus, all measurements were performed using this offset.

6.3.2 Droplet viscosity screening

Rendering the fluidic system more hydrophobic (see Materials and Methods 6.2.3), proved to be absolutely crucial for reproducible droplet exchange in the fluid cell. After the treatment, the alternating injection of water and aqueous sample droplets was initiated. Fig. 6.6 shows the measurement of sample droplets containing increasing concentrations of urea. The measured sideband frequencies (a) were converted into the corresponding eigenfrequency (b) and quality factor (c) by solving Eqs. 6.3a and 6.3b. The data is not baseline corrected, because it displays excellent stability in water as well as in fluorinated oil. A zoom of one droplet region is shown in Fig. 6.7. As the droplet moves across the fluid cell, the oil-water interface passes the microcantilever, leading to a transition region of a few 100 ms, where the laser beams are scattered. The PI and PLL controllers, respectively, adjust the laser intensity and laser position on the detector (PSD) and the tracked frequencies, resulting in a new stable value. The difference in eigenfrequency between oil and water is ~ 60 kHz and caused primarily by the density variation. In contrast, the quality factor shifts by a value of ~ 4, mainly caused by the difference in viscosity.

Hydrodynamic models have been employed to determine the viscosity and mass density of the fluid surrounding a microcantilever [50, 125]. These relate the measured eigenfrequencies and quality factors to the fluid properties. A single-point calibration in water (mass density: 998 kg/m^3, viscosity: 1.0 mPa·s at 20°C), described in Ref. [50], is necessary to account for variations in the dimensions and mechanical properties of the microcantilevers. As shown in Fig. 6.8, the measured viscosity values coincide well with reference values, whereas the mass density shows rather large deviations. The eigenfrequency is strongly coupled to changes in mass density, in contrast, the viscosity mostly influences the quality factor [50]. Because the quality factor, i.e., viscosity, is determined by the relative position of the side-

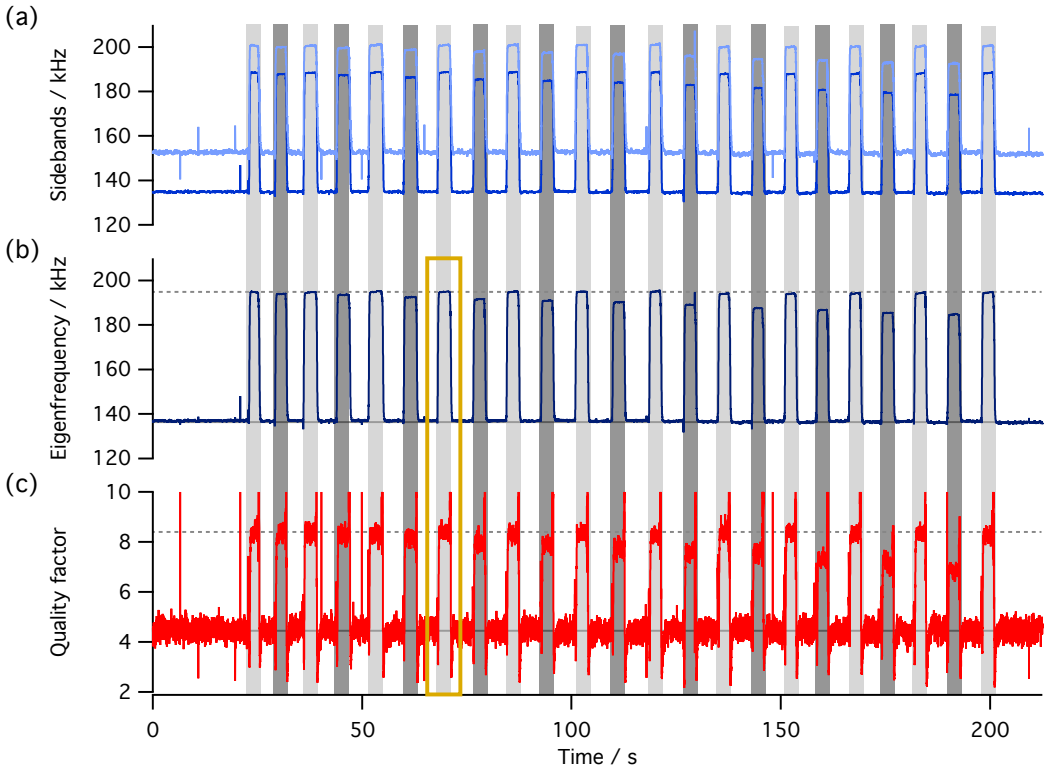

Figure 6.6: (a) Sideband frequencies, $f_{+\Delta\phi}$ and $f_{-\Delta\phi}$, and derived (b) eigenfrequency f_n and (c) quality factor Q_n (Eqs. 6.3a and 6.3b), obtained on the repeated sequential passage of oil, water droplets (light grey areas), oil, and aqueous sample droplets (dark grey areas) with increasing urea concentration; a droplet of water preceded each sample to ensure baseline stability (compare to dashed lines) and purge the fluid cell. The yellow box represents the region shown in Fig. 6.7.

bands, it is more robust to absolute errors in the measured sideband frequencies. In contrast the eigenfrequency is more prone to systematic errors, leading to deviating density values. This, however, does not constrain the quality of the viscosity measurements.

6.4 Conclusions

We present a method to characterize the viscosity and mass density of μL-droplets using resonant nanomechanical cantilevers. Separation of sample droplets in a two-phase configuration with fluorinated oil is crucial to avoid dispersion and can be applied to many sensing principles. The challenge to follow changes in the eigenfrequency and quality factor (damping) of the resonator with high time resolution was addressed by phase-locked loop frequency tracking two sidebands of a higher-mode resonance. The time resolution of the

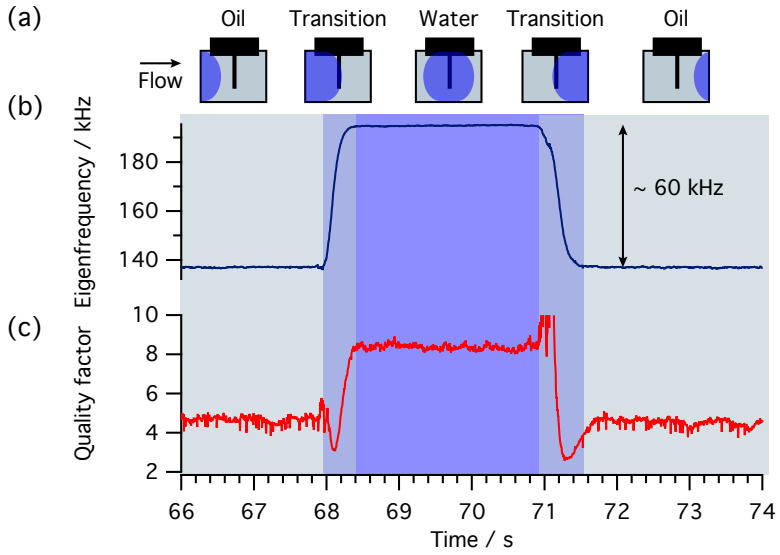

Figure 6.7: (a) Schematic representation of a droplet passage and the measured changes in (b) eigenfrequency and (c) quality factor. When the oil-water interface passes the micro-cantilever, the laser beams are scattered and the PI and PLL controllers adjust to the new values, resulting in a transition region of few 100 ms. Immersed in water, a new stable value is achieved, until the droplet is replaced by oil again. The scale of the quality factor in panel (c) is limited to 10, as higher values were only obtained in the transition region.

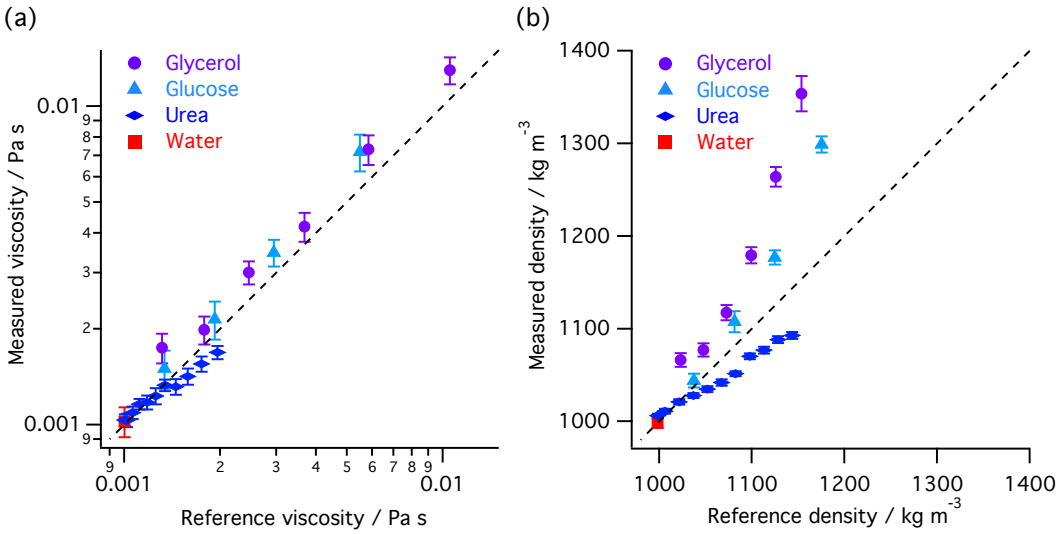

Figure 6.8: (a) Viscosities and (b) mass densities determined after a single-point calibration in water and compared to reference values.

detection system was of the order of milliseconds, whereas the throughput is around one second per sample droplet. The short interaction time between the sample and the sensor might further reduce unspecific adsorption of solutes to the microcantilever, which introduces spurious frequency shifts.

Acknowledgements

The authors acknowledge Henning Stahlberg (C-CINA, University of Basel) for providing facilities and financial support, Shirley A. Müller (C-CINA, University of Basel) for critically reading the manuscript, Hans Peter Lang and François Huber (Institute of Physics, University of Basel) for help with cantilever preparation and Stefan Arnold and Andrej Bieri (C-CINA, University of Basel) for fruitful discussions.

Chapter 7

Conclusions & Outlook

7.1 Conclusions

In this thesis, the influence of fluid surrounding a resonating microcantilever and its application for fluid characterization, i.e. viscosity and mass density sensing, were investigated. Thereby, higher modes of vibration (higher harmonics) were considered to access a broader frequency range and to increase the precision.
First, a suitable excitation and detection method to drive and read-out the resonators in liquid was identified and implemented; photothermal excitation, where an intensity modulated laser is used to periodically and locally heat the cantilever and, thus, induces mechanical vibration proved suitable. The advantage of this method is its direct energy transfer, therefore, only exciting the cantilever and not its surroundings, which would lead to spurious resonances. A modified optical beam deflection system, that allowed the incident laser beam to be perpendicular to the cantilever surface, was implemented for detection. It is less susceptible to refractive index changes in the probed liquid, than classical beam deflection systems, where the laser beam incidents inclined. The wavelengths of the used lasers were matched to the optical properties of the cantilever material. Laser induced heating and the cantilever excitation efficiency were calculated, measured and optimized, based on these findings. Main advantages of a fully optical excitation and detection system are the complete separation of the electronic setup from the fluidic system, simple and rapid sensor replacement and a good signal-to-noise ratio. Its major disadvantage is that samples need to be optically transparent, i.e., high transmission at the laser wavelengths of 405 nm and 780 nm is essential. Furthermore, a laser beam alignment is required prior to a measurement. Despite those drawbacks, optical detection of micro- and nanomechanical resonators remains the most abundant method, due to its accuracy and robustness. Especially in liquid, implementation of on-chip actuation and read-out principles on micrometer sized structures is difficult due to the electrical connections and their insulation.

In a next step, the dynamic behavior of microcantilevers in a confined liquid environment, e.g, a microfluidic channel, was measured. To this end, a solid surface was approached to the cantilever that was vibrating at several higher modes. Below a certain critical separation distance, the surface started influencing the frequencies and quality factors of the cantilever. The critical separation distance decreased for the frequencies, but increased for the quality factors with mode number. This somewhat surprising behavior is attributed to the more complex three-dimensional flow field generated by higher mode vibrations. Critical dimensions for a fluid cell were determined from the results and considered in the design.
Several applications for fluid characterization, i.e., viscosity and mass density measurements, were evaluated. Therefore, an approximation of the hydrodynamic load was developed, covering the accessed high-frequency regime. First, measurements on resonance spectra were performed to determine the properties of reference solutions with as little as 5 μL of sample. A viscosity and density range of 1–20 mPa·s and 1.0–1.2 g·mL^{-1}, respectively, was covered. To investigate the ability of the sensor to monitor time-resolved processes, free-radical polymerization reactions were characterized. The shear-thinning properties of the polymer solutions were detected by the sensor, however, at the expense of the mass density information. In future, simultaneously measuring several modes of vibration opens the possibility for rheological measurements over a broad frequency range.
Limitations of the sensing principle are the dynamic range for viscosity sensing and interference by unspecific adsorption of solutes to the cantilever. The dynamic range is mainly limited due to the strong viscous forces encountered with micrometer sized cantilevers, i.e., small Reynolds numbers. This causes the resonances to overdamp at moderate viscosities. This limitation can be addressed by increasing the cantilever dimensions, thereby entailing the trade-off of a higher sample consumption. Unspecific adsorption to the cantilever leads to spurious shifts in the dynamic properties that are misleadingly interpreted as changes in fluid properties. To reduce unspecific adsorption, the surface of the cantilever was passivated. Furthermore, monitoring the static deflection of the cantilever can be used as an indication for adsorption events. Whereas no such problems occurred for pure liquids, solutions of small molecular species and neutral polymers, unspecific adsorption proved challenging when working with charged molecules, such as many proteins.
Finally, a new detection method was employed, where a single cantilever resonance is tracked using two phase-locked loops (PLL), resulting in a very high time resolution of about 1 ms. To segment samples, fluorinated oil and a custom built automatic sampler were used, resulting in sample droplets of about 1 μL, total sample consumption of about 10 μL, and measurements times in the order of 1 s per sample. Besides the advantages of minute sample consumption and very short measurement times, this method might prove less susceptible to unspecific adsorption due to the short interaction times between the cantilever and the samples; few seconds compared to minutes at which adsorption kinetics usually occur.

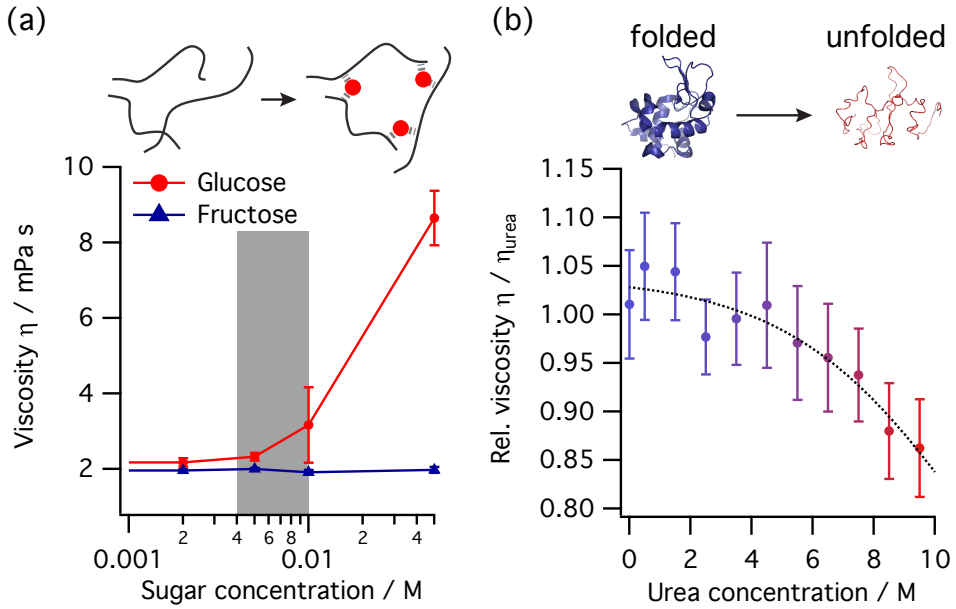

Figure 7.1: Changes in viscosity of (a) glucose-sensing polymers after adding glucose and fructose (pH = 10, at $\sim$ 170 kHz, the gray area indicates physiological blood glucose levels; graph courtesy Roger Krenger [207]) and (b) during denaturation of egg-white lysozyme (relative to the viscosity of urea, at $\sim$ 190 kHz; the dotted line is a guide to the eye; lysozyme structure: PDB 4QEQ).

7.2 Outlook

The developed microfluidic viscosity and mass density sensor opens a variety of applications. We recently started to perform proof-of-concept experiments to evaluate the ability of the sensor to monitor glucose levels and protein folding states. The glucose sensing is based on stimulus-responsive polymers and was performed using the method described in Chapter 5. Polyacrylamide was functionalized with glucose-binding groups that cross-link the polymer, leading to an increase in viscosity [207]. Figure 7.1a shows that the viscosity of the polymer strongly responds to glucose, whereas it is unaffected by fructose. Such response can be used to relate the viscosity of the solution to the surrounding glucose levels, making it an attractive alternative to electrochemical blood glucose sensors [208, 209].

To evaluate the performance of the sensor concerning biological samples, the droplet screening setup discussed in Chapter 6 was used to monitor the chemical denaturation of egg-white lysozyme. Urea causes the protein to unfold from a compact tertiary structure into a flexible random coil, inducing changes in viscosity [210]. Figure 7.1b shows the relative viscosity of 0.5 mM lysozyme with increasing urea concentration. A decrease in relative viscosity was observed, even though other micro-viscometric techniques reported an increase during

bovine serum albumin unfolding [92]. The difference might be due to the rheological properties of protein solutions [35], i.e., the viscosity depends on the measurement frequency ($\sim$ 190 kHz in the present case).

Many polymers and biological samples show rheological, i.e., non-Newtonian, behavior [34]. A rheological fluid not only has a viscosity but also a certain elasticity, referred to as loss and storage moduli, respectively [34]. It might be very interesting to account for and measure such effects in future. Recent fluid dynamic models allow to convert the resonance spectrum of the fundamental mode cantilever vibration into the rheological properties of the surrounding fluid. However, the mass density of the fluid needs to be known or determined by a complementary method [211]. To cover a broad frequency range, cantilevers of different dimensions can be employed [73]. Even though, such application is very promising, there is still a lack of theoretical models considering higher-mode vibrations in non-Newtonian fluids. Higher modes would allow to cover a broad frequency range, using a single cantilever. Such micro-rheological measurements could be used to characterize amyloid fibril formation [212] or hybridization of RNA and DNA [213].

Appendix A

Setup and instrumentation

Contents

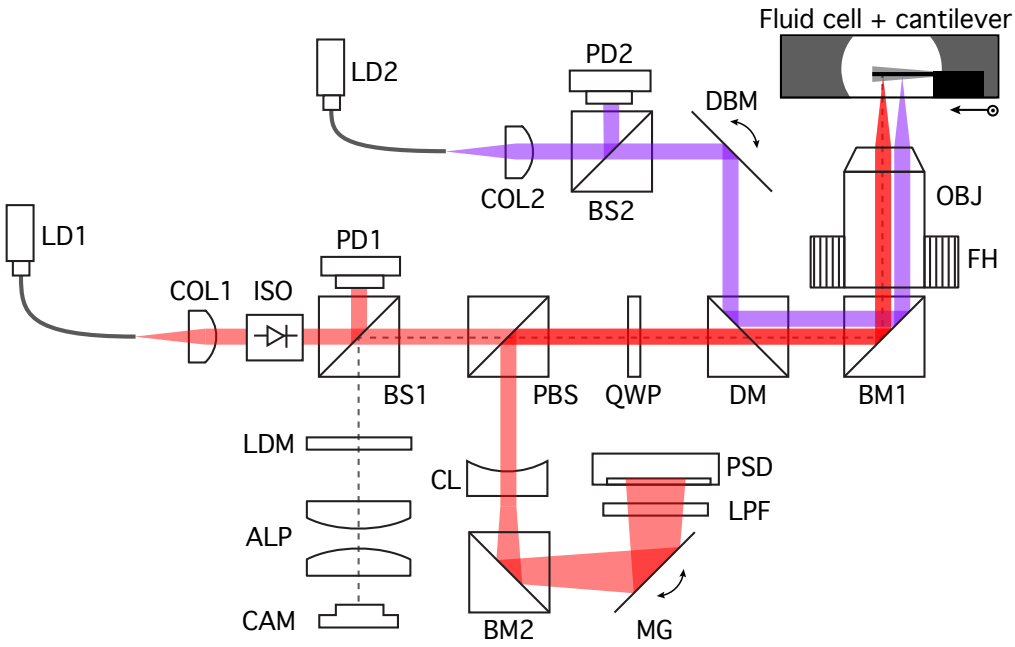

Figure A.1: Schematic diagram of the optical setup; the fluid channel containing the vibrating microcantilever is depicted in the top right corner and is mounted on a manual xy-stage. All parts are described in Table A.1.

A.1 Experimental setup

A.1.1 Overview

This sections aims to give a comprehensive description of the developed optical setup. Figure A.1 shows a complete schematic diagram. All used parts are listed in Table A.1. Briefly, resonances of a microcantilever were excited by photothermal excitation using an intensity-modulated 405 nm diode laser (LD2). The resulting vibration was detected by an optical beam deflection system formed by a 780 nm diode laser (LD1) and a position-sensitive detector (PSD). Optical access for a camera (CAM) is provided for visual inspection and simpler alignment of the laser spots on the cantilever. Both the PSD and CAM are equipped with optical filters (LPF and LDM) to block scattered light originating from the excitation laser (LD2). Figure A.2 shows a photograph of the basic optical setup used for the measurements in Chapter 3, 5 and 6. The modification of the sample stage for the squeeze-film damping measurements is shown in Figure A.3 (Chapter 4).

Table A.1: Optical parts shown in Figure A.1 (ARC: anti-reflective coating, S+K: Schäfter + Kirchhoff).

Acronym	Descripion	Properties	Supplier	Part Number
ALP	Achromatic lens pair	$f_1 = f_2 = 100$ mm	Thorlabs	MAP10100100-A
BM1	Broadband mirror	400 – 750 nm, $R > 0.99$ at 785 / 405 nm	Thorlabs	BB1-E02
BM2	Elliptical broadband mirror	750 – 1100 nm, $R = 0.998$ at 785 nm	Thorlabs	BBE1-E03
BS1	Pellicle beam-splitter	$R : T = 50 : 50$	Thorlabs	CM1-BP150
BS2	Beam-splitter	$R : T = 8 : 92$	Thorlabs	CM1-BP108
CAM	GigE CMOS camera	resolution 752×480, 67 fps	Allied Vision	GC750C
CL	Concave lens	$f = -50$ mm, ARC: 650-1050 nm	Thorlabs	LC1715-B
COL1	Fiber collimation package	FC/APC, $w_G = 2.64$ mm	Thorlabs	TC12APC-780
COL2	Fiber collimation package	FC/PC, $w_G = 2.12$ mm	Thorlabs	TC12FC-405
DBM	Dual-band mirror	$R > 0.99$ at 400 / 800 nm	Thorlabs	UFM10R
DM	Dichroic mirror	$T = 0.97$ at 785 nm, $R = 0.97$ at 405 nm	Thorlabs	DMLP567
FH	Focussing housing	0.5 mm per revolution	Thorlabs	SM1ZM
ISO	Optical isolator	760 – 800 nm, $T = 0.86$	Thorlabs	IO-3D-780-VLP
LD1	Fiber-coupled diode laser	$\lambda = 785$ nm, $P_{\text{max}} = 10$ mW, FC/APC	S + K	51nanoFCM
LD2	Fiber-coupled diode laser	$\lambda = 406$ nm, $P_{\text{max}} = 30$ mW, FC/PC	Thorlabs	LP406-SF20
LDM	Long-pass dichroic mirror	$\lambda_{\text{cut-off}} = 425$ nm	Thorlabs	DMLP425
LPF	Optical long-pass filter	$\lambda_{\text{cut-on}} = 750$ nm	Thorlabs	FEL0750
MG	Mirror galvanometer	500 nm – 2.0 μm, res. 14 μrad, BW = 1 kHz	Thorlabs	GSV011
OBJ	Objective	Mag. = 4x, N.A. = 0.10, WD = 18.5 mm	Thorlabs	RMS4X
PBS	Polarizing beam-splitter	ARC 620 – 1000 nm	Thorlabs	CM1-PBS252
PD1	Photodiode	BW = 2.4 MHz, $R = 0.48$ A/W at 780 nm	Thorlabs	PDA100A-EC
PD2	Photodiode	BW = 10 MHz, $R = 0.16$ A/W at 405 nm	Thorlabs	PDA36A -EC
PSD	Position-sensitive detector	$R = 0.63$ A/W at 940 nm, $C = 90$ pF	SiTek	2L10_SU7
QWP	Quarter-wave plate	ARC 400–800 nm	Thorlabs	AQWP05M-600

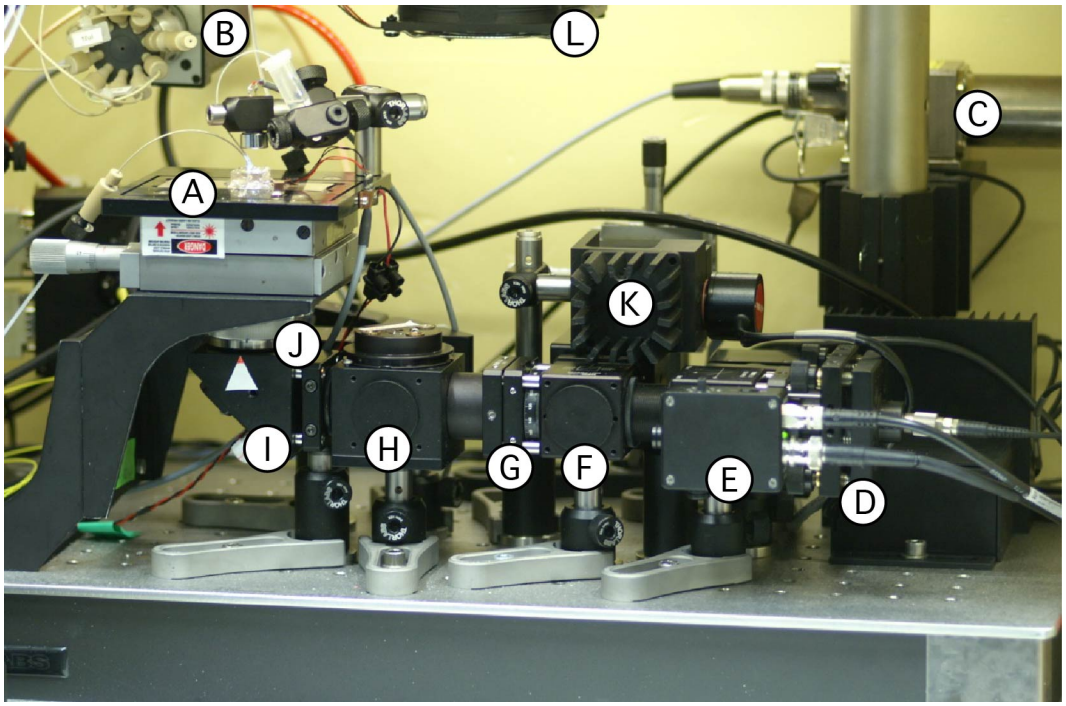

Figure A.2: Photograph of the basic experimental setup; the abbreviations refer to Figure A.1 and Table A.1. (A) Temperature controlled fluid cell stage, (B) 10-port valve equipped with two sample loops (10 μL and 50 μL), (C) fiber-coupled 780 nm diode laser (LD1) and (D) fiber-collimator (COL1) and optical isolator (ISO) for the detection laser, (E) detection laser monitoring photodiode (PD1), (F) polarizing beam-splitter (PBS), (G) lambda-quarter plate (QWP), (H) dichroic mirror (DM), (I) broadband mirror (BM1), (J) high-precision focusing housing (FH) accommodating the $4\times$ objective (OBJ) to focus the laser spots on the cantilever, and (K) mirror galvanometer (MG) covering the position-sensitive detector (PSD) in the back. The excitation diode laser and its alignment optics are concealed behind the dichroic mirror (H), broadband mirror (I) and sample stage (A). The fan of the enclosure temperature control system is visible at the top (L).

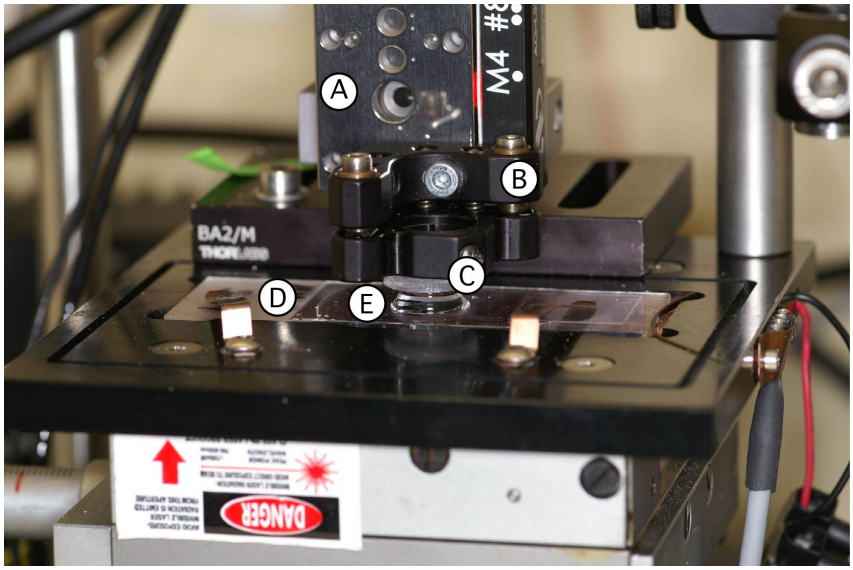

Figure A.3: Photograph of the experimental setup used for the squeeze-film damping measurements. (A) Encoded linear piezo motor (CONEX-AG-LS25-27P, Newport), (B) kinematic mirror mount (KM05/M, Thorlabs) to adjust the angular alignment of the (C) upper PDMS surface, (D) glass slide with a PDMS sheet with a circular hole in the middle to accommodate the cantilever chip, and (E) liquid confined between the glass slide and upper PDMS surface.

A.1.2 Laser spot size measurement and focussing

The spot size of the lasers on the cantilever is an important figure, especially when working with higher modes of vibration where the beam wavelength becomes comparable to the spot diameter. To focus the lasers and measure the minimal spot sizes a modified knife-edge method was used [160]. The intensity profile of a laser beam can be approximated by a 2-dimensional Gaussian shape

$$I(x,y) = I_0 \exp\left(-\frac{(x-x_0)^2+(y-y_0)^2}{w_G^2}\right). \tag{A.1}$$

w_G is the radius of the Gaussian beam, where the intensity is decreased by $1/e$, (x_0, y_0) the spot position, I_0 the peak intensity and (x, y) the coordinates in the plane perpendicular to the direction of propagation. If a sharp edge is gradually introduced into the beam path, light is successively blocked. For small spot sizes the edge of a microcantilever can be used [214]. In contrast to the classical knife-edge method where the beam is blocked by a sharp edge, the cantilever inserted in the beam reflects a certain portion of the light back onto the position-sensitive detector. The resulting intensity pattern as a function of cantilever edge position is equal to the convolution of a step function with the Gaussian beam profile (see Figure A.4).

$$P(x) = \frac{1}{2}\left(1 + \mathrm{erf}\left(\frac{x-x_0}{w_G}\right)\right), \tag{A.2}$$

with erf being the error function. By fitting this equation to the measured intensity data, recorded at different positions x, the Gaussian beam radius w_G can be determined. The method allows to determine the laser spot size using a LabVIEW script without modifying the setup. To focus the laser spots, the distance z between the objective and the cantilever was varied while recording the beam radius. The beam radius around the focal point is described by [215]

$$w_G(z) = w_{G,0}\left(1 + \frac{(z-z_0)\lambda M^2}{2\pi w_G^2}\right)^{\frac{1}{2}}, \tag{A.3}$$

where $w_{G,0}$ is the spot radius in focus, λ the laser wavelength, z_0 the offset of the focus and M^2 a factor considering deviation from an ideal Gaussian beam. Figure A.5 shows a fit of $w_G(z)$ to the data (λ = 780 nm) resulting in the following parameters: $w_{G,0}$ = 12.4 μm, z_0 = 220 μm, and M^2 = 4.0. To focus the detection laser beam, the distance z was set to z_0. In addition, the spot size of the excitation laser was measured in focus and was 28.6 μm. The focussing procedure was only repeated when a new cantilever chip type of different thickness was used.

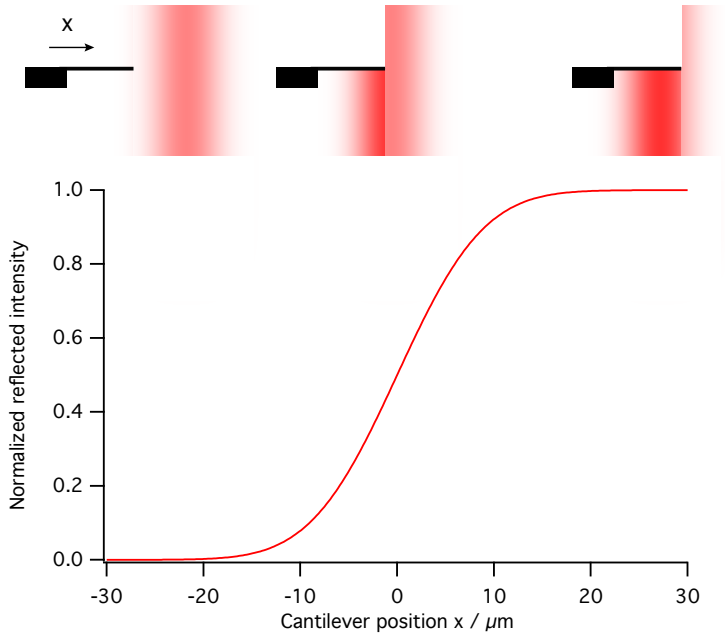

Figure A.4: Knife-edge method to determined the laser spot size, using the intensity of the light reflected back from the cantilever. A smaller the spot results in a steeper slope of the profile. The intensity profile represents a laser spot with $w_G = 10$ μm. The beam diameter in the top panel is largely exaggerated.

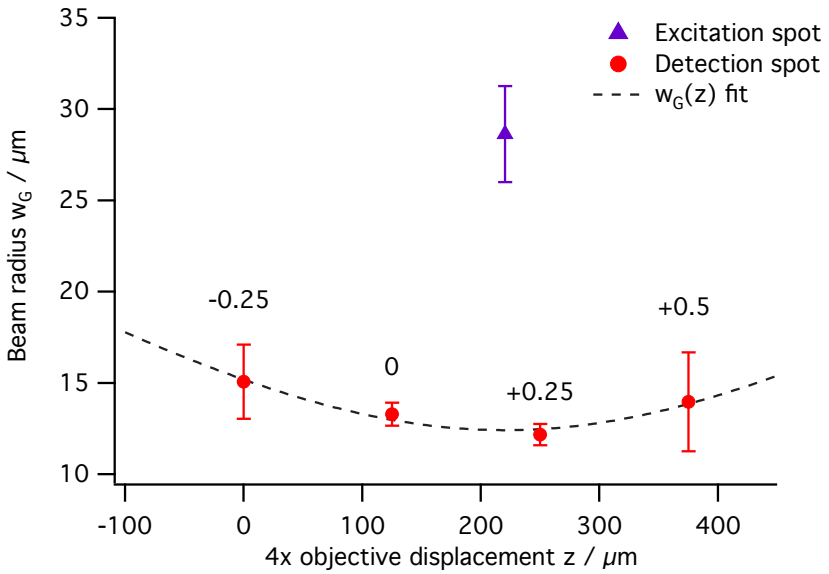

Figure A.5: Gaussian beam radius of the detection and excitation laser. The numbers above the values indicate the number of revolutions on the focussing housing (FH).

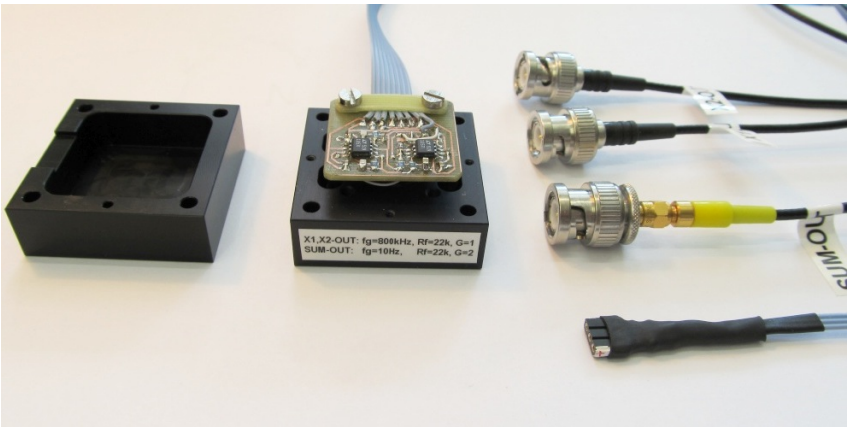

Figure A.6: Photograph of the disassembled PSD. The two dual high-speed JFET op amps (LT1057) are visible on the printed circuit board (image courtesy Andreas Tonin).

A.1.3 Position-sensitive detector (PSD)

PSD electronics

The electronic board to read-out the SiTek 2L10 high linearity position-sensitive detector (PSD, 2L10_SU7) was developed by the electronics workshop at the Institute of Physics. It is optimized for a large measurement bandwidth. Figure A.6 shows the disassembled casing with the detector facing downwards. The connections are (starting at the back): channel X2 (black BNC), channel X1 (black BNC), the SUM signal (yellow BNC), and the $\pm$15 V power supply (three-pin plug, white: +15 V, middle; COM, floating if ground is provided through BNC connectors; opposite white: -15 V). To assess the measurement bandwidth, the PSD electronics were simulated using LTspice (Linear Technology simulation program with integrated circuit emphasis). The circuit diagram is shown in Figure A.7, the photocurrent is represented by an AC current source (100 μA). The capacitance of the PSD is represented by C1 (90 pF) and is the bandwidth-limiting factor [216]. The transimpedance amplifier (current to voltage converter, I/V-converter) LT1057S is equipped with feedback resistor R2 (22 kΩ) and feedback capacitor C2 (6.8 pF). The downstream differential amplifier with nominal bandwidth of 1 MHz (SIM910/SIM911, Stanford Research Systems) is represented by C3, R1 and C4. To benchmark the simulated behavior of the electronics, the gain of the PSD was measured. Therefore, a red light-emitting diode (LED) was intensity modulated at certain frequencies and the resulting amplitudes of channel X1 and X2 were displayed on an oscilloscope. The measured and simulated -3 dB point bandwidths were 755 kHz and 798 kHz, respectively. As shown in Figure A.8, the simulated gain describes the bandwidth very well, however, it overestimates the amplifier overshoot.

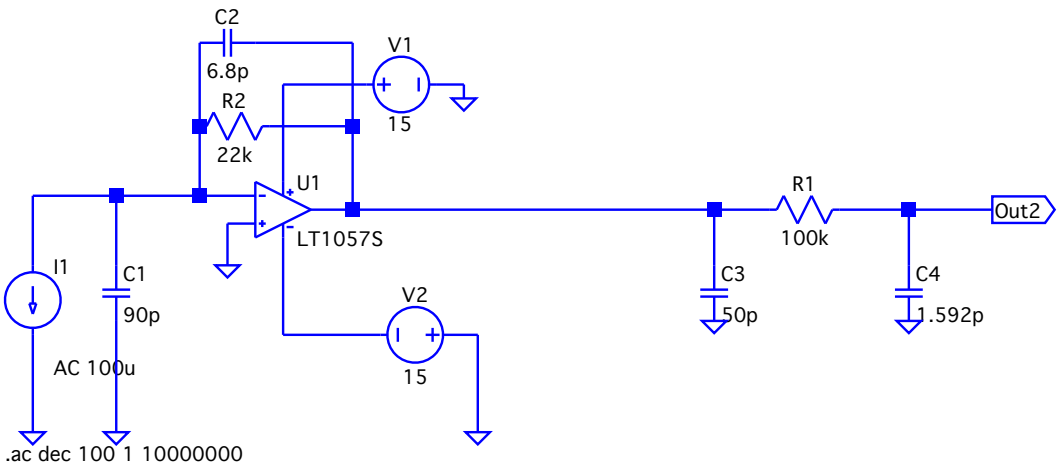

Figure A.7: Minimum circuit representation of the PSD electronics for the LTspice simulation.

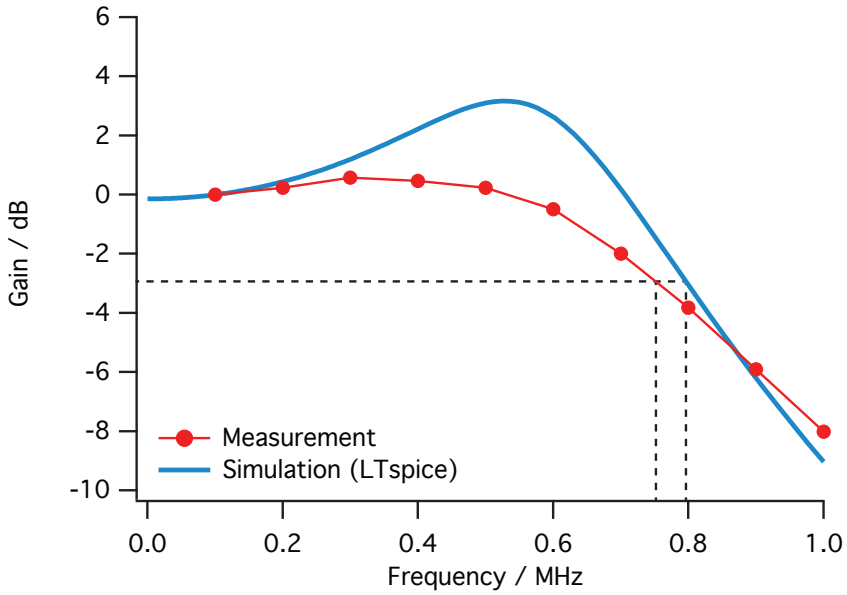

Figure A.8: Bandwidth of the position-sensitive detector.

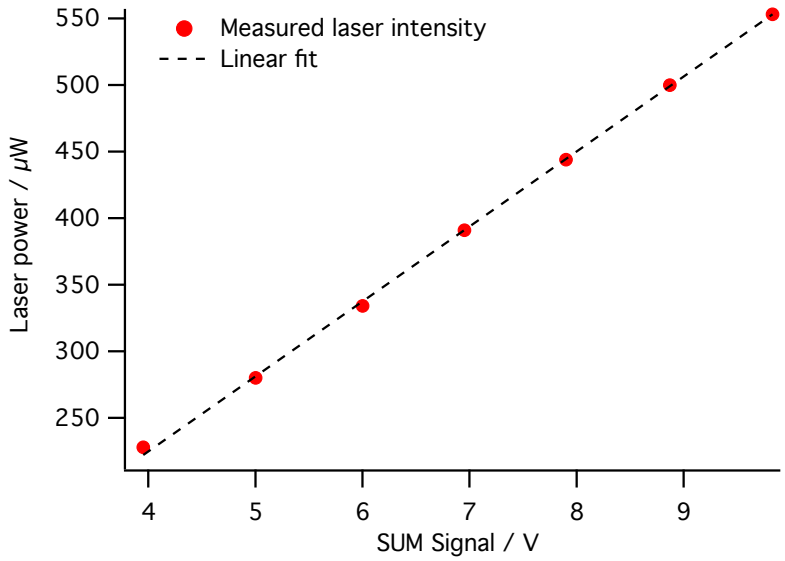

Figure A.9: PSD Intensity calibration.

PSD intensity and response calibration

The absolute intensity on the PSD is represented by the SUM signal, which is generated by summing, amplifying ($2\times$) and low-pass filtering (10 Hz) channel X1 and X2 on the PCB. For calibration, the intensity on the PSD was compared to the one measured using an optical power meter (PM100D equipped with photodiode power sensor S120C, Thorlabs). Figure A.9 shows the calibration curve with an excellent linear behavior (Pearson's r = 0.9997): $P = 55.9\mu\text{W/V} \times SUM$, where the sum signal SUM is in V and the corresponding laser power P in μW. Next, the response of the PSD was measured by displacing the laser spot on the PSD by defined intervals and monitoring the $10\times$ amplified DC differential signal (SIM911, Stanford Research Systems). Because the generated photocurrent depends on the incident light intensity, the procedure was repeated for different laser powers (Figure A.10, left panel). The responsivity of the PSD can then be expressed as a function of SUM in V (Figure A.10, right panel): $S_{\text{PSD}} = -23.6\,\text{V/m} + 968\,\text{m}^{-1} \times SUM$ (Pearson's r = 0.9988). At common SUM signals of $\sim$ 7 V, the responsivity is 6.75 mV/μm.

A.1.4 Radio-frequency modulation of the detection laser

The intrinsic noise sources of laser diodes are quantum noise and mode hopping [217]. Quantum noise only becomes significant when the laser diode is operated close to its threshold current and mode hopping is eliminated by a constant current control and stable temperature. In an optical beam deflection arrangement further noise sources need to be considered. Light reflected back into the laser resonator causes "optical feedback noise" [217].

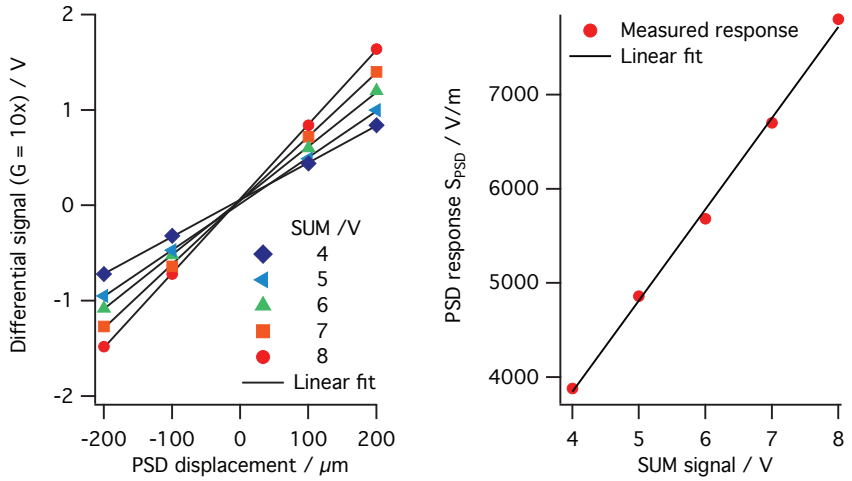

Figure A.10: PSD differential signal and responsivity at different laser powers (after 10× amplification using a SIM910/SIM911, SRS).

To avoid this, the detection laser was equipped with an optical isolator (ISO in Figure A.1), blocking reflected light. Furthermore, incident laser light interfering with the beam reflected from the cantilever can cause large fluctuations in the intensity, referred to as "optical interference noise" [217]. The magnitude of this effect is increased in the developed setup, because incident and reflected laser beams overlap, due to the fact that the incident angle is normal to the cantilever surface. To suppress optical interference noise, the coherence length of the laser diode was shortened by radio-frequency (RF) modulation of the laser intensity [217]. This furthermore avoids mode hopping even at fluctuating temperature.
To evaluate the RF modulation a test circuit shown in Figure A.11 was developed. The voltage controlled oscillator (VCO, ZX95-310-A+, Mini-Circuits) was supplied and tuned using two LM317 variable voltage regulators. The frequency was adjusted to roughly 300 MHz, using the tune voltage. An LDM9T/M (Thorlabs) laser diode mount with integrated temperature control was employed. An internal bias-T, schematically represented by L1 and C5, allowed to RF-modulate the DC laser current supplied by a LDC202C (Thorlabs) current controller. Figure A.12 shows transient intensity spikes when the RF-modulation was switched off. However, switching it on resulted in a stable intensity output. This finding led to the installation of 51nanoFCM diode laser (51nanoFCM-785-10-H06-P-5-2-28-0-150, Schäfter+Kirchhoff) with an integrated 300 MHz RF-modulation. For stable operation a linear power supply was used (PSL05, Schäfter+Kirchhoff).

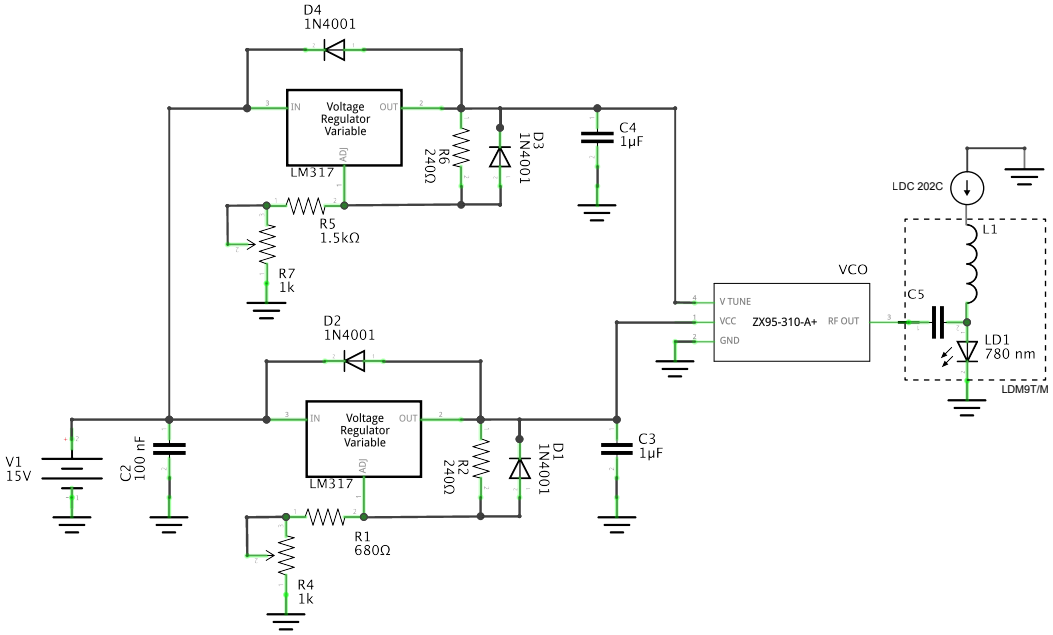

Figure A.11: Test circuit for radio-frequency modulation of the detection laser.

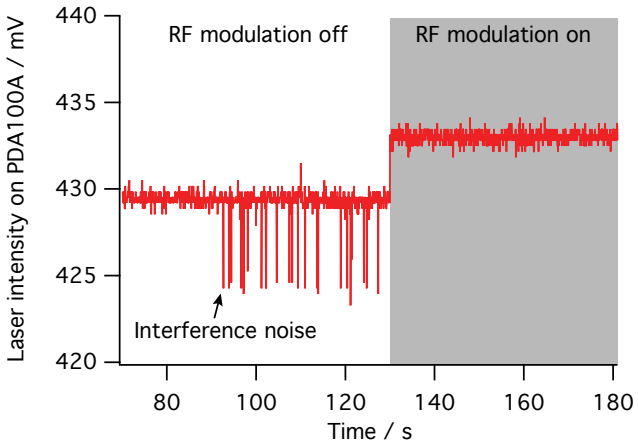

Figure A.12: Suppression of optical interference noise by radio-frequency (RF) modulation of the detection laser intensity.

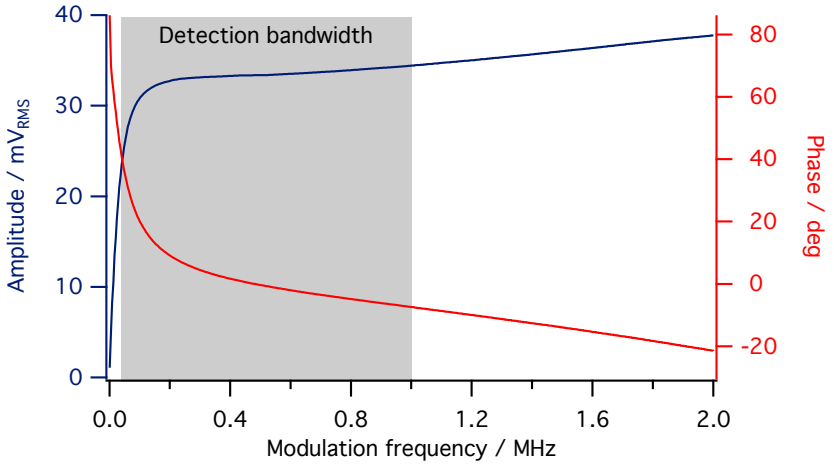

Figure A.13: Excitation laser intensity amplitude and phase response. The bandwidth of the optical beam deflection detection system is indicated.

A.1.5 Excitation laser response

While modulating the excitation laser (see LD2 in Figure A.1) intensity through the bias-T integrated in the diode mount (TCLDM9), the dynamic response was recorded on the monitoring photodiode (see PD2 in Figure A.1, PDA36A, Thorlabs). The diode was operated in constant current mode ($I = 40$ mA) using a laser diode controller (LDC201CU, Thorlabs) and temperature stabilized by thermoelectric element (using a TED200C controller, Thorlabs). Figure A.13 shows the amplitude and phase response of the laser diode. The sharp decrease in amplitude and phase shift below 100 kHz is due to the cut-off frequency of the bias-T. However, in the detection bandwidth of the optical beam deflection system the signal is sufficiently constant.

A.1.6 Estimation of the amplitudes of vibration

Equation 3.1 in (Chapter 3) is used to geometrically relate the deflection of the cantilever Δz to the laser spot displacement on the PSD ΔD:

$$\Delta z = \frac{L}{4}\frac{S_{\text{opt}}}{S_n}\Delta D. \tag{A.4}$$

The "optical lever sensitivity", S_{opt}, is calculated using geometrical optics:

$$S_{\text{opt}} = \frac{|f_2|}{n_{H_2O}\left(\frac{d_{H_2O}}{n_{H_2O}} + \frac{d_{\text{glass}}}{n_{\text{glass}}} + \frac{d_{\text{air}}}{n_{\text{air}}}\right)(|f_2| + d_{\text{PSD}})}. \tag{A.5}$$

Table A.2: Parameters to estimate the amplitude of vibration.

Parameter	IBM (chapter 3)	MikroMasch
Cantilever length L	500 μm	250, 300, 350 μm
d_{H_2O} (chip thickness)	0.5 mm	0.3 mm
d_{glass} (glass slide thickness)	1 mm	1 mm
d_{air} (glass – objective)	43.5 mm	43.7 mm
d_{PSD} (concave lens – PSD)	95 mm	160 mm
S_{opt} (optical lever sens.)	5.821	4.015
S_n (normalized mode sens.)	mode dependent, see text ($S_n = 1$ for $n = 1$)	
G_{el} (amplifier gain)	10	1
S_{PSD} (PSD responsivity)	$S_{PSD} \approx 968 V_{SUM}$	
$\Delta z/\Delta V$ ($V_{SUM} = 7$ V, $n = 1$)	107 nm/V	370, 444, 518 nm/V

Constant parameters are the focal length of the concave lens, $f_2 = -50$ mm and refractive indices, $n_{H_2O} = 1.33$, $n_{glass} = 1.50$, $n_{air} = 1.00$. The length d_{air} depends on the effective focal length of the 4× objective $d_{obj} = 45$ mm (RMS4X, Thorlabs) and the thickness of the glass slide d_{glass} and cantilever chip d_{H_2O}: $d_{air} \approx d_{obj} - (d_{glass} + d_{H_2O})$.
The "normalized mode sensitivity", S_n, was omitted in Equation 3.1, because $S_n = 1$ for static deflections. However, when considering higher mode vibrations it has to be included due to the higher angular tip deflection, $S_n = \frac{d\Phi_n/dx}{d\Phi_1/dx}$. For the first eight modes it is equal to $S_{n=1} = 1.000$, $S_{n=2} = 3.473$, $S_{n=3} = 5.702$, $S_{n=4} = 7.988$, $S_{n=5} = 10.27$, $S_{n=6} = 12.55$, $S_{n=7} = 14.83$, and $S_{n=8} = 17.12$.
To relate the actual measured voltage ΔV, either a DC voltage for static deflection or an AC voltage for cantilever vibration, the sensitivity of the PSD, S_{PSD}, and the gain of the downstream electronics, G_{el}, need to be considered.

$$\Delta D = \frac{10}{G_{el}} \frac{\Delta V}{S_{PSD}}. \tag{A.6}$$

The gain of the amplifier G_{el} either was $10\times$ when using the SRS SIM911 or $1\times$ if directly wired to the Zurich Instruments HF2 lock-in amplifier. The responsivity of the PSD depends on the incident intensity measured as sum signal V_{SUM}: $S_{PSD} \approx 968 V_{SUM}$. Combining the above equations allows to relate the measured voltage ΔV to the cantilever deflection Δz:

$$\Delta z = 2.5 L \frac{S_{opt}}{S_n} \frac{\Delta V}{G_{el} S_{PSD}}. \tag{A.7}$$

Table A.2 provides all parameters required to calculate the cantilever displacement. For the MikroMasch levers, where the measured AC voltages are on the order of $\Delta V_{rms} \sim 1$ mV in water, the amplitudes of vibration are $\Delta z \sim 0.1$ nm.

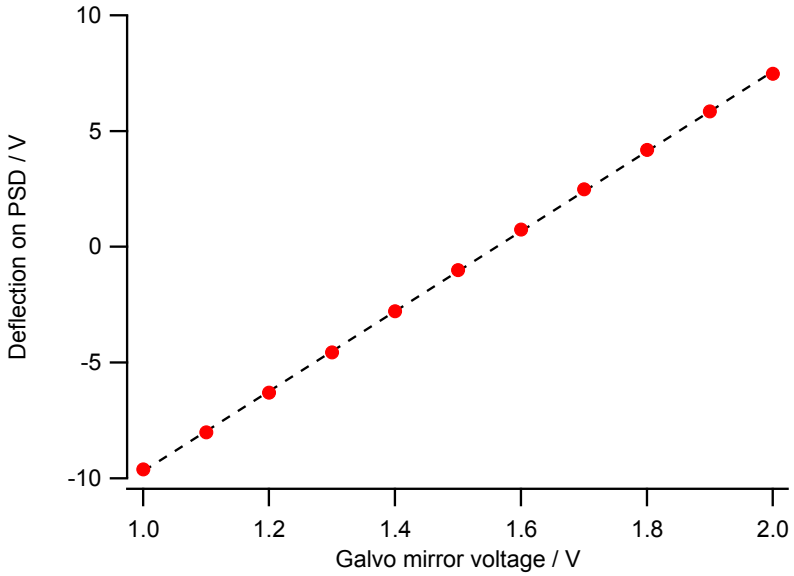

Figure A.14: Galvanic mirror response at different control voltages.

A.1.7 Mirror galvanometer calibration

The galvanic mirror (GSV011, Thorlabs), used to center the laser spot on the PSD, was characterized by reading the 10× amplified deflection signal after applying a certain voltage to the coil controlling the mirror position. The response was 17.27 $V_{deflection}/V_{coil}$ and showed a good linearity over the whole range of the PSD (Pearson's $r = 0.9999$, see Figure A.14).

A.1.8 Temperature control

Enclosure temperature control

An air-to-air thermoelectric assembly (AA-040-12-22, Laird Technologies) with a Peltier current controller (TC3212-RS232, CoolTronic) was used to stabilize the setup enclosure. The temperature to be controlled was measured with a 3-wire Pt1000 at the air intake of the inside cooling fins of the thermoelectric assembly (Temperatur-Istwert). A fan is continuously circulating air inside the enclosure. To stabilize the temperature to 20°C (Temperatur-Sollwert1), the Peltier current is controlled by a PID feedback loop. All parameters can be reconfigured using the RS232 interface on the controller. Figure A.15 shows the parameters, which resulted in an appropriate temperature stability. The outer cooling fins are temperature monitored using a second 3-wire Pt1000 (Temperatur Sensor 3) and a fan is activated above 25°C (Maximal-Temperatur) and below 15°C (Minimal-Temperatur). The controller output stage is inactivated if the outer cooling fin temperature exceeds 60°C (Temperatur-Grentzwert3).

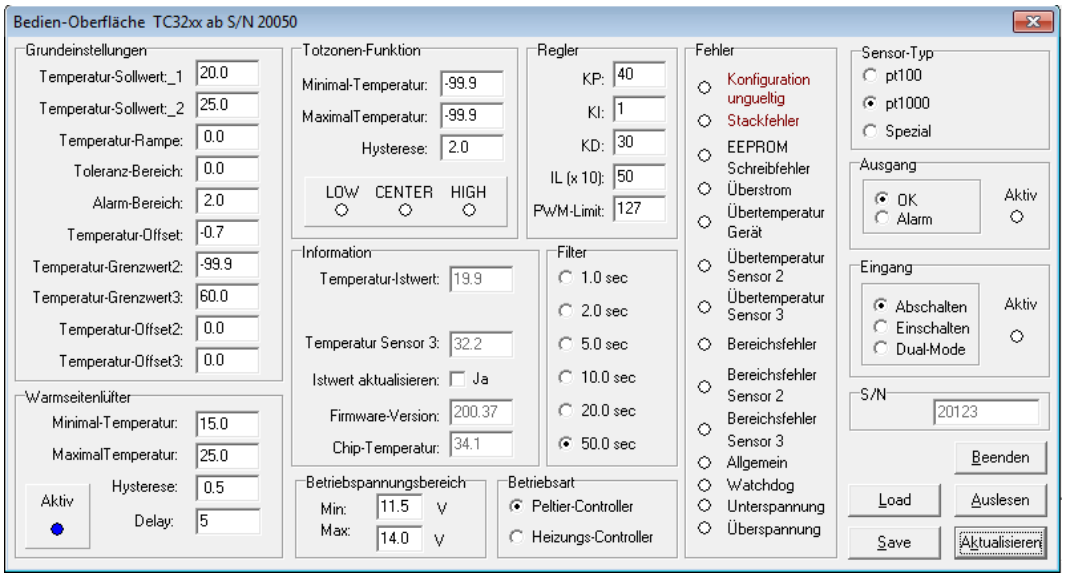

Figure A.15: Enclosure temperature control settings (TC3212-RS232).

Fluid cell temperature control

A 4-wire Pt1000 resistance thermometer connected to a high-precision analog measurement transducer LKM214 (linearity error <0.1% full scale) was used to measure the fluid cell temperature. The LKM214 was customized to a range from 0°C – 40°C, resulting in an output from 0 V – 10 V. The Pt1000 was inserted into a cavity in the PDMS fluid cell which fastens it on the glass slide, close to the fluid channel. Two Peltier elements (CP08,63,06, Laird Technology) were clamped between two copper plates to ensure good thermal contact; one in contact with the glass slide, the other one with the underlying holder serving as a heat sink (see Figure A.16). To thermally insulate the copper plates they are held in place by a polyoxymethylene (POM) frame. The Peltier current was controlled by a software PID controller implemented in LabVIEW. The PID parameters were determined using the LabVIEW PID auto-tune function based on the Ziegler-Nichols method [218] followed by manual optimization: proportional gain K_c = 0.500, integral time T_i = 2.700 min and derivative time T_d = 0.001 min. The output signal of the PID controller was amplified (6827A, Hewlett-Packard) and the resulting current (± 0.6 A) applied to the Peltier elements. The glass slide in between the copper plate and the Pt1000 sensor has a large thermal inertia, resulting in a slow feedback (see Figure A.17). Nevertheless a very good precision of ± 0.01°C was obtained.

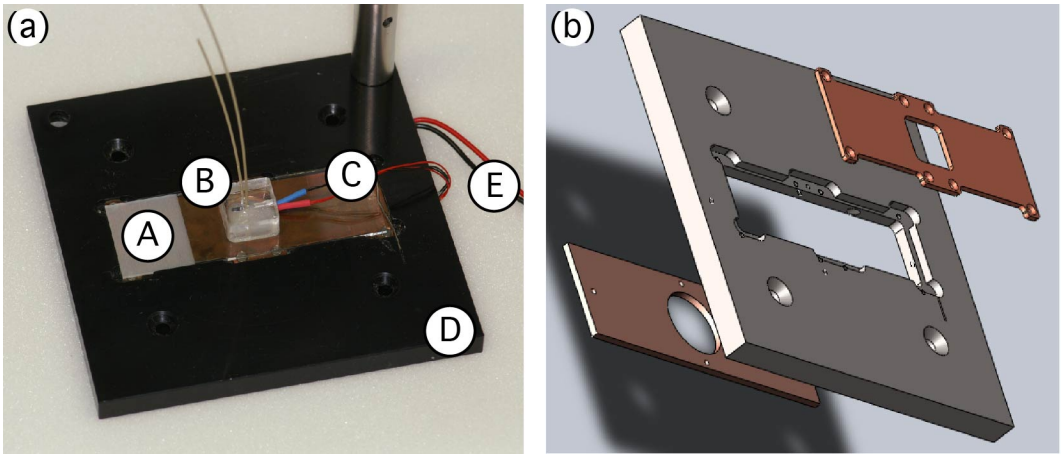

Figure A.16: (a) Photograph of the sample stage. (A) Glass slide with the bonded (B) PDSM fluid cell. The upper copper plate is visible underneath the glass. (C) 4-wire Pt1000 temperature sensor, (D) polyoxymethylene (POM) frame, (E) electrical connections to the Peltier elements between the copper plates.(b) Exploded view of the CAD sample stage drawing.

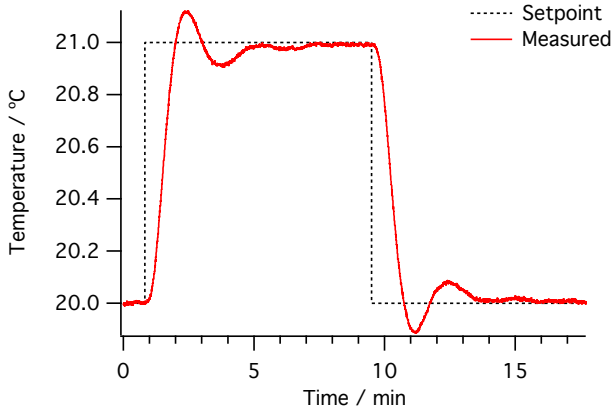

Figure A.17: Measured response of the PID control loop to stabilize the fluid cell temperature.

A.2 Cantilever preparation

The protocol to clean the cantilevers and passivate them with short ethylene glycol chains is described below.

A.2.1 Cleaning

- Prepare piranha solution (ATTENTION: highly corrosive and oxidizing): 3 mL 30% H_2O_2 (hydrogen peroxide) + 3 mL H_2SO_4 96% (sulfuric acid)
- Immerse cantilever chips for 30 min in piranha solution
- 4× H_2O rinse
- 1× isopropanol rinse
- Dry on dust-free tissue

A.2.2 Silicon passivation

Oligo(ethylene glycol)-silane (OEG)

2-[Methoxy(polyethyleneoxy)propyl]trimethoxysilane, 90%, 6-9 PE-units
$(C_2H_4O)_nC_7H_{18}O_4Si$, n = 6 – 9
ABCR, AB111226 (CAS 65994-07-02)
Density 1.076 g/mL
MW 458.61 g/mol – 590.77 g/mol, average 524.69 g/mol

Passivation in 5 mM OEG-silane in toluene (water-free)

- Prepare 50 mM OEG-silane stock solution: 50 μL 2 M silane in 2 mL toluene (both water-free, under Ar)
- Place 200 μL 50 mM OEG silane in 1.8 mL toluene (final concentration: 5 mM) in a teflon container
- Incubate cantilever chips for 1 h at room temperature

Passivation in 10 mM OEG-silane in ethanol (obsolete method)

- Prepare 10 μL OEG-thiol in 2 mL ethanol in a teflon container
- Incubate cantilever chips for 30 min at room temperature

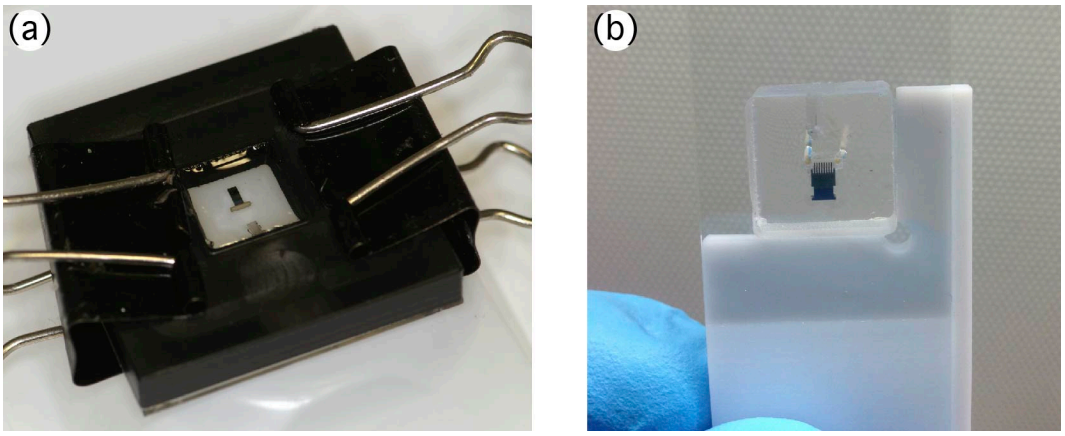

Figure A.18: (a) Molding the fluid cell: The black polyoxymethylene (POM) frame retains the liquid PDMS on the mold during curing. In the center, the chip and tubing forming the chip cavity and fluid channel, respectively, are visible. (b) Freshly bonded fluid cell, the white alignment tool is subsequently removed.

A.2.3 Gold passivation

Oligo(ethylene glycol)-thiol (OEG)

(11-mercaptoundecyl)tetra(ethylene glycol)
$C_{19}H_{40}O_5S$
Asemblon 674508-250MG 04221CJ
Density 0.997 g/mL
MW 380.58 g/mol
200 mM OEG-thiol stock solution: 250 mg OEG-thiol in 3.3 mL ethanol

Passivation in 1 mM OEG-thiol in ethanol

- Prepare 10 mM OEG-thiol solution: Dissolve 50 μL of 200 mM OEG-thiol in 0.95 mL ethanol
- Place 15 μL 10 mM OEG-thiol and 135 μL ethanol in an Eppendorf cap (fits two cantilever chips)
- Incubate the cantilever chips for 15 min at room temperature

A.3 PDMS fluid cell fabrication

The following section provides the protocol to fabricate the PDMS fluid cell and bond it to a glass slide (see Figure A.18).

A.3.1 Materials and preparation

- Polydimethylsiloxane (PDMS): SYLGARD 184 Silicone Elastomer, Dow Corning
- Biopsy stamp: Harris Uni-Core I.D. 0.5mm, Z708771-25EA, Sigma-Aldrich
- Nanopure water
- Isopropanol (2-propanol)
- Razor blade
- Scotch tape
- Dust-free tissues
- Clean gas/air supply for drying
- Glass slides (Menzel-Gläser microscope slides, cut edges, 76×26 mm, AA00000112E, Thermo Scientific):
  - Rinse with water
  - Rinse with isopropanol
  - Wipe with dust-free tissue
  - Rinse isopropanol
  - Dry under gas flow
- Mold: MikroMasch chip (w/o cantilevers) + 1/32" PEEK tubing or IBM chip (w/o cantilevers) + 1 mm glass rod as a negative for the fluid channel and chip cavity (see Figure A.18a, center):
  - Remove PDMS deposits with razor blade
  - Rinse with water
  - Rinse with isopropanol
  - Dry under gas flow

A.3.2 Fluid cell molding

- Molding:
  - Mix base/curing agent 10/1 (e.g. 5 g base and 0.5 g curing agent)
  - Properly mix until milky (air bubbles)
  - Degas (house vacuum 30 min or until bubbles disappear)
  - Pour onto mold
  - Bake at 60°C over night (at least 4 hours)

  - Remove mold

- Tubing connections:
  - Punch tubing connection with biopsy stamp from below (from inside to outside)
  - Insert two 1/32" PEEK tubings (length $\approx$ 10 cm)

- Clean lower face of the PDMS (face which is bonded):
  - Strip with scotch tape
  - Rinse with isopropanol
  - Dry under gas flow

A.3.3 Fluid cell bonding

O_2-Plasma cleaner (30 W, PDC-002, Harrick Plasma)

- Toggle switch main power and pump OFF
- Check if oxygen bottle is open and gas selector valve on oxygen
- Load sample (PDMS and glass slide with face to activate up) in vacuum chamber
- Close the door and vent valve
- Toggle pump switch ON
- Wait 2 min
- Toggle main power switch ON
- Wait for plasma to ignite (10 – 20 s)
- 30 sec plasma treatment
- Toggle main power switch OFF
- Slowly open the venting valve partially
- Toggle pump switch OFF
- Completely open the venting valve
- Open the vacuum chamber door
- Unload samples
- Mount cantilever chip in the cavity
- Place PDMS on glass slide, starting from one edge using the alignment tool
- Optional: Bake on heat plate or oven at 60°C, 0.5 – 1 h

A.4 Control and analysis software

The software to control the instrument was developed using LabVIEW (National Instruments) and the scripts used for data analysis were written in IGOR Pro (Wavemetrics).

A.4.1 Instrument control software

The first version (V.1) of the instrument control developed in LabVIEW (Figures A.19 and A.20) was programmed to continuously load resonance spectra of multiple modes of vibration from an Anritsu MS4630B vector network analyzer. A data analysis routine fitted the resonance peak with a driven damped harmonic oscillator model to track the eigenfrequencies and quality factors of multiple resonances in real-time (see Figure A.19). The second panel is used to monitor the laser intensity, control the temperature, the syringe pump and the 10-port valve and to write the monitored values into a log-file (see Figure A.20). The second version (V.2) of the software (Figure A.21) is able to control a Zurich Instruments HF2 lock-in amplifier. The GUI to control the measurement parameters was arranged in a more compact manner.

A.4.2 Analysis software

The data analysis scripts written in IGOR Pro can be accessed by a GUI menu (Figure A.22). It provides tools for analyzing spectral data (Chapter 5), squeeze-film damping data (Chapter 4), and dual phase-locked loop data (Chapter 6). The software allows to store key parameters as the cantilever and calibration fluid properties (Figure A.23).

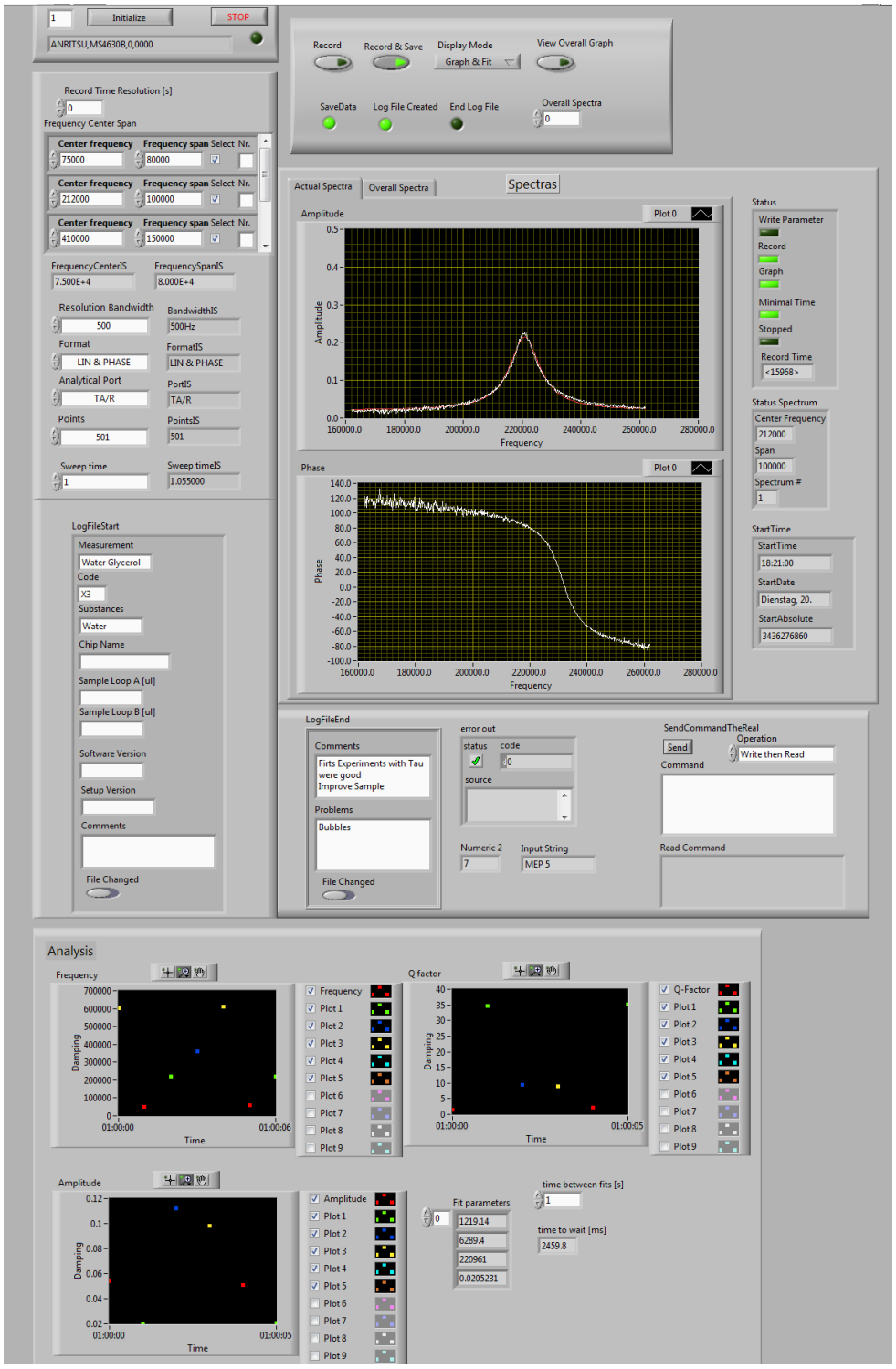

Figure A.19: LabVIEW instrument control software V.1, panel A: Anritsu MS4630B vector network analyzer control (top); real-time analysis (bottom).

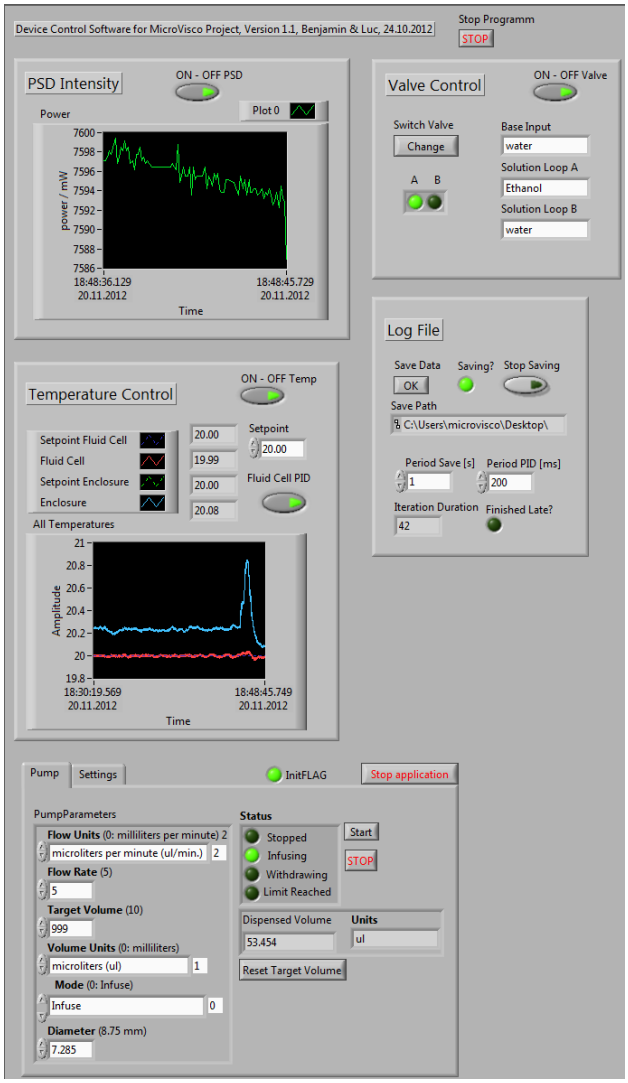

Figure A.20: LabVIEW instrument control software V.1, panel B (from top left, clockwise): Laser intensity monitor; 10-port valve control; parameter logging; syringe pump control; temperature control.

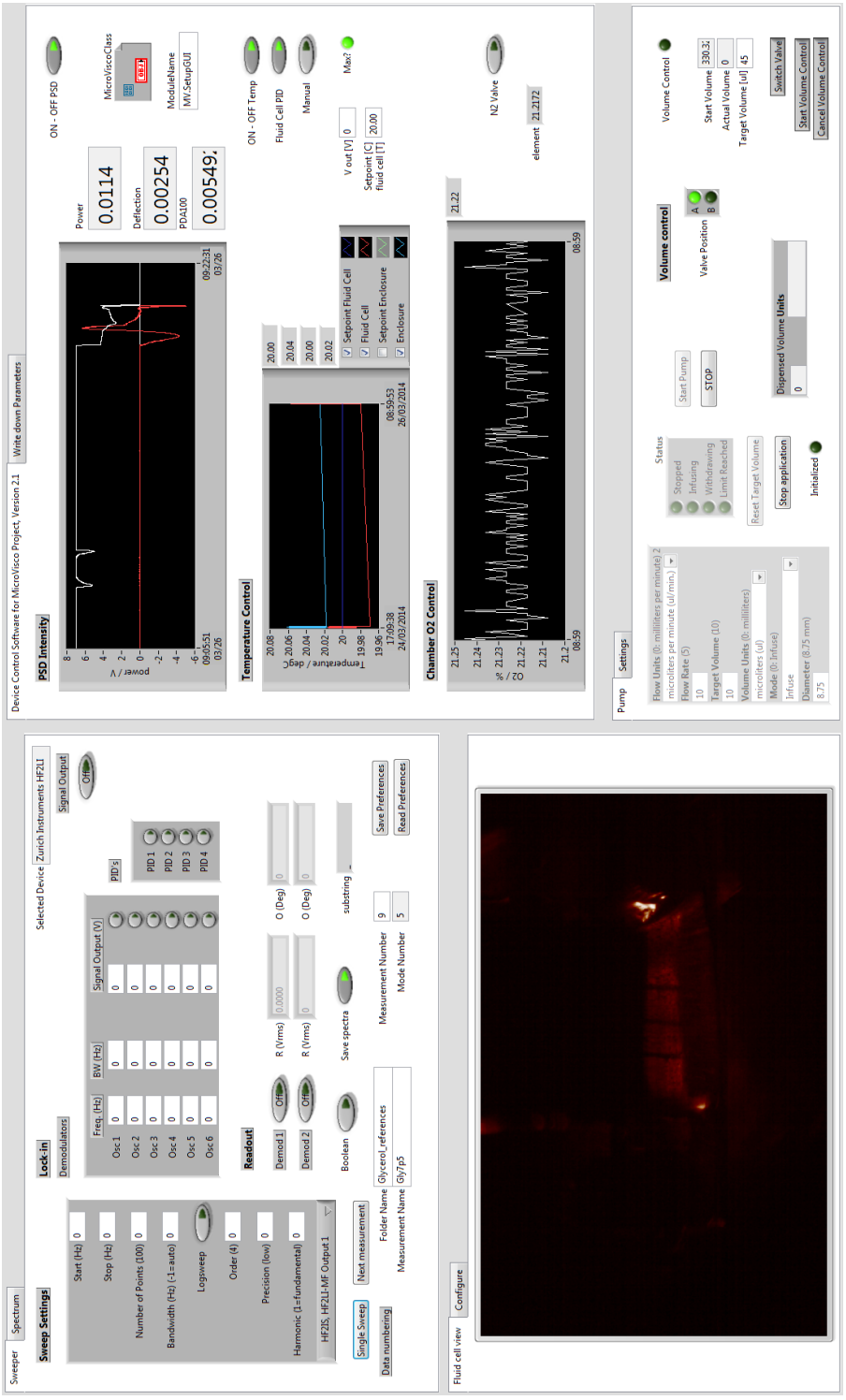

Figure A.21: LabVIEW instrument control software V.2. Panels (from left top, clockwise): Zurich Instruments HF2 lock-in amplifier control; laser intensity, temperature and atmosphere monitoring; syringe pump control; fluid cell camera.

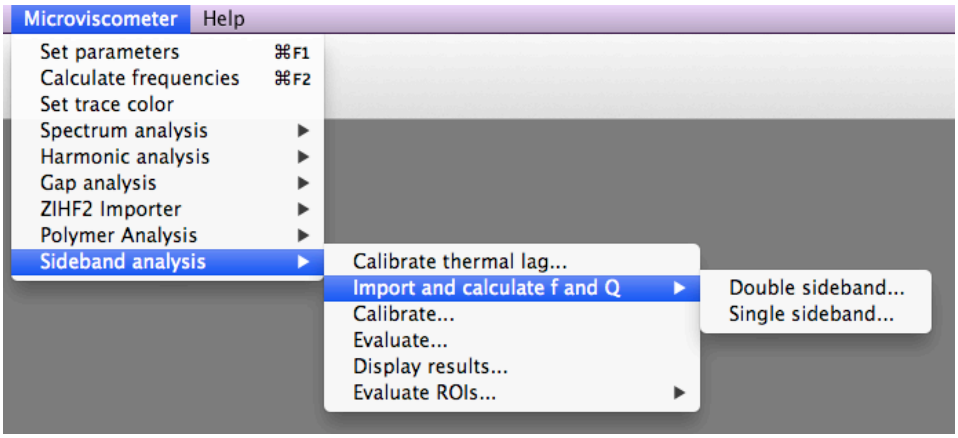

Figure A.22: Analysis software: All relevant data analysis procedures can be accessed by a GUI menu in IGOR Pro.

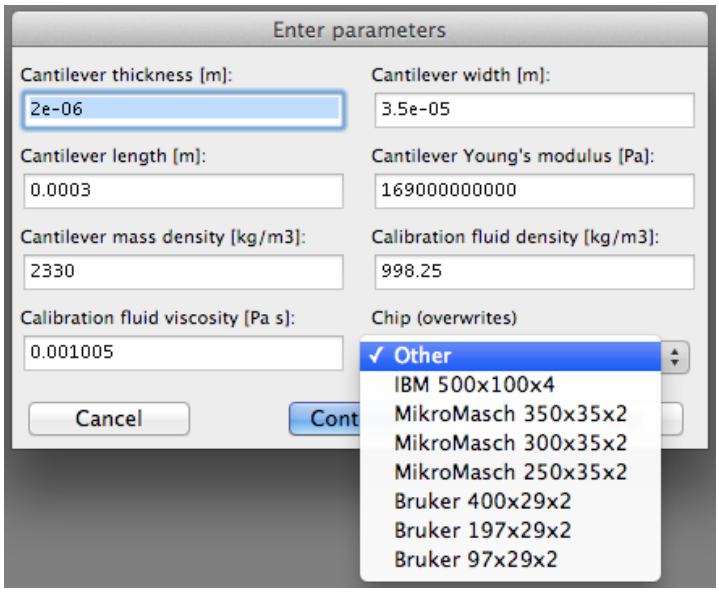

Figure A.23: Analysis software: The cantilever and calibration fluid properties are set prior to each analysis. The properties of commonly employed cantilevers can be loaded.

Appendix B

Material properties

B.1 Cantilever chips

The cantilevers employed in this thesis were provided by IBM Research Labs Rüschlikon and MikroMasch. The nominal properties are provided in Table B.1.

B.2 Viscosity and mass density reference measurements

To measure the viscosity and mass density of the glycerol, glucose and sucrose solutions, an AMVn rolling-ball viscometer (Anton Paar) and DMA 4500M density meter (Anton Paar) were employed. The viscometer was equipped with a capillary of diameter 1.6 mm (17732284) and a steel ball (diameter 1.5 mm, density 7.850 g/cm^3) operated at a tilt angle of 70° with four repeats per sample. All measurements were performed at 293.15 K and are shown in Table B.2. About 0.3 mL and 1 mL of sample were required for the viscosity and density measurements, respectively.

Table B.1: Employed cantilevers.

Type	Dimensions / μm			Spring constant
	Length L	Width b (w)	Thickness h (t)	k_{cal} / N/m
IBM	500	100	4	2.16
MikroMasch	350	35	2	0.28
NSC12/Tipless/noAl	300	35	2	0.44
	250	35	2	0.76

Table B.2: Viscosity and mass density reference measurements of glycerol, glucose and sucrose solutions

Sample	Mass density ρ / g/cm^3	viscosity η / mPa s
Water	0.99825	1.0016
Glycerol % (w/w)		
10	1.02311	1.3132
20	1.04772	1.7797
30	1.07265	2.4607
40	1.09942	3.6775
50	1.12586	5.8426
60	1.15369	10.5172
Glucose % (w/w)		
10	1.03731	1.3357
20	1.08135	1.9225
30	1.12471	2.9467
40	1.17539	5.4900
Sucrose % (w/w)		
10	1.03946	1.3487
30	1.12879	3.2080
40	1.17806	6.1139
50	1.22980	14.7774

Appendix C

Supporting Information: Influence of squeeze-film damping on higher-mode microcantilever vibrations in liquid

C.1 Data analysis routine

Figure C.1 shows the data analysis routine programmed in Wavemetrics IGOR Pro:

1. **Import data:** Resonance spectra stored as binary files are imported.
2. **Automatic peak identification:** The peaks are automatically detected in an amplitude spectrum recorded far from the surface. The peak positions and peak widths are assigned as initial parameters for the fit in step 4.
3. **Define fit range / exclusion of spectra:** The fit range can be limited using two sliders (gray areas). Spurious spectra recorded in contact with the cantilever can be excluded from fitting.
4. **Data fitting:** The model describing the phase response (Equation 4 in main text) is fitted to the data using a Levenberg-Marquardt algorithm resulting in the eigenfrequency f_n and quality factor Q_n for each mode n.
5. **Data alignment:** The data of the fundamental mode ($n = 1$) is fitted to the model of Tung *et al.* [127] (Equation 4.2 in main text) to accurately determine the gap.
6. **Post analysis:** Added mass a_m and damping coefficients c are calculated (Equations 4.7 and 4.9 in main text).

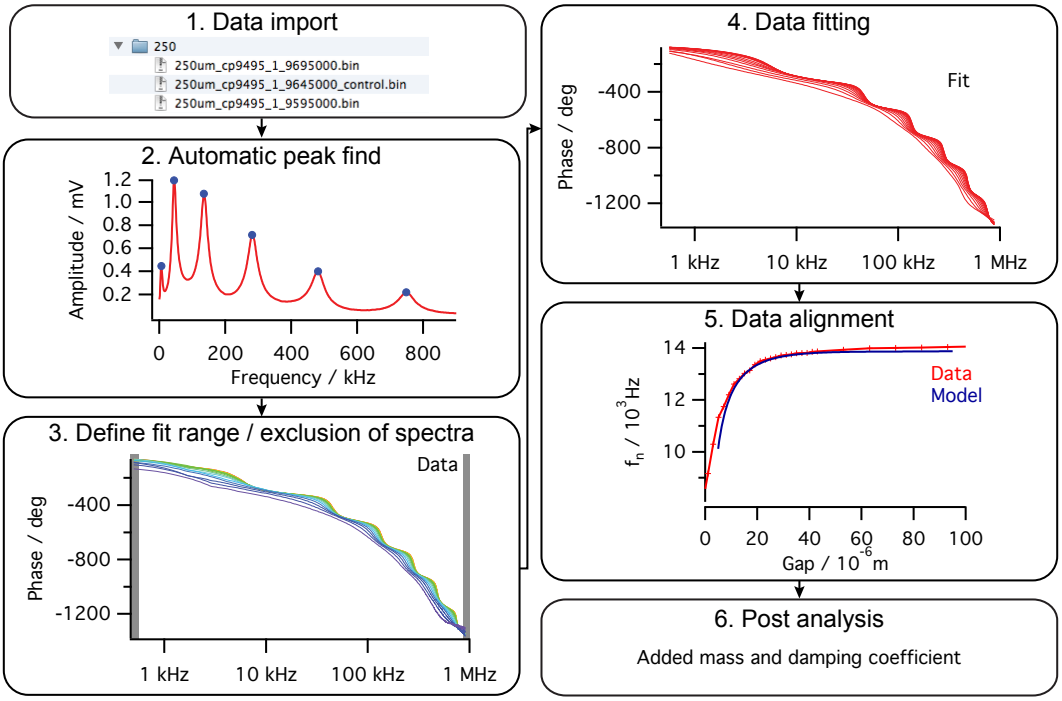

Figure C.1: Data analysis routine.

Table C.1: Employed cantilevers (NSC12/tipless/noAl, MikroMasch).

Length / μm	Width / μm	Thickness / μm	Spring constant / N/m
250	35	2	0.76
300	35	2	0.44
350	35	2	0.28

C.2 Data on 300 μm $\times$ 35 μm $\times$ 2 μm and 350 μm $\times$ 35 μm $\times$ 2 μm microcantilevers

In addition to the data shown in the manuscript (250 μm x 35 μm x 2 μm cantilevers), the behavior of two longer cantilevers was determined. The dimensions and calculated spring constants [105] of all employed cantilevers are provided in Table C.1. Amplitude and phase spectra at different cantilever-surface gaps g are shown in Figure C.2. Due to the lower spring constants of the longer cantilevers the spacing between the vibrational modes is smaller (compare to Figure 4.3). This allowed vibrational modes up to mode 5 (300 μm x 35 μm x 2 μm) and mode 6 (350 μm x 35 μm x 2 μm) to be detected. Higher modes were beyond the frequency bandwidth of the employed optical beam deflection system.

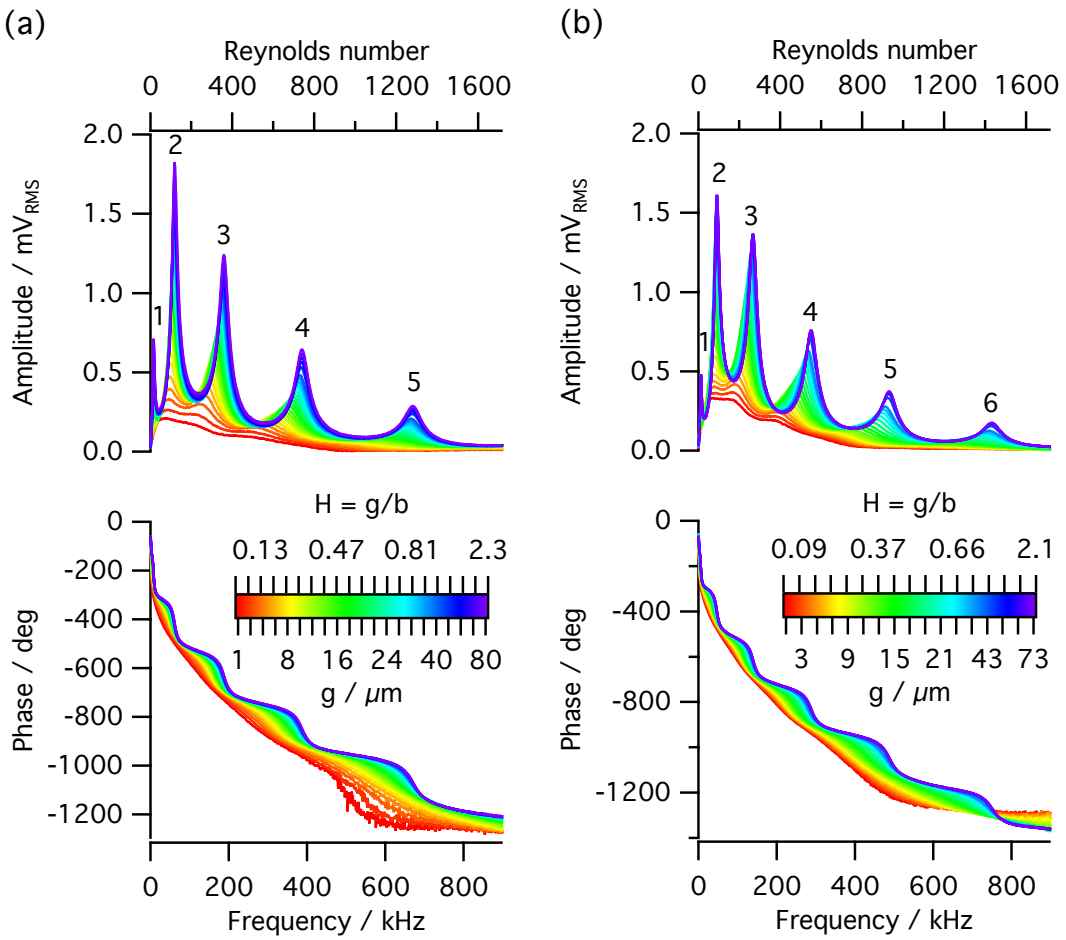

Figure C.2: The amplitude (upper plot) and phase (lower plot) response of (a) a 300 μm x 35 μm x 2 μm and (b) a 350 μm x 35 μm x 2 μm microcantilever vibrating in water at different distances from a surface are shown as a function of frequency and the corresponding Reynolds number (*Re*). The flexural mode numbers are written above the resonance peaks. Absolute (g) and normalized (H) cantilever-surface separations are indicated. The color scale is not linear; far from the surface the increment in g was set larger because the effect diminishes (superimposed purple curves). The spectra are overlayed; the red curves (small g) are at the back.

In general, the data obtained using the longer cantilevers are more distorted compared to those obtained using 250 μm long cantilevers (main manuscript, Figures 4.3 and 4.5). We attribute this to the higher modal overlap in the spectra recorded at small gaps between the cantilever and the approaching surface. The increased overlap is due to the lower spring constants of the longer cantilevers. Furthermore, due to the lower modal frequencies of these cantilevers, the fundamental mode resonance peak is clipped by the lower frequency limit of the employed detection electronics. This leads to inaccuracies in the extracted eigenfrequencies and quality factors for the fundamental mode (see Figures C.3 and C.4; compare to Figure 4.5). Hence, the data was aligned to the second mode of vibration, where the model of Tung *et al.* [127] is still sufficiently accurate (dashed black line in Figures C.3a and C.4a). As shown in Figure C.5, the characteristic gap, a measure of the range of squeeze-film damping, was calculated normalized to the second mode of vibration for the longer cantilevers. This does not allow quantitative comparison to the data in Figure 4.7, which is aligned to the fundamental mode. However, qualitative comparison shows that there is good agreement, i.e., the characteristic gaps decrease for the eigenfrequencies and increase for the quality factors with mode number. Furthermore, the results indicate that the characteristic gap does not solely depend on the mode number n, but also the length of the cantilever. Therefore, the squeeze film damping is most likely characterized by (i) the frequency (Reynolds number) and (ii) beam wavelength, represented by a normalized mode number that depends on the vibrational mode as well as the length of the cantilever [125].

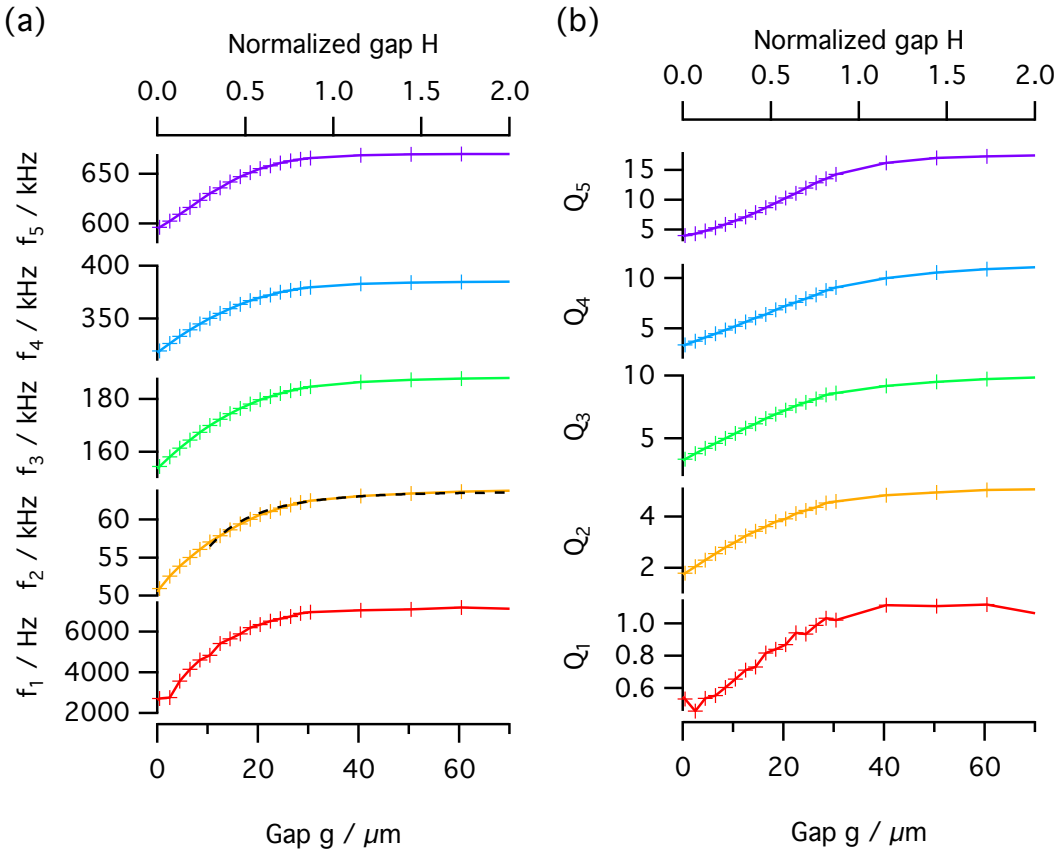

Figure C.3: (a) Eigenfrequencies and (b) quality factors of a 300 μm x 35 μm x 2 μm cantilever. The dashed line in (a) represents the model of Tung *et al.* [127] employed to align the data at mode $n = 2$.

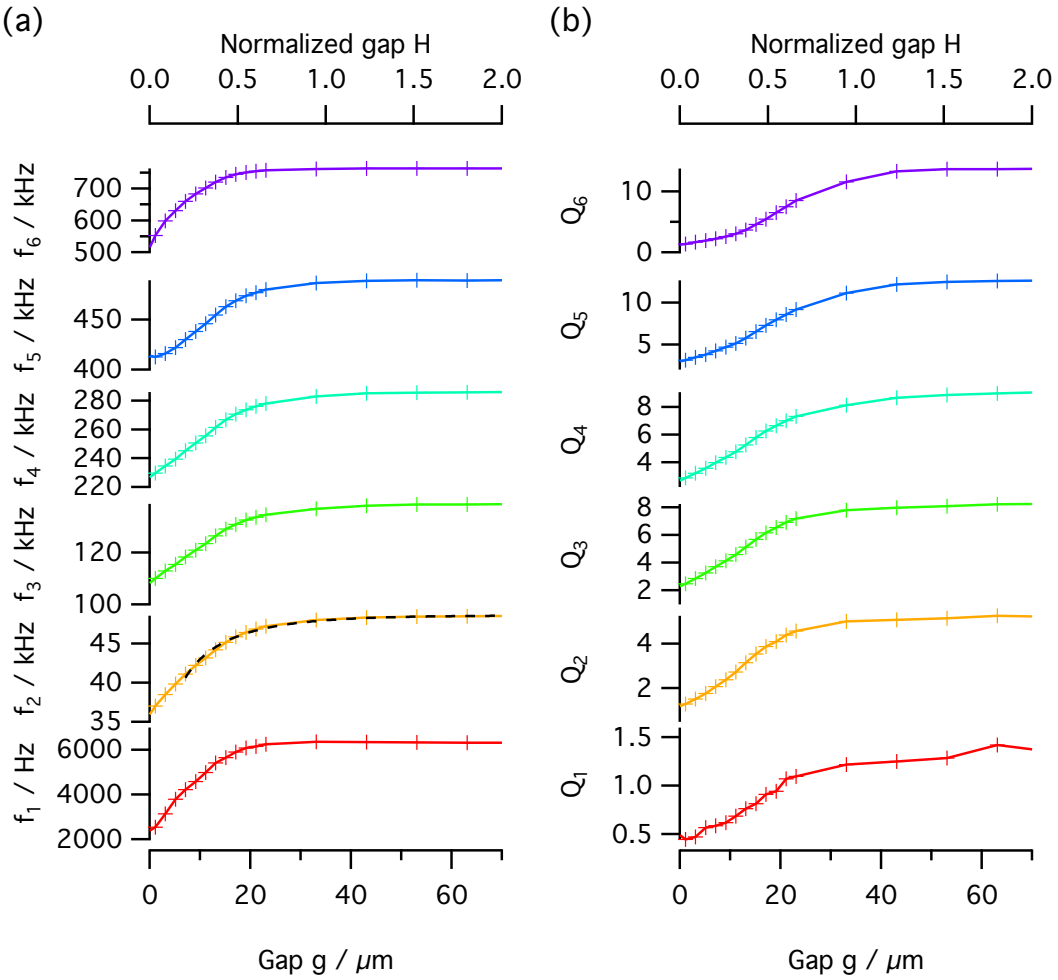

Figure C.4: (a) Eigenfrequencies and (b) quality factors of a 350 μm x 35 μm x 2 μm cantilever. The dashed line in (a) represents the model of Tung *et al.* [127] employed to align the data at mode $n = 2$.

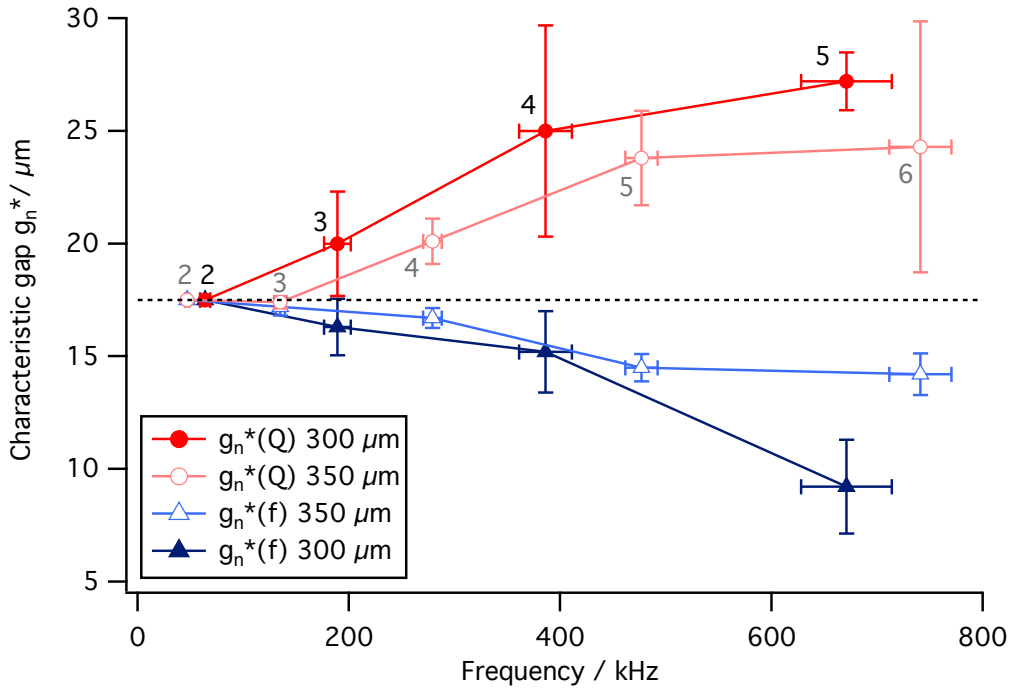

Figure C.5: The characteristic gap g_n^* for 300 μm x 35 μm x 2 μm and 350 μm x 35 μm x 2 μm cantilevers. As discussed in the text, g_n^* was normalized to the second mode of vibration ($n = 2$) at $g_2^* = 17.5$ μm (dashed line). It is the cantilever-surface gap, where the frequencies (blue triangles) dropped to (94.0 ± 0.4)% and the quality factors (red circles) to (72.9 ± 3.4)% of their initial values. The means $\pm$ SD (N = 3) are shown and mode numbers n are indicated.

Appendix D

Supporting information: Real-time viscosity and mass density sensors requiring microliter sample volume based on nanomechanical resonators

Reproduced with permission from Analytical Chemistry **85**(18), 8676–8683 (2013), **DOI:** 10.1021/ac4014918.

Abstract

This Supporting Information provides details on determination of the eigenfrequencies, quality factors and calibration parameters; the approximation of the hydrodynamic function; finite element analysis of the laser induced increase in temperature; the data analysis of two-phase flow experiments; and the analysis of the acrylamide polymerization by rheokinetic models.

D.1 Determination of the eigenfrequencies, quality factors and calibration parameters

Analysis was performed using scripts written for IGOR Pro (WaveMetrics, Lake Oswego, OR, USA). To determine the eigenfrequency f_n and quality factor Q_n of flexural mode n of a fluid loaded cantilever, a damped harmonic oscillator model [23] was fitted to the measured amplitude and phase spectra (500 data points each) of every flexural mode n individually by a least-squares fitting algorithm:

Table D.1: Parameter values used for the measurements in reference fluids based on amplitude (amp) and phase (pha) spectra. Values for the first (fundamental) mode are not given, because its eigenfrequency is below the high-pass frequency of the excitation.

mode	α_n	κ_n	f_n/ kHz		Q_n		$f_{n,\mathrm{vac}}$ / kHz		$C_{n,\mathrm{cal}}$	
n			amp	pha	amp	pha	amp	pha	amp	pha
1	1.875	0.375	-	-	-	-	-	-	-	-
2	4.694	0.939	52.0	51.9	11.2	11.2	158.8	158.6	0.92	0.92
3	7.855	1.571	149.3	149.2	18.8	18.8	422.5	422.2	0.94	0.94
4	10.996	2.199	292.4	292.3	27.0	26.8	774.5	774.3	0.98	0.97
5	14.137	2.827	471.4	471.4	34.3	33.9	1177.6	1177.6	0.99	0.98
6	17.279	3.456	701.7	701.9	42.2	41.0	1663.0	1663.4	1.01	0.98

$$A(f) = \frac{a_0 f_n^2}{\sqrt{(f_n^2 - f^2)^2 + \left(\frac{f_n f}{Q_n}\right)^2}} + a_{\mathrm{slope}} f + a_{\mathrm{off}} \qquad Q_n \gg 1, \tag{D.1}$$

$$\phi(f) = \arctan\left(\frac{Q_n\left(f_n^2 - f^2\right)}{f_n f}\right) + p_{\mathrm{slope}} f + p_{\mathrm{off}} \qquad Q_n \gg 1, \tag{D.2}$$

where the frequency f is the independent variable. The parameter a_0 is the angular deflection amplitude; the slope a_{slope} and the offset a_{off} approximate the influence of neighboring peaks on the amplitude; the phase slope p_{slope} takes into account phase lags originating from the electronics and photothermal excitation; the phase offset p_{off} considers phase offsets due to lower resonances. The fit was masked to a width equal to 3 to 5 times the full width at half maximum (FWHM) around the eigenfrequency of the peak. Table D.1 gives eigenvalues α_n, normalized mode numbers κ_n; measured eigenfrequencies f_n and quality factors Q_n in water; and the vacuum frequency $f_{n,\mathrm{vac}}$ and quality factor calibration constant $C_{n,\mathrm{cal}}$, which are separately calibrated for the amplitude and phase for a cantilever immersed in water. The deviations between values derived from amplitude or phase are minimal.

D.2 Correction parameters for the approximated hydrodynamic function

The correction parameters for the approximated hydrodynamic function (eq D.3) for various values of κ_n are given in Table D.2. Calculated values for $\kappa_n = \{0.1, 0.2, \ldots, 20.0\}$ and $\log Re = \{0.00, 0.01, \ldots, 8.00\}$ were interpolated by a cubic spine function and saved in a lookup table. For analysis, values were accessed by table lookup using linear interpolation.

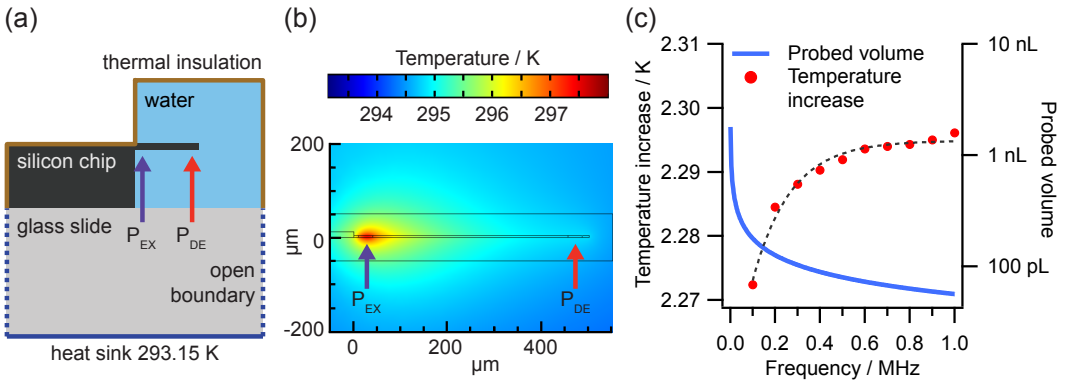

Figure D.1: Finite element analysis of laser heating: (a) Schematic of the model and the applied boundary conditions, (b) temperature profile along the central cross-section of the cantilever with the incident lasers P_{EX} and P_{DE} and (c) average temperature increase inside the volume probed by the cantilever; the dashed line is a guide for the eye.

$$\Gamma = (a + b \cdot \Re\left[\Gamma_{\kappa_n \to \infty}(Re, \kappa_n)\right]) + i \left(Re^{-c} + d \cdot \Im\left[\Gamma_{\kappa_n \to \infty}(Re, \kappa_n)\right]\right) \quad \text{for} \quad Re \geq 10^3. \tag{D.3}$$

D.3 Finite element analysis of the laser induced increase in temperature

Laser induced heating has been reported to introduce systematic errors in the viscosity and mass density results determined by microcantilevers [57, 219]. To estimate the laser induced increase in temperature inside the volume probed by the cantilever, a three-dimensional finite element analysis was performed using COMSOL Multiphysics (version 4.2). The cantilever only probes fluid within the viscous boundary-layer δ [33], which is in the order of a micrometer for the given frequencies. Because both faces of the cantilever are in contact with the fluid, the probed volume is equal to $2Lw\delta$, where L and w are the length and the width of the cantilever.

Figure D.1a shows a schematic illustration of the model and the applied boundary conditions. The excitation and detection laser were modeled as boundary heat sources P_{EX} and P_{DE} on the bottom surface of the cantilever, thus neglecting absorption of the surrounding fluid. The laser beam diameter was 30 μm for each. Because the penetration depth of the optical field is very thin compared to the thickness of the cantilever, the absorbed power was estimated to be $P_{\mathrm{abs}} = P_{\mathrm{in}}\,(1 - R(\lambda))$, where P_{in} is the incident laser power and $R(\lambda)$

Table D.2: Correction parameters for the approximated hydrodynamic function for different values of the normalized mode number κ_n.

κ_n	a	b	c	d
0.1	-88.9142	3.5314	0.3921	2.1525
0.2	-44.0620	3.5395	0.3959	2.1351
0.3	-28.3220	3.4539	0.3886	2.0054
0.4	-20.5674	3.3852	0.3875	1.9206
0.5	-15.8876	3.3100	0.3887	1.8518
0.6	-12.7768	3.2354	0.3888	1.7700
0.7	-10.5385	3.1549	0.3896	1.6934
0.8	-8.8430	3.0678	0.3905	1.6182
0.9	-7.5319	2.9818	0.3921	1.5513
1.0	-6.4962	2.8995	0.3930	1.4798
1.5	-3.4900	2.5264	0.4008	1.2009
2.0	-2.1239	2.2311	0.4114	1.0253
2.5	-1.4001	2.0075	0.4229	0.9198
3.0	-0.9762	1.8365	0.4339	0.8560
3.5	-0.7131	1.7080	0.4454	0.8241
4.0	-0.5396	1.6083	0.4553	0.8034
4.5	-0.4207	1.5303	0.4650	0.7953
5.0	-0.3369	1.4697	0.4737	0.7918
5.5	-0.2743	1.4184	0.4822	0.7937
6.0	-0.2277	1.3773	0.4908	0.8000
6.5	-0.1915	1.3424	0.4984	0.8056
7.0	-0.1631	1.3127	0.5059	0.8131
7.5	-0.1410	1.2889	0.5128	0.8203
8.0	-0.1227	1.2673	0.5202	0.8300
8.5	-0.1076	1.2482	0.5271	0.8385
9.0	-0.0950	1.2314	0.5334	0.8460
9.5	-0.0845	1.2166	0.5400	0.8547
10.0	-0.0755	1.2033	0.5460	0.8621
11.0	-0.0617	1.1821	0.5581	0.8770
12.0	-0.0512	1.1641	0.5698	0.8908
13.0	-0.0431	1.1492	0.5800	0.9019
14.0	-0.0368	1.1372	0.5912	0.9139
15.0	-0.0318	1.1266	0.6017	0.9238
16.0	-0.0277	1.1172	0.6116	0.9327
17.0	-0.0244	1.1097	0.6216	0.9410
18.0	-0.0216	1.1028	0.6313	0.9484
19.0	-0.0193	1.0967	0.6405	0.9547
20.0	-0.0173	1.0912	0.6496	0.9606

the reflectance at wavelength λ. The boundary conditions were set as follows: As a conservative estimate, the PDMS (polydimethylsiloxane) fluid cell was assumed to be thermally insulating; the vertical faces of the glass slide were set as open boundaries, because the glass slide exceeds the dimensions of the fluid cell; the bottom of the glass slide, being in contact with the peltier temperature control, was modeled as a heat sink at a constant temperature of 293.15 K.
The simulated temperature profile is shown in Figure D.1b. A confined hot spot forms close to the clamped end of the cantilever, where the excitation laser beam P_{EX} is absorbed. The detection laser beam P_{DE} does not cause significant heating, because $> 97\%$ of its incident power is reflected. Figure D.1c gives the average temperature increase inside the volume probed by the cantilever. The increase in temperature inside the probed volume is below 2.3 K for all frequencies and is taken into account by a calibration step.

D.4 Data analysis of two-phase flow experiments

A hydrocarbon oil carrier fluid was used to separate aqueous samples in the two-phase flow experiments. Due to the different refractive indices of the two fluids and the interfacial forces, which deflect the cantilever, the laser beams are scattered during liquid phase exchange. During this time (about 3 s) the detection laser beam is not entirely incident on the position-sensitive detector leading to a temporary decrease in laser power (Figure D.2a). This results in a distorted spectrum and deviations in the determined viscosity and density values. Therefore, an algorithm was applied rejecting data (with a delay of 3 s due to the spectra acquisition time) that is recorded below a certain detection laser power threshold (400 μW, Figure D.2a). The density and viscosity raw data is shown in Figure D.2b and c and the processed data in Figure 6 in the main paper.

D.5 Rheokinetic analysis of acrylamide polymerization

As discussed in the main paper an unexpected [40] decrease in mass density was measured during acrylamide polymerization. The theoretical framework applied is only valid for Newtonian fluids. As observed, non-Newtonian behavior arising from shear-thinning will lead to deviations. The actual mass densities of water (H_2O) and the polyacrylamide (PAa) solution were determined using a DMA 4500 M density meter (Anton Paar, Graz, Austria): $\rho_{\mathrm{H_2O}} = 998.2$ kg/m^3 and $\rho_{\mathrm{PAa}} = 1010.6$ kg/m^3. Because the difference in density between water and polyacrylamide solution is small (1.2%), the data was additionally analyzed while holding the density constant at 998.2 kg/m^3. Consequently, the viscosity was directly determined from the quality factor only. The results for analysis with variable density (as displayed in the main paper) and constant density are shown in Figure D.3. The viscosity values for both analyses are consistent, showing that the viscosity is almost unaffected by the

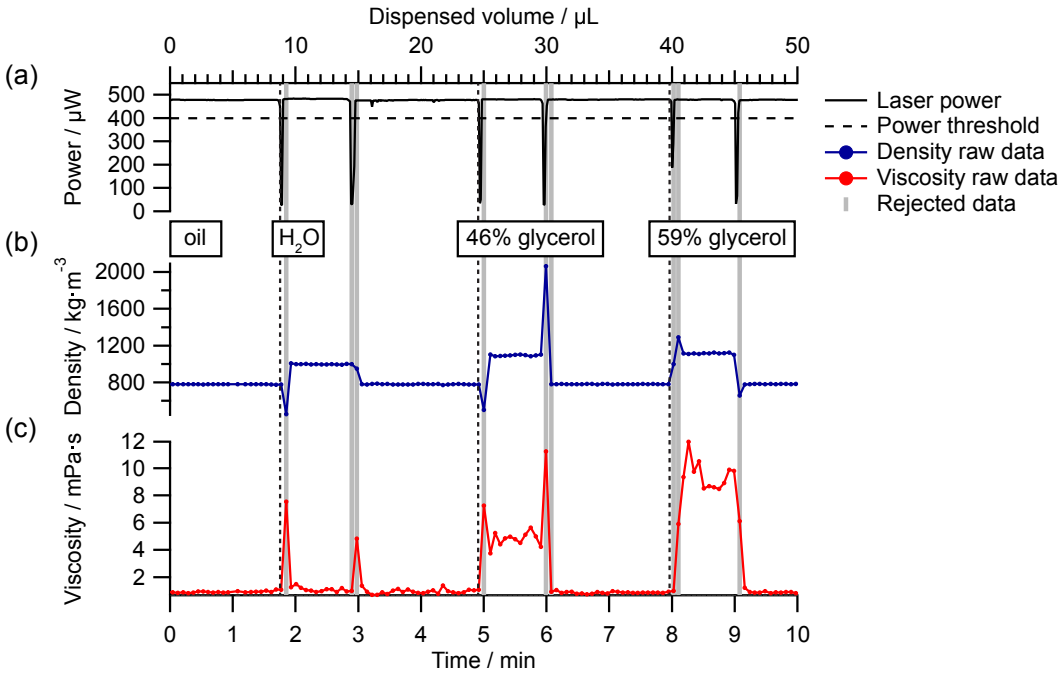

Figure D.2: (a) Detection laser intensity and raw data of the (b) mass density and (c) viscosity. Data points recorded below an intensity threshold (dashed black line) were excluded (vertical grey lines).

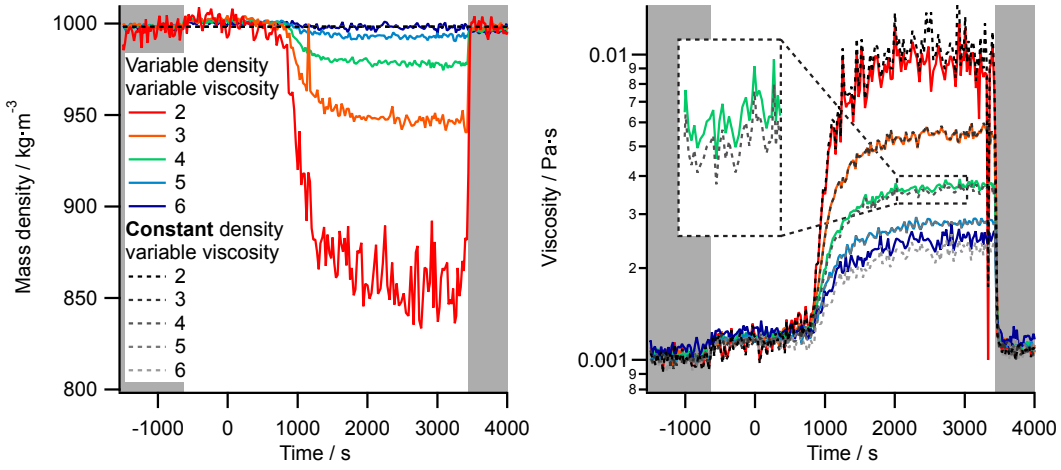

Figure D.3: Viscosity and mass density of the acrylamide polymerization; shaded areas indicate water rinses. Data was analyzed with variable density / variable viscosity (solid colored lines; displayed in the main paper) and constant density / variable viscosity (dashed grey lines). The viscosity values are in good agreement for both analyses.

density decrease, which is an artifact caused by the non-Newtonian behavior of the polymer solution.

The theoretical framework introduced by Kulichikhin, Malkin, Polushkina, and Kulichikhin [196] was employed to describe the rheokinetics of the acrylamide polymerization reaction. To fit the viscosity data, equation 16 from this reference was used as follows:

$$\eta(t) = \begin{cases} \eta_0 \left(1 + K'_n \left[\frac{M_0}{I_0}\left(1 + \frac{1}{I_0\kappa_i(t-t_0)}\right)\right]^a \left[1 - \frac{1}{(1+I_0\kappa_i(t-t_0))^x}\right]^{a+b}\right) & t - t_0 > 0 \\ \eta_0 & t - t_0 \leq 0 \end{cases} \tag{D.4}$$

$$x = \frac{\kappa^*}{\sqrt{\kappa_i}} = \frac{\kappa_p}{\sqrt{\kappa_i \kappa_t}}, \tag{D.5}$$

with the following parameters from reference [196]: a = 3.4, b = 6, κ_i = 0.025 $\text{mol}^{-1}\text{s}^{-1}$, κ^* = 3.14 $\text{mol}^{-0.5}\text{s}^{-0.5}$ and I_0 = 4.4 mM, M_0 = 478 mM. η_0 is the viscosity of the monomer solution (baseline). An induction period caused by atmospheric oxygen is taken into account by lag-time t_0. Coefficient K'_n is a function of the initial concentration, temperature and shear-thinning effects and, therefore, depends on the flexural mode of vibration n. The parameters η_0, t_0 and K'_n are determined by least-squares fitting of eq D.4 to the viscosity data and provided in Table D.3. Combining equation 6 and 15 from reference [196], gives the following expression to describe the degree of conversion β:

Table D.3: Parameters determined by fitting eq D.4 to the viscosity data.

mode	t_0/s	η_0/mPa · s	$K'_n/10^{-10}$
2	599.2	1.21	9.306
3	562.4	1.19	4.10348
4	564.5	1.21	2.36746
5	558.5	1.18	1.56347
6	593.3	1.24	1.19768
mean	575.6	1.21	N/A
SD	19.1	0.02	N/A

$$\beta(t) = \sqrt[a+b]{\left(\frac{\eta(t)-\eta_0}{\eta_0 K'_n}\left[\frac{I_0}{M_0}\frac{I_0\kappa_i(t-t_0)}{1+I_0\kappa_i(t-t_0)}\right]^a\right)} \quad \text{for} \quad \eta(t)-\eta_0 \geq 0. \tag{D.6}$$

The degree of conversion $\beta(t)$ was determined by inserting the viscosity $\eta(t)$ at each point in time and is shown in Figure 7b of the main paper. In the initial stage of the reaction, $\eta(t)-\eta_0$ can become negative due to random fluctuations in the baseline. This results in a negative term under the root which cannot be determined.

To extrapolate the degree of conversion at the end of the reaction from the rheokinetic data, parameter β_∞ was introduced in equation 13 from reference [196]. Thus, the equation describes the degree of conversion β of a first order reaction with a second order initiation reaction and a final degree of conversion β_∞:

$$\beta(t) = \beta_\infty\left(1-(1+I_0\kappa_i(t-t_0))^{-\frac{\kappa_p}{\sqrt{\kappa_i\kappa_t}}}\right). \tag{D.7}$$

Eq D.7 was fitted to the degree of conversion data of all modes simultaneously, while holding I_0, κ_p, κ_i, and κ_t at the values provided above. This resulted in $\beta_\infty = 95.3\%$ and $t_0 = 538$ s. The small deviation of t_0 from the lag-times determined directly from the viscosity data (Table D.3), is most likely due to the weak viscosity-concentration dependence in the initial stage of the reaction impairing their precise determination.

Appendix E

Supporting Information: Automated high-throughput viscometer using resonant nano-mechanical sensors

E.1 openBEB macros

The openBEB macros [181] used to control the automatic sampler are provided below.

MV.AutosamplerTest.macro

```
#
!store::endVial=10
!store::indexVial=0
!store::Vial=1
!store::index=0
#
!do::1::index
#goto vials and aspirate sample
.!do::{endVial}::indexVial
..!calc::Vial=({indexVial}+2)
..!include::AS.gotoVial::vialPos=1
..!include::AS.aspirateSample::waitTime=2000
..!include::AS.gotoVial::vialPos={Vial}
..!include::AS.aspirateSample::waitTime=2000
.!include::AS.gotoVial::vialPos=1
.!include::AS.aspirateSample::waitTime=2000
```

AS.aspirateSample.macro

```
#
!default::waitTime=1000
#
```

```
!tellmodule::microVisco.autosampler
.zEnable
.setzTargetPosition::-76
.gotozPosition
.sendBoolean
.sendzSteps
.setzPosition
.wait::10
.zDisable
.sendBoolean
#wait time inside vial
.wait::{waitTime}
#
.zEnable
.setzTargetPosition::0
.gotozPosition
.sendBoolean
.sendzSteps
.setzPosition
.wait::10
.zDisable
.sendBoolean
#waittime in FC-40 (ms)
.wait::2000
```

AS.gotoVial.macro

```
#
!default::vialPos=1
#
!tellmodule::microVisco.autosampler
.rotEnable
.setVialTargetPosition::{vialPos}
.gotoRotPosition
.sendBoolean
.sendRotSteps
.setRotPosition
.wait::10
.rotDisable
.sendBoolean
#end
```

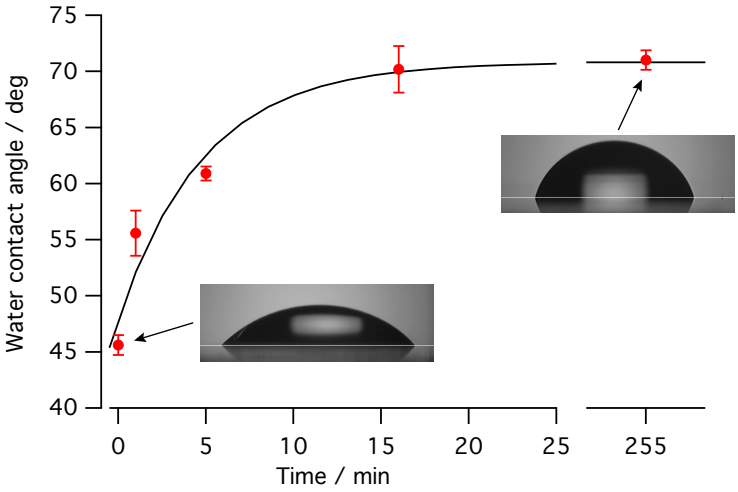

Figure E.1: Water contact angle on glass slides after different treatment times with PDMS solutions (*Regenabweiser*). The solid black line represents a fitted Langmuir adsorption kinetics and the error bars the standard deviation for perpendicular views on the water droplet. Insets: image of the droplets on an untreated (0 min) and saturated (255 min) surface.

E.2 Surface modification

A PDMS-based chemical to render surfaces hydrophobic (*Regenabweiser*, Stolz GmbH, Germany) was used to treat the fluidic system, including the fluid cell. This is crucial for homogeneous and reproducible droplet handling [203]. To assess treatment times, glass slides were incubated in *Regenabweiser* for 0 min, 1 min, 5 min, 16 min, 30 min and 255 min. Contact angles were measured using the setup described in reference [220] and analyzed using the LB-ADSA (low-bond axisymmetric drop shape analysis) plug-in [221] in ImageJ [222]. As shown in Fig. E.1, the treatment rendered the surface more hydrophobic resulting in a change in contact angle from $(45.6 \pm 0.9)^\circ$ to $(71.0 \pm 0.9)^\circ$ (untreated versus 255 min treated, mean $\pm$ SD). After 17 min treatment time, 99% of the final contact angle value was reached. To assess the long-term stability the surfaces were immersed in water for 3 days. The untreated surface became more hydrophilic $(32.4 \pm 0.2)^\circ$, whereas the treated hydrophobic surface remained stable $(69.5 \pm 0.8)^\circ$.

E.3 Automatic sampler

The automatic sampler, used to aspirate microliter samples in a two-phase configuration with fluorinated oil, was operated by two linear stepper motors. Figure E.2 shows a photograph and Figure E.3 the connection diagram between the motor controllers (SAMATRONIC 101),

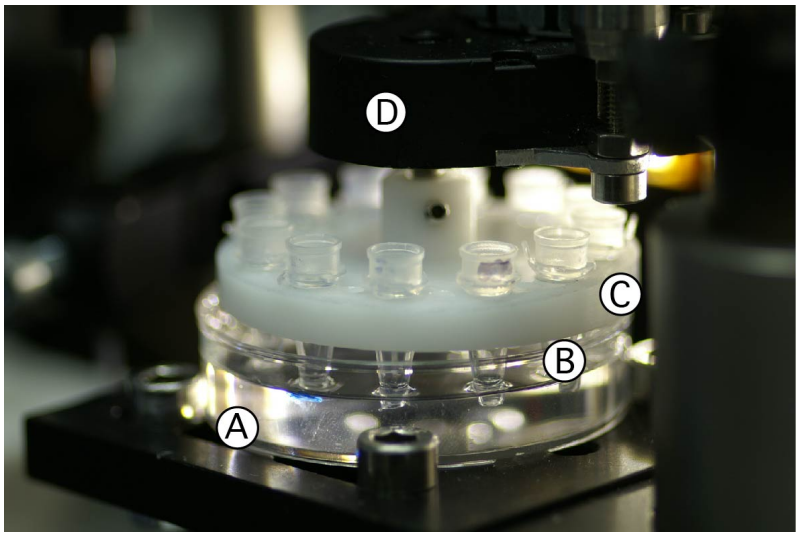

Figure E.2: Photograph of the automatic sampler. (A) Fluorinated oil (FC-40) bath, (B) open-ended sample vials partially immersed in the oil, and (C) rotating stage connected to the (D) rotational stepper motor. The capillary and z-motor to aspirate sample are not visible.

the CMOS analog switches (DG445, Maxim) serving as TTL-inverters and the LabVIEW DAQ card (NI USB-6009, National Instruments).

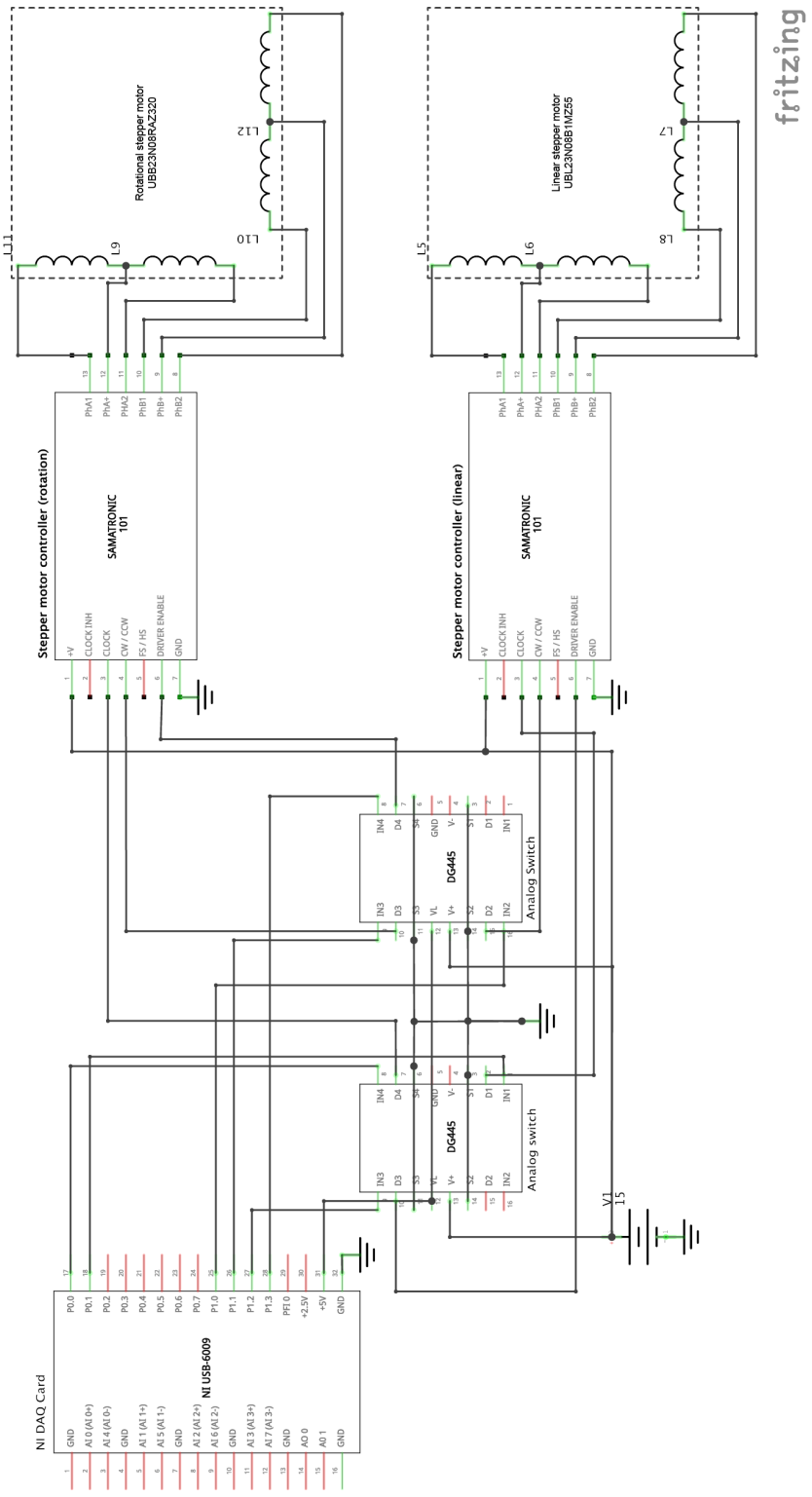

Figure E.3: Circuit to drive the stepper motors of the automatic sampler.

List of Abbreviations

^{1}H-NMR	Proton-nuclear magnetic resonance.
AFM	Atomic force microscopy.
APS	Ammonium persulfate.
DDHO	Driven damped harmonic oscillator.
FEM/A	Finite element method / analysis.
LD	Laser diode.
MEMS	Microelectromechanical system.
OEG-silane	2-(methoxy(polyethyleneoxy)propyl)trimethoxysilane.
OEG-thiol	(1-Mercapto-11-undecyl)tetra(ethyleneglycol).
PD	Photodiode.
PDMS	Polydimethylsiloxane (SYLGARD®184).
PEEK	Polyether ether ketone.
PID	Proportional-integral-derivative (controller).
PLL	Phase-locked loop.
PSD	Position-sensitive detector.
RF	Radio-frequency.
SD	Standard deviation.
SHO	Simple harmonic oscillator.
TEMED	Tetramethylethylenediamine.

List of Symbols

a_0	Amplitude of vibration (m).
a_m	Added mass coefficient, $a_m = \frac{m_f}{m_c}$.
b, w	Width of the cantilever (m).
c	Total damping coefficient per unit length (Pa·s).
c_s	Structural damping coefficient per unit length (Pa·s).
c_{sound}	Speed of sound (m/s), for water $c_{\text{sound}} = 1482$ m/s.
c_v	Viscous damping coefficient per unit length (Pa·s).
E	Young's modulus (Pa), for silicon $E = 169$ GPa.
f_n	Eigenfrequency of mode n (Hz).
$f_{0,n}$	Vacuum frequency (undamped eigenfrequency) of mode n (Hz).
F	Force per unit length (N/m).
F_{drive}	Driving force per unit length (N/m).
F_{hydro}	Hydrodynamic force per unit length (N/m).
g	Gap between cantilever and surface (m).
h, t	Thickness of the cantilever (m).
H	Normalized gap between cantilever and surface, $H = \frac{g}{b}$.
I_z	Area moment of inertia (m^4), for a rectangular beam $I_z = \frac{bh^3}{12}$.
k_{B}	Boltzmann constant, $k_{\text{B}} = 1.3806488 \cdot 10^{-23}$ J/K.
k_{eff}	Effective spring constant (N/m).
KC	Keulegan-Carpenter number, $KC = 2\pi \frac{a_0}{b}$.
Kn	Knudsen number, $Kn = \frac{\lambda^*}{b}$.
L	Length of cantilever (m).
m_c	Mass of the cantilever (kg).
$m_{\text{eff},n}$	Effective mass of mode n (kg).

m_f	Co-moving fluid mass (kg).
M	Bending moment (N·m).
n	Flexural mode of vibration.
p	Pressure (Pa).
Q_n	Quality factor of mode n.
Re	The Reynolds number of an oscillating beam, $Re = \frac{\rho b^2 \omega}{\eta}$.
T	Temperature (K), $T = 293.15$ K if not otherwise indicated.
u	Flow velocity field.
u	Flow velocity (m/s).
V	Shear force (N).
w_G	Gaussian beam radius (m).
$W(x,t)$	Deflection function of the cantilever as a function of lateral position x and time t, $W(x,t) = \Phi(x)\Psi(t)$.
$(\beta_n L)$, α_n	Eigenvalue of the n-th flexural mode of vibration, $(\beta_n L) = 1.875, 4.694, 7.855, \cdots \simeq \pi\left(n - \frac{1}{2}\right)$.
Γ	The hydrodynamic function.
$\dot{\gamma}$	Rate of shear deformation, strain rate (1/s).
γ	Linear thermal expansion coefficient (1/K).
δ	Viscous boundary layer, $\delta = \sqrt{\frac{2\eta}{\omega\rho}}$ (m).
η, η_f	(Dynamic) viscosity of fluid (Pa·s), for water $\eta = 1.00$ mPa·s.
η_r	Relative viscosity, for a solution with solvent viscosity η_0, $\eta_r = \frac{\eta}{\eta_0}$.
$[\eta]$	Intrinsic viscosity, for spherical particles $[\eta] = 2.5$.
κ, κ_n	Normalized mode number, $\kappa_n = (\beta_n L)\frac{b}{L}$.
λ	Wavelength of electromagnetic radiation (m).
λ^*	Mean free path of molecules in a fluid (m).
μ_c	Linear mass density of the cantilever (kg/m), $\mu_c = \rho_c bh$.
μ_f	Linear mass density of the co-moving fluid (kg/m).
ρ_c	Mass density of the cantilever (kg/m^3), for silicon $\rho_c = 2330$ kg/m^3.

ρ, ρ_f	Mass density of the fluid (kg/m^3), for water $\rho_f = 998.25$ kg/m^3.
σ	Shear stress (Pa).
ς	Normalized wave number, $\varsigma = \frac{\omega b}{c_{\text{sound}}}$.
τ_{th}	Time constant of the photothermal excitation (s).
$\Phi(x)$	Spatial deflection function of the cantilever (eigenfunction, mode shape) as a function of lateral position x.
ϕ	Phase-lag between the excitation and the mechanical vibration (rad).
φ	Volume fraction of a solute.
$\Psi(t)$	Temporal deflection function of the cantilever as a function of time t.
ω_n	Angular eigenfrequency of mode n, $\omega_n = 2\pi f_n$ (rad/s).
∇	Nabla operator, $\nabla = \left(\frac{\partial}{\partial x_1}, \ldots, \frac{\partial}{\partial x_i}\right)$.
$\Im[z]$	Imaginary part of complex expression z.
$\Re[z]$	Real part of complex expression z.

Bibliography

[1] G. Binnig, C. F. Quate, and C. Gerber, "Atomic force microscope.", *Phys. Rev. Lett.*, vol. 56, no. 9, pp. 930–933, 1986. DOI: 10.1103/PhysRevLett.56.930 (cited on p. 1).

[2] T. Thundat, P. I. Oden, and R. J. Warmack, "Microcantilever sensors", *Microscale Thermophys. Eng.*, vol. 1, no. 3, pp. 185–199, 1997. DOI: 10.1080/108939597200214 (cited on p. 1).

[3] N. V. Lavrik, M. J. Sepaniak, and P. G. Datskos, "Cantilever transducers as a platform for chemical and biological sensors", *Rev. Sci. Instrum.*, vol. 75, no. 7, p. 2229, 2004. DOI: 10.1063/1.1763252 (cited on pp. 1–3).

[4] K. M. Goeders, J. S. Colton, and L. A. Bottomley, "Microcantilevers: sensing chemical interactions via mechanical motion.", *Chem. Rev.*, vol. 108, no. 2, pp. 522–542, 2008. DOI: 10.1021/cr0681041 (cited on pp. 1, 2, 4, 5).

[5] P. S. Waggoner and H. G. Craighead, "Micro- and nanomechanical sensors for environmental, chemical, and biological detection", *Lab Chip*, vol. 7, no. 10, p. 1238, 2007. DOI: 10.1039/b707401h (cited on pp. 1, 2).

[6] J. K. Gimzewski, C. Gerber, E. Meyer, and R. R. Schlittler, "Observation of a Chemical-Reaction Using a Micromechanical Sensor", *Chem. Phys. Lett.*, vol. 217, no. 5-6, pp. 589–594, 1994. DOI: 10.1016/0009-2614(93)E1419-H (cited on p. 1).

[7] A. Boisen, S. Dohn, S. S. Keller, S. Schmid, and M. Tenje, "Cantilever-like micromechanical sensors", *Rep. Prog. Phys.*, vol. 74, no. 3, p. 036 101, 2011. DOI: 10.1088/0034-4885/74/3/036101 (cited on pp. 2, 4, 5).

[8] T. Braun, M. K. Ghatkesar, N. Backmann, W. Grange, P. Boulanger, L. Letellier, H. P. Lang, A. Bietsch, C. Gerber, and M. Hegner, "Quantitative time-resolved measurement of membrane protein–ligand interactions using microcantilever array sensors", *Nat. Nanotechnol.*, vol. 4, no. 3, pp. 179–185, 2009. DOI: 10.1038/NNANO.2008.398 (cited on p. 2).

[9] G. Popescu, K. Park, M. Mir, and R. Bashir, "New technologies for measuring single cell mass", *Lab Chip*, vol. 14, no. 4, p. 646, 2014. DOI: 10.1039/c3lc51033f (cited on p. 2).

[10] M. K. Ghatkesar, V. Barwich, T. Braun, J.-P. Ramseyer, C. Gerber, M. Hegner, H. P. Lang, U. Drechsler, and M. Despont, "Higher modes of vibration increase mass sensitivity in nanomechanical microcantilevers", *Nanotechnology*, vol. 18, no. 44, p. 445 502, 2007. DOI: 10.1088/0957-4484/18/44/445502 (cited on pp. 3, 52, 77).

[11] J. Tamayo, D. Ramos, J. Mertens, and M. Calleja, "Effect of the adsorbate stiffness on the resonance response of microcantilever sensors", *Appl. Phys. Lett.*, vol. 89, no. 22, p. 224 104, 2006. DOI: 10.1063/1.2388925 (cited on p. 3).

[12] R. R. Grüter, Z. Khan, R. Paxman, J. W. Ndieyira, B. Dueck, B. A. Bircher, J. L. Yang, U. Drechsler, M. Despont, R. A. McKendry, and B. W. Hoogenboom, "Disentangling mechanical and mass effects on nanomechanical resonators", *Appl. Phys. Lett.*, vol. 96, no. 2, p. 023 113, 2010. DOI: 10.1063/1.3285169 (cited on p. 3).

[13] M. Spletzer, A. Raman, and R. Reifenberger, "Elastometric sensing using higher flexural eigenmodes of microcantilevers", *Appl. Phys. Lett.*, vol. 91, no. 18, p. 184 103, 2007. DOI: 10.1063/1.2803215 (cited on pp. 3, 52).

[14] S. Dohn, R. Sandberg, W. Svendsen, and A. Boisen, "Enhanced functionality of cantilever based mass sensors using higher modes", *Appl. Phys. Lett.*, vol. 86, no. 23, p. 233 501, 2005. DOI: 10.1063/1.1948521 (cited on pp. 3, 52).

[15] K. Nieradka, H. Stegmann, and T. Gotszalk, "Focused ion beam milling and deposition techniques in validation of mass change value and position determination method for micro and nanomechanical sensors", *J. Appl. Phys.*, vol. 112, no. 11, p. 114 509, 2012. DOI: 10.1063/1.4768715 (cited on p. 3).

[16] I. Stachiv, A. I. Fedorchenko, and Y. L. Chen, "Mass detection by means of the vibrating nanomechanical resonators", *Appl. Phys. Lett.*, vol. 100, no. 9, p. 093 110, 2012. DOI: 10.1063/1.3691195 (cited on p. 3).

[17] D. Kim, S. Hong, J. Jang, and J. Park, "Simultaneous determination of position and mass in the cantilever sensor using transfer function method", *Appl. Phys. Lett.*, vol. 103, no. 3, p. 033 108, 2013. DOI: 10.1063/1.4813839 (cited on p. 3).

[18] M. S. Hanay, S. Kelber, A. K. Naik, D. Chi, S. Hentz, E. C. Bullard, E. Colinet, L. Duraffourg, and M. L. Roukes, "Single-protein nanomechanical mass spectrometryin real time", *Nat. Nanotechnol.*, vol. 7, no. 9, pp. 602–608, 2012. DOI: 10.1038/nnano.2012.119 (cited on p. 3).

[19] T. P. Burg, M. Godin, S. M. Knudsen, W. Shen, G. Carlson, J. S. Foster, K. Babcock, and S. R. Manalis, "Weighing of biomolecules, single cells and single nanoparticles in fluid", *Nature*, vol. 446, no. 7139, pp. 1066–1069, 2007. DOI: 10.1038/nature05741 (cited on p. 3).

[20] S. Olcum, N. Cermak, S. C. Wasserman, K. S. Christine, H. Atsumi, K. R. Payer, W. Shen, J. Lee, A. M. Belcher, S. N. Bhatia, and S. R. Manalis, "Weighing nanoparticles in solution at the attogram scale", *Proc. Natl. Acad. Sci. U.S.A.*, 2014. DOI: 10.1073/pnas.1318602111 (cited on p. 3).

[21] M. M. Modena, Y. Wang, D. Riedel, and T. P. Burg, "Resolution enhancement of suspended microchannel resonators for weighing of biomolecular complexes in solution", *Lab Chip*, vol. 14, no. 2, p. 342, 2013. DOI: 10.1039/c3lc51058a (cited on p. 3).

[22] M. F. Khan, S. Kim, D. Lee, S. Schmid, A. Boisen, and T. Thundat, "Nanomechanical identification of liquid reagents in a microfluidic channel", *Lab Chip*, vol. 14, pp. 1302–1307, 2014. DOI: 10.1039/c3lc51273h (cited on p. 3).

[23] T. Braun, V. Barwich, M. K. Ghatkesar, A. H. Bredekamp, C. Gerber, M. Hegner, and H. P. Lang, "Micromechanical mass sensors for biomolecular detection in a physiological environment", *Phys. Rev. E*, vol. 72, no. 3, p. 031 907, 2005. DOI: 10.1103/PhysRevE.72.031907 (cited on pp. 3, 72, 137).

[24] S. Kim, K. D. Kihm, and T. Thundat, "Fluidic applications for atomic force microscopy (AFM) with microcantilever sensors", *Exp. Fluids*, vol. 48, no. 5, pp. 721–736, 2010. DOI: 10.1007/s00348-010-0830-3 (cited on pp. 3, 10, 68).

[25] A. Labuda, K. Kobayashi, D. Kiracofe, K. Suzuki, P. H. Gruetter, and H. Yamada, "Comparison of photothermal and piezoacoustic excitation methods for frequency and phase modulation atomic force microscopy in liquid environments", *AIP Adv.*, vol. 1, no. 2, 2011. DOI: 10.1063/1.3601872 (cited on pp. 4, 40).

[26] B. W. Hoogenboom, P. L. T. M. Frederix, J. L. Yang, S. J. Martin, Y. Pellmont, M. Steinacher, S. Zach, E. Langenbach, H. J. Heimbeck, A. Engel, and H. J. Hug, "A Fabry–Perot interferometer for micrometer-sized cantilevers", *Appl. Phys. Lett.*, vol. 86, no. 7, pp. 074 101–074 101, 2005. DOI: 10.1063/1.1866229 (cited on p. 4).

[27] S. Nishida, D. Kobayashi, T. Sakurada, T. Nakazawa, Y. Hoshi, and H. Kawakatsu, "Photothermal excitation and laser Doppler velocimetry of higher cantilever vibration modes for dynamic atomic force microscopy in liquid", *Rev. Sci. Instrum.*, vol. 79, no. 12, p. 123 703, 2008. DOI: 10.1063/1.3040500 (cited on p. 5).

[28] J. Tamayo, P. M. Kosaka, J. J. Ruz, Á. San Paulo, and M. Calleja, "Biosensors based on nanomechanical systems", *Chem. Soc. Rev.*, vol. 42, no. 3, p. 1287, 2013. DOI: 10.1039/c2cs35293a (cited on p. 5).

[29] S. R. Turns, "Thermodynamic properties, property relationships and processes", in *Thermodynamics - Concepts and Applications*, Cambridge University Press, 2006, pp. 46–170, ISBN: 978-0521850421 (cited on p. 5).

[30] F. Irgens, *Rheology and Non-Newtonian Fluids*. Springer, 2014, ISBN: 978-3-319-01053-3 (cited on pp. 6, 7, 9).

[31] G. K. Batchelor, *An Introduction to Fluid Dynamics*. Cambridge, UK: Cambridge University Press, 1967, ISBN: 978-0-521-66396-0 (cited on pp. 6, 7, 77).

[32] W. M. Haynes, "Concentrative properties of aqueous solutions: density, refractive index, freezing point depression, and viscosity", in *CRC Handbook of Chemistry and Physics*, CRC Press, 2012, pp. 5–1235–148–, ISBN: 1-4822-0867-9 (cited on pp. 6, 86).

[33] A. Maali, C. Hurth, R. Boisgard, C. Jai, T. Cohen-Bouhacina, and J.-P. Aimé, "Hydrodynamics of oscillating atomic force microscopy cantilevers in viscous fluids", *J. Appl. Phys.*, vol. 97, no. 7, p. 074 907, 2005. DOI: 10.1063/1.1873060 (cited on pp. 7, 27–30, 32, 73, 139).

[34] R. G. Larson, *The structure and rheology of complex fluids*, ser. Topics in Chemical Engineering. New York, Oxford: Oxford University Press, 1999, ISBN: 978-0-19-512197-1 (cited on pp. 7–10, 100).

[35] V. Sharma, A. Jaishankar, Y.-C. Wang, and G. H. McKinley, "Rheology of globular proteins: apparent yield stress, high shear rate viscosity and interfacial viscoelasticity of bovine serum albumin solutions", *Soft Matter*, vol. 7, no. 11, p. 5150, 2011. DOI: 10.1039/c0sm01312a (cited on pp. 8–10, 100).

[36] P. Dontula, C. W. Macosko, and L. E. Scriven, "Does the Viscosity of Glycerin Fall at High Shear Rates?", *Ind. Eng. Chem. Res.*, vol. 38, no. 4, pp. 1729–1735, 1999. DOI: 10.1021/ie9805685 (cited on p. 10).

[37] M. Pelton, D. Chakraborty, E. Malachosky, P. Guyot-Sionnest, and J. Sader, "Viscoelastic Flows in Simple Liquids Generated by Vibrating Nanostructures", *Phys. Rev. Lett.*, vol. 111, no. 24, p. 244 502, 2013. DOI: 10.1103/PhysRevLett.111.244502 (cited on p. 10).

[38] W. P. Cox and E. H. Merz, "Correlation of dynamic and steady flow viscosities", *J. Polym. Sci.*, vol. 28, no. 118, pp. 619–622, 1958. DOI: 10.1002/pol.1958.1202811812 (cited on p. 10).

[39] B. A. Haleem and P. R. Nott, "Rheology of particle-loaded semi-dilute polymer solutions", *J. Rheol.*, vol. 53, no. 2, p. 383, 2009. DOI: 10.1122/1.3073753 (cited on p. 10).

[40] W. M. Kulicke, R. Kniewske, and J. Klein, "Preparation, characterization, solution properties and rheological behaviour of polyacrylamide", *Prog. Polym. Sci.*, vol. 8, no. 4, pp. 373–468, 1982. DOI: 10.1016/0079-6700(82)90004-1 (cited on pp. 10, 82, 141).

[41] M. L. Mather, M. Rides, C. R. G. Allen, and P. E. Tomlins, "Liquid viscoelasticity probed by a mesoscale piezoelectric bimorph cantilever", *J. Rheol.*, vol. 56, no. 1, p. 99, 2012. DOI: 10.1122/1.3670732 (cited on p. 10).

[42] B. Jakoby, R. Beigelbeck, F. Keplinger, F. Lucklum, A. Niedermayer, E. K. Reichel, C. Riesch, T. Voglhuber-Brunnmaier, and B. Weiss, "Miniaturized sensors for the viscosity and density of liquids–performance and issues.", *IEEE Trans Ultrason Ferroelectr Freq Control*, vol. 57, no. 1, pp. 111–120, 2010. DOI: 10.1109/TUFFC.2010.1386 (cited on pp. 10, 86).

[43] P. Rust, I. Leibacher, and J. Dual, "Temperature Controlled Viscosity and Density Measurements on a Microchip with High Resolution and Low Cost", *Procedia Engineering*, vol. 25, pp. 587–590, 2011. DOI: 10.1016/j.proeng.2011.12.146 (cited on p. 10).

[44] S. Inaba, K. Akaishi, T. Mori, and K. Hane, "Analysis of the resonance characteristics of a cantilever vibrated photothermally in a liquid", *J. Appl. Phys.*, vol. 73, no. 6, pp. 2654–2658, 1993. DOI: 10.1063/1.353060 (cited on pp. 10, 40).

[45] P. I. Oden, G. Y. Chen, R. A. Steele, R. J. Warmack, and T. Thundat, "Viscous drag measurements utilizing microfabricated cantilevers", *Appl. Phys. Lett.*, vol. 68, no. 26, pp. 3814–3816, 1996. DOI: 10.1063/1.116626 (cited on p. 10).

[46] M. K. Ghatkesar, E. Rakhmatullina, H. P. Lang, C. Gerber, M. Hegner, and T. Braun, "Multi-parameter microcantilever sensor for comprehensive characterization of Newtonian fluids", *Sens. Actuators B Chem.*, vol. 135, no. 1, pp. 133–138, 2008. DOI: doi:10.1016/j.snb.2008.08.012 (cited on pp. 10, 27, 68).

[47] N. Ahmed, D. F. Nino, and V. T. Moy, "Measurement of solution viscosity by atomic force microscopy", *Rev. Sci. Instrum.*, vol. 72, no. 6, pp. 2731–2734, 2001. DOI: 10.1063/1.1368856 (cited on pp. 10, 68).

[48] O. Cakmak, N. Kilinc, E. Ermek, A. Mostafazadeh, C. Elbuken, G. G. Yaralioglu, and H. Urey, "LoC sensor array platform for real-time coagulation measurements", in *Micro Electro Mechanical Systems (MEMS), 2014 IEEE 27th International Conference on*, 2014, pp. 330–333. DOI: 10.1109/MEMSYS.2014.6765643 (cited on pp. 11, 12).

[49] M. Heinisch, E. K. Reichel, I. Dufour, and B. Jakoby, "Sensors and Actuators A: Physical", *Sens. Actuators A Phys.*, vol. 214, pp. 245–251, 2014. DOI: 10.1016/j.sna.2014.04.020 (cited on pp. 11, 12).

[50] B. A. Bircher, L. Duempelmann, K. Renggli, H. P. Lang, C. Gerber, N. Bruns, and T. Braun, "Real-time viscosity and mass density sensors requiring microliter sample volume based on nanomechanical resonators.", *Anal. Chem.*, vol. 85, no. 18, pp. 8676–8683, 2013. DOI: 10.1021/ac4014918 (cited on pp. 11, 12, 14, 42, 54, 55, 86–89, 93).

[51] O. Cakmak, C. Elbuken, E. Ermek, A. Mostafazadeh, I. Baris, B. E. Alaca, I. H. Kavakli, and H. Urey, "Microcantilever based disposable viscosity sensor for serum and blood plasma measurements", *Methods*, vol. 63, pp. 225–232, 2013. DOI: 10.1016/j.ymeth.2013.07.009 (cited on pp. 11, 12).

[52] D. Hur and J. H. Lee, "Determination of Liquid Density and Viscosity Using a Self-Actuating Microcantilever", *Jpn. J. Appl. Phys.*, vol. 52, p. 056 601, 2013. DOI: 10.7567/JJAP.52.056601 (cited on pp. 11, 12).

[53] P. Rust, D. Cereghetti, and J. Dual, "A micro-liter viscosity and density sensor for the rheological characterization of DNA solutions in the kilo-hertz range", *Lab Chip*, vol. 13, no. 24, p. 4794, 2013. DOI: 10.1039/c3lc50857a (cited on pp. 11, 12, 86, 90).

[54] L. Xu, G. Zhang, L. Zhao, Y. Zhao, Z. Jiang, Rahman-Hebitul, H. Wang, and Z. Liu, "A fluid viscosity sensor with resonant trapezoidal micro cantilever", in *Assembly and Manufacturing (ISAM), 2013 IEEE International Symposium on*, 2013, pp. 131–134. DOI: 10.1109/ISAM.2013.6643507 (cited on pp. 11, 12).

[55] R. Paxman, J. Stinson, A. Dejardin, R. A. McKendry, and B. W. Hoogenboom, "Using Micromechanical Resonators to Measure Rheological Properties and Alcohol Content of Model Solutions and Commercial Beverages", *Sensors*, vol. 12, no. 5, pp. 6497–6507, 2012. DOI: 10.3390/s120506497 (cited on pp. 11, 12, 68, 78, 86).

[56] M. Youssry, N. Belmiloud, B. Caillard, C. Ayela, C. Pellet, and I. Dufour, "A straightforward determination of fluid viscosity and density using microcantilevers: from experimental data to analytical expressions", *Sens. Actuators A Phys.*, vol. 172, pp. 40–46, 2011. DOI: 10.1016/j.sna.2011.02.025 (cited on pp. 11, 12, 68, 78).

[57] M. Hennemeyer, S. Burghardt, and R. W. Stark, "Cantilever micro-rheometer for the characterization of sugar solutions", *Sensors*, vol. 8, no. 1, pp. 10–22, 2008. DOI: 10.3390/s8010010 (cited on pp. 11, 12, 68, 78, 86, 139).

[58] A. M. Schilowitz, D. G. Yablon, E. Lansey, and F. R. Zypman, "Measuring hydrocarbon viscosity with oscillating microcantilevers", *Measurement*, vol. 41, no. 10, pp. 1169–1175, 2008. DOI: 10.1016/j.measurement.2008.03.007 (cited on pp. 11, 12, 86).

[59] N. McLoughlin, S. L. Lee, and G. Hähner, "Temperature dependence of viscosity and density of viscous liquids determined from thermal noise spectra of uncalibrated atomic force microscope cantilevers", *Lab Chip*, vol. 7, no. 8, pp. 1057–1061, 2007. DOI: 10.1039/b705787c (cited on pp. 11, 12, 68).

[60] T. L. Wilson, G. A. Campbell, and R. Mutharasan, "Viscosity and density values from excitation level response of piezoelectric-excited cantilever sensors", *Sens. Actuators A Phys.*, vol. 138, no. 1, pp. 44–51, 2007. DOI: doi:10.1016/j.sna.2007.04.050 (cited on pp. 11, 12, 78).

[61] N. McLoughlin, S. L. Lee, and G. Hähner, "Simultaneous determination of density and viscosity of liquids based on resonance curves of uncalibrated microcantilevers", *Appl. Phys. Lett.*, vol. 89, p. 184 106, 2006. DOI: 10.1063/1.2374867 (cited on pp. 11, 12, 68).

[62] M. Papi, G. Arcovito, M. De Spirito, M. Vassalli, and B. Tiribilli, "Fluid viscosity determination by means of uncalibrated atomic force microscopy cantilevers", *Appl. Phys. Lett.*, vol. 88, no. 19, 2006. DOI: 10.1063/1.2200588 (cited on pp. 11, 12).

[63] S. Boskovic, J. W. M. Chon, P. Mulvaney, and J. E. Sader, "Rheological measurements using microcantilevers", *J. Rheol.*, vol. 46, no. 4, pp. 891–899, 2002. DOI: 10.1122/1.1475978 (cited on pp. 11, 12, 68, 73, 86).

[64] C. Bergaud and L. Nicu, "Viscosity measurements based on experimental investigations of composite cantilever beam eigenfrequencies in viscous media", *Rev. Sci. Instrum.*, vol. 71, no. 6, pp. 2487–2491, 2000. DOI: 10.1063/1.1150640 (cited on pp. 11, 12, 27, 68).

[65] W. Y. Shih, X. Li, H. Gu, W.-H. Shih, and I. A. Aksay, "Simultaneous liquid viscosity and density determination with piezoelectric unimorph cantilevers", *J. Appl. Phys.*, vol. 89, no. 2, p. 1497, 2001. DOI: 10.1063/1.1287606 (cited on p. 11).

[66] M. Villa and M. Paul, "Stochastic dynamics of micron-scale doubly clamped beams in a viscous fluid", *Phys. Rev. E*, vol. 79, no. 5, p. 056 314, 2009. DOI: 10.1103/PhysRevE.79.056314 (cited on p. 11).

[67] B. Weiss, E. K. Reichel, and B. Jakoby, "Modeling of a clamped–clamped beam vibrating in a fluid for viscosity and density sensing regarding compressibility", *Sens. Actuators A Phys.*, vol. 143, no. 2, pp. 293–301, 2008. DOI: 10.1016/j.sna.2007.11.029 (cited on p. 11).

[68] C. Riesch, F. Keplinger, E. K. Reichel, and B. Jakoby, "Frequency response of a micromachined doubly-clamped vibrating beam for the measurement of liquid properties", in *2008 IEEE International Ultrasonics Symposium Proceedings*, IEEE, 2008, pp. 1022–1025, ISBN: 978-1-4244-2428-3. DOI: 10.1109/ULTSYM.2008.0247 (cited on p. 11).

[69] E. K. Reichel, B. Weiss, C. Riesch, A. Jachimowicz, and B. Jakoby, "A novel micromachined liquid property sensor utilizing a doubly clamped vibrating beam", in *Proc. Eurosensors XX*, Göteborg, Sweden, 2006, pp. 114–115 (cited on p. 11).

[70] R. Cox, F. Josse, S. M. Heinrich, O. Brand, and I. Dufour, "Characteristics of laterally vibrating resonant microcantilevers in viscous liquid media", *J. Appl. Phys.*, vol. 111, p. 014 907, 2012. DOI: 10.1063/1.3674278 (cited on p. 11).

[71] B. N. Johnson and R. Mutharasan, "Persistence of bending and torsional modes in piezoelectric-excited millimeter-sized cantilever (PEMC) sensors in viscous liquids - 1 to 10^3 cP", *J. Appl. Phys.*, vol. 109, no. 6, p. 066 105, 2011. DOI: 10.1063/1.3554677 (cited on p. 11).

[72] M. F. Khan, S. Schmid, P. E. Larsen, Z. J. Davis, W. Yan, E. H. Stenby, and A. Boisen, "Sensors and Actuators B: Chemical", *Sens. Actuators B Chem.*, vol. 185, pp. 456–461, 2013. DOI: 10.1016/j.snb.2013.04.095 (cited on pp. 11, 86).

[73] E. Lemaire, B. Caillard, M. Youssry, and I. Dufour, "High-frequency viscoelastic measurements of fluids based on microcantilever sensing: New modeling and experimental issues", *Sens. Actuators A Phys.*, vol. 201, pp. 230–240, 2013. DOI: 10.1016/j.sna.2013.07.022 (cited on pp. 12, 100).

[74] I. Dufour, E. Lemaire, and B. Caillard, "MEMS-based Measurement of Rheological Fluid Properties", in *Proceedings SENSOR 2013*, 2013, pp. 598–603. DOI: 10.5162/sensor2013/D7.4 (cited on p. 12).

[75] I. Dufour, A. Maali, Y. Amarouchene, C. Ayela, B. Caillard, A. Darwiche, M. Guirardel, H. Kellay, E. Lemaire, F. Mathieu, C. Pellet, D. Saya, M. Youssry, L. Nicu, and A. Colin, "The Microcantilever: A Versatile Tool for Measuring the Rheological Properties of Complex Fluids", *Journal of Sensors*, vol. 2012, p. ID 719898, 2012. DOI: 10.1155/2012/719898 (cited on p. 12).

[76] M. Youssry, B. Caillard, C. Ayela, C. Pellet, and I. Dufour, "Microrheology of Newtonian Fluids using Microcantilever", in *Proceedings of the IASTED International Conference Nanotechnology and Applications (NANA 2010)*, Cambridge, Massachusetts, USA: ACTA Press, 2010, pp. 540–546. DOI: 10.2316/P2010.707-018 (cited on p. 12).

[77] N. Belmiloud, I. Dufour, A. Colin, and L. Nicu, "Vibrating Microcantilevers : Tools for Microrheology", in *THE XV INTERNATIONAL CONGRESS ON RHEOLOGY: The Society of Rheology 80th Annual Meeting*, AIP, 2008, pp. 1159–1161. DOI: 10.1063/1.2964501 (cited on p. 12).

[78] S. Cerimovic, R. Beigelbeck, H. Antlinger, J. Schalko, B. Jakoby, and F. Keplinger, "Sensing viscosity and density of glycerol–water mixtures utilizing a suspended plate MEMS resonator", *Microsys. Technol.*, 2012. DOI: 10.1007/s00542-012-1437-9 (cited on p. 12).

[79] C. Riesch, E. K. Reichel, A. Jachimowicz, J. Schalko, P. Hudek, B. Jakoby, and F. Keplinger, "A suspended plate viscosity sensor featuring in-plane vibration and piezoresistive readout", *J. Micromech. Microeng.*, vol. 19, no. 7, p. 075 010, 2009. DOI: 10.1088/0960-1317/19/7/075010 (cited on pp. 12, 68).

[80] O. Brand, J. M. English, S. A. Bidstrup, and M. Allen, "Micromachined viscosity sensor for real-time polymerization monitoring", in *Solid State Sensors and Actuators, 1997. TRANSDUCERS '97 Chicago., 1997 International Conference on*, 1997, pp. 121–124. DOI: 10.1109/SENSOR.1997.613597 (cited on p. 12).

[81] K. Waszczuk, T. Piasecki, K. Nitsch, and T. Gotszalk, "Application of piezoelectric tuning forks in liquid viscosity and density measurements", *Sens. Actuators B Chem.*, vol. 160, no. 1, pp. 517–523, 2011. DOI: 10.1016/j.snb.2011.08.020 (cited on p. 12).

[82] H. Helle, H. Välimäki, and J. Lekkala, "Comparing a 10 MHz thickness–shear mode quartz resonator with a commercial process viscometer in monitoring resol manufacture process", *Sens. Actuators B Chem.*, vol. 81, no. 2, pp. 133–140, 2002. DOI: 10.1016/S0925-4005(01)00943-1 (cited on p. 12).

[83] K. Han, K. Zhu, and G. Bahl, "Opto-mechano-fluidic viscometer", *Appl. Phys. Lett.*, vol. 105, no. 1, p. 014 103, 2014. DOI: 10.1063/1.4887369 (cited on p. 12).

[84] I. Sinn, T. Albertson, P. Kinnunen, D. N. Breslauer, B. H. McNaughton, M. A. Burns, and R. Kopelman, "Asynchronous Magnetic Bead Rotation Microviscometer for Rapid, Sensitive, and Label-Free Studies of Bacterial Growth and Drug Sensitivity", *Anal. Chem.*, vol. 84, no. 12, pp. 5250–5256, 2012. DOI: 10.1021/ac300128p (cited on p. 12).

[85] Y. Zhang, X. Wu, Y. Wang, S. Zhu, B. Z. Gao, and X.-C. Yuan, "Measurement of the microscopic viscosities of microfluids with a dynamic optical tweezers system", *Laser Phys.*, vol. 24, no. 6, p. 065 601, 2014. DOI: 10.1088/1054-660X/24/6/065601 (cited on p. 12).

[86] S. Parkin, G. Knöner, T. Nieminen, N. Heckenberg, and H. Rubinsztein-Dunlop, "Picoliter viscometry using optically rotated particles", *Phys. Rev. E*, vol. 76, no. 4, 2007. DOI: 10.1103/PhysRevE.76.041507 (cited on p. 12).

[87] R. Patois, P. Vairac, and B. Cretin, "Near-field acoustic densimeter and viscosimeter", *Rev. Sci. Instrum.*, vol. 71, no. 10, p. 3860, 2000. DOI: 10.1063/1.1286308 (cited on p. 12).

[88] X. Tang and B. Zheng, "A PDMS viscometer for assaying endoglucanase activity", *Analyst*, vol. 136, no. 6, p. 1222, 2011. DOI: 10.1039/c0an00913j (cited on p. 12).

[89] N. Srivastava and M. A. Burns, "Analysis of Non-Newtonian Liquids Using a Microfluidic Capillary Viscometer", *Anal. Chem.*, vol. 78, no. 5, pp. 1690–1696, 2006. DOI: 10.1021/ac0518046 (cited on p. 12).

[90] C. J. Pipe and G. H. McKinley, "Microfluidic rheometry", *Mech. Res. Commun.*, vol. 36, no. 1, pp. 110–120, 2009. DOI: 10.1016/j.mechrescom.2008.08.009 (cited on pp. 12, 68).

[91] J. Lee and A. Tripathi, "Intrinsic Viscosity of Polymers and Biopolymers Measured by Microchip", *Anal. Chem.*, vol. 77, no. 22, pp. 7137–7147, 2005. DOI: 10.1021/ac050932r (cited on pp. 12, 68).

[92] S. Choi and J.-K. Park, "Microfluidic Rheometer for Characterization of Protein Unfolding and Aggregation in Microflows", *Small*, vol. 6, no. 12, pp. 1306–1310, 2010. DOI: 10.1002/smll.201000210 (cited on pp. 12, 86, 100).

[93] Y. J. Kang, S. Y. Yoon, K.-H. Lee, and S. Yang, "A Highly Accurate and Consistent Microfluidic Viscometer for Continuous Blood Viscosity Measurement", *Artificial Organs*, vol. 34, no. 11, pp. 944–949, 2010. DOI: 10.1111/j.1525-1594.2010.01078.x (cited on p. 12).

[94] N. Jiang, J. Fan, S. Zhang, T. Wu, J. Wang, P. Gao, J. Qu, F. Zhou, and X. Peng, "Sensors and Actuators B: Chemical", *Sens. Actuators B Chem.*, vol. 190, pp. 685–693, 2014. DOI: 10.1016/j.snb.2013.09.062 (cited on p. 12).

[95] C. Hurth, B. Duane, D. Whitfield, S. Smith, A. Nordquist, and F. Zenhausern, "Automation of a high-speed imaging setup for differential viscosity measurements", *J. Appl. Phys.*, vol. 114, no. 24, p. 244 701, 2013. DOI: 10.1063/1.4840855.1 (cited on p. 12).

[96] B. A. Bircher, L. Duempelmann, H. P. Lang, C. Gerber, and T. Braun, "Photothermal excitation of microcantilevers in liquid: effect of the excitation laser position on temperature and vibrational amplitude", *Micro Nano Lett.*, vol. 8, no. 11, pp. 770–774, 2013. DOI: 10.1049/mnl.2013.0352 (cited on pp. 14, 53, 54, 63).

[97] B. A. Bircher, R. Krenger, and T. Braun, "Influence of squeeze film damping on higher-mode microcantilever vibrations in liquid", *EPJ Tech. Instrum.*, vol. 1, p. 10, 2014. DOI: 10.1140/epjti/s40485-014-0010-6 (cited on pp. 14, 90).

[98] J.-S. Wenzler, M. Imboden, T. Dunn, D. G. Mohanty, and. Pritiraj, "Nanomechanical Resonators", in *Handbook of Nanophysics: Functional Nanomaterials*, CRC Press, 2010, pp. 1–21, ISBN: 9781420075526 (cited on pp. 15, 17–19).

[99] J. M. Knudsen and P. G. Hjorth, "Harmonic Oscillators", in *Elements of Newtonian Mechanics*, Berlin Heidelberg: Springer, 2000, pp. 389–409, ISBN: 978-3-642-57234-0 (cited on pp. 15, 17).

[100] S. M. Han, H. Benaroya, and T. Wei, "Dynamics of transversely vibrating beams using four engineering theories", *J. Sound. Vib.*, vol. 225, no. 5, pp. 935–988, 1999. DOI: 10.1006/jsvi.1999.2257 (cited on p. 18).

[101] M. I. Younis, *MEMS Linear and Nonlinear Statics and Dynamics*. Springer, 2011, ISBN: 978-1-4419-6020-7. DOI: 10.1007/978-1-4419-6020-7 (cited on pp. 19, 20).

[102] M. Hoummady, E. Farnault, T. Yahiro, and H. Kawakatsu, "Simultaneous optical detection techniques, interferometry, and optical beam deflection for dynamic mode control of scanning force microscopy", *J. Vac. Sci. Technol. B*, vol. 15, no. 4, pp. 1539–1542, 1997. DOI: 10.1116/1.589395 (cited on p. 22).

[103] T. E. Schäffer and H. Fuchs, "Optimized detection of normal vibration modes of atomic force microscope cantilevers with the optical beam deflection method", *J. Appl. Phys.*, vol. 97, no. 8, p. 083 524, 2005. DOI: 10.1063/1.1872202 (cited on p. 23).

[104] D. Ramos, J. Tamayo, J. Mertens, and M. Calleja, "Photothermal excitation of microcantilevers in liquids", *J. Appl. Phys.*, vol. 99, no. 12, p. 124 904, 2006. DOI: 10.1063/1.2205409 (cited on pp. 23, 40, 43, 75).

[105] F. Lochon, I. Dufour, and D. Rebiere, "An alternative solution to improve sensitivity of resonant microcantilever chemical sensors: comparison between using high-order modes and reducing dimensions", *Sens. Actuators B Chem.*, vol. 108, pp. 979–985, 2005. DOI: 10.1016/j.snb.2004.11.086 (cited on pp. 23, 130).

[106] J. Kokavecz and A. Mechler, "Spring constant of microcantilevers in fundamental and higher eigenmodes", *Phys. Rev. B*, vol. 78, no. 17, p. 172 101, 2008. DOI: 10.1103/PhysRevB.78.172101 (cited on pp. 24, 75).

[107] A. T. Jones, "Vibration of beams immersed in a liquid", *Exp. Mech.*, vol. 10, no. 2, pp. 84–88, 1970. DOI: 10.1007/BF02320137 (cited on p. 25).

[108] T. Naik, E. K. Longmire, and S. C. Mantell, "Dynamic response of a cantilever in liquid near a solid wall", *Sens. Actuators A Phys.*, vol. 102, no. 3, pp. 240–254, 2003. DOI: 10.1016/S0924-4247(02)00398-9 (cited on pp. 25, 53, 57, 62).

[109] F. Lochon, I. Dufour, and D. Rebiere, "A microcantilever chemical sensors optimization by taking into account losses", *Sens. Actuators B Chem.*, vol. 118, no. 1-2, pp. 292–296, 2006. DOI: 10.1016/j.snb.2006.04.034 (cited on pp. 27, 77).

[110] D. Kiracofe and A. Raman, "On eigenmodes, stiffness, and sensitivity of atomic force microscope cantilevers in air versus liquids", *J. Appl. Phys.*, vol. 107, no. 3, pp. –, 2010. DOI: 10.1063/1.3284206 (cited on p. 27).

[111] J. E. Sader, "Frequency response of cantilever beams immersed in viscous fluids with applications to the atomic force microscope", *J. Appl. Phys.*, vol. 84, no. 1, pp. 64–76, 1998. DOI: 10.1063/1.368002 (cited on pp. 27–30, 68, 72, 86).

[112] C. Vančura, I. Dufour, S. M. Heinrich, F. Josse, and A. Hierlemann, "Analysis of resonating microcantilevers operating in a viscous liquid environment", *Sens. Actuators A Phys.*, vol. 141, no. 1, pp. 43–51, 2008. DOI: doi:10.1016/j.sna.2007.07.010 (cited on pp. 27, 73).

[113] C. A. Van Eysden and J. E. Sader, "Small amplitude oscillations of a flexible thin blade in a viscous fluid: Exact analytical solution", *Phys. Fluids*, vol. 18, no. 12, p. 123 102, 2006. DOI: 10.1063/1.2395967 (cited on pp. 27, 73).

[114] H. Bruus, *Theoretical Microfluidics*, ser. Oxford Master Series in Physics. Oxford University Press, 2008, ISBN: 978-0-19-923508-7 (cited on pp. 27, 29, 32).

[115] L. Bocquet and E. Charlaix, "Nanofluidics, from bulk to interfaces", *Chem. Soc. Rev.*, vol. 39, no. 3, p. 1073, 2010. DOI: 10.1039/b909366b (cited on p. 27).

[116] J. W. M. Chon, P. Mulvaney, and J. E. Sader, "Experimental validation of theoretical models for the frequency response of atomic force microscope cantilever beams immersed in fluids", *J. Appl. Phys.*, vol. 87, no. 8, pp. 3978–3988, 2000. DOI: 10.1063/1.372455 (cited on pp. 27, 30, 68).

[117] M. K. Ghatkesar, T. Braun, V. Barwich, J.-P. Ramseyer, C. Gerber, M. Hegner, and H. P. Lang, "Resonating modes of vibrating microcantilevers in liquid", *Appl. Phys. Lett.*, vol. 92, no. 4, p. 043 106, 2008. DOI: 10.1063/1.2838295 (cited on pp. 27, 68).

[118] J. Jensen and M. Hegner, "Predictions of the Compressible Fluid Model and its Comparison to Experimental Measurements of Q Factors and Flexural Resonance Frequencies for Microcantilevers", *Journal of Sensors*, vol. 2012, p. ID 258381, 2012. DOI: 10.1155/2012/258381 (cited on pp. 27, 33).

[119] F.-J. Elmer and M. Dreier, "Eigenfrequencies of a rectangular atomic force microscope cantilever in a medium", *J. Appl. Phys.*, vol. 81, no. 12, pp. 7709–7714, 1997. DOI: 10.1063/1.365379 (cited on p. 28).

[120] Y. Hirai, R. Mori, H. Kikuta, N. Kato, K. Inoue, and Y. Tanaka, "Resonance characteristics of micro cantilever in liquid", *Jpn. J. Appl. Phys.*, vol. 37, no. 12B, pp. 7064–7069, 1998. DOI: 10.1143/JJAP.37.7064 (cited on p. 28).

[121] S. Kirstein, M. Mertesdorf, and M. Schonhoff, "The influence of a viscous fluid on the vibration dynamics of scanning near-field optical microscopy fiber probes and atomic force microscopy cantilevers", *J. Appl. Phys.*, vol. 84, no. 4, pp. 1782–1790, 1998. DOI: 10.1063/1.368335 (cited on pp. 28, 29).

[122] T. Açıkalın, A. Raman, and S. V. Garimella, "Two-dimensional streaming flows induced by resonating, thin beams", *J. Acoust. Soc. Am.*, vol. 114, no. 4, pp. 1785–1795, 2003. DOI: 10.1121/1.1610453 (cited on p. 28).

[123] C. P. Green and J. E. Sader, "Frequency response of cantilever beams immersed in viscous fluids near a solid surface with applications to the atomic force microscope", *J. Appl. Phys.*, vol. 98, no. 11, p. 114 913, 2005. DOI: 10.1063/1.2136418 (cited on pp. 28, 29, 31, 52, 53, 63, 71).

[124] C. A. Van Eysden and J. E. Sader, "Resonant frequencies of a rectangular cantilever beam immersed in a fluid", *J. Appl. Phys.*, vol. 100, no. 11, p. 114 916, 2006. DOI: 10.1063/1.2401053 (cited on pp. 28, 73, 74).

[125] C. A. Van Eysden and J. E. Sader, "Frequency response of cantilever beams immersed in viscous fluids with applications to the atomic force microscope: arbitrary mode order", *J. Appl. Phys.*, vol. 101, no. 4, p. 044 908, 2007. DOI: 10.1063/1.2654274 (cited on pp. 28–31, 33, 34, 56, 57, 64, 68, 72–74, 80, 82, 86, 93, 132).

[126] D. W. Dareing, D. Yi, and T. Thundat, "Vibration response of microcantilevers bounded by a confined fluid", *Ultramicroscopy*, vol. 107, no. 10-11, pp. 1105–1110, 2007. DOI: 10.1016/j.ultramic.2007.02.048 (cited on pp. 28, 52).

[127] R. C. Tung, A. Jana, and A. Raman, "Hydrodynamic loading of microcantilevers oscillating near rigid walls", *J. Appl. Phys.*, vol. 104, no. 11, p. 114 905, 2008. DOI: 10.1063/1.3033499 (cited on pp. 28, 29, 31, 32, 52, 53, 56, 61, 63, 64, 129, 132–134).

[128] C. A. Van Eysden and J. E. Sader, "Frequency response of cantilever beams immersed in compressible fluids with applications to the atomic force microscope", *J. Appl. Phys.*, vol. 106, no. 9, p. 094 904, 2009. DOI: 10.1063/1.3254191 (cited on pp. 28, 29, 33, 73).

[129] D. R. Brumley, M. Willcox, and J. E. Sader, "Oscillation of cylinders of rectangular cross section immersed in fluid", *Phys. Fluids*, vol. 22, no. 5, p. 052 001, 2010. DOI: 10.1063/1.3397926 (cited on pp. 28, 29).

[130] M. T. Clark, J. E. Sader, J. P. Cleveland, and M. R. Paul, "Spectral properties of microcantilevers in viscous fluid", *Phys. Rev. E*, vol. 81, no. 4, p. 046 306, 2010. DOI: 10.1103/PhysRevE.81.046306 (cited on pp. 28, 29).

[131] M. Aureli, C. Pagano, and M. Porfiri, "Nonlinear finite amplitude torsional vibrations of cantilevers in viscous fluids", *J. Appl. Phys.*, vol. 111, no. 12, p. 124 915, 2012. DOI: 10.1063/1.4730383 (cited on pp. 28, 29).

[132] M. Aureli, M. E. Basaran, and M. Porfiri, "Nonlinear finite amplitude vibrations of sharp-edged beams in viscous fluids", *J. Sound. Vib.*, vol. 331, no. 7, pp. 1624–1654, 2012. DOI: 10.1016/j.jsv.2011.12.007 (cited on pp. 28, 29, 32, 73).

[133] E. Grimaldi, M. Porfiri, and L. Soria, "Finite amplitude vibrations of a sharp-edged beam immersed in a viscous fluid near a solid surface", *J. Appl. Phys.*, vol. 112, no. 10, p. 104 907, 2012. DOI: 10.1063/1.4765029 (cited on pp. 28, 29, 53).

[134] A. L. Facci and M. Porfiri, "Analysis of three-dimensional effects in oscillating cantilevers immersed in viscous fluids", *J Fluid. Struct.*, vol. 38, pp. 205–222, 2013. DOI: 10.1016/j.jfluidstructs.2012.11.006 (cited on pp. 28–30).

[135] C. N. Phan, M. Aureli, and M. Porfiri, "Finite amplitude vibrations of cantilevers of rectangular cross sections in viscous fluids", *J Fluid. Struct.*, vol. 40, no. C, pp. 52–69, 2013. DOI: 10.1016/j.jfluidstructs.2013.03.013 (cited on pp. 28, 29).

[136] B. A. Bircher, "Micromechanical Real-Time Sensors to Measure the Viscosity and Density of Liquids", Master's thesis, University of Basel, 2010 (cited on p. 30).

[137] R. J. Clarke, S. M. COX, P. M. Williams, and O. E. Jensen, "The drag on a microcantilever oscillating near a wall", *J. Fluid Mech.*, vol. 545, pp. 397–426, 2005. DOI: 10.1017/S0022112005006907 (cited on p. 31).

[138] R. F. Berg, M. Yao, and C. H. Panzarella, "Hydrodynamic Force on a Cylinder Oscillating at Low Frequency", Tech. Rep. NASA/CR-2007-215050, E-16266, 2007 (cited on p. 32).

[139] M. Tatsuno and P. W. Bearman, "A Visual Study of the Flow Around an Oscillating Circular-Cylinder at Low Keulegan-Carpenter Numbers and Low Stokes Numbers", *J. Fluid Mech.*, vol. 211, pp. 157–182, 1990. DOI: 10.1017/S0022112090001537 (cited on p. 32).

[140] V. A. Del Grosso and C. W. Mader, "Speed of sound in pure water", *J. Acoust. Soc. Am.*, vol. 52, p. 1442, 1972. DOI: 10.1121/1.1913258 (cited on p. 33).

[141] N. Jalili and K. Laxminarayana, "A review of atomic force microscopy imaging systems: application to molecular metrology and biological sciences", *Mechatronics*, vol. 14, no. 8, pp. 907–945, 2004. DOI: 10.1016/j.mechatronics.2004.04.005 (cited on p. 40).

[142] B. N. Johnson and R. Mutharasan, "Biosensing using dynamic-mode cantilever sensors: A review", *Biosens. Bioelectron.*, vol. 32, no. 1, pp. 1–18, 2012. DOI: 10.1016/j.bios.2011.10.054 (cited on pp. 40, 49).

[143] T. E. Schäffer, J. P. Cleveland, F. Ohnesorge, D. A. Walters, and P. K. Hansma, "Studies of vibrating atomic force microscope cantilevers in liquid", *J. Appl. Phys.*, vol. 80, no. 7, pp. 3622–3627, 1996. DOI: 10.1063/1.363308 (cited on p. 40).

[144] A. Maali, C. Hurth, T. Cohen-Bouhacina, G. Couturier, and J.-P. Aimé, "Improved acoustic excitation of atomic force microscope cantilevers in liquids", *Appl. Phys. Lett.*, vol. 88, no. 16, p. 163 504, 2006. DOI: 10.1063/1.2196052 (cited on p. 40).

[145] H. Asakawa and T. Fukuma, "Spurious-free cantilever excitation in liquid by piezoactuator with flexure drive mechanism", *Rev. Sci. Instrum.*, vol. 80, no. 10, p. 103 703, 2009. DOI: 10.1063/1.3238484 (cited on p. 40).

[146] W. Han, S. M. Lindsay, and T. Jing, "A magnetically driven oscillating probe microscope for operation in liquids", *Appl. Phys. Lett.*, vol. 69, no. 26, pp. 4111–4113, 1996. DOI: 10.1063/1.117835 (cited on p. 40).

[147] S. Venkatesh and B. Culshaw, "Optically activated vibrations in a micromachined silica structure", *Electron. Lett.*, vol. 21, no. 8, pp. 315–317, 1985. DOI: 10.1049/el:19850223 (cited on p. 40).

[148] T. S. J. Lammerink, M. Elwenspoek, and J. H. J. Fluitman, "Optical excitation of micro-mechanical resonators", in *IEEE Micro Electro Mechanical Systems, MEMS 1991*, Nara, Japan: IEEE, 1991, pp. 160–165, ISBN: 0-87942-641-1. DOI: 10.1109/MEMSYS.1991.114788 (cited on p. 40).

[149] G. C. Ratcliff, D. A. Erie, and R. Superfine, "Photothermal modulation for oscillating mode atomic force microscopy in solution", *Appl. Phys. Lett.*, vol. 72, no. 15, pp. 1911–1913, 1998. DOI: 10.1063/1.121224 (cited on p. 40).

[150] A. Labuda, K. Kobayashi, Y. Miyahara, and P. H. Grütter, "Retrofitting an atomic force microscope with photothermal excitation for a clean cantilever response in low Q environments", *Rev. Sci. Instrum.*, vol. 83, no. 5, p. 053 703, 2012. DOI: 10.1063/1.4712286.1 (cited on p. 40).

[151] S. W. Stahl, E. M. Puchner, and H. E. Gaub, "Photothermal cantilever actuation for fast single-molecule force spectroscopy", *Rev. Sci. Instrum.*, vol. 80, no. 7, p. 073 702, 2009. DOI: 10.1063/1.3157466 (cited on p. 40).

[152] D. Ramos, J. Mertens, M. Calleja, and J. Tamayo, "Phototermal self-excitation of nanomechanical resonators in liquids", *Appl. Phys. Lett.*, vol. 92, no. 17, p. 173 108, 2008. DOI: 10.1063/1.2917718 (cited on p. 40).

[153] S. Nishida, D. Kobayashi, H. Kawakatsu, and Y. Nishimori, "Photothermal excitation of a single-crystalline silicon cantilever for higher vibration modes in liquid", *J. Vac. Sci. Technol. B*, vol. 27, no. 2, pp. 964–968, 2009. DOI: 10.1116/1.3077487 (cited on pp. 40, 76).

[154] S. Wang, X. Wang, Y. Liu, and B. Huang, "Parameter optimization of microcantilevers optically excited by a semiconductor laser with optical feedback", *Optik*, vol. 120, no. 13, pp. 676–682, 2009. DOI: 10.1016/j.ijleo.2008.02.019 (cited on p. 40).

[155] B. Ilic, S. Krylov, and H. G. Craighead, "Theoretical and experimental investigation of optically driven nanoelectromechanical oscillators", *J. Appl. Phys.*, vol. 107, no. 3, p. 034 311, 2010. DOI: 10.1063/1.3305464 (cited on pp. 40, 42).

[156] D. Kiracofe, K. Kobayashi, A. Labuda, A. Raman, and H. Yamada, "High efficiency laser photothermal excitation of microcantilever vibrations in air and liquids", *Rev. Sci. Instrum.*, vol. 82, no. 1, p. 013 702, 2011. DOI: 10.1063/1.3518965 (cited on p. 40).

[157] S. Kim and K. D. Kihm, "Experimental verification of the temperature effects on Sader's model for multilayered cantilevers immersed in an aqueous medium", *Appl. Phys. Lett.*, vol. 89, no. 6, p. 061 918, 2006. DOI: 10.1063/1.2240737 (cited on pp. 40, 77).

[158] J. R. Barnes, R. J. Stephenson, C. N. Woodburn, S. J. O'Shea, M. E. Welland, T. Rayment, J. K. Gimzewski, and C. Gerber, "A femtojoule calorimeter using micromechanical sensors", *Rev. Sci. Instrum.*, vol. 65, no. 12, pp. 3793–3798, 1994. DOI: 10.1063/1.1144509 (cited on pp. 40, 42).

[159] M. Vassalli, V. Pini, and B. Tiribilli, "Role of the driving laser position on atomic force microscopy cantilevers excited by photothermal and radiation pressure effects", *Appl. Phys. Lett.*, vol. 97, no. 14, p. 143 105, 2010. DOI: 10.1063/1.3497074 (cited on pp. 40, 43).

[160] M. A. C. de Araújo, R. Silva, E. de Lima, D. P. Pereira, and P. C. de Oliveira, "Measurement of Gaussian laser beam radius using the knife-edge technique: improvement on data analysis.", *Appl. Opt.*, vol. 48, no. 2, pp. 393–396, 2009. DOI: 10.1364/AO.48.000393 (cited on pp. 41, 106).

[161] R. Mishra, W. Grange, and M. Hegner, "Rapid and reliable calibration of laser beam deflection system for microcantilever-based sensor setups", *Journal of Sensors*, vol. 2012, p. ID 617386, 2012. DOI: 10.1155/2012/617386 (cited on p. 41).

[162] D. Ramos, J. Mertens, M. Calleja, and J. Tamayo, "Study of the origin of bending induced by bimetallic effect on microcantilever", *Sensors*, vol. 7, no. 9, pp. 1757–1765, 2007. DOI: 10.3390/s7091757 (cited on p. 42).

[163] S. Shen, A. Narayanaswamy, S. Goh, and G. Chen, "Thermal conductance of bimaterial microcantilevers", *Appl. Phys. Lett.*, vol. 92, no. 6, p. 063 509, 2008. DOI: 10.1063/1.2829999 (cited on pp. 42, 44).

[164] C. Liu, D. Zhang, H. Zhang, and J. Z. Jiang, "Dynamic characteristics of micro-optothermal expansion and optothermal microactuators", *Micro Nano Lett.*, vol. 4, no. 1, pp. 9–15, 2009. DOI: 10.1049/mnl:20080044 (cited on pp. 42, 47).

[165] B. G. Burke and D. A. LaVan, "Laser heating and detection of bilayer microcantilevers for non-contact thermodynamic measurements", *Appl. Phys. Lett.*, vol. 102, no. 2, p. 021 916, 2013. DOI: 10.1063/1.4776197 (cited on pp. 42, 45, 47).

[166] A. M. Moulin, R. J. Stephenson, and M. E. Welland, "Micromechanical thermal sensors: Comparison of experimental results and simulations", *J. Vac. Sci. Technol. B*, vol. 15, no. 3, pp. 590–596, 1997. DOI: 10.1116/1.589297 (cited on p. 42).

[167] *COMSOL Multiphysics - Modeling Guide, VERSION 3.5a*, COMSOL, 2008 (cited on p. 43).

[168] P. Paolino, B. Tiribilli, and L. Bellon, "Direct measurement of spatial modes of a microcantilever from thermal noise", *J. Appl. Phys.*, vol. 106, no. 9, p. 094 313, 2009. DOI: 10.1063/1.3245394 (cited on p. 44).

[169] C. Canetta and A. Narayanaswamy, "Sub-picowatt resolution calorimetry with a bimaterial microcantilever sensor", *Appl. Phys. Lett.*, vol. 102, no. 10, p. 103 112, 2013. DOI: 10.1063/1.4795625 (cited on p. 47).

[170] S. Joshi, S. Hung, and S. Vengallatore, "Design strategies for controlling damping in micromechanical and nanomechanical resonators", *EPJ Tech. Instrum.*, vol. 1, p. 5, 2014. DOI: 10.1186/epjti5 (cited on p. 52).

[171] S. Basak, A. Raman, and S. V. Garimella, "Hydrodynamic loading of microcantilevers vibrating in viscous fluids", *J. Appl. Phys.*, vol. 99, no. 11, p. 114 906, 2006. DOI: 10.1063/1.2202232 (cited on pp. 52, 57, 64).

[172] C. Harrison, E. Tavernier, O. Vancauwenberghe, E. Donzier, K. Hsu, A. R. H. Goodwin, F. Marty, and B. Mercier, "On the response of a resonating plate in a liquid near a solid wall", *Sens. Actuators A Phys.*, vol. 134, no. 2, pp. 414–426, 2007. DOI: 10.1016/j.sna.2006.06.023 (cited on pp. 52, 53, 62).

[173] P. Decuzzi, A. Granaldi, and G. Pascazio, "Dynamic response of microcantilever-based sensors in a fluidic chamber", *J. Appl. Phys.*, vol. 101, no. 2, p. 024 303, 2007. DOI: 10.1063/1.2426966 (cited on p. 52).

[174] R. Garcia and E. T. Herruzo, "The emergence of multifrequency force microscopy", *Nat. Nanotechnol.*, vol. 7, no. 4, pp. 217–226, 2012. DOI: 10.1038/nnano.2012.38 (cited on pp. 52, 64).

[175] M. Kawakami, Y. Taniguchi, Y. Hiratsuka, M. Shimoike, and D. A. Smith, "Reduction of the damping on an AFM cantilever in fluid by the use of micropillars", *Langmuir*, vol. 26, no. 2, pp. 1002–1007, 2010. DOI: 10.1021/la902472h (cited on p. 52).

[176] A. Maali, T. Cohen-Bouhacina, C. Jai, C. Hurth, R. Boisgard, J.-P. Aimé, D. Mariolle, and F. Bertin, "Reduction of the cantilever hydrodynamic damping near a surface by ion-beam milling", *J. Appl. Phys.*, vol. 99, no. 2, p. 024 908, 2006. DOI: 10.1063/1.2163996 (cited on pp. 52, 57).

[177] M. Bao and H. Yang, "Squeeze film air damping in MEMS", *Sens. Actuators A Phys.*, vol. 136, no. 1, pp. 3–27, 2007. DOI: 10.1016/j.sna.2007.01.008 (cited on p. 52).

[178] C. Rankl, V. Pastushenko, F. Kienberger, C. M. Stroh, and P. Hinterdorfer, "Hydrodynamic damping of a magnetically oscillated cantilever close to a surface", *Ultramicroscopy*, vol. 100, no. 3-4, pp. 301–308, 2004. DOI: 10.1016/j.ultramic.2003.12.014 (cited on p. 53).

[179] S. Kim and K. D. Kihm, "Temperature dependence of the near-wall oscillation of microcantilevers submerged in liquid environment", *Appl. Phys. Lett.*, vol. 90, no. 8, p. 081 908, 2007. DOI: 10.1063/1.2680052 (cited on p. 53).

[180] A. Fornari, M. Sullivan, H. Chen, C. Harrison, K. Hsu, F. Marty, and B. Mercier, "Experimental observation of inertia-dominated squeeze film damping in liquid", *J. Fluids Eng.*, vol. 132, no. 12, p. 121 201, 2010. DOI: 10.1115/1.4003150 (cited on p. 53).

[181] C. Ramakrishnan, A. Bieri, N. Sauter, S. Roizard, P. Ringler, S. A. Müller, K. N. Goldie, K. Enimanev, H. Stahlberg, B. Rinn, and T. Braun, "openBEB: open biological experiment browser for correlative measurements.", *BMC Bioinformatics*, vol. 15, p. 84, 2014. DOI: 10.1186/1471-2105-15-84 (cited on pp. 54, 89, 145).

[182] V. Pini, B. Tiribilli, C. M. C. Gambi, and M. Vassalli, "Dynamical characterization of vibrating AFM cantilevers forced by photothermal excitation", *Phys. Rev. B*, vol. 81, no. 5, p. 054 302, 2010. DOI: 10.1103/PhysRevB.81.054302 (cited on pp. 57, 90, 91).

[183] D. Sparks, R. Smith, M. Straayer, J. Cripe, R. Schneider, A. Chimbayo, S. Anasari, and N. Najafi, "Measurement of density and chemical concentration using a microfluidic chip", *Lab Chip*, vol. 3, no. 1, pp. 19–21, 2003. DOI: 10.1039/b211429a (cited on p. 68).

[184] J. Zhang, C. Dai, X. Su, and S. J. O'Shea, "Determination of liquid density with a low frequency mechanical sensor based on quartz tuning fork", *Sens. Actuators B Chem.*, vol. 84, pp. 123–128, 2002. DOI: 10.1016/S0925-4005(02)00012-6 (cited on p. 68).

[185] D. Sparks, R. Smith, V. Cruz, N. Tran, A. Chimbayo, D. Riley, and N. Najafi, "Dynamic and kinematic viscosity measurements with a resonating microtube", *Sens. Actuators A Phys.*, vol. 149, no. 1, pp. 38–41, 2009. DOI: 10.1016/j.sna.2008.09.013 (cited on p. 68).

[186] A. J. Ricco and S. J. Martin, "Acoustic wave viscosity sensor", *Appl. Phys. Lett.*, vol. 50, no. 21, pp. 1474–1476, 1987. DOI: 10.1063/1.97804 (cited on p. 68).

[187] Y. Liu, R. DiFoggio, K. Sanderlin, L. Perez, and J. Zhao, "Measurement of density and viscosity of dodecane and decane with a piezoelectric tuning fork over 299–448K and 0.1–137.9MPa", *Sens. Actuators A Phys.*, vol. 167, no. 2, pp. 347–353, 2011. DOI: 10.1016/j.sna.2011.03.017 (cited on p. 68).

[188] N. Doy, G. McHale, M. I. Newton, C. Hardacre, R. Ge, J. M. MacInnes, D. Kuvshinov, and R. W. Allen, "Small volume laboratory on a chip measurements incorporating the quartz crystal microbalance to measure the viscosity-density product of room temperature ionic liquids", *Biomicrofluidics*, vol. 4, no. 1, p. 014 107, 2010. DOI: 10.1063/1.3353379 (cited on p. 68).

[189] D. C. Duffy, J. C. McDonald, O. J. A. Schueller, and G. M. Whitesides, "Rapid Prototyping of Microfluidic Systems in Poly(dimethylsiloxane)", *Anal. Chem.*, vol. 70, no. 23, pp. 4974–4984, 1998. DOI: 10.1021/ac980656z (cited on p. 71).

[190] N.-S. Cheng, "Formula for the Viscosity of a Glycerol–Water Mixture", *Ind. Eng. Chem. Res.*, vol. 47, no. 9, pp. 3285–3288, 2008. DOI: 10.1021/ie071349z (cited on pp. 71, 78, 79).

[191] L. W. Bosart and A. O. Snoddy, "Specific Gravity of Glycerol", *Ind. Eng. Chem.*, vol. 20, no. 12, pp. 1377–1379, 1928. DOI: 10.1021/ie50228a032 (cited on pp. 71, 78, 79).

[192] T. Fukuma, "Wideband low-noise optical beam deflection sensor with photothermal excitation for liquid-environment atomic force microscopy", *Rev. Sci. Instrum.*, vol. 80, no. 2, p. 023 707, 2009. DOI: 10.1063/1.3086418 (cited on p. 75).

[193] P. B. Johnson and R. W. Christy, "Optical-Constants of Noble-Metals", *Phys. Rev. B*, vol. 6, no. 12, pp. 4370–4379, 1972. DOI: 10.1103/PhysRevB.6.4370 (cited on p. 76).

[194] T. Squires and S. R. Quake, "Microfluidics: Fluid physics at the nanoliter scale", *Rev. Mod. Phys.*, vol. 77, no. 3, pp. 977–1026, 2005. DOI: 10.1103/RevModPhys.77.977 (cited on p. 79).

[195] R. Seemann, M. Brinkmann, T. Pfohl, and S. Herminghaus, "Droplet based microfluidics", *Rep. Prog. Phys.*, vol. 75, no. 1, 2012. DOI: 10.1088/0034-4885/75/1/016601 (cited on p. 79).

[196] S. G. Kulichikhin, A. Y. Malkin, O. M. Polushkina, and V. G. Kulichikhin, "Rheokinetics of free-radical polymerization of acrylamide in an aqueous solution", *Polym. Eng. Sci.*, vol. 37, no. 8, pp. 1331–1338, 1997. DOI: 10.1002/pen.11779 (cited on pp. 80–82, 143, 144).

[197] M. Youssry, E. Lemaire, B. Caillard, A. Colin, and I. Dufour, "On-chip characterization of the viscoelasticity of complex fluids using microcantilevers", *Meas. Sci. Technol.*, vol. 23, no. 12, p. 125 306, 2012. DOI: 10.1088/0957-0233/23/12/125306 (cited on p. 82).

[198] C. Ricciardi, G. Canavese, R. Castagna, I. Ferrante, A. Ricci, S. L. Marasso, L. Napione, and F. Bussolino, "Integration of microfluidic and cantilever technology for biosensing application in liquid environment", *Biosens. Bioelectron.*, vol. 26, no. 4, pp. 1565–1570, 2010. DOI: 10.1016/j.bios.2010.07.114 (cited on p. 82).

[199] A. S. Bhangale, K. L. Beers, and R. A. Gross, "Enzyme-Catalyzed Polymerization of End-Functionalized Polymers in a Microreactor", *Macromolecules*, vol. 45, pp. 7000–7008, 2012. DOI: 10.1021/ma301178k (cited on p. 82).

[200] S. J. Sigg, F. Seidi, K. Renggli, T. B. Silva, G. Kali, and N. Bruns, "Horseradish Peroxidase as a Catalyst for Atom Transfer Radical Polymerization", *Macromol. Rapid Commun.*, vol. 32, no. 21, pp. 1710–1715, 2011. DOI: 10.1002/marc.201100349 (cited on p. 82).

[201] O. Cakmak, E. Ermek, N. Kilinc, S. Bulut, I. Baris, I. H. Kavakli, G. G. Yaralioglu, and H. Urey, "A cartridge based sensor array platform for multiple coagulation measurements from plasma", *Lab Chip*, vol. 15, pp. 113–120, 2014. DOI: 10.1039/C4LC00809J (cited on p. 86).

[202] J. Goodbread, M. Sayir, K. Hausler, and J. Dual, "Method and device for measuring the characteristics of an oscillating system", pat. 605 203, 1998 (cited on pp. 86, 89).

[203] B. Subramanian, N. Kim, W. Lee, D. A. Spivak, D. E. Nikitopoulos, R. L. McCarley, and S. A. Soper, "Surface Modification of Droplet Polymeric Microfluidic Devices for the Stable and Continuous Generation of Aqueous Droplets", *Langmuir*, vol. 27, no. 12, pp. 7949–7957, 2011. DOI: 10.1021/la200298n (cited on pp. 89, 147).

[204] F. Gielen, L. van Vliet, B. T. Koprowski, S. R. A. Devenish, M. Fischlechner, J. B. Edel, X. Niu, A. J. deMello, and F. Hollfelder, "A Fully Unsupervised Compartment-on-Demand Platform for Precise Nanoliter Assays of Time-Dependent Steady-State Enzyme Kinetics and Inhibition", *Anal. Chem.*, vol. 85, no. 9, pp. 4761–4769, 2013. DOI: 10.1021/ac400480z (cited on p. 89).

[205] T. R. Albrecht, P. Grütter, D. Horne, and D. Rugar, "Frequency modulation detection using high-Q cantilevers for enhanced force microscope sensitivity", *J. Appl. Phys.*, vol. 69, no. 2, p. 668, 1991. DOI: 10.1063/1.347347 (cited on p. 90).

[206] R. J. F. Bijster, J. de Vreugd, and H. Sadeghian, "Phase lag deduced information in photo-thermal actuation for nano-mechanical systems characterization", *Appl. Phys. Lett.*, vol. 105, no. 7, p. 073 109, 2014. DOI: 10.1063/1.4893461 (cited on p. 90).

[207] R. Krenger, "Nanomechanical resonators for fluid characterization: Applications and limitations", Master's thesis, University of Basel, 2014 (cited on p. 99).

[208] X. Huang, S. Li, J. S. Schultz, Q. Wang, and Q. Lin, "A MEMS affinity glucose sensor using a biocompatible glucose-responsive polymer", *Sens. Actuators B Chem.*, vol. 140, no. 2, pp. 603–609, 2009. DOI: 10.1016/j.snb.2009.04.065 (cited on p. 99).

[209] X. Huang, S. Li, E. Davis, C. Leduc, Y. Ravussin, H. Cai, B. Song, D. Li, D. Accili, R. Leibel, Q. Wang, and Q. Lin, "A MEMS differential viscometric sensor for affinity glucose detection in continuous glucose monitoring", *J. Micromech. Microeng.*, vol. 23, no. 5, p. 055 020, 2013. DOI: 10.1088/0960-1317/23/5/055020 (cited on p. 99).

[210] R. L. Baldwin and B. H. Zimm, "Are denatured proteins ever random coils?", *Proc. Natl. Acad. Sci. U.S.A.*, vol. 97, no. 23, pp. 12 391–12 392, 2000. DOI: 10.1073/pnas.97.23.12391 (cited on p. 99).

[211] I. Dufour, E. Lemaire, B. Caillard, H. Debéda, C. Lucat, S. M. Heinrich, F. Josse, and O. Brand, "Effect of hydrodynamic force on microcantilever vibrations: Applications to liquid-phase chemical sensing", *Sens. Actuators B Chem.*, vol. 192, pp. 664–672, 2014. DOI: 10.1016/j.snb.2013.10.106 (cited on p. 100).

[212] S. Jordens, P. A. Rühs, C. Sieber, L. Isa, P. Fischer, and R. Mezzenga, "Bridging the Gap between the Nanostructural Organization and Macroscopic Interfacial Rheology of Amyloid Fibrils at Liquid Interfaces", *Langmuir*, vol. 30, no. 33, pp. 10 090–10 097, 2014. DOI: 10.1021/la5020658 (cited on p. 100).

[213] A. H. Rosenberg and F. W. Studier, "Intrinsic viscosity of native and single-stranded T7 DNA and its relationship to sedimentation coefficient", *Biopolymers*, vol. 7, no. 5, pp. 765–774, 1969. DOI: 10.1002/bip.1969.360070511 (cited on p. 100).

[214] J. D. Adams, A. Nievergelt, B. W. Erickson, C. Yang, M. Dukic, and G. E. Fantner, "High-speed imaging upgrade for a standard sample scanning atomic force microscope using small cantilevers", *Rev. Sci. Instrum.*, vol. 85, no. 9, p. 093 702, 2014. DOI: 10.1063/1.4895460 (cited on p. 106).

[215] H. Y. Sun, "Thin lens equation for a real laser beam with weak lens aperture truncation", *Opt. Eng.*, vol. 37, no. 11, pp. 2906–2913, 1998. DOI: 10.1117/1.601877 (cited on p. 106).

[216] R. Enning, D. Ziegler, A. Nievergelt, R. Friedlos, K. Venkataramani, and A. Stemmer, "A high frequency sensor for optical beam deflection atomic force microscopy", *Rev. Sci. Instrum.*, vol. 82, no. 4, p. 043 705, 2011. DOI: 10.1063/1.3575322 (cited on p. 108).

[217] T. Fukuma, M. Kimura, K. Kobayashi, K. Matsushige, and H. Yamada, "Development of low noise cantilever deflection sensor for multienvironment frequency-modulation atomic force microscopy", *Rev. Sci. Instrum.*, vol. 76, no. 5, p. 053 704, 2005. DOI: 10.1063/1.1896938 (cited on pp. 110, 111).

[218] J. G. Ziegler and N. B. Nichols, "Optimum settings for automatic controllers", *Trans. ASME*, vol. 64, pp. 759–768, 1942 (cited on p. 116).

[219] R. Motamedi and P. M. Wood-Adams, "Measurement of fluid properties using an acoustically excited atomic force microscope micro-cantilever", *J. Rheol.*, vol. 54, no. 5, pp. 959–980, 2010. DOI: 10.1122/1.3460907 (cited on p. 139).

[220] T. C. Kaufmann, A. Engel, and H.-W. Rémigy, "A Novel Method for Detergent Concentration Determination", *Biophys. J.*, vol. 90, no. 1, pp. 310–317, 2006. DOI: 10.1529/biophysj.105.070193 (cited on p. 147).

[221] A. F. Stalder, T. Melchior, M. Müller, D. Sage, T. Blu, and M. Unser, "Colloids and Surfaces A: Physicochemical and Engineering Aspects", *Colloid Surface A*, vol. 364, no. 1-3, pp. 72–81, 2010. DOI: 10.1016/j.colsurfa.2010.04.040 (cited on p. 147).

[222] C. A. Schneider, W. S. Rasband, and K. W. Eliceiri, "NIH Image to ImageJ: 25 years of image analysis", *Nat. Methods*, vol. 9, no. 7, pp. 671–675, 2012. DOI: 10.1038/nmeth.2089 (cited on p. 147).

Publications and Meetings

Peer-reviewed articles

B. A. Bircher, R. Krenger, and T. Braun, "Automated high-throughput viscometer using resonant nanomechanical sensors", *In preparation*, 2015.

B. A. Bircher, R. Krenger, and T. Braun, "Influence of squeeze film damping on higher-mode microcantilever vibrations in liquid", *EPJ Tech. Instrum.*, vol. 1, p. 10, 2014. DOI: 10.1140/epjti/s40485-014-0010-6.

B. A. Bircher, L. Duempelmann, H. P. Lang, C. Gerber, and T. Braun, "Photothermal excitation of microcantilevers in liquid: effect of the excitation laser position on temperature and vibrational amplitude", *Micro Nano Lett.*, vol. 8, no. 11, pp. 770–774, 2013. DOI: 10.1049/mnl.2013.0352.

B. A. Bircher, L. Duempelmann, K. Renggli, H. P. Lang, C. Gerber, N. Bruns, and T. Braun, "Real-time viscosity and mass density sensors requiring microliter sample volume based on nanomechanical resonators.", *Anal. Chem.*, vol. 85, no. 18, pp. 8676–8683, 2013. DOI: 10.1021/ac4014918.

S. Kemmerling, S. A. Arnold, B. A. Bircher, N. Sauter, C. Escobedo, G. Dernick, A. Hierlemann, H. Stahlberg, and T. Braun, "Single-cell lysis for visual analysis by electron microscopy.", *J. Struct. Biol.*, vol. 183, no. 3, pp. 467–473, 2013. DOI: 10.1016/j.jsb.2013.06.012.

R. R. Grüter, Z. Khan, R. Paxman, J. W. Ndieyira, B. Dueck, B. A. Bircher, J. L. Yang, U. Drechsler, M. Despont, R. A. McKendry, and B. W. Hoogenboom, "Disentangling mechanical and mass effects on nanomechanical resonators", *Appl. Phys. Lett.*, vol. 96, no. 2, p. 023 113, 2010. DOI: 10.1063/1.3285169.

Conference proceedings

B. A. Bircher and T. Braun, "Microcantilever vibrations to characterize fluids with high temporal resolution", in *Proceedings of the 11th Nanomechanical Sensing Workshop (NMC) 2014*, Madrid, Spain, 2014, pp. 26–27.

B. A. Bircher, L. Duempelmann, K. Renggli, H. P. Lang, C. Gerber, and T. Braun, "Higher mode vibrations of nanomechanical resonators for time-resolved liquid viscosity and mass density measurements", in *Proceedings of the 10th Nanomechanical Sensing Workshop (NMC) 2013*, Stanford University, Stanford, CA, 2013, pp. 252–253.

Oral presentations

B. A. Bircher, "Label-free characterization of chemical and biological processes through fluid properties", in *SNI Annual Meeting 2014*, Lenzerheide, Switzerland, 2014.

B. A. Bircher, "High-speed characterization of fluids using microcantilevers", in *11th Nanomechanical Sensing Workshop (NMC) 2014*, Madrid, Spain, 2014.

B. A. Bircher, "Time-resolved viscosity and mass density measurements unsing nanomechanical resonators", in *10th Nanomechanical Sensing Workshop (NMC) 2013*, Stanford, CA, USA, 2013.

B. A. Bircher, "in situ viscosity measurements using micromechanical resonators", in *ICN+T 2012*, Paris, France, 2012.

Poster presentations

B. A. Bircher, R. Krenger, J. Pollard, H. Stahlberg, J. Köser, N. Bruns, and T. Braun, "High-speed viscosity screening using microcantilevers", in *Swiss Nano Convention 2014*, Windisch, Switzerland, 2014.

B. A. Bircher, L. Duempelmann, K. Renggli, H. P. Lang, C. Gerber, N. Bruns, and T. Braun, "Time-resolved viscosity and mass density measurements using nanomechanical resonators in microliter volumes", in *PhD summer school: Micro- and nanotechnology for label-free sensing*, Technical University of Denkmark (DTU), Lyngby, Denmark, 2013.

B. A. Bircher, L. Duempelmann, K. Renggli, H. P. Lang, C. Gerber, N. Bruns, and T. Braun, "Time-resolved Viscosity Measurements using Microliter Samples to Monitor Polymerization", in *Swiss Nano Convention 2013*, Basel, Switzerland, 2013.

B. A. Bircher, H. P. Lang, C. Gerber, H. Stahlberg, and T. Braun, "Towards label- and functionalization-free sensing of molecular interactions", in *1st International SystemsX Conference on Systems Biology*, Basel, Switzerland, 2011.